Physics and modelling of unsteady turbulent flows around aerodynamic and hydrodynamic structures at high Reynold number by numerical simulation

Damien Szubert

To cite this version:

Damien Szubert. Physics and modelling of unsteady turbulent flows around aerodynamic and hydrodynamic structures at high Reynold number by numerical simulation. Fluids mechanics [physics.class-ph]. Institut National Polytechnique de Toulouse - INPT, 2015. English. NNT : 2015INPT0071 . tel-04246095

HAL Id: tel-04246095
https://theses.hal.science/tel-04246095
Submitted on 17 Oct 2023

THÈSE

En vue de l'obtention du

DOCTORAT DE L'UNIVERSITÉ DE TOULOUSE

Délivré par :

Institut National Polytechnique de Toulouse (INP Toulouse)

Discipline ou spécialité :

Dynamique des fluides

Présentée et soutenue par :

M. DAMIEN SZUBERT
le lundi 29 juin 2015

Titre :

ANALYSE PHYSIQUE ET MODELISATION D'ECOULEMENTS TURBULENTS INSTATIONNAIRES AUTOUR D'OBSTACLES AERODYNAMIQUES A HAUT NOMBRE DE REYNOLDS PAR SIMULATION NUMERIQUE

Ecole doctorale :

Mécanique, Energétique, Génie civil, Procédés (MEGeP)

Unité de recherche :

Institut de Mécanique des Fluides de Toulouse (I.M.F.T.)

Directeur(s) de Thèse :

MME MARIANNA BRAZA
M. GILLES HARRAN

Rapporteurs :

M. BRUNO KOOBUS, UNIVERSITE MONTPELLIER 2
M. GEORGE BARAKOS, UNIVERSITY OF LIVERPOOL

Membre(s) du jury :

M. ALAIN DERVIEUX, INRIA SOPHIA ANTIPOLIS, Président
M. FLAVIEN BILLARD, DASSAULT AVIATION, Membre
M. FRANK THIELE, TECHNISCHE UNIVERSITAT BERLIN, Membre
M. GILLES HARRAN, INP TOULOUSE, Membre
M. JEAN-PAUL DUSSAUGE, UNIVERSITE AIX-MARSEILLE 1, Membre
Mme MARIANNA BRAZA, INP TOULOUSE, Membre

Contents

Acknowledgements

These three years and half spent in the Institut de Mécanique des Fluides de Toulouse let me time and opportunities to meet many people, researchers, colleagues, students, and friends I want to thank here.

I want above all to express my deepest thanks to my supervisor Marianna BRAZA, who offered to me the opportunity to work in a practical way on fluid dynamics, and more particularly on turbulence modelling in the context of the Computational Fluid Dynamics, involving various test cases described in this manuscript. I was able to experience supervision of small groups of students, exchanging with them on technical and scientifical aspects. I also thank her a lot for helping me to survive in Stanford during summer 2014 after loosing my credit card, just before leaving France. Finally, I appreciated a lot the discussions we had concerning our vision of the World, society and humanity, with our respective experience and skills.

I am also very thankful to Prof. George Barakos for discussions we had regarding relations between research and industry, and for sharing is point of view regarding the situation of research more generally. I thank him as well as Flavien Billard, for their comments and corrections of this manuscript, as well as for sharing their special point of view on specific test cases.

I thank Prof. George Barakos and Prof. Bruno Koobus for having accepted the invitation to review my thesis. I also wish to thank all other members of the examining committee: Alain Dervieux, Jean-Paul Dussauge, Gilles Harran and Prof. Frank Thiele. I also thank Loïc Boudet, from DGA, and Prof. Julian Hunt, for taking part of the discussion during the defense. I would like to particularly thank Prof. Hunt for sharing his experience and his knowledge that conducted, among other, to the redaction of an article published in the Journal of Fluid Dynamics.

I want to express special thanks to Fernando Grossi, who helped a lot on physical and technical aspects when I arrived at IMFT for my internship and then for the beginning of my PhD while he was in first year of his PhD, as well as during congresses. I appreciated a lot his point of view regarding the environment and method of work.

I would not have been able to do all the work presented here withtout the precious assistance of Yannick Hoarau, regarding mesh generation in particular, but also for technical, programming aspects, despite his huge amount of work, and I am very grateful for this. For this last point, I also want to thank Jan Vos, from

CFS Engineering, coordinator of the NSMB consortium, and who recieved me few days in his head quarters for implementing the transition model based on transport equations in NSMB.

My deepest gratitude to Parviz Moin, director of the Center for Turbulence Research, and his team, who received Marianna and me in Stanford during summer 2014, and Ik Jang, for the collaboration there. It was a great opportunity to discover a different work environment as well as the culture and lifestyle in Stanford and in the Bay Area in general.

I thank again Gilles Harran, as well as Alain Sévrain, for their precious contribution to improve my expertise in signal processing as well as in fluid-structure interactions.

My grateful thanks to Thibaut Deloze, Ioannis Asproulias, Wouter Van Veen, Antonio Jimenez Garcia, Saul Ferriera Perez, Vilas Shinde, Rogier Giepman and the BEI students for their precious contributions to the work presented in this manuscript. I also thank them, as well as Rémi Bourguet, Johannes Scheller, Mathieu Marrant, Julie Albagnac, Simon Gsell and Christophe Korbuly for the enjoyable moments we had at the lab.

I thank all the services of the laboratory, from administration (Florence Colombies, Nadine Mandement, Aurélie Labrador, Denis Bourrel, Sandrine Chupin) to computing, reprography, documentation, as well as the direction of the lab, François Charru and Éric Climent, and of the group EMT2, Carlo Cossu, that allow researchers and students to work in a great environment in the IMFT and contribute to the cohesion of the research teams.

Finally, my relatives. First of all, Lucas, who offered me opportunities to breath, to relieve, to open my mind, and to consider more and less seriously the future. I thank him for this and for his support during tough moments, during the finale rush in particular. I thank also Yann, with whom I shared more or less a similar journey, and for funny and cultural moments we had in Toulouse as well as for the discussions about the world in general. Thank you Amély, for being there for years, even if I moved quite far from you and you little family. I gratefully thank my parents, who really cared about my appetite and curiosity to explore and discover that crazy, incredible world, as well as my brother and sister.

A huge thank to Ciel mon doctorat. Any PhD student will understand.

The work presented in this memoir has been made possible thanks to the fellowship of the DGA (Direction Général de l'Armement) and the funding allocated by the ANR (Agence Nationale pour la Recherche) in the context of the Baresafe project (ANR-11-MONU-0004)

Nomenclature

Latin symbols

a	Speed of sound
c	Chord length
C_D	Drag coefficient
C_L	Lift coefficient
C_p	Pressure coefficient, $C_p = (P - P_\infty)/(0.5\rho_\infty U_\infty^2)$
d_w	Wall distance
D	Cylinder diameter
f_{VK}	Vortex-shedding frequency of the von Kármán instability
H	Shape factor
k	Turbulent kinetic energy
l	Turbulence length scale
L	Distance between cylinders center
P	Static pressure
Re	Chord and diameter-based Reynolds number
Re_θ	Momentum-thickness Reynolds number, $\rho\theta U_\infty/\mu$
$\mathrm{Re}_{\theta t}$	Transition onset momentum-thickness Reynolds number
Re_ν	Vorticity Reynolds number, $\rho y^2\Omega/\mu$
St	Strouhal number ($\mathrm{St} = f_{VK}D/U_\infty$)
t	Physical time
$t*$	Non-dimensionalised time ($t* = tU_\infty/c$ or $t* = tU_\infty/D$)
Tu	Turbulence intensity, $100(2k/3)^{1/2}/U$
U	Local velocity
U_∞	Inlet reference velocity
x_t	Laminar-turbulent transition location

Greek symbols

δ_{99}	Boundary-layer thickness
δ^*	Displacement thickness
δ_{ij}	Kronecker delta
ε	Turbulence dissipation rate
γ	Intermittency factor
γ_{f}, γ_{air}	specific heat ratio of the fluid and air
λ_θ	Pressure gradient parameter
μ	Dynamic viscosity
ν	Kinematic viscosity, μ/ρ
ν_t	Eddy viscosity
ω	Specific turbulence dissipation rate
Ω	Absolute value of vorticity
ρ	Fluid density
θ	Momentum thickness

Abbreviations

ATAAC	Advanced Turbulence Simulation for Aerodynamic Application Challenges
BSL	Menter's Baseline model
CFD	Computational Fluid Dynamics
DDES	Delayed Detached-Eddy Simulation
DNS	Direct Numerical Simulation
MIV	Movement induced vibration
NSMB	Navier-Stokes Multiblock
OSBLI	Oblique-shock/boundary-layer interaction
PIV	Particle Image Velocimetry
POD	Proper Orthogonal Decomposition
PSD	Power Spectral Density
RANS	Reynolds-averaged Navier-Stokes
RMS	Root mean square, $\mathrm{RMS}(x) = \sqrt{1/N\,(x_1^2 + x_2^2 + \ldots + x_N^2)}$
SA	Spalart-Allmaras one-equation model
SST	Shear Stress Transport model
SWBLI	Shock-wave/boundary-layer interaction
TFAST	Transition Location Effect on Shock-Wave/Boundary-Layer Interaction
TNT	Turbulent/non-turbulent
TUD	Technische Universiteit Delft or Delft University of Technology
URANS	Unsteady Reynolds-averaged Navier-Stokes
VIV	Vortex induced vibration
WM-LES	Wall-modelled Large Eddy Simulation

Mathematics

∇	Gradient, $\nabla \mathbf{U}(\mathbf{x}) = \left(\frac{\partial U_x(\mathbf{x})}{\partial x}, \frac{\partial U_y(\mathbf{x})}{\partial y}, \frac{\partial U_z(\mathbf{x})}{\partial z}\right)$, with $\mathbf{x} = (x, y, z)$
$\nabla\cdot$	Divergence, $\nabla \cdot \mathbf{U}(\mathbf{x}) = \mathrm{div}(\mathbf{U}(\mathbf{x})) = \frac{\partial U_x(\mathbf{x})}{\partial x} + \frac{\partial U_y(\mathbf{x})}{\partial y} + \frac{\partial U_z(\mathbf{x})}{\partial z}$
$\otimes$	Tensor product

Chapter 1

Introduction

Contents

1.1 Objectives of this thesis

The present thesis investigates high-Reynolds number unsteady turbulent flows interacting with the solid wall from the low subsonic to the high-transonic and supersonic regimes, by means of numerical simulation. A specific attention is paid to the prediction of unsteady separation, including fluid-structure interaction aspects, as well as shock/boundary-layer and shock-vortex interaction. A considerable effort is devoted in the state of the fundamental research and applications domains in order to improve the simulation and turbulence modelling approaches (statistical (RANS, URANS), Large-Eddy Simulations (LES) and Hybrid (RANS-LES)) for the prediction of unsteady separation and reattachment, of natural instabilities and vortex structures responsible for movement induced vibration and acoustic noise around bodies, as well as prediction of shock-wave/boundary-layer interaction, a crucial issue for next generation of ‘laminar’ wing design with reduced drag and

CO_2 emissions. A considerable effort is devoted internationally in order to provide more efficient High-Fidelity (Hi-Fi) approaches and to carry out modal analysis by suitable and specific methods, in order to elaborate reliable Reduced Order Modelling (ROM), which will allow for faster design cycles. The need of improvement of Hi-Fi and ROM approaches has been emphasized in a number of important international conferences as the 4th and 5th hybrid RANS-LES methods symposia (2012[1], 2014[2]), the ERCOFTAC symposium "Unsteady separation in Fluid-Structure interaction" 2013[3], the biannual "Center for Turbulence Research" summer programme 2014[4] and the "Whither Turbulence and Big Data" symposium 2015, among other. Through these meetings clearly appears the continuous need of advancing in turbulence modelling efforts in crucial regimes governed by strong adverse pressure gradients, by movement/deformation of the solid structure and by compressibility effects in order to provide more improved predictions for the design.

This thesis aims at contributing in this context by studying turbulence modelling approaches and their ability to capture important phenomena and crucial instabilities arising in aerodynamics and hydrodynamics, as well as the unsteady loads evolution, crucial for the design and to develop a detailed physical analysis of the flow phenomena arising in the near-wall and near-wake regions. Furthermore, it aims at providing a detailed modal analysis of the complex flow structure in order to prepare efficient reconstruction of the fields able to be used further on in ROM. These investigations have been carried out by means of well focused test-cases from the European Research programmes of the FP7: ATAAC[5] (Advanced Turbulence simulations for Aerodynamic Application Challenges), coordinated by DLR - Göttingen, and TFAST[6] (Transition location effect on shock wave boundary layer interaction), coordinated by IMP - Gdansk (Polish Academy of Science), as well as from the national ANR[7] (Agence Nationale pour la Recherche) research programme Baresafe (Simulation of Safety Barrier Reliability), coordinated by EDF (Electricité de France).

1.2 Governing equations in fluid dynamics

In his Ph.D. thesis manuscript, Grossi (2014) described in a very comprehensive way the principles of the transport and governing equations in fluid dynamics. This section re-uses his work.

Fluid motion is governed by three fundamental laws: conservation of mass, of momentum and of energy. These principles can be expressed through conservation laws, which describe the evolution of the conserved quantities in a given domain by means of transport equations. In the governing equations of fluid dynamics the flowfield is treated as a continuous medium. This means that the mean free path of the fluid molecules is assumed to be very small compared to the length scale charac-

---

[1] Fu et al. (2012), http://www.hrlm-4th.org

[2] Girimaji et al. (2014)

[3] http://www.smartwing.org/ercoftac

[4] https://ctr.stanford.edu

[5] http://cfd.mace.manchester.ac.uk/ATAAC/WebHome

[6] http://tfast.eu/

[7] http://www.agence-nationale-recherche.fr

teristic of the problem (e.g. the diameter of a cylinder or the chord of an airfoil) so that the interaction between the fluid molecules is much more important than their individual motion. Therefore, the whole system can be investigated using continuum mechanics imagining a fluid particle a as very large number of fluid molecules within a small volume. All flow properties (as velocity, pressure, temperature, viscosity, etc.) are in fact mean properties which reflect the statistical motion of the fluid molecules at each point of the flowfield.

1.2.1 General transport equation

Assuming that ϕ is a scalar conserved quantity per unit volume and that V is an arbitrary control volume fixed in space, the conservation law of ϕ states that the amount of this quantity inside V can vary as a result of its net flux across the surface S enclosing V and due to volume and surface sources of ϕ only. This law can be formalized in integral form as:

$$\frac{\partial}{\partial t}\int_V \phi dV = -\int_S (\mathbf{F_C}\cdot\mathbf{n})\,dS - \int_S (\mathbf{F_D}\cdot\mathbf{n})\,dS + \int_V Q_V dV + \int_S (\mathbf{Q_S}\cdot\mathbf{n})\,dS. \tag{1.1}$$

The term on the left-hand side of Eq. 1.1 is the time variation of the total amount of ϕ inside V. The flux of ϕ across the volume boundaries is usually split into two components of different physical nature. $\mathbf{F_C}$ is the 'convective flux', which corresponds to the time rate of ϕ crossing the surface S per unit surface. Convective fluxes are directional, being proportional to and aligned with the local flow velocity $\mathbf{U} = [U_x, U_y, U_z]^T$ and are given by $\mathbf{F_C} = \phi\mathbf{U}$. The second contribution, $\mathbf{F_D}$, is called 'diffusive flux' and is proportional and opposite to the gradient of ϕ. It is generalized by the 'law of Fick':

$$\mathbf{F_D} = -\kappa\rho\nabla\left(\frac{\phi}{\rho}\right). \tag{1.2}$$

where κ is a diffusivity coefficient. The physical mechanism of diffusion is related to molecular agitation and can have a net effect even in a fluid at rest if the distribution of ϕ is inhomogeneous. The minus signs in front of the fluxes are due to the fact that the surface normal vector $\mathbf{n}$ is considered positive when pointing outwards (i.e. the dot products are negative when ϕ enters the control volume). Q_V and $\mathbf{Q_S}$ are the volume and surface sources, respectively. The resulting expression is a convection-diffusion equation in integral form, which allows the fluxes to be discontinuous (as in the case of shock-waves). Moreover, in the absence of volume forces, the variation of the conserved variable inside the control volume depends only on the net flux of ϕ across the boundaries. A local differential form of the conservation law can be easily derived from the integral form. Using the divergence theorem (Gauss' theorem), the surface integrals in Eq. 1.1 can be replaced by volume integrals of the divergences of the fluxes and surface sources. Also, assuming that the control volume is fixed in space, the time derivative on the left-hand side of the equation can be placed inside the integral (Reynolds' transport theorem). Finally, since the integral form is written for an arbitrary control volume, the volume integrals can be dropped, yielding:

$$\frac{\partial \phi}{\partial t} = -\nabla \cdot \mathbf{F_C} - \nabla \cdot \mathbf{F_D} + Q_V + \nabla \cdot \mathbf{Q_S}, \tag{1.3}$$

which is valid at any point in the flowfield and requires the fluxes to be continuously differentiable (which is not always the case). It shows that surface sources are mathematically equivalent to fluxes and may be regarded in the same way. Moreover, if an equation is in conservative form, all the space derivative terms can be grouped as a divergence operator. Substituting the expressions obtained for the fluxes and rearranging the terms, one obtains:

$$\frac{\partial \phi}{\partial t} = -\nabla \cdot (\phi \mathbf{U}) + \nabla \cdot \left[\kappa\rho \left(\frac{\phi}{\rho}\right)\right] + Q_V + \nabla \cdot \mathbf{Q_S}. \tag{1.4}$$

In general, convective fluxes are non linear and yield first-order spatial derivatives while diffusive fluxes generate second-order ones. In the case where the conserved quantity is a vector, each component of $\boldsymbol{\phi}$ can be regarded as a scalar quantity and the above equations can be applied. Alternatively, the equations written for a scalar property can be slightly modified, replacing the fluxes and surface sources by tensors and the volume source by a vector. Hence, the integral conservation equation for a vector reads:

$$\frac{\partial}{\partial t}\int_V \boldsymbol{\phi} dV = -\int_S \left(\overline{\overline{\mathbf{F_C}}} \cdot \mathbf{n}\right) dS - \int_S \left(\overline{\overline{\mathbf{F_D}}} \cdot \mathbf{n}\right) dS + \int_V \mathbf{Q_V} dV + \int_S \left(\overline{\overline{\mathbf{Q_S}}} \cdot \mathbf{n}\right) dS. \tag{1.5}$$

where $\overline{\overline{\cdot}}$ stands for tensor. In differential form, Eq. 1.5 becomes:

$$\frac{\partial \boldsymbol{\phi}}{\partial t} = -\nabla \cdot \overline{\overline{\mathbf{F_C}}} - \nabla \cdot \overline{\overline{\mathbf{F_D}}} + \mathbf{Q_V} + \overline{\overline{\mathbf{Q_S}}}. \tag{1.6}$$

Using tensorial notation (for the sake of simplicity), the convective and diffusive fluxes are given by:

$$(F_C)_{ij} = \phi_i U_j, \qquad (F_D)_{ij} = -\kappa\rho \frac{\partial}{\partial x_j}\left(\frac{\phi_i}{\rho}\right). \tag{1.7}$$

1.2.2 The Navier-Stokes equations

In this section, the three fundamental conservation laws that describe fluid motion are derived, namely the continuity equation, the momentum equation and the energy equation. For viscous flows, the resulting set of equations is commonly known as the ‘Navier-Stokes equations’.

1.2.2.1 Continuity equation

The principle of conservation of mass in a fluid is expressed through the continuity equation, which states that mass cannot be created nor destroyed in the system. The transported quantity is the fluid density ρ, which is a scalar quantity and has units of mass per unity volume. The continuity equation does not present a diffusive flux term since there is no mass diffusion in a fluid at rest. By replacing ϕ by ρ in

Eq. 1.1 and suppressing all source terms, the integral formulation of the continuity equation is obtained:

$$\frac{\partial}{\partial t}\int_V \rho dV + \int_S \rho(\mathbf{U}\cdot\mathbf{n})ds = 0. \tag{1.8}$$

The term in the left-hand side of Eq. 1.8 represents the time rate of change of mass inside a given control volume and the surface integral on the right side is the total mass flow across its boundaries. For the latter, negative values mean a net flux entering the control volume while positive ones correspond to an outflow. Applying Gauss' and Reynolds' theorems, the continuity equation written in differential form reads:

$$\frac{\partial\rho}{\partial t} + \nabla\cdot(\rho\mathbf{U}) = 0. \tag{1.9}$$

For incompressible flows, ρ is constant and Eq. 1.9 reduces to $\nabla\cdot\mathbf{U} = 0$.

1.2.2.2 Momentum equation

Newton's second law states that the variation of the momentum of a body is equal to the net force acting on it. By applying this fundamental principle to a fluid, one obtains the momentum equation, which expresses the conservation of momentum in the fluid system. Since the momentum of a infinitesimally small fluid element of volume dV is defined as $\rho\mathbf{U}dV$, the transported variable in the momentum equation is the momentum per unit volume $\rho\mathbf{U}$, which is a vector quantity. Alternatively, the conservation of momentum can be expressed by means of three separated transport equations for the individual components of momentum ρU_x, ρU_y and ρU_z. As the continuity equation, the momentum equation has no diffusive flux since, by definition, the velocity (and thus the momentum) is zero in a fluid at rest. Hence, Eq. 1.5 applied for the transport of momentum yields:

$$\frac{\partial}{\partial t}\int_V \rho\mathbf{U}dV + \int_S \rho\mathbf{U}\left(\mathbf{U}\cdot\mathbf{n}\right)dS = \int_V \mathbf{Q_V}dV + \int_S\left(\overline{\overline{\mathbf{Q_S}}}\cdot\mathbf{n}\right)dS. \tag{1.10}$$

where the volume sources $\mathbf{Q_V}$ represent all existing body forces per unit volume, which act over dV and are also called external or volume forces (e.g. Coriolis, gravitational, centrifugal and electromagnetic forces). The surface sources $\overline{\overline{\mathbf{Q_S}}}$ represent the second kind of forces that act on a fluid element: the surface (or internal) forces. In this group, there are the static pressure and the viscous stresses, which have a net effect only on the boundary of the volume. The pressure P exerted by the surroundings acts in the direction normal to S, pointing inwards the fluid element. Therefore, the surface sources can be computed as $-P\overline{\overline{\mathbf{I}}} + \overline{\overline{\boldsymbol{\sigma}}}$, where $\overline{\overline{\mathbf{I}}}$ is the unit tensor and $\overline{\overline{\boldsymbol{\sigma}}}$ is the viscous stress tensor. In aerodynamics, the effect of the gravitational force on the fluid elements can be neglected and other volume sources are usually not present. Hence, the momentum equation becomes:

$$\frac{\partial}{\partial t}\int_V \rho\mathbf{U}dV + \int_S \rho\mathbf{U}\left(\mathbf{U}\cdot\mathbf{n}\right)dS = -\int_S P\left(\overline{\overline{\mathbf{I}}}\cdot\mathbf{n}\right)dS + \int_S\left(\overline{\overline{\sigma}}\cdot\mathbf{n}\right)dS, \tag{1.11}$$

or in differential form:

$$\frac{\partial \rho \mathbf{U}}{\partial t} + \nabla \cdot (\rho \mathbf{U} \otimes \mathbf{U}) = -\nabla P + \nabla \cdot \overline{\overline{\sigma}}. \tag{1.12}$$

Since air behaves as a Newtonian fluid, the shear stresses are proportional to the velocity gradients. Using tensorial notation, the general form of the viscous stress tensor σ_{ij} reads:

$$\sigma_{ij} = \mu \left(\frac{\partial U_j}{\partial x_i} + \frac{\partial U_i}{\partial x_j} \right) + \lambda \frac{\partial U_k}{\partial x_k} \delta_{ij}, \tag{1.13}$$

where the first index in the subscript indicates the direction normal to the plane on which the stress is acting while the second one gives its direction. If $i = j$ the component is a 'normal stress' and otherwise, a 'shear stress'. Shear stresses are generated by the friction resulting from the relative motion of a body immersed in a fluid or of different fluid layers. In Eq. 1.13, μ is the dynamic viscosity and λ is the second viscosity of the fluid. According to Stoke's hypothesis for a Newtonian fluid in local thermodynamic equilibrium:

$$\lambda + \frac{2}{3}\mu = 0. \tag{1.14}$$

This relation is called 'bulk viscosity' and is a property of the fluid. It is responsible for the energy dissipation in a fluid of smooth temperature distribution submitted to expansion or compression at a finite rate. So far, there is no experimental evidence that Eq. 1.14 does not hold except for extremely high temperatures or pressures. Using relation 1.14, Eq. 1.13 becomes:

$$\sigma_{ij} = \mu \left(\frac{\partial U_j}{\partial x_i} + \frac{\partial U_i}{d} \partial x_j \right) - \frac{2\mu}{3} \frac{\partial U_k}{\partial x_k} \delta_{ij}. \tag{1.15}$$

Although the viscous stresses were derived as being surface sources, they play the role of diffusive fluxes of momentum (thus requiring fluid motion), with the dynamic viscosity acting as the diffusion coefficient.

1.2.2.3 Energy equation

In fluid dynamics, the conservation law for energy is obtained from the application of the first law of thermodynamics to a control volume. It expresses the fact that the time variation of the total energy inside a control volume is obtained from the balance between the work of the external forces acting on the volume and the net heat flux into it. In the energy equation, the transported quantity is the total energy per unit volume ρE, where E is the total energy per unit mass. It is defined as the sum of the internal energy per unit mass e (a state variable) and the kinetic energy per unit mass $|\mathbf{U}|^2/2$. The transport equation features a diffusive flux term which depends only on the gradient of e since, by definition, $\mathbf{U} = 0$ at rest. It accounts for the effects of thermal conduction related to molecular agitation and is given by $\mathbf{F_D} = -\gamma_{\mathrm{f}} \rho \kappa \nabla e$, where γ_{f} is the ratio of specific heat coefficients of the considered fluid, $\gamma_{\mathrm{f}} = c_p/c_v$. For dry air at 20°C, $\gamma_{\mathrm{air}} = 1.4$. Since the internal energy can be expressed in terms of the static temperature T by $e = c_v T$, heat diffusion is more usually described using Fourrier's law:

$$\mathbf{F_D} = -\gamma_{\mathrm{f}} \rho \kappa \nabla e = -\kappa \nabla T, \tag{1.16}$$

where k is the thermal conductivity coefficient ($k = c_p \rho \kappa$) and the negative sign accounts for the fact that heat is transferred from high- towards low-temperature regions.

Surface sources contribute to the energy equation through the work done by the pressure and viscous stresses (both normal and shear parts) acting on the boundaries of the fluid element $\mathbf{Q_S} = -p\mathbf{U} + (\overline{\overline{\sigma}} \cdot \mathbf{U})$. Therefore, neglecting the work done by body forces as well as that of internal energy sources (e.g. radiation, chemical reactions, etc.), the integral form of the energy equation reads:

$$\begin{aligned}\frac{\partial}{\partial t}\int_V \rho E dV + \int_S \rho E(\mathbf{U}\cdot\mathbf{n})dS = -\int_S P(\mathbf{U}\cdot\mathbf{n})dS \\ + \int_S (\overline{\overline{\sigma}}\cdot\mathbf{U})\cdot\mathbf{n}dS + \int_S k\left(\nabla T\cdot\mathbf{n}\right)dS,\end{aligned} \tag{1.17}$$

which is also frequently written in terms of the total enthalpy:

$$H = h + \frac{|\mathbf{U}|^2}{2} = E + \frac{P}{\rho}, \tag{1.18}$$

where h is the enthalpy per unit mass. This yields:

$$\frac{\partial}{\partial t}\int_V \rho E dV + \int_S \rho H(\mathbf{U}\cdot\mathbf{n})dS = \int_S (\overline{\overline{\sigma}}\cdot\mathbf{U})\cdot\mathbf{n}dS + \int_S k\left(\nabla T\cdot\mathbf{n}\right)dS, \tag{1.19}$$

In differential form, Eq. 1.17 can be rewritten as:

$$\frac{\partial \rho E}{\partial t} + \nabla\cdot\rho\mathbf{U}E = -\nabla\cdot P\mathbf{U} + \nabla\cdot(\overline{\overline{\sigma}}\cdot\mathrm{U}) + \nabla\cdot\left(k\nabla T\right). \tag{1.20}$$

1.2.2.4 Additional relations

In order to close the system of the Navier-Stokes equations, additional relations between the flowfield variables are needed. In aerodynamics, the air is usually modeled as a perfect gas and, therefore, a thermodynamic relation between the state variables P, ρ and T can be obtained by means of the equation of state:

$$P = \rho R T, \tag{1.21}$$

where $R = c_p - c_v$ is the gas constant per unit mass (for a perfect gas, c_p, c_v and thus γ_{f} and R are constants). In compressible viscous flow, heating due to high velocity gradients is responsible for variations in the fluid viscosity. To account for such effect, a common practice in aerodynamics is to adopt Sutherland's law (Sutherland, 1893), which expresses the dynamic viscosity μ of an ideal gas as a function of temperature only as:

$$\frac{\mu}{\mu_{\mathrm{ref}}} = \left(\frac{T}{T_{\mathrm{ref}}}\right)^{3/2}\frac{T_{\mathrm{ref}}+S}{T+S}. \tag{1.22}$$

μ_{ref} is a reference viscosity corresponding to the reference temperature T_{ref}, and the constant S is the Sutherland's parameter (or Sutherland's temperature). Values commonly used for air are $\mu_{\mathrm{ref}} = 1.715 \times 10^{-5}$ Pa.s, $T_{\mathrm{ref}} = 273.15$ K and $S = 110.4$ K. Sutherland's Law gives reasonably good results at transonic and supersonic speeds. For hypersonic flows, however, more elaborated formulas are usually employed.
The thermal conductivity coefficient k varies with temperature in a similar way to μ. For this reason, the Reynolds' analogy is frequently used to compute k, reading:

$$k = c_p \frac{\mu}{\mathrm{Pr}} \tag{1.23}$$

where Pr if the Prandtl number, which is usually taken as 0.72 for air.

1.2.3 The Reynolds-averaged Navier-Stokes equations

According to 'Morkovin's hypothesis', the effect of density fluctuations on turbulent eddies in wall-bounded flows is insignificant provided that they remain small compared to the mean density. Indeed, this hypothesis is verified up to Mach numbers of about five (Blazek, 2005) and, therefore, a common approach in turbulence modeling is to apply 'Reynolds averaging' to the flow variables (otherwise one should use Favre averaging).

In Reynolds averaging, the flow variables are decomposed into two parts: a mean part and a fluctuating part. The velocity, for instance, is represented as $U = \overline{U} + U'$, where $\overline{U}$ is its mean value and U' its instantaneous fluctuation. For stationary turbulent flows, $\overline{U}$ is normally computed using time-averaging, which is the most common Reynolds-averaging procedure and is appropriate for a large number of engineering problems. Time-averaging can also be used for problems involving very slow mean flow oscillations that are not turbulent in nature, as long as the characteristic time scale of such oscillations is much larger than that of turbulence. In this way, the mean velocity is computed as:

$$\overline{U} = \lim_{T \to \infty} \int_{t}^{t+T} U dt \tag{1.24}$$

Also, by definition, the average of U' i is zero. Substituting the flow variables in the Navier-Stokes equations by Reynolds-averaged ones and taking the average, obtains in differential form:

$$\frac{\partial \overline{\rho}}{\partial t} + \frac{\partial}{\partial x_i}(\overline{\rho}\overline{U_i}) = 0, \tag{1.25}$$

$$\frac{\partial}{\partial t}(\overline{\rho}\overline{U_i}) + \frac{\partial}{\partial x_j}(\overline{\rho}\bar{U}_i\bar{U}_j) = -\frac{\partial \overline{P}}{\partial x_i} + \frac{\partial}{\partial x_j}(\overline{\sigma_{ij}} + \tau_{ij}), \tag{1.26}$$

$$\frac{\partial}{\partial t}\left(\overline{\rho}\overline{E}\right) + \frac{\partial}{\partial x_j}\left(\overline{\rho}\bar{U}_j\overline{E}\right) = -\frac{\partial}{\partial x_j}\left(\bar{P}\bar{U}_j\right) + \frac{\partial}{\partial x_j}\left[(\overline{\sigma_{ij}} + \tau_{ij})\right] + \frac{\partial}{\partial x_j}\left(k\frac{\partial \overline{T}}{\partial x_j} + q_{t_j}\right). \tag{1.27}$$

The only difference between the Reynolds-averaged Navier-Stokes (RANS) equations shown above and the original set of Navier-Stokes equations is the existence of a turbulent stress tensor $\tau_{ij} = -\bar{\rho}\overline{U_i'U_j'}$ (also called Reynolds stress tensor) and of a turbulent transport of heat q_{t_j}. Both quantities are computed by means of additional equations (the so-called 'turbulence models') whose equations are reported in appendix A page 135.

1.2.4 The eddy-viscosity assumption

In the previous subsection, the Reynolds-averaged Navier-Stokes equations were presented and the turbulent stress tensor τ_{ij} and the turbulent heat flux q_{ij} were introduced. In this thesis, all turbulence models make use of Boussinesq hypothesis (Boussinesq, 1877), which relates the turbulent stresses to the mean-flow velocity gradients by:

$$\tau_{ij} = 2\mu_t S_{ij} - \frac{2}{3}\rho k \delta_{ij}, \tag{1.28}$$

where μ_t is a scalar 'eddy viscosity' (also called turbulent viscosity) and S_{ij} is the mean strain-rate tensor.

The Boussinesq hypothesis assumes that the principal axes of the turbulent stress and mean strain-rate tensors are collinear and is unable to capture anisotropy effects of the normal turbulent stresses. In practice, however, Eq. 1.28 provides accurate results for many engineering applications, including aerodynamic flows.

Based on the concept of eddy viscosity, the turbulent heat flux is then calculated by means of the 'Reynolds analogy':

$$q_{t_j} = -k_t \frac{\partial T}{\partial x_j} = -c_p \frac{\mu_t}{\mathrm{Pr}_t} \frac{\partial T}{\partial x_j}, \tag{1.29}$$

where k_t is the turbulent thermal conductivity coefficient and Pr_t is the turbulent Prandtl number (which for air is 0.9).

1.2.5 Organised-Eddy Simulation

Details of the Organised-Eddy Simulation (OES) method used in the 3D configuration of a tandem cylinders (chapter 2 page 13) as well as in the 2D simulation of a supercritical airfoil (chapter 3 page 51) have been published in Bourguet et al. (2008). This method was described as follows: The statistical turbulence modelling offers robustness of the simulations in this region at high Reynolds numbers but it has proven a strong dissipative character that tends to damp crucial instabilities occuring in turbulent flows around bodies, as for example low frequency modes as von Kármán instability, buffet or flutter phenomenon. The OES (Organised-Eddy Simulation) approach offers an alternative that is robust and captures the above physical phenomena. This approach consists in splitting the energy spectrum in a first part that regroups the organised flow structures (resolved part) and a second part that includes the chaotic processes due to the random turbulence (to be modelled). In the time-domain, the spectrum splitting leads to phase--averaged Navier-Stokes equations (Jin and Braza, 1994). A schematic illustration of the OES approach is presented in Fig. 1.1. The turbulence spectrum to be modelled is extended from low to high wavenumber range and statistical turbulence modelling considerations can be adopted inducing robustness properties. However, the use of standard URANS modelling is not sufficient in this case. In non-equilibrium turbulence, the inequality

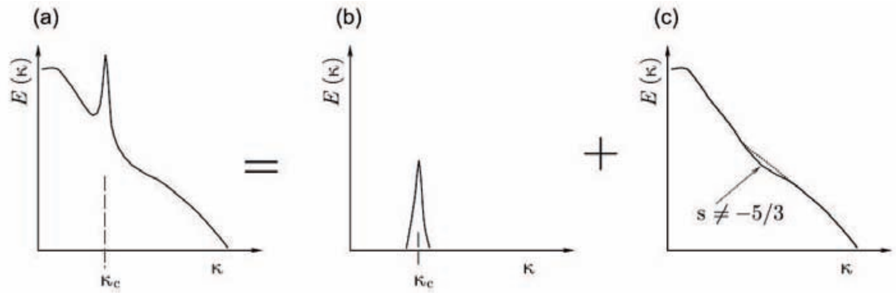

Figure 1.1: Sketch of the energy spectrum splitting in OES: (a) energy spectrum, (b) coherent part (resolved) and (c) random, chaotic part (modelled). k_c denotes coherent process wavenumber.

between turbulence production and dissipation rate modifies drastically the shape and slope of the turbulence spectrum in the inertial range (Fig. 1.1), comparing to the equilibrium turbulence, according to Kolmogorov's cascade (slope equals to $-5/3$). This modification has been quantified by the experimental study of Braza et al. (2006). Therefore, the turbulence scales used in standard URANS modelling have to be reconsidered in OES, to capture the effects due to the non-linear interaction between the coherent structures and the random turbulence. In the context of the OES approach, a modification of the turbulence scales in two-equation models was achieved on the basis of the second-order moment closure (Bourdet et al., 2007). By using the Boussinesq law 1.28 as well as the dissipation rate and the turbulent stresses evaluated by DRSM, a reconsidered eddy-diffusivity coefficient was derived. It was shown that the C_μ values were lower (order of 0.02) than the equilibrium turbulence value ($C_\mu = 0.09$) in two-equation modelling. Furthermore, the turbulence damping near the wall needed also to be revisited because of the different energy distribution between coherent and random processes in non-equilibrium near-wall regions. A damping law with a less abrupt gradient than in equilibrium turbulence was suggested, $f_\mu = 1 - \exp(-0.0002y^+ - 0.000064y^{+2})$ (Jin and Braza, 1994). The efficiency of the OES approach in 2D and 3D has been proven in a number of strongly detached high Reynolds number flows, especially around wings (Hoarau et al., 2006), as well as in the context of DES (El Akoury, 2007).

1.3 Thesis outline

This Ph.D. was a great opportunity to work on three main test-cases, covering a wide range of Mach numbers at high Reynolds numbers, by means of advanced statistical CFD methods.

The first configuration is a tandem of two inline cylinders at Mach number 0.12. The main flow features in static as well as in dynamic case, with the downstream cylinder free to move crosswise, is studied at this subsonic velocity. The results are given in chapter 2 (page 13). The transonic flow around two different supercritical airfoils, in the Mach number range 0.70–0.75, is next studied. Detailed results of the study around the OAT15A airfoil, involving time-frequency as well as POD analysis, and introducing a stochastic forcing method focussing on the Turbulent/-non-Turbulent interfaces prediction, are presented in chapter 3 (page 51) by means of an article published in the Journal of Fluids and Structures (Szubert et al., 2015b) in included in this manuscript. The V2C profil has also been studied in the context of the TFAST european project in 2D and 3D, involving laminar/turbulent transition location study, and the results have been detailed in an article submitted to the European Journal of Mechanics – B\Fluids, and also included in this manuscript (section 3.2 page 81. Finally, the predictive capabilities of a hybrid RANS-LES model, on the one hand, and of a wall-modelled LES, on the other hand, have been analysed during the summer programme 2014 handled by the Center for Turbulence Research, CA. All the results of this study are presented in chapter 4 (page 117) by means of the proceeding following the programme. The last chapter (page 129) is the conclusion of this manuscript. Appendices have also be written for extra contributions, such as a page/poster containing the equations of the $\gamma - \mathrm{Re}_\theta$ two-equation transition model for implementation consideration, as this work as been done during this Ph.D., or a short user guide of the post-processing software Tecplot, for future users to benefit my knowledge of this complex but powerful software.

Chapter 2

Tandem of two inline cylinders

Contents

The tandem cylinder arrangement is a canonical problem to advance modeling techniques for flow interactions. Tandem cylinders with similar diameters can be found in several locations on a landing gear, such as multiple wheels, axles, and hydraulic lines. This configuration can be found in cooling, venting systems, or platform support. In section 2.1, the modelling capabilities as well as the physics around two static inline cylinders are studied. In section 2.2, the fluid-structure problems are considered by giving one degree of freedom in translation to the downstream cylinder.

2.1 Flow analysis - Static case

2.1.1 Context

The 36-month ATAAC (Advanced Turbulence Simulation for Aerodynamic Application Challenges) European project, ended in 2012, handled sereval geometries with the aim of investigating the capabilities of turbulence modelling approaches available in CFD methods to model complex aerodynamic flows at high Reynolds number. 21 partners focussed on restricted set of CFD approaches: Differential Reynolds Stress Models (DRSMs), advanced Unsteady RANS models, Scale-Adaptive Simulation (SAS), Wall Modelled LES and different hybrid RANS-LES coupling schemes. Basic URANS models show indeed their limits in the case of complex situations such as stall, detached flows, high-lift applications, swirling flows, buffet, etc.

The tandem of two inline cylinders have been selected as one of the test cases handled for this project. The averaged and unsteady characteristics of the flow, in the flow and at the surface of the two cylinders, had previously been studied in a series of experiments performed in NASA Langley Research Center leading to a detailed set of data.

This configuration is a model for interaction problems commonly encountered in airframe noise configurations (e.g. hydraulic lines, support and hoses on a landing gear, Fig. 2.1). It involves many complex flow phenomena: separation of turbulent boundary layer and free shear layer roll-up, interaction of unsteady wake of the front cylinder with the downstream one, unsteady massively separated flow in the wake of the rear cylinder, etc. In this context, in a “noise-prediction” orientation of the numerical study in particular, conventional unsteady RANS approaches are not applicable and the capability of the aforementioned numerical methods to accurately reproduce the flow and predict noise have been investigated during the ATAAC project.

Figure 2.1: Main landing gear of a Cessna 404 Titan.

The flow around a single cylinder and the wake past of it have been well invastigated at moderate and high Reynolds numbers, experimentally (e.g. Roshko, 1954; Williamson, 1992; Perrin et al., 2007) and numerically (e.g. Braza et al., 1986; Persillon and Braza, 1998; Braza et al., 2001), identifying several flow regimes as a function of the Reynolds number. The flow is laminar up to Re ≈ 200, with two symmetrical recirculation vortices just downstream the cylinder. From Re ≈ 40, the symmetry is broken due to the stream pertubations and the counter rotating vortices are alternatively detached and convected in the flow. This two-dimensional phenomenon generates a series of vortices called the von Kármán street. The vortices are detached periodically and the corresponding frequency of the detachment is non dimensionalised to give the Strouhal number:

$$\mathrm{St} = \frac{f_{VK}\, D}{U_\infty} \tag{2.1}$$

where f_{VK} is the frequency of the vortices detachment (two successive detachments of the counter-rotating vortices is one period of the phenomenon), D the diameter of the cylinder (or the characteristic length of the body) and U_∞ the freestream velocity of the flow. The Strouhal number depends on the body shape and the Reynolds number. This periodical detachment is caracterised by a time evolution of the aerodynamic forces applying on the body at f_{VK} for the perpendicular ones (lift) and $f_{VK}/2$ for the streamwise ones (drag). Close to $\mathrm{Re} \approx 200$, three-dimensional effects can be observed: the von Kármán vortices ondulate in the crosswise direction, parallel to the cylinder, with a wavelength of about $4D$. For Reynolds numbers higher than 200, this wavelength is reduced to $1D$ and first turbulence phenomena develop in the wake. The flow is fully turbulent for $\mathrm{Re} > 300$ which is the case in this study, as the Reynolds number equals to 166,000 as detailed in the next section.

A first synthesis of numerical simulations carried out for this test case was carried out by Lockhard, regrouping 13 contributions involving different modelling approaches, as well as previous simulations by Khorrami et al. (2007), using URANS SST. These simulations indicated that the majority of the approaches captured quite well the Strouhal number of the vortex shedding frequency around the first cylinder, ($\mathrm{St} = 0.24$). Furthermore, as is seen in the ATAAC European program, the DES approaches better capture the complex vortex dynamics of the present flow, especially the formation of Kelvin-Helmholtz vortices in the separated shear layers. In the experimental context, it was found that the shear layers formed downstream of the first cylinder wrap around the second cylinder and interact non-linearly with the complex turbulence background, producing predominant frequencies in the energy spectrum, in the range of acoustic noise. Moreover, the numerical studies reported by Lockard in the context of the workshop for airframe noise computation, evaluated the mean drag coefficient provided by the different simulations, that had shown quite a dispersion among the different studies, with a most probable mean value of order 0.484 around the first cylinder.

2.1.2 Test-case description

Three series of experiments have been carried out on this geometry. The first set was conducted in the subsonic, atmospheric NASA-Langley Basic Aerodynamics Research Tunnel (BART; Fig. 2.2), and aimed at analysing the overall flow properties around the cylinders, by means of Particle Image Velocimetry (PIV) and hot-wire measurements (phase 1 of BART experiments, Jenkins et al., 2005). The second set of experiments was conducted in the same wind tunnel and aimed at measuring detailed average and unsteady pressure distribution at the surface of the cylinder, using static pressure orifices and piezoresistive, differential pressure transducers on the two cylin-

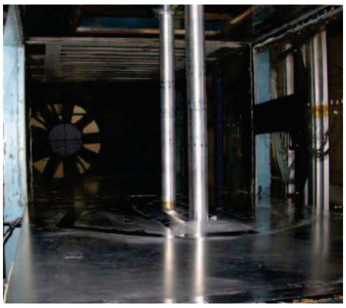

Figure 2.2: Experimental set-up.

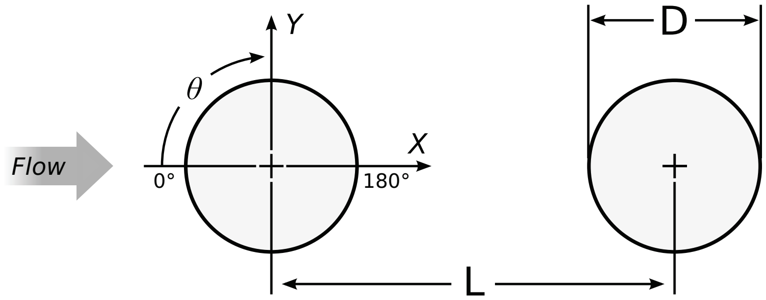

Figure 2.3: Diagram of the cylinders tandem and coordinate reference system.

ders (phase 2, Jenkins et al., 2006). The cylinders diameter has been slightly increased for this study to accommodate the pressure tubing and electrical wiring, but flow velocity has been adapted to keep the same Reynolds number, 1.66×10^5. The freestream turbulence level measured in this wind tunnel was less than 0.10%. Finally, the acoustic environment of this configuration have been studied in the Quiet Flow Facility (QFF) at NASA Langley (Lockard et al., 2007). While the QFF is an open jet facility specifically designed for anechoic testing, the flow has been adapted to obtain the same shedding frequency as in the BART experiments. All the facility dimensions and the flow properties are summarised in Table 2.1, in the next section presenting the numerical method. To ensure a fully turbulent shedding process, the boundary layers on the upstream cylinder were tripped between azimuthal locations of 50 and 60 degrees and −50 and −60 degrees

2.1.3 Numerical method

This study has been carried out by using the Navier-Stokes Multiblock (NSMB) solver. The main properties of this code have been presented in Szubert et al. (2015b), among other articles. This article details a major part of the work achieved during this Ph.D. study and has been included in this manuscript in subsection 3.1.1 of chapter 3, page 52. The reader is invited to read the section of this article dedicated to the NSMB code.

In the context of the ATAAC programme, the numerical study has been performed with non-dimensional parameters. The velocity, the density, the temperature and the cylinders diameter have been set to the unity. This leads to the value of 43.2579 for the static pressure P and the gas constant:

$$P = \rho R T, \qquad a = \sqrt{\gamma_{\text{air}} R T}, \qquad M = \frac{U}{a} \tag{2.2}$$

Finally:

$$P = R = \frac{1}{M^2 \gamma_{\text{air}}} \tag{2.3}$$

The time has also been non-dimentionalised as follows: $t^* = tU_\infty / D$.

The main numerical and experimental parameters can be compared in Table 2.1. H/D is the non-dimensionalised height or span of the cylinders, and W/D is the non-dimensionalised width of the wind tunnel in the test section.

	BART		**QFF**	**CFD**
	Phase 1	*Phase 2*		
D	0.04445 m	0.05715 m	0.05715 m	1
L/D	3.7			
H/D	16.0	12.4	16.0	3
W/D	22.9	17.8	10.7	17.8
Mach	0.1635	0.1285	0.1274	0.1285
U_∞	56.0 m.s^{-1}	44.0 m.s^{-1}	43.4 m.s^{-1}	1
Re	1.66×10^5			

Table 2.1: Experimental and numerical main parameters of the tandem cylinders geometry and flow

The 4$^{\text{th}}$ order skewsymmetric central scheme has been used for the space discretisation. Implicit time integration using the dual time stepping technique with 3 Gauss-Seidel iterations has been performed. Since NSMB solves the compressible Navier-Stokes and models equations, the preconditioning of Weiss and Smith (1995) is used to solve the flow at the Mach number 0.1285. This choice has been validated by Marcel (2011) for a Mach 0.18 flow through a confined bundle of cylinders by using the same CFD code.

The grid has been provided by the NTS (New Technologies and Services) partner from Saint Petersburg, Russia, in the context of the ATAAC programme. The grid is divided in 16 blocks of the parallel computation, and have approximately 156,000 volume cells. The gridlines are shown in Fig. 2.4 for the whole domain and around the two cylinders. The grid is slightly refined around the downstream cylinder has more turbulence is expected. The non-dimentionnalized first-cell height around this cylinder is 3.4×10^{-5} while it is 5×10^{-5} for the upstream one. The total length of the domain is $44D$.

On the solid wall, impermeability and no-slip conditions are employed. The far-field conditions are characteristic variables with extrapolation in time. The upstream turbulence intensity is set to TU = 0.08%.

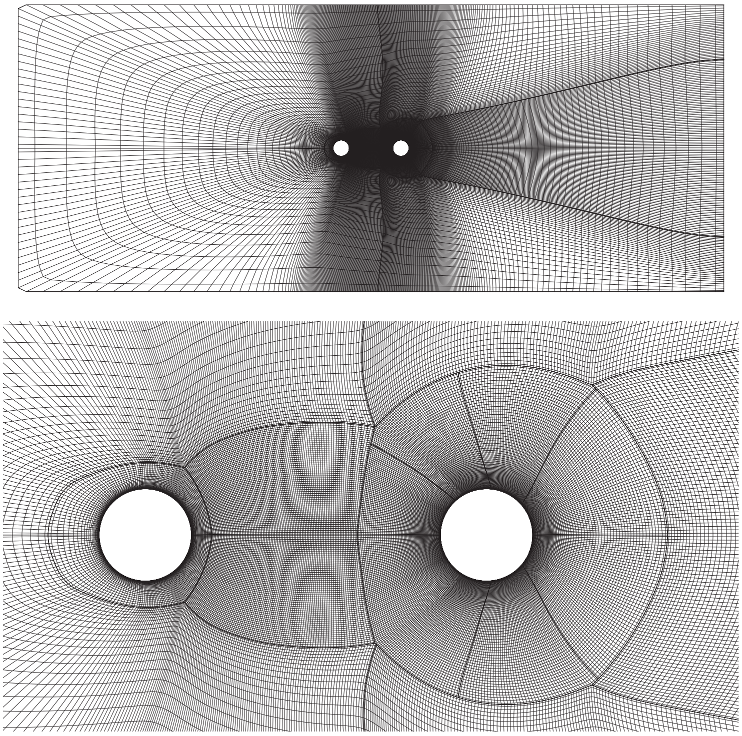

Figure 2.4: Multiblock domain of the tandem of cylinders.

2.1.4 Results

2.1.4.1 Flow overview

Eight snapshots of the vorticity field from a preliminary k-ω-SST simulation covering one period of the von Kármán phenomenon can be observed in Fig. 2.5. The main characteristic of the field is that the vortex shedding occurs at the same frequency for the two cylinders, due to the wake of the first cylinder that intensively influences the generation of vortices by the second cylinder. The distance $L/D = 3.7$ between the two cylinder is optimal to observe this phenomenon. In case of a smaller or a bigger distance, the vortex shedding would be in phase opposition between the two cylinders, generating a more complexe wake downstream the whole geometry. After this preliminary overview of the flow structure, a numerical study is carried out in order to determine the best convergence criterion and turbulence models to simulate this test case. These parameters don't change the overall flow structure and the above description remains valid.

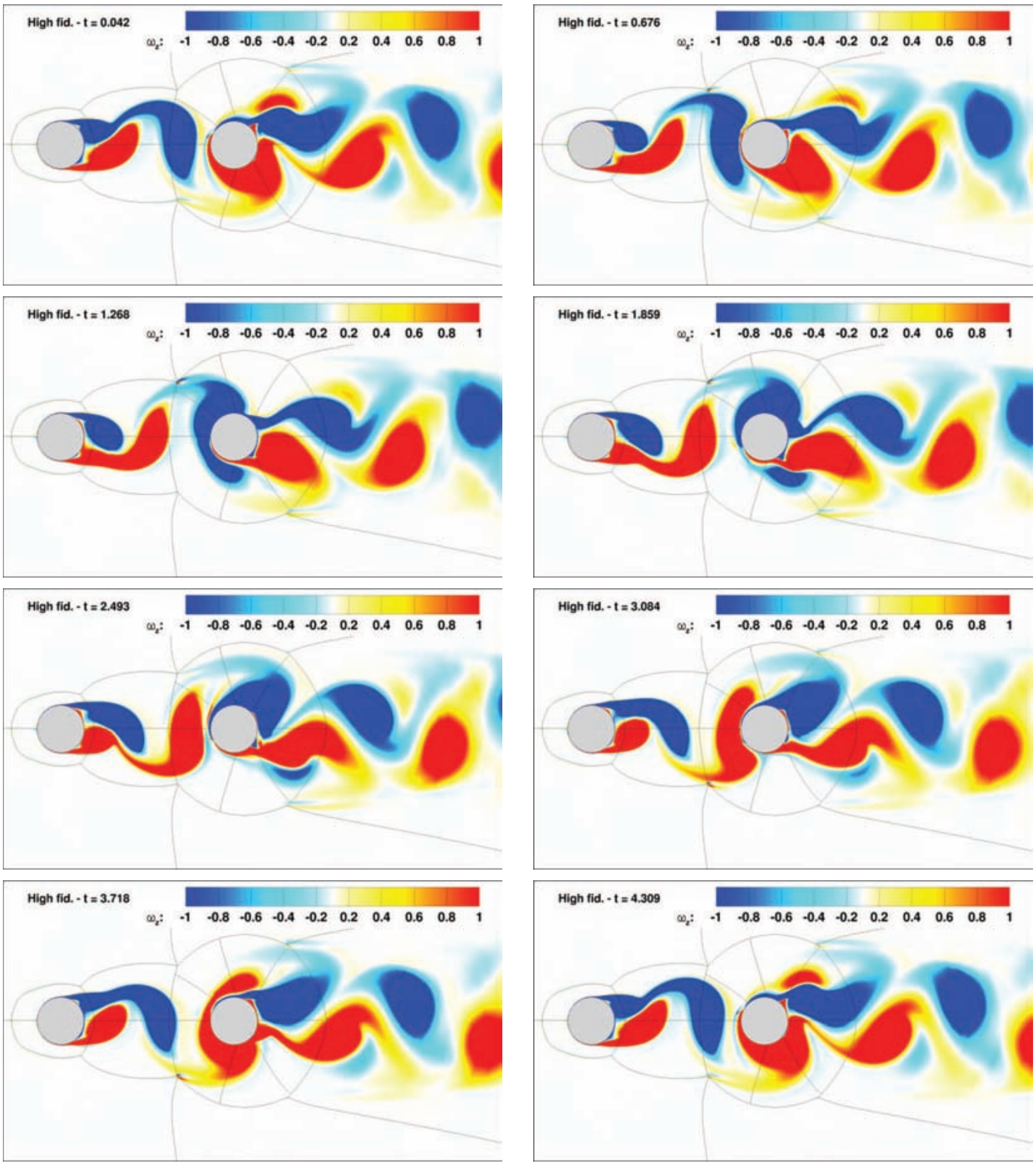

Figure 2.5: Snapshots of the vorticity field by k-ω-SST simulation covering one period of von Kármán.

2.1.4.2 Convergence study

In the context of the dual-time stepping, a sensitivity study of the physical results regarding the tolerance of the convergence criterion is first carried out. The convergence criterion at the inner step n is defined by the ratio between the L_2-norm of the density equation residual at the inner step n and the one at the initial inner step. It is calculated at each inner computation step and when the tolerance is reached, the physical solution is saved at the current physical time step and the process goes on at the next outerstep. The system of equations needs to converge enough to provide a good prediction of the physical solution. However, a very low tolerance implies long computation time to reach the requested value and becomes useless compared to the numerical uncertainties (time and grid resolutions, computer precision). This study is performed to determine the better tolerence for the three-dimensional computations.

For this study, the k-ω-SST model of Menter (1994) (see also section A.2.3.2 of appendix A, page 141) is used, as it is well designed for flows under high pressure gradient, and the non-dimensionalised time step $\Delta t^* = 0.00845$ has been chosen from the ATAAC programme.

The RMS value of the lift and drag coefficient fluctuations of the two cylinders are calculated at each outerstep. The last steps are plotted in Fig. 2.6 for the three tolerance values analysed. The curves trend shows at first glance that the difference between the two smaller tolerances is less than between 10^{-3} and 10^{-4}. While the physical solutions were well converged, small oscillations are visible in the RMS values and are due to numerical resolution.

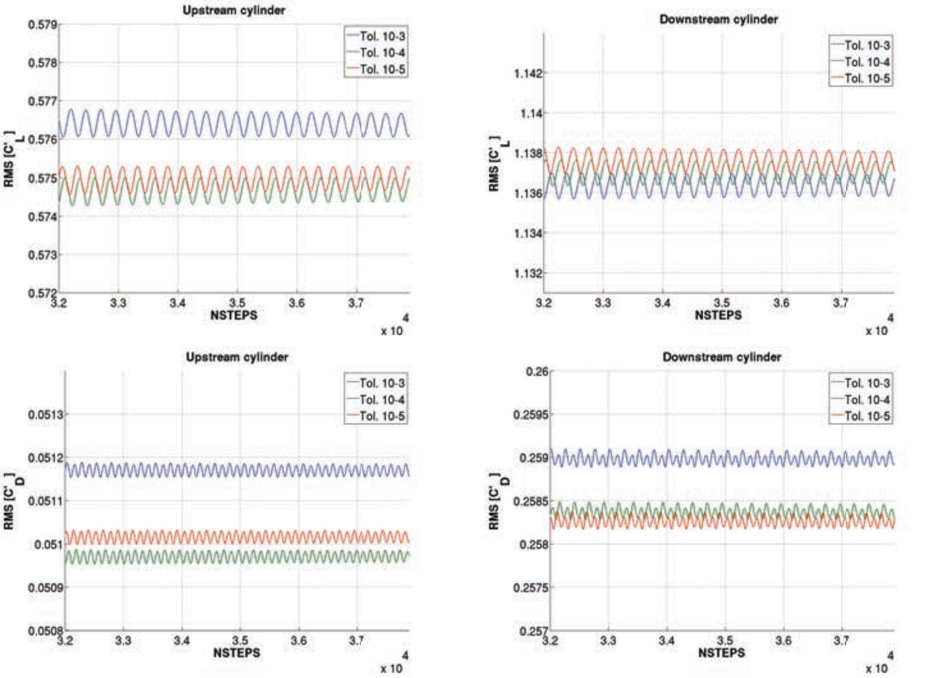

Figure 2.6: Evolution of the RMS values of the lift and drag coefficients fluctuations for three convergence tolerances.

The final values of the RMS, as well as the mean of the lift and drag coefficients, are reported in Table 2.2 for a quantitative comparison. The three tolerances give

Tol.	Upstream cylinder				Downstream cylinder			
	$\overline{C_D}$	$\overline{C_L}$	RMS(C'_L)	RMS(C'_D)	$\overline{C_D}$	$\overline{C_L}$	RMS(C'_L)	RMS(C'_D)
10^{-3}	0.7997	0.0022	0.0512	0.5765	0.2035	-0.0020	0.2590	1.1363
10^{-4}	0.7990	0.0028	0.0509	0.5746	0.2047	-0.0036	0.2584	1.1370
10^{-5}	0.7991	0.0027	0.0510	0.5749	0.2045	-0.0049	0.2583	1.1377

Table 2.2: Mean values of the lift and drag coefficients and RMS values of their fluctuactions for the two cylinders.

very close results with a difference $< 1\%$, except for the mean lift value on both cylinders. Between 10^{-3} and 10^{-4}, $\overline{C_L}$ is increased by 20% on the first cylinder and 44% on the second one, while between 10^{-4} and 10^{-5}, $\overline{C_L}$ is 4% smaller on the upstream cylinder, and 27% higher on the downstream one. In the spirit of getting meaningful physical results in a reasonnable computation time, the tolerance 10^{-4} is retained for the the remaining simulations.

2.1.4.3 Turbulence model study

A similar comparison is carried out to compare the results of four turbulence models. The mean and RMS values of the lift and drag coefficient time evolution are reported in Table 2.3. The Edwards and Chandra (1996) modified Spalart and Allmaras (1994) (see also section A.1.1 of appendix A, page 135) and the k-ω-SST (Menter, 1994 and section A.2.3.2 page 141) give very close results in mean and amplitude. The k-ω-BSL (Menter, 1994 and section A.2.3.1 page 139) is more dissipative and as a consequence, the amplitude of the aerodynamic coefficients are smaller.

Models	Upstream cylinder				Downstream cylinder			
	$\overline{C_D}$	$\overline{C_L}$	RMS(C'_L)	RMS(C'_D)	$\overline{C_D}$	$\overline{C_L}$	RMS(C'_L)	RMS(C'_D)
SA-E	0.7826	0.0028	0.0742	0.6246	0.2008	0.0018	0.3068	1.3295
k-ω-SST	0.7990	0.0028	0.0509	0.5746	0.2047	-0.0036	0.2581	1.1370
k-ω-BSL	0.5567	0.0011	0.0167	0.2523	0.2852	-0.0054	0.1246	0.8045

Table 2.3: Mean values of the lift and drag coefficients and RMS values of their fluctuactions for three turbulence models.

The mean streamlines in the wake of each cylinder are plotted for the three turbulence models in Fig. 2.7. The overall prediction of the flow is similar between the three models and the experiment (Fig. 2.8) and the symmetry between the upper and lower sides of the flow is observed. However, they predict slight different size of the recirculation area, in particular none of them matches the experimental measurements.

The non-dimensionalised streamwise velocity at $y = 0$ measured in the wake of the two cylinders is plotted in Fig. 2.9, and the recirculation lengths $(x \wedge U(x) = 0)$ are reported in Table 2.4. In the BART experiment, the second recirculation has been reduced by 80% compared to the first. This difference might by due to the position of the cylinders compared to each other. The velocity in the wake of the

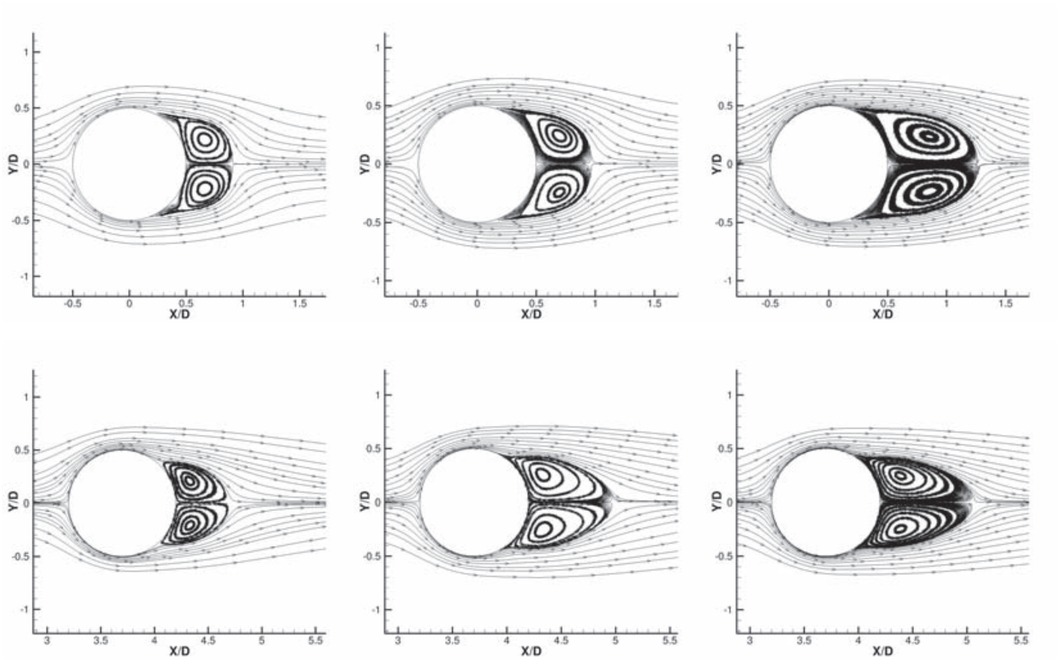

(A) (B) (C)

Figure 2.7: Comparison of the mean streamlines in the wake of the upstream (top) and the downstream (bottom) cylinders. (A) SA-E, (B) k-ω-SST, (C) k-ω-BSL.

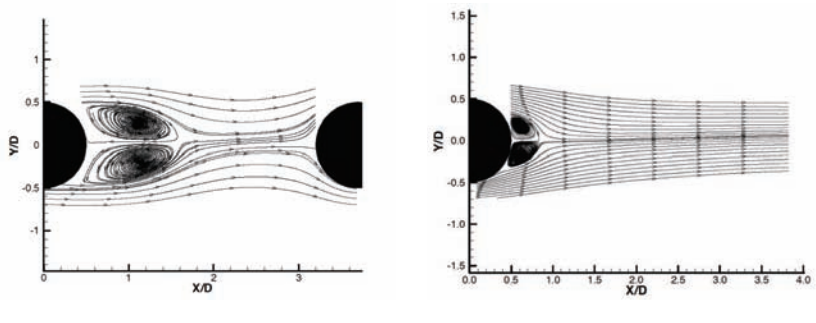

(A) (B)

Figure 2.8: Mean stream lines from PIV measurments. (A) Upstream cylinder, (B) Downstream cylinder (Jenkins et al., 2005).

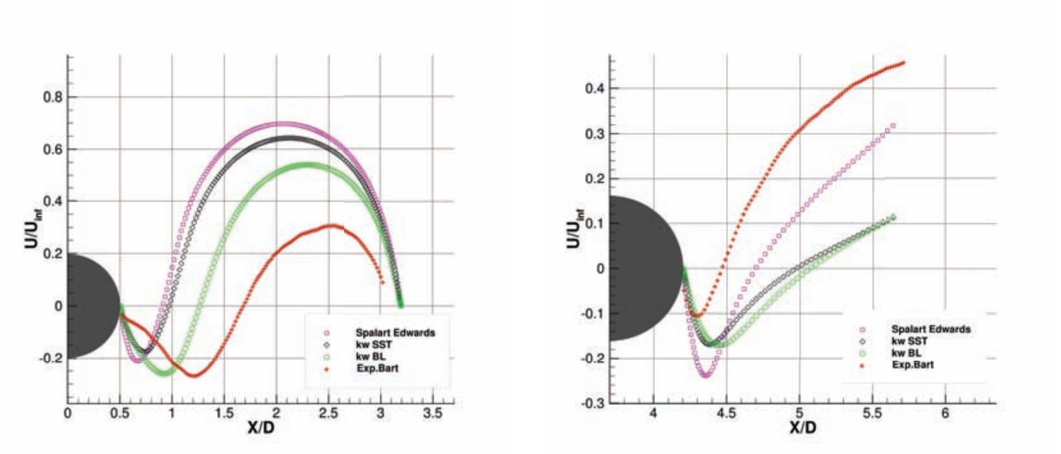

(A) (B)

Figure 2.9: Comparison between turbulence models en experiment of normalised streamwise velocity in the wake. (A) Upstream cylinder, (B) Downstream cylinder.

first cylinder is limited by the presence of the second cylinder and this favours the development of the vortices before they detach, while this is not the case for the second cylinder. However, this phenomenon is not observed in the simulations, which give an opposite trend, and the difference between the two regions is less important (SA-E and k-ω-SST: +20%, k-ω-SST: +67%).

Models/Source	**L_{recirc}/D**	
	Upstream cyl.	**Downstream cyl.**
PIV (Jenkins et al., 2005)	1.2	0.25
SA-E	0.4	0.5
k-ω-SST	0.45	0.75
k-ω-BSL	0.75	0.9

Table 2.4: Recirculation length downstream each cylinder.

Spectral analysis

A spectral analysis is carried out on the time evolution of the lift and drag coefficients recorded at a physical time step $\Delta t^* = 0.00845$, the same as the simulation itself. All signals are 17751 sample length, and are processed by the Welch's method (Welch, 1967) with the following parameters:

- Window: Hanning,
- Window size: $N_{wind} = 8192$ samples,
- Overlap: 65%,

- Zero padding: $N_{FFT} = 2^{18} = 262144$.

These parameters give the following resolutions:

- $\Delta f \approx 4.5 \times 10^{-4}$ Hz,
- $B \approx 5.8 \times 10^{-2}$ Hz.

where $\Delta f = 1/(\Delta t^* N_{FFT})$ is directly related to the signal points available, and $B = \alpha/(N_{wind}\Delta t^*)$ is the dynamic resolution given by the window definition and parameters (among which α). The spectra of the lift coefficient, for the two cylinders, are plotted in Fig. 2.10. The major peak is identified as well as few harmonics. As can be noticed, the frequency content is very similar between the two cylinders and the main frequencies appears for both. The main peak is identified to the Strouhal number. Indeed, the lift evolution is the same as the vortex shedding: it is maximum when a vortex detaches on the upper side of the cylinder, minimum when a vortex detaches on its lower side. Due to the symmetry in the streamwise direction, the drag gives twice this frequency (Fig. 2.11): it is maximum just before each vortex detachment. The Strouhal numbers are reported in Table 2.5 and are compared to the experimental value. The k-ω-BSL model predicts the exact frequency of the vortex shedding while the other models are closed to 0.241 (SA-E: +1%, k-ω-SST: −3%).

Models/Source	Strouhal (St $= f_{VK}D/U_\infty$)
PIV (Jenkins et al., 2005)	0.241
SA-E	0.244
k-ω-SST	0.234
k-ω-BSL	0.241

Table 2.5: Comparison of Strouhal numbers.

Upstream cyl. **Downstream cyl.**

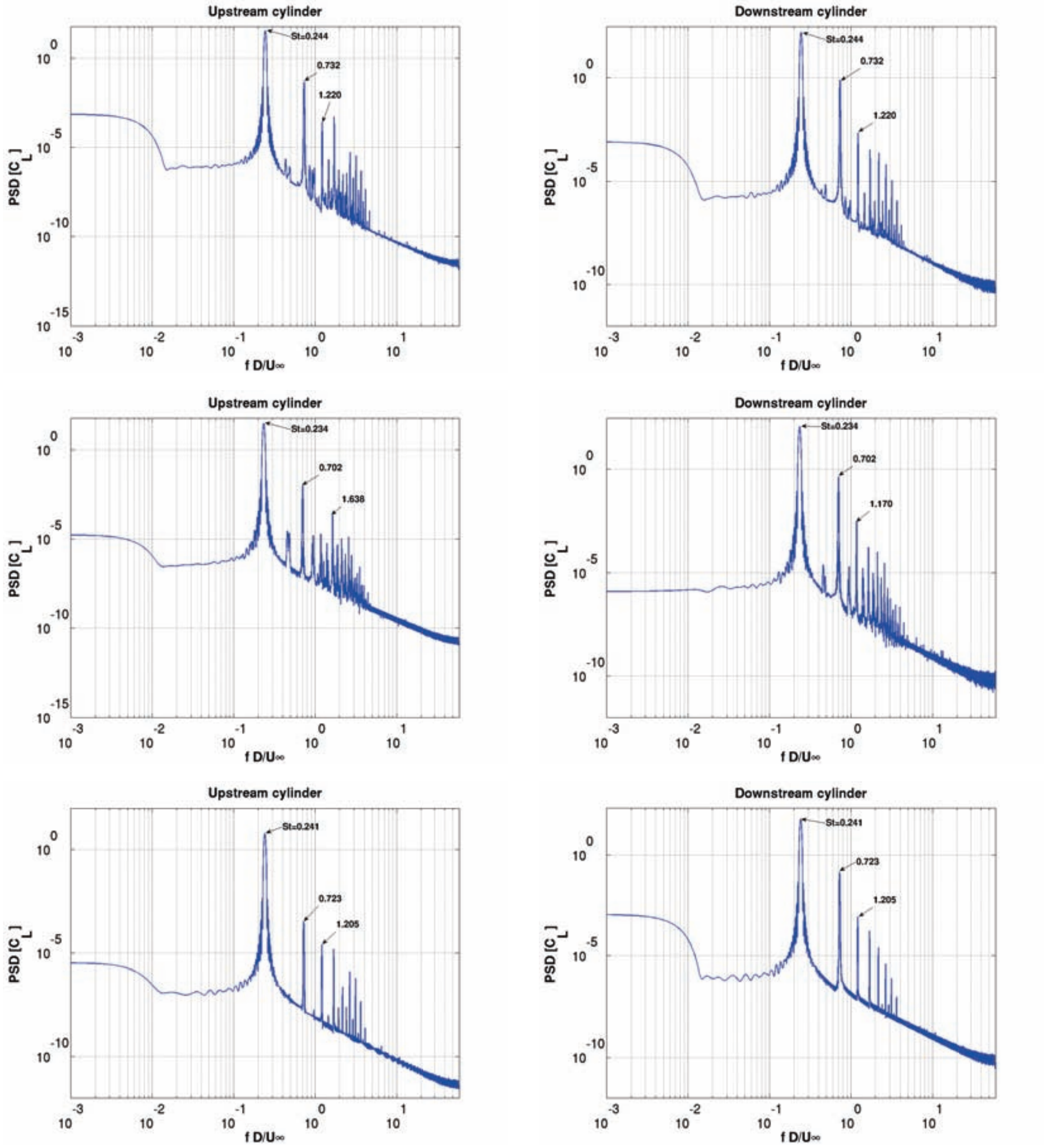

Figure 2.10: PSD of the **lift** coefficient time evolution for the two cylinders. Top: SA, middle: k-ω-SST, bottom: k-ω-BSL.

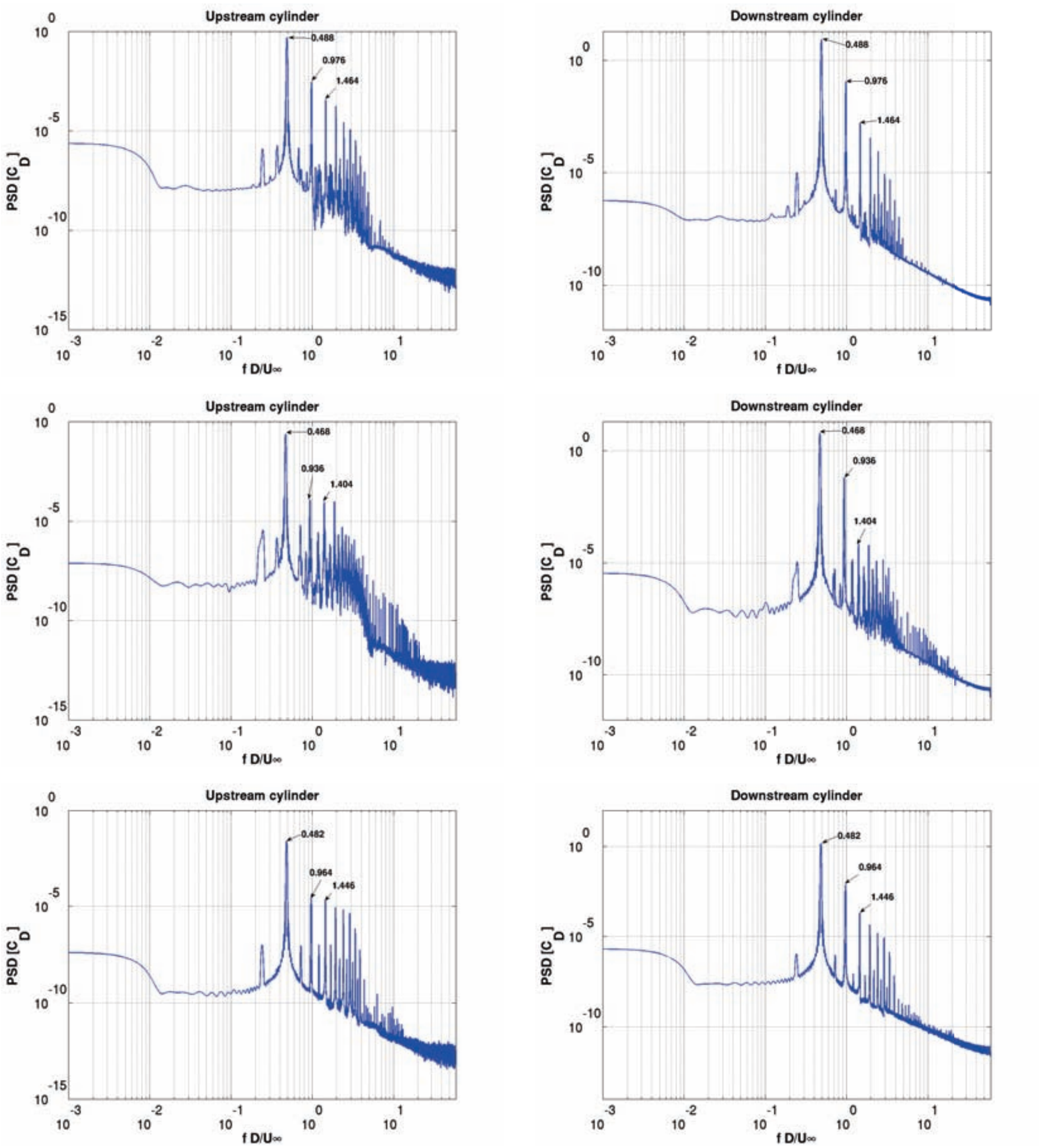

Upstream cyl. **Downstream cyl.**

Figure 2.11: PSD of the **drag** coefficient time evolution for the two cylinders. Top: SA, middle: k-ω-SST, bottom: k-ω-BSL.

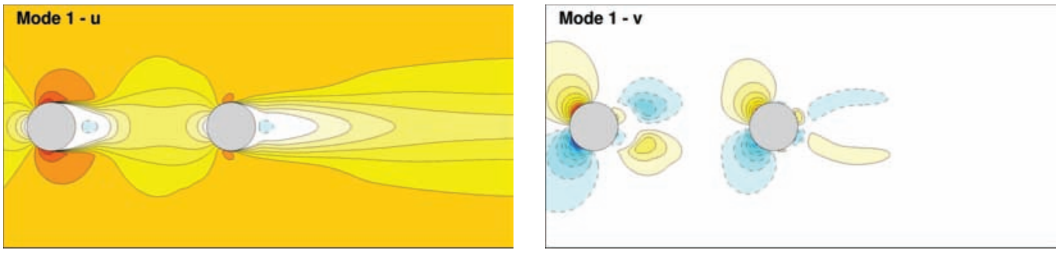

Figure 2.12: First POD mode of the streamwise (left) and crosswise (right) velocity components.

2.1.4.4 POD analysis

The Proper Orthogonal Decomposition (POD) is a mathematical technique used to analyzed complex physical systems of a great number of degrees of freedom, allowing to represent these systems in an optimal way. This method is applied in a wide range of scientifical fields such that signal and image processing, chemistery, medecine, oceanography, meteorology. In the context of the fluid dynamics, this method has been introduced by (Lumley, 1967) to analyse the coherent structures in a turbulent flow, which are usually of high energy, the lowest energy range corresponding to the random fluctuations. The current POD analysis is carried out based on the 'separable POD' (Holmes et al., 1996). The objective is to find an approximation of the physical flow as follows:

$$\mathbf{U}(\mathbf{x},t) = \bar{\mathbf{U}}(\mathbf{x}) + \mathbf{u}(\mathbf{x},t) = \bar{\mathbf{U}}(\mathbf{x}) + \sum_{n=2}^{N_{\mathrm{POD}}} a_n(t)\boldsymbol{\phi}_n(\mathbf{x}), \tag{2.4}$$

where $\boldsymbol{\phi}_n(\mathbf{x})$ are the shape (spatial) functions and $a_n(t)$ are the associated temporal coefficients. In the context of this study, the 'snapshot POD' (Sirovich, 1987; Aubry et al., 1991) is used to determine the temporal coefficients from the time correlations arised from the snapshots generated during the simulation. The spatial modes are determined by projecting the physical field on these temporal coefficients. A fortran code developed in our research group as been used to read the data, calculate the temporal coefficients and spatial modes and write results. Here, 1132 snapshots of the streamwise and crosswise velocity components, generated from a k-ω-SST simulation every $t^* = 0.04225$, 5 times the simulation time step, are used covering 10 periods of vortex shedding. The first POD mode corresponds to the mean field as it is included in the original database (Fig. 2.12). Shape functions from modes 2 to 6 are plotted in Fig. 2.13, and are clearly identified to the von Kármán phenomenon, giving sub-spatial frequencies as the mode order increases. Shape functions of the next 5 modes are plotted in Fig. 2.14. They confirm the tendency of the subdivision of the spatial modes structures as their range increases. Moreover, the higher shape values move from the vortex shedding area to the shear-layer one, characterised by Kelvin-Helmotz vortices. The tendency is confirmed at higher-range modes (Fig. 2.15).

The time evolution of the temporal coefficients are plotted in the Fig. 2.16 and 2.17. For the first mode, the constant time evolution confirms the property of the first mode which represents the mean field. Other modes are associated two by two, corresponding to two different phases, similarly to the shape functions, and

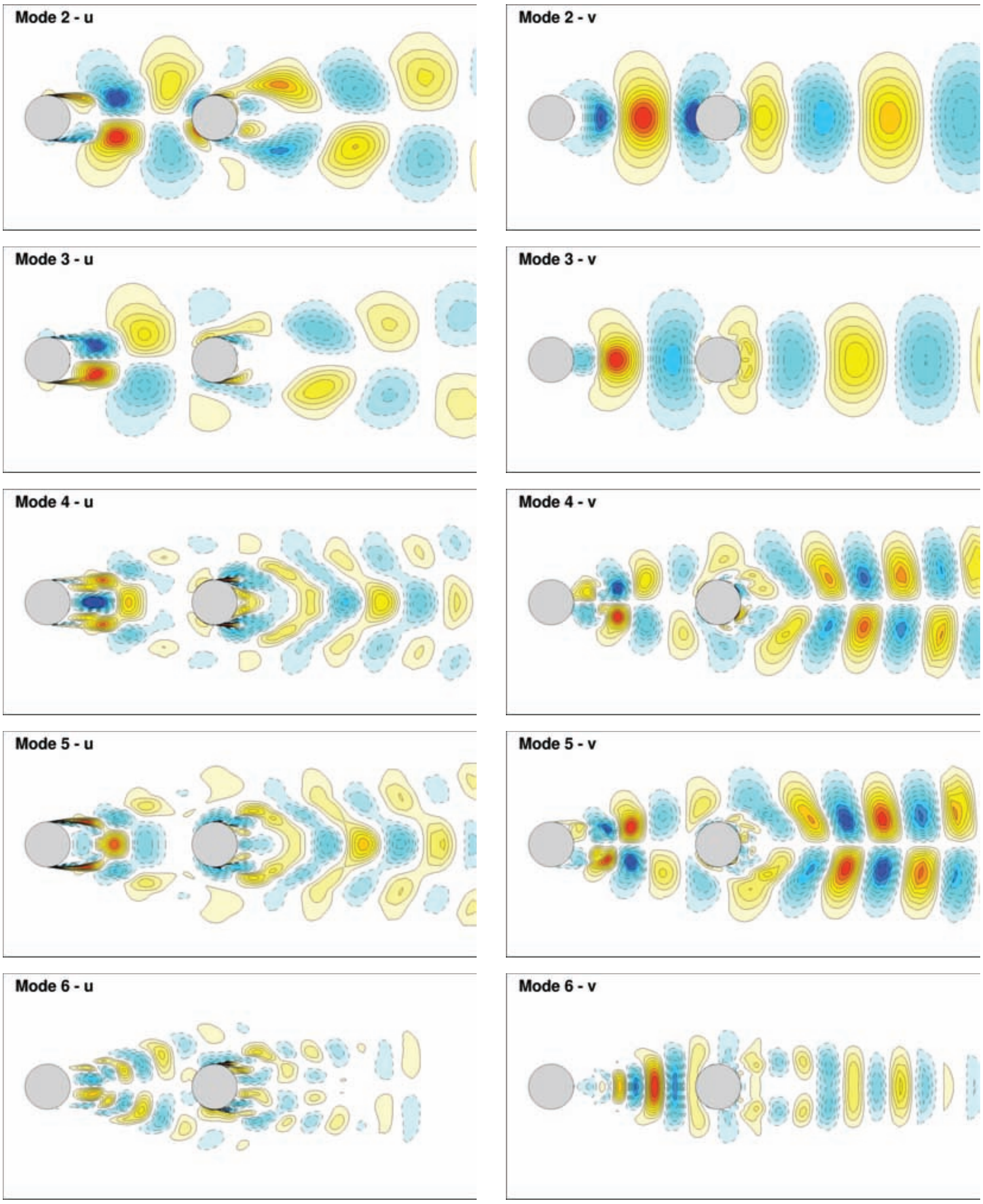

Figure 2.13: POD modes 2 to 6 of the streamwise (left) and crosswise (right) velocity components.

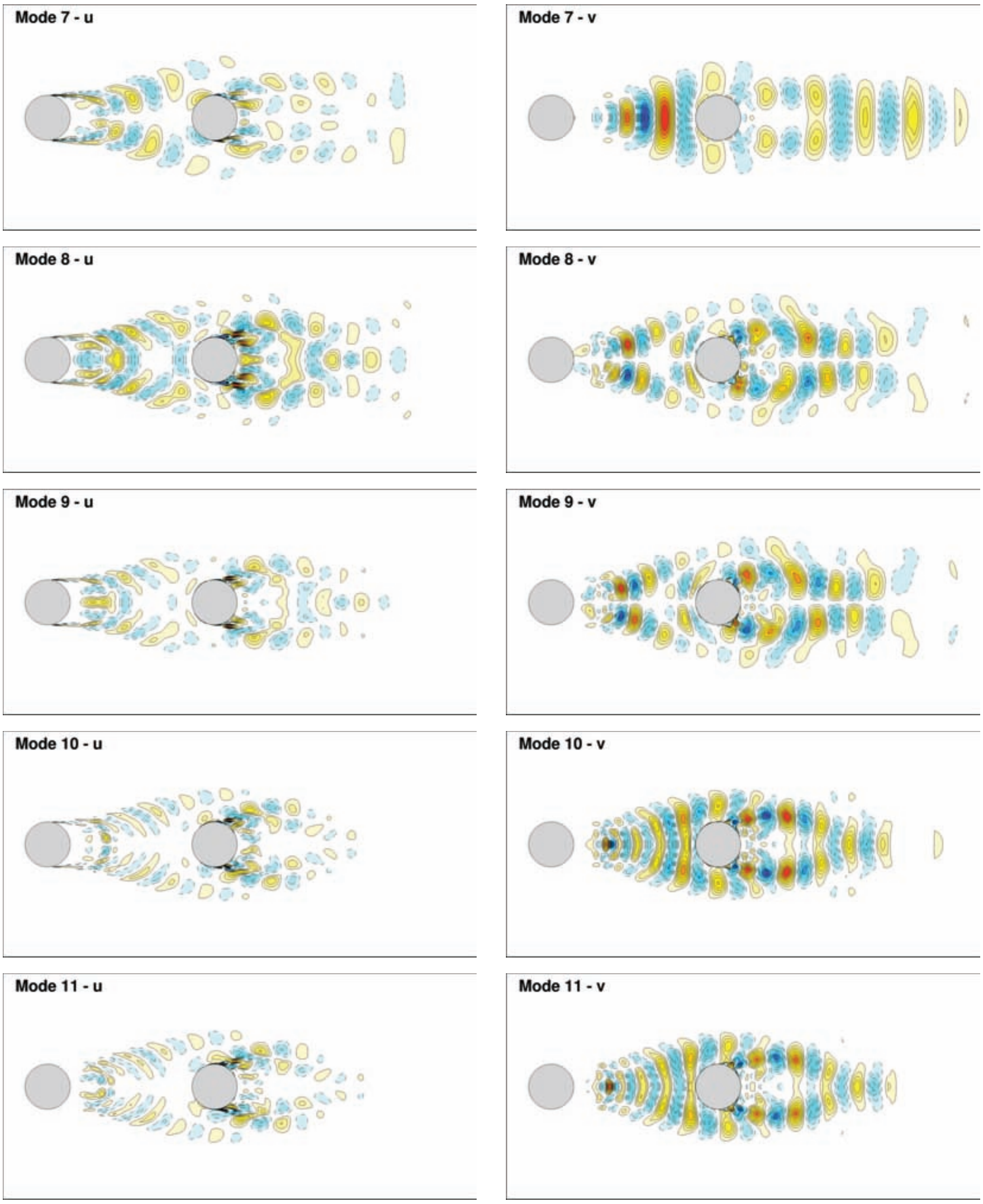

Figure 2.14: POD modes 7 to 11 of the streamwise (left) and crosswise (right) velocity components.

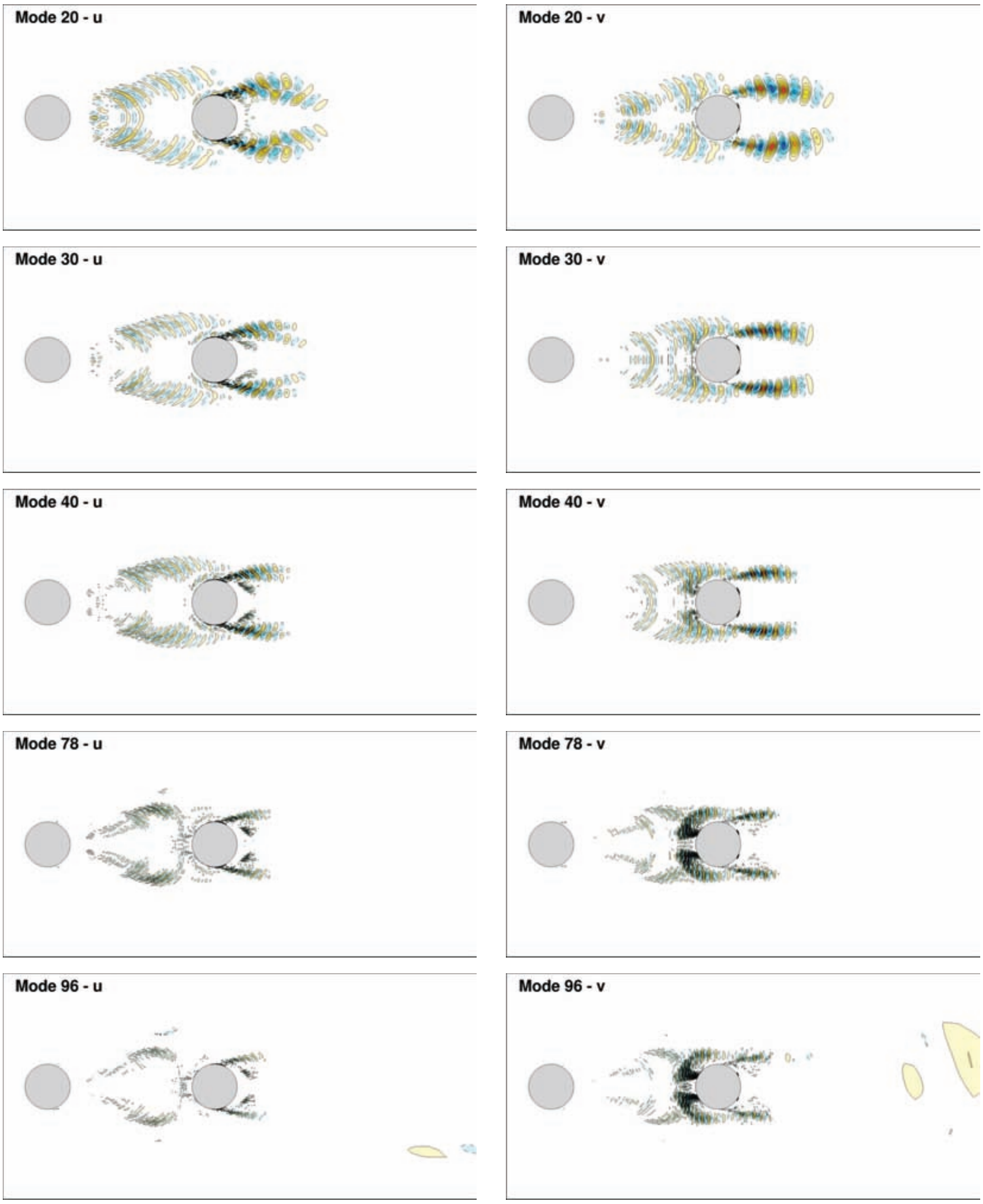

Figure 2.15: Higher-range POD modes of the streamwise (right) and crosswise (left) velocity components.

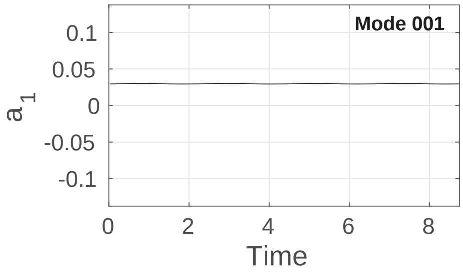

Figure 2.16: Temporal coefficient time evolution of first POD mode.

are periodical. This illustrates the link between the POD and the Fourier Series Expansion. The flow itself is very periodical and statistically quasi-stationnary. The POD temporal coefficients corresponds to an harmonic decomposition on the mode $\cos(2\pi kt/T)$ and $\sin(2\pi kt/T)$, with $k \geqslant 1$ and T the period of the physical phenomenon (Holmes et al., 1996). This explains the phase shift of the $\pi/2$ of the temporal signals and of the shape function (spatial translation) for each mode pair. Phase or Lissajous curves are plotted in Fig. 2.18 and show the periodicity of the signals (closed curves) as well as the increase of their frequency.

Spectra of the temporal coefficients are plotted in Fig. 2.19, as well as marks of harmonics of the main non-dimensionalised frequency of 0.231, and confirms the mode pair groups and the division of the main signals frequency by two from a pair to the next one.

Finally, the modes energy, related to the proper value found during the POD process, are plotted in the Fig. 2.20. It corresponds to the relative 'information' of the physical flow contained in each mode. The efficiency of the POD process is characterised by the accumulation of this information in the first modes. As the mean flow was included in the snapshots database, the first mode is the most energetic and contains 90% of the total information, and the next pair of modes represents 9% of the total enery, giving 99% of the flow field information contained in the first 3 modes, and 99.99% in the first 11 modes. Moreover, pair groups (modes 2-3, 4-5, etc...) are also visible in the energy distribution.

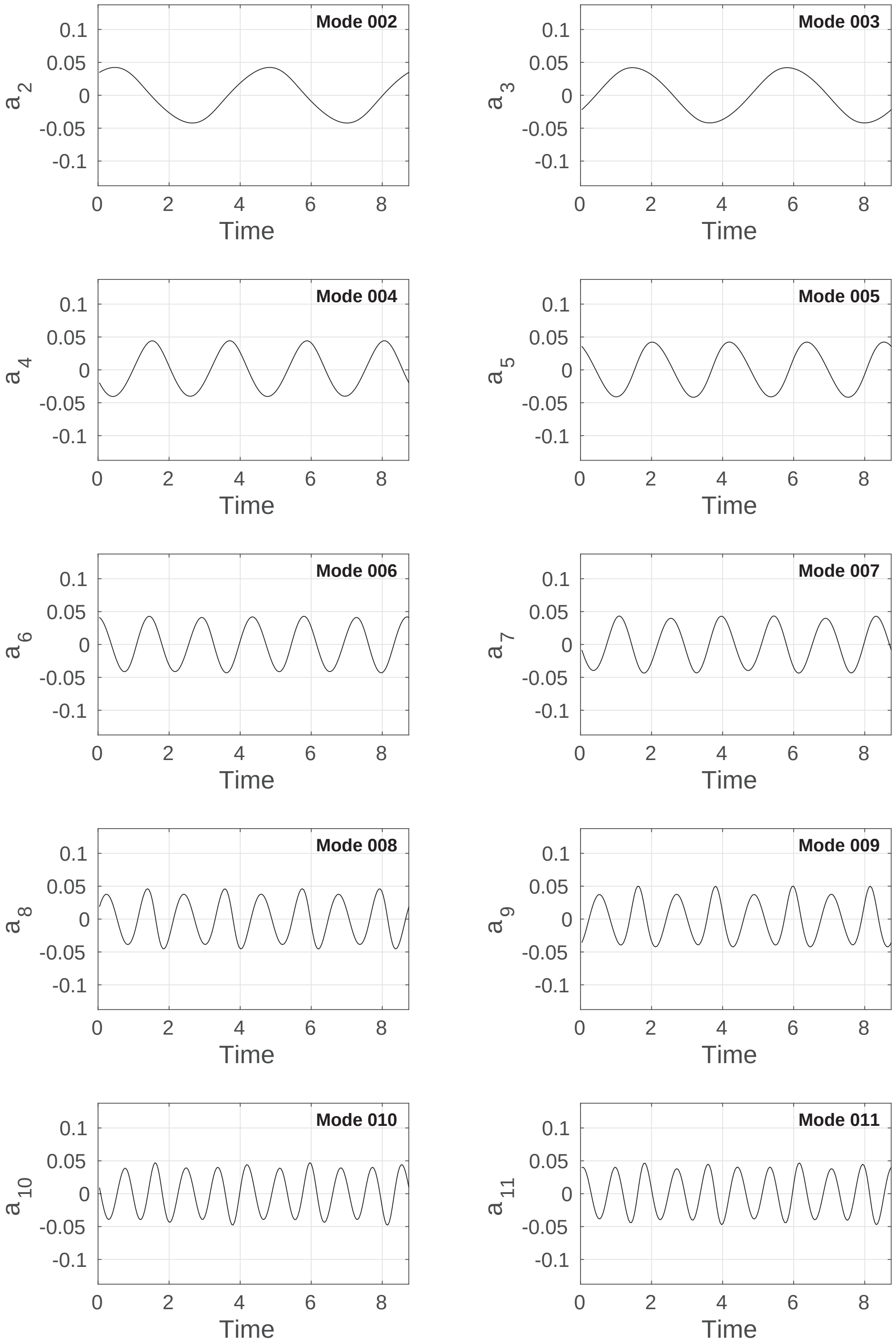

Figure 2.17: Temporal coefficient time evolution of POD modes 2 to 11.

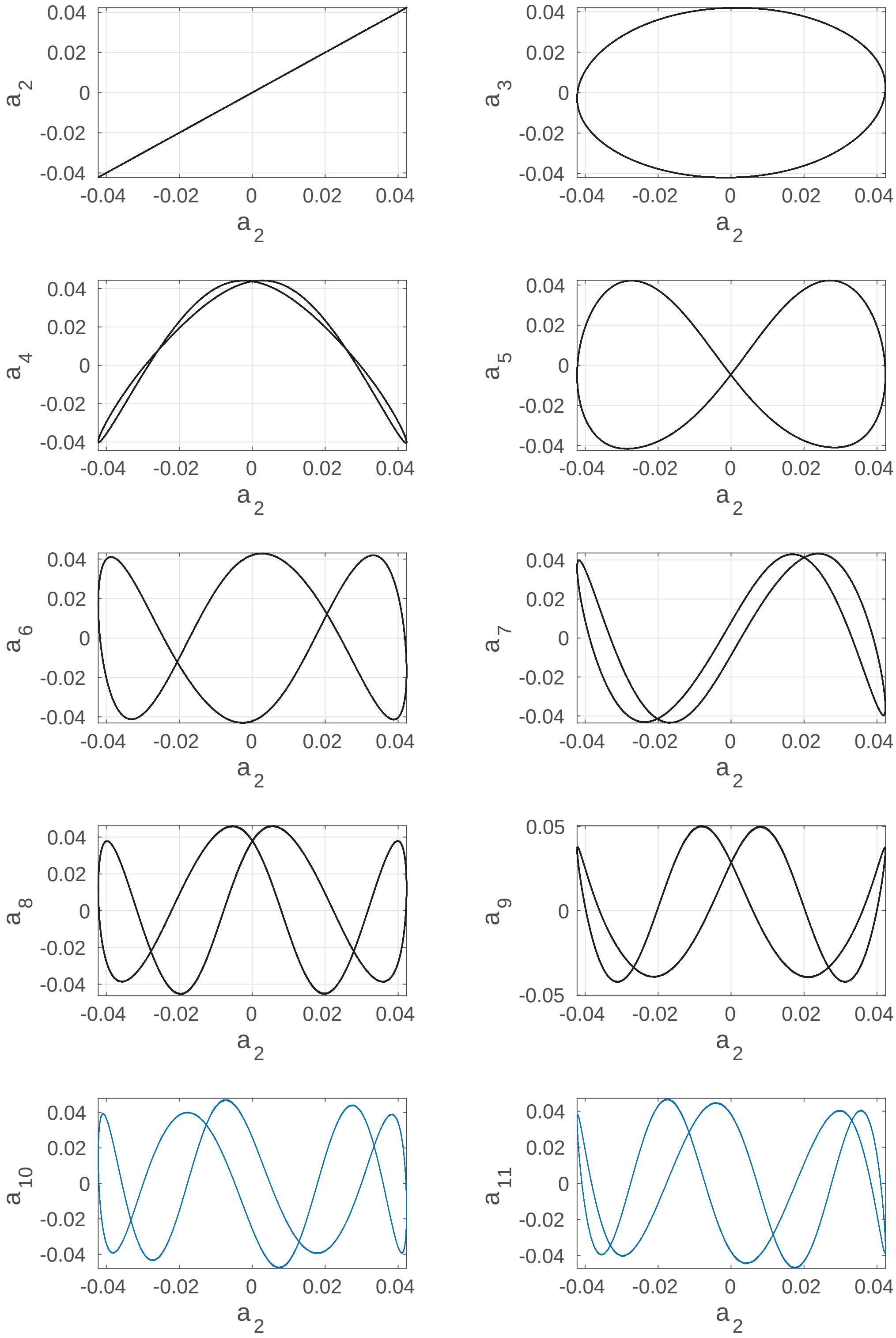

Figure 2.18: Lissajous curves associated to the temporal coefficients up to POD mode 11.

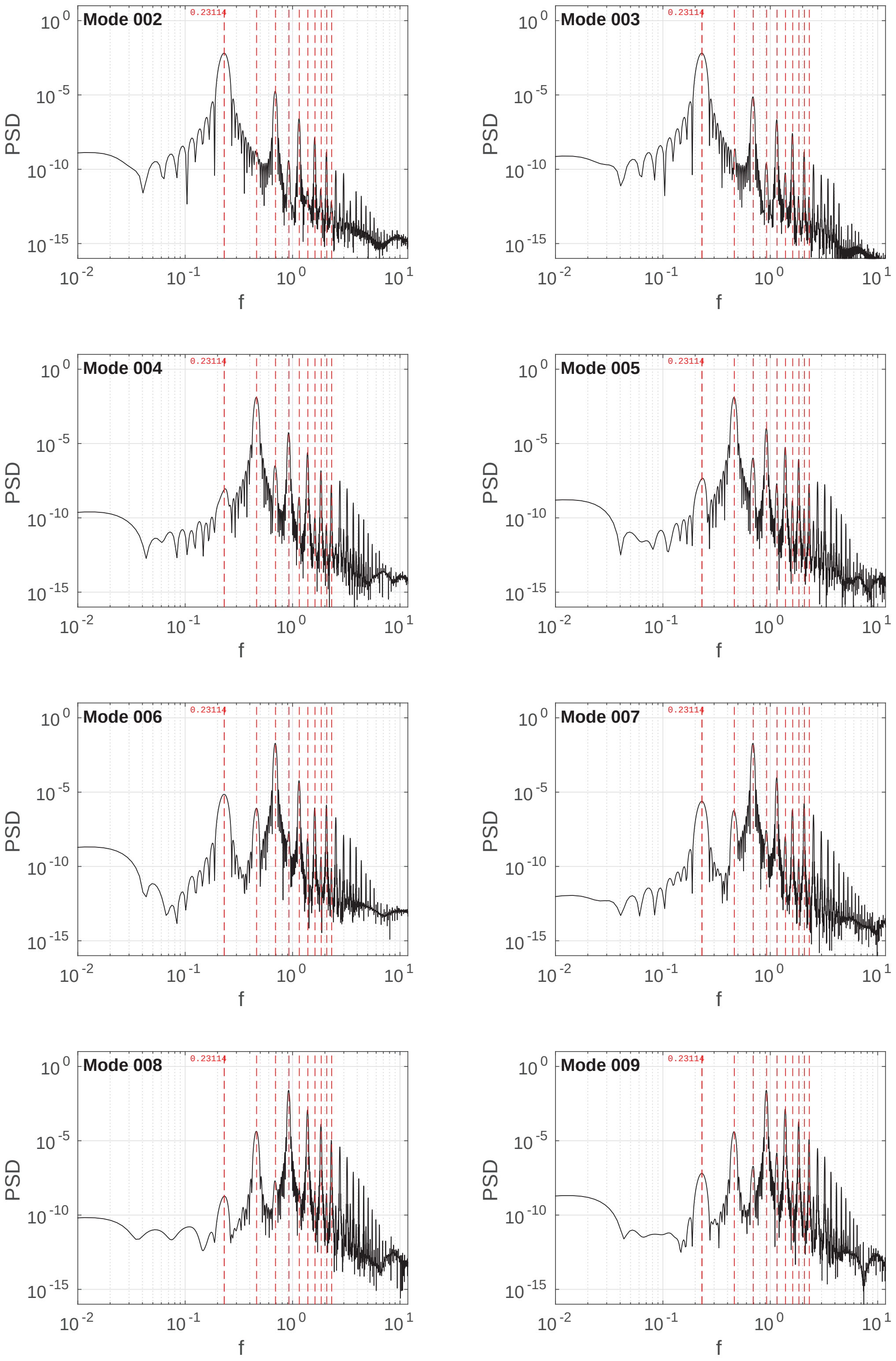

Figure 2.19: PSD associated to the temporal coefficients up to POD mode 9 (non-dimensionalised frequencies).

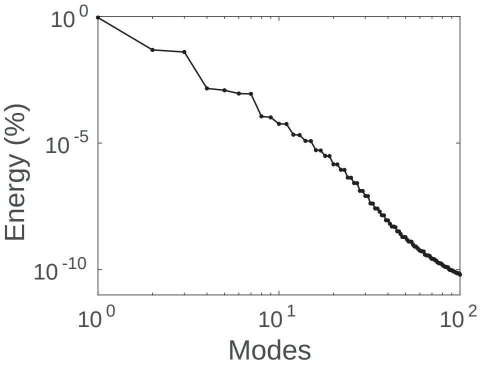

Figure 2.20: Energy distribution of the POD modes.

Reconstruction

The velocity fields are reconstructed from a limited number of POD modes using the relation 2.4 (here, $N_{\text{POD}} = 3$, 5 and 41). The vorticity is then calculated and compared to the original high-fidelity unprocessed field (snapshots form the simulation). They are plotted at $0 \times T_{VK}$ and $T_{VK}/4$ in Fig. 2.21, and $2T_{VK}/4$ (left) and $3T_{VK}/4$ in Fig. 2.21, T_{VK} being the period of the von Kármán vortex shedding. While their shapes are different from the orginal ones, the vortical structures are already reconstructed with only 3 modes (including the first mode). With 11 modes, their spatial expension is very close to the high-fidelity simulation. However, some spatial oscillation remains, in particular between the two cylinders. They disappear by adding more modes to the reconstruction (here, 30 more modes), where the vorticity field is almost qualitatively identical to the original one.

For a more detailed analysis of the reconstruction capabilities, the time evolution of the streamwise velocity component are recorded at 6 positions (Fig. 2.23). The signal from high-fidelity simulation is compared to reconstructions with 3, 5, 7 and 11 modes in Fig. 2.24, and with 11, 21 and 41 modes in Fig. 2.25. With only 3 modes, the overall periodicity of the signal is reproduced with a sinusoidal shape, but higher-frequency variations are not captured at all and more modes are needed, which is an expected result. While 99.99% of the flow information is contained in the first 11 modes as previously said, based on the proper values, some abrupt time variations of the flow are still not captured and up to 21 modes are necessary to reconstruct them (points 4 and 5 in particular). As said at the beginning of this subsection, the Proper Orthogonal Decomposition is used here to identify to most energetic modes inside a turbulent flow. The basis of the decomposition can also be used to build Reduced-Order Models (ROM) with a much more limited number of degrees of freedom than the URANS or other high-fidelity computations, allowing for faster computations. The capabilites and the speed of the ROM to model the fluid dynamics is directly related to the number of modes chosen to build the POD basis and thus the details one wants to model through the ROM. The reader can find an application of the ROM on an incompressible flow and a development of this method in the case of a compressible case in Bourguet (2008); Bourguet et al. (2011).

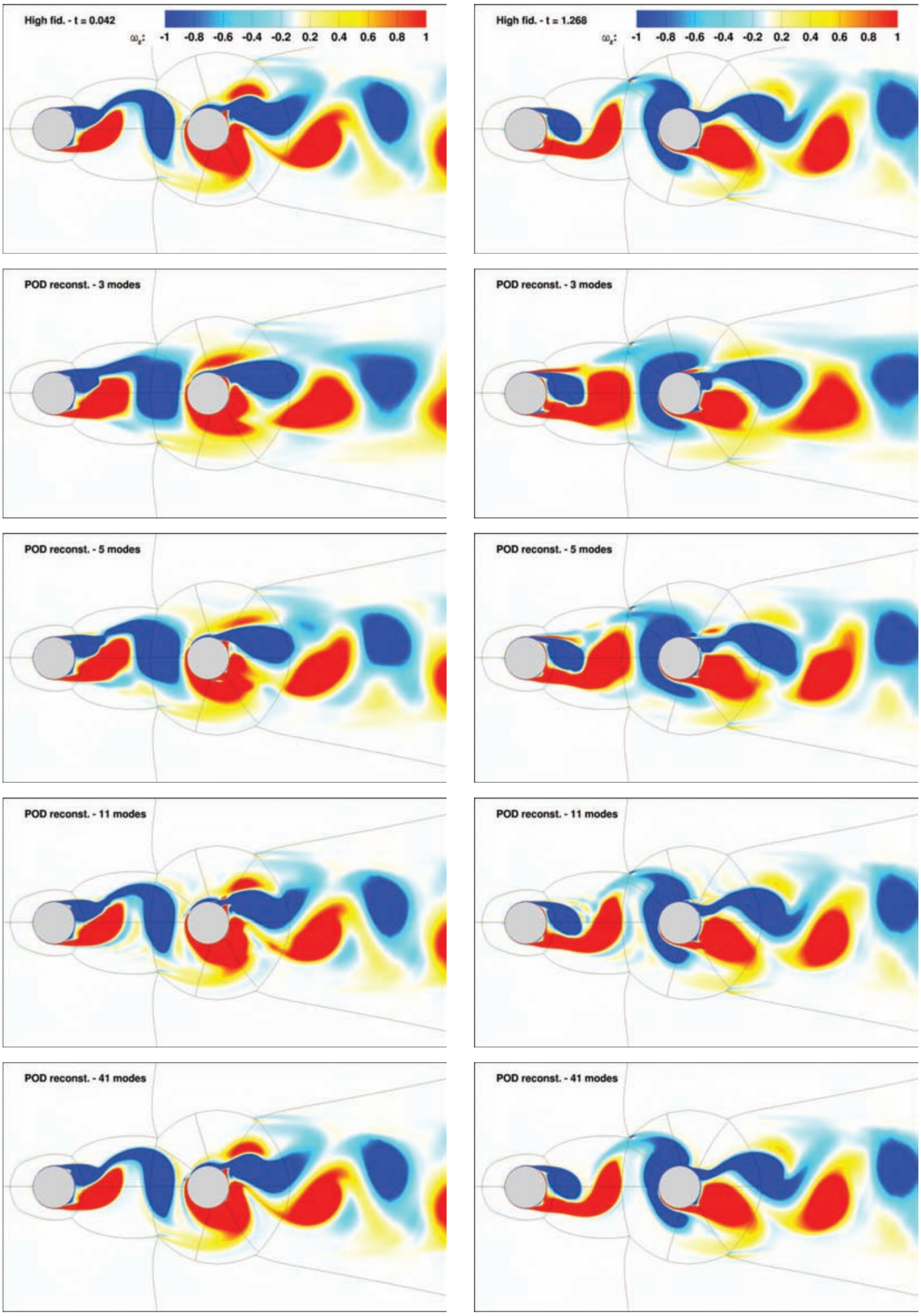

Figure 2.21: Vorticity field from URANS (top) and POD reconstruction from 3, 5 and 41 modes at $0 \times T_{VK}$ (left) and $T_{VK}/4$ (right) in static case.

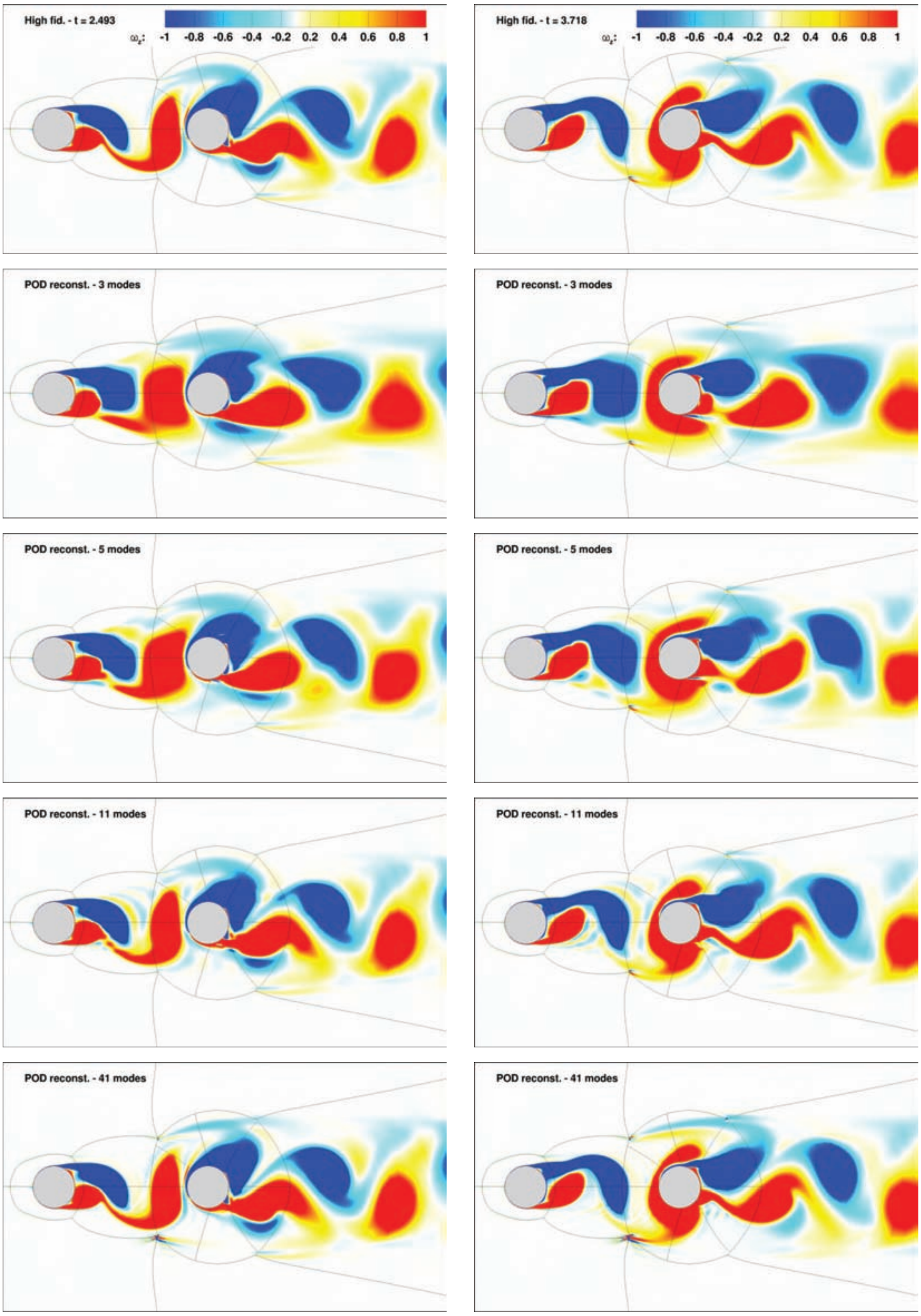

Figure 2.22: Vorticity field from URANS (top) and POD reconstruction from 3, 5 and 41 modes at $2T_{VK}/4$ (left) and $3T_{VK}/4$ (right) in static case.

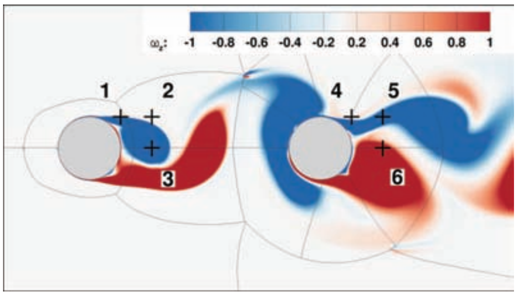

Figure 2.23: Monitoring locations for the reconstructed velocity analysis.

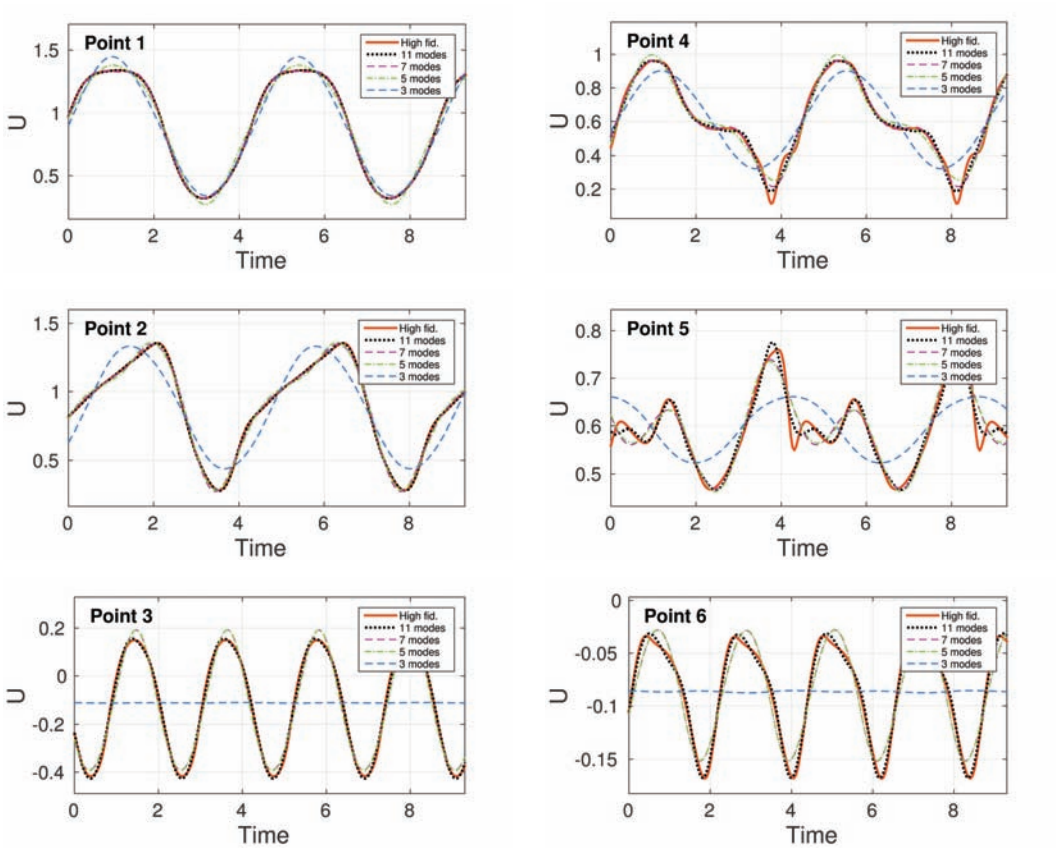

Figure 2.24: Time evolution of the streamwise high-fidelity and reconstructed velocity components for 3, 5, 7 and 11 modes.

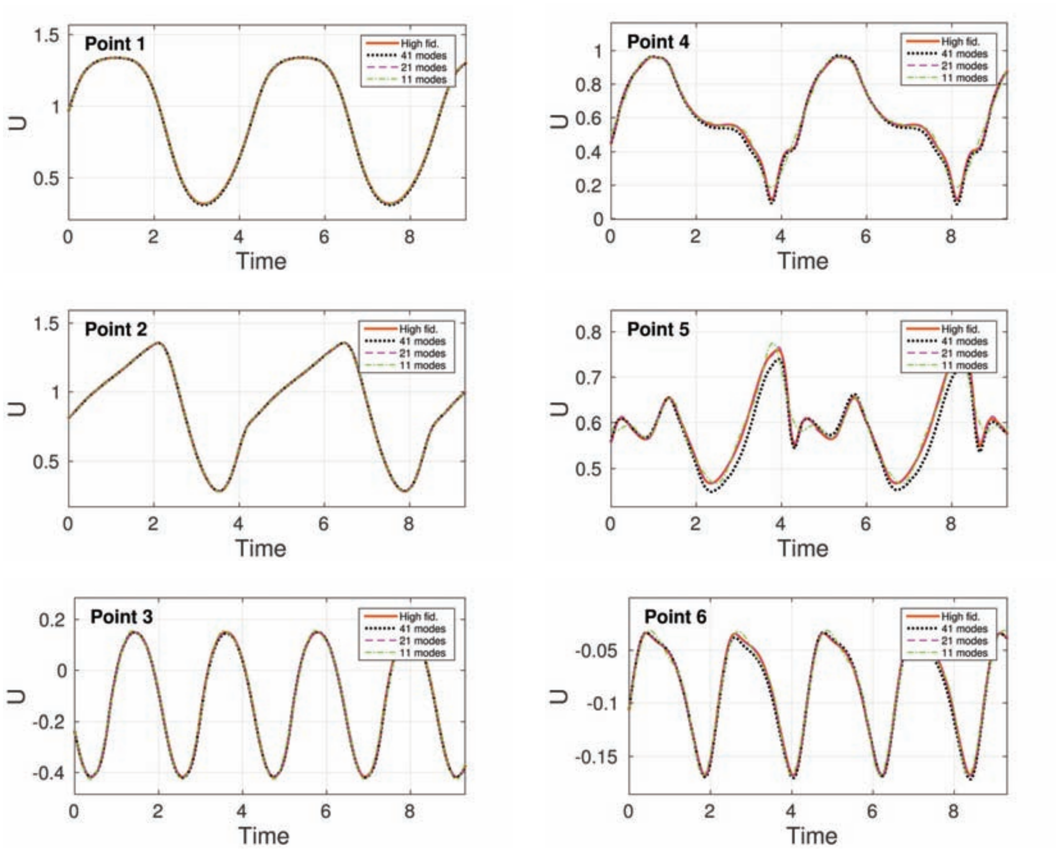

Figure 2.25: Time evolution of the streamwise high-fidelity and reconstructed velocity components for 11, 21 and 41 modes.

2.1.5 3D Simulations

Based on the results presented in the previous subsection, 3D simulations have been carried out by our research team. Some of them have been published (Skopek et al., 2012) and are briefly recalled here for comparison purpose. DDES-k-ω-SST and DDES-k-ω-OES simulation have been performed on a 3D mesh of 16 million volumes cells. The span of the domain was $H/D = 3$.

A slice of the 3D field is plotted in Fig. 2.26, and can be compared to the field of vorticity from 2D k-ω-SST simulation (Fig. 2.5). As expected, the resolution of the eddy structures is much better in the case the hybrid modelling, which compared well with the experiment in a qualitative point of view (Fig. 2.27). In particular the shear layer from the detachment point, at top and bottom of the two cylinders, is better defined, and the Kelvin-Helmholtz vortices are well captured.

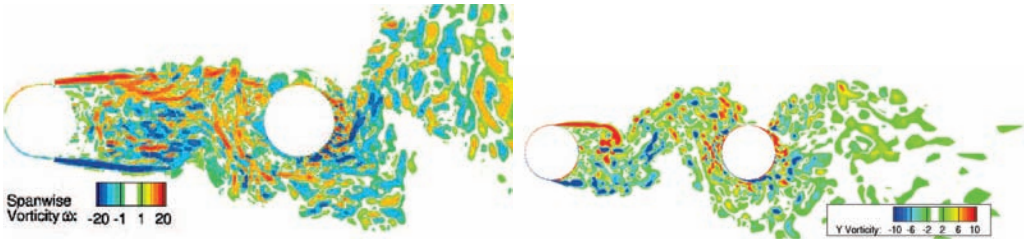

Figure 2.26: 2D view (slice) of the instantaneous spanwise vorticity field (left: DDES-k-ω-SST, right: DDES-k-ω-OES; Skopek et al., 2012).

Similarly to the 2D simulation (Fig. 2.7) mean streamlines have been plotted in Fig. 2.28 allowing for a direct comparison between experiment (PIV) and 3D simulation (DDES-k-ω-OES) in the gap region. At first glance, it seems the numerical result matches better the experimental one. The comparison of the mean streamwise velocity profiles in the gap region and downstream the rear cylinder (Fig. 2.29) confirms this observation.

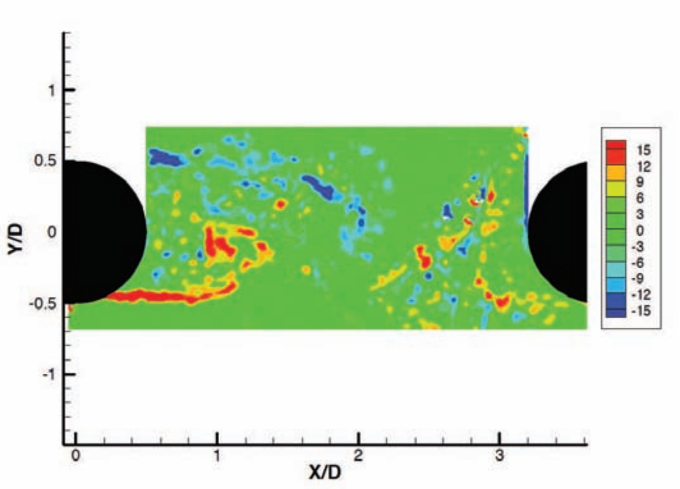

Figure 2.27: Instantaneous spanwise vorticity field from PIV measurements (Jenkins et al., 2005).

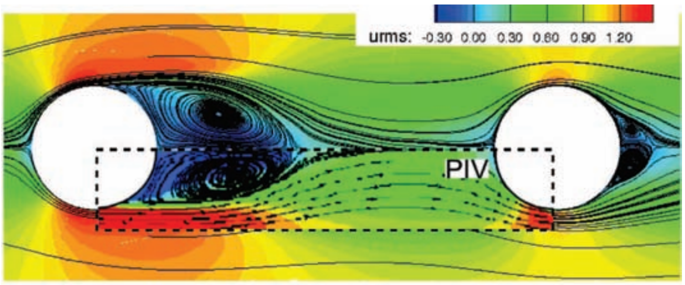

Figure 2.28: Mean velocity streamlines and field comparison between PIV and DDES-k-ω-OES (Skopek et al., 2012).

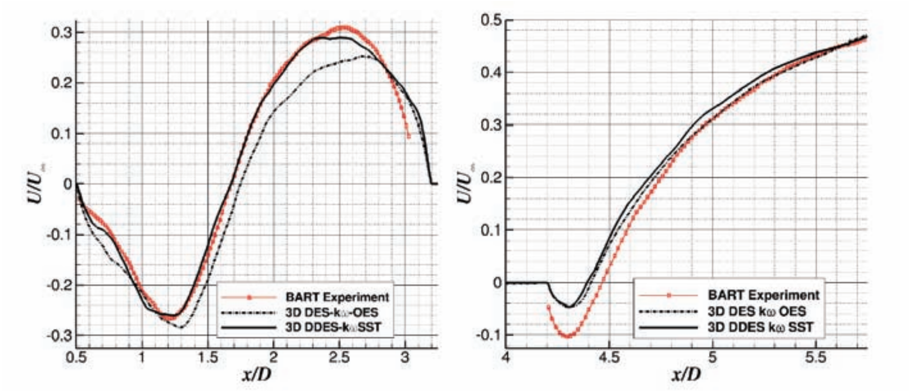

Figure 2.29: Mean streamwise velocity profiles comparison at $y = 0$ between PIV, DDES-k-ω-SST and DDES-k-ω-OES.

2.2 Fluid-structure interaction - Dynamic case

2.2.1 Introduction

The tandem cylinders configuration is related to the sizing of the heat exchangers in nuclear reactor technology. The configuration is also a model problem related to Movement Induced Vibration (MIV) dynamics extracted from a more complex cylinders bundle configuration as pointed out in the national research project ANR-Baresafe coordinated by EDF and including partnership of the main nuclear engineering industrial partners in France, CEA and AREVA. In this context, the objective is to propose High-Fidelity CFD-CSM approaches able to predict the loads (amplitudes and frequencies) as a function of the structural parameters (reduced velocity and the mass-damping number; Scruton number) with sufficient accuracy as required for design. Furthermore, the objective is to develop efficient low-order decomposition and reconstruction of the flow dynamics coupled with the structural dynamics, for further use in Reduced Order Modelling (ROM) which will enable faster design cycles for the end user. The present thesis aims at providing efficient turbulence modelling for the CFD part, coupled with the solid structure's motion by means of the Arbitrary Lagrangian-Eulerian method (ALE) and to simulate the spontaneous vibrational instability onset, when the structural parameters coupled with the fluid's velocity and time scales overpass critical limits.

Beyond the static configuration studied in the ATAAC European programme and as a link with the ANR-Baresafe program, the fluid-structure interaction will be examined, leading to vibration of the downstream cylinder in the tandem, because of the shearing mechanisms and vortex shedding developed past the upstream cylinder. This problem is also related to the vibrations occuring in the landing gear cylindrical supports.

A suitable POD reconstruction will be presented applied to the vibrational case, on view of further use in the Reduced Order Modelling context.

2.2.2 Results

2.2.2.1 Fluid-structure interaction

Fig. 2.30 presents the evolutions of the lift coefficient in comparison with the position of the downstream cylinder versus time, for Scruton number Sc $= 1$. For low values of the reduced velocity up to 3, these evolutions are in phase, showing synchronisation between the force and displacement. This indicates a 'lock-in' mechanism corresponding to the Vortex Induced Vibration (VIV) as depicted also in the simulations by Shinde et al. (2014) in a cylinders bundle configuration. At reduced velocity value of 4, a slight phase lag occurs, which becomes more pronounced and progressively increases in the reduced velocity range $[5, 10]$. This behaviour indicates the passage to the Movement Induced Vibration (MIV), where the phase lag increases and is associated to vibrational instability which can lead to negative damping (Fig. 2.31).

The Strouhal number of the lift oscillations does not considerably vary as a function of the reduced velocity (Table 2.6). The Strouhal number of the downstream cylinder position is practically constant in the VIV range and decreases in the MIV

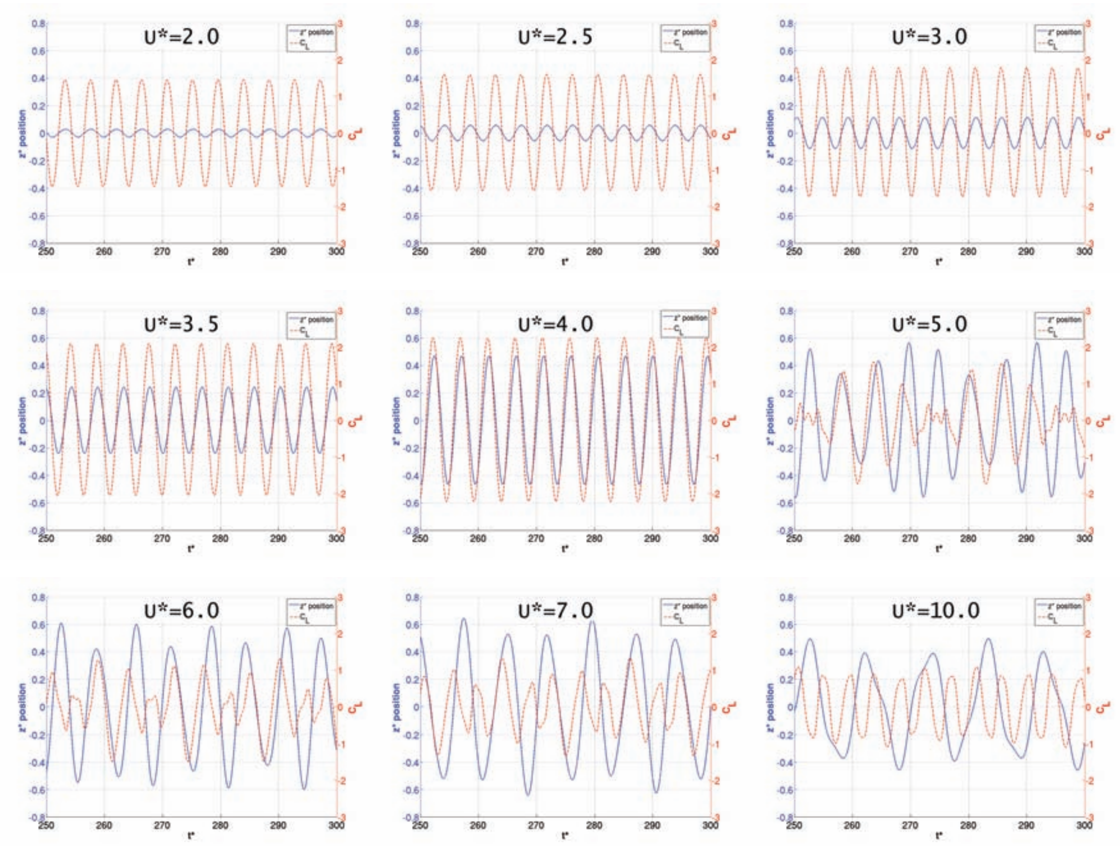

Figure 2.30: Position and lift coefficient of the downstream cylinder for reduced velocities between 2.0 and 10.0.

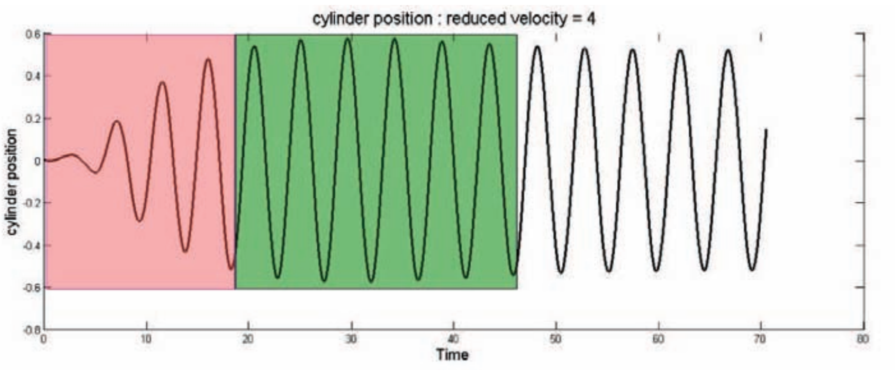

Figure 2.31: Transitional phase of the cylinder vibrations (red: amplification, green: saturation).

$\mathbf{u}^*$	2.0	2.5	3.0	3.5	4.0	5.0	6.0	7.0	10.0
St($\mathbf{C_L}$) Up.	0.228	0.227	0.227	0.222	0.212	0.227	0.228	0.227	0.228
St($\mathbf{C_L}$) Down	0.228	0.227	0.227	0.222	0.212	0.181	0.228	0.227	0.228
St($\mathbf{z}^*$) Down	0.228	0.227	0.227	0.222	0.212	0.181	0.155	0.135	0.098

Table 2.6: Comparison of Strouhal numbers vs reduced velocities in dynamic case (Up.: upstream cylinder, Down: downstream cylinder).

range of the reduced velocities. This behaviour is also shown in Fig. 2.32, where the values are reported. In this figure, f_{S0} corresponds to the non-dimensionalised natural frequency of the cylindrical structure.

Fig. 2.35 shows the flow structure from the Q-criterion for the DDES-k-ω-OES computations of the vibrational case with Scruton number of 1 and reduced velocity of 3. The spanwise vortex structures past the downstream cylinder undergo a drastic modification of their wavelength, which displays strong dislocation patterns regarding the static case (Skopek et al., 2012). A 3D-POD analysis is under progress in order to provide a space-time tracking as presented in Szubert et al. (2015b) and discussed in section 3.1.1 page 52 for the flow around a supercritical aerofoil. A two-dimensional view of the flow pattern is provided in Fig. 2.33 and 2.34 in the section dedicated to the POD analysis.

2.2.2.2 POD analysis

Similarly to the static case (subsection 2.1.4.4 page 27), an attempt of POD analysis is carried out in the dynamic case.

Fig. 2.33 and 2.34 show the result after POD analysis carried out for the dynamic case. Because of the moving boundary of the downstream cylinder, POD has been applied on the number of snapshots classified according to a phase-splitting of the displacement evolution within 8 intervals within one period of von Kármán vortex shedding. In each interval, the hypothesis of small displacement has been made. Snapshots were recorded at the simulation time step, $\Delta t^* = 0.00845$. The POD reconstructions are compared with instantaneous fields of different phases at $0 \times T_{VK}$ and $T_{VK}/4$ in the first figure, and $2T_{VK}/4$ and $3T_{VK}/4$ in the second figure, where T_{VK} is the period of the von Kármán vortex shedding. A good comparison has been obtained regarding the moving grid in the context of the fluid-structure interaction.

This kind of POD reconstruction is promising to use for the construction of a Reduced Order Model, where the present POD basis can be used for the Galerkin projection of the present High-system of transport equations. This issue is being used in the context of the ANR-Baresafe research project.

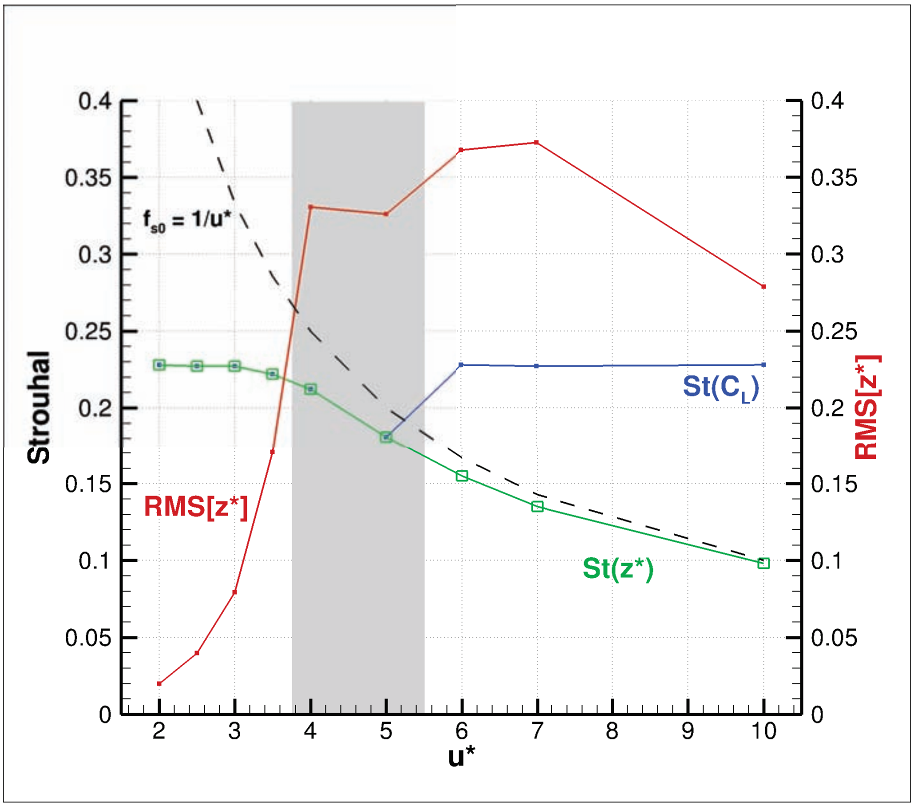

Figure 2.32: Non-dimensionalised frequency of the lift coefficient (blue) and position of the downstream cylinder (green) and RMS value of the position fluctuations (red).

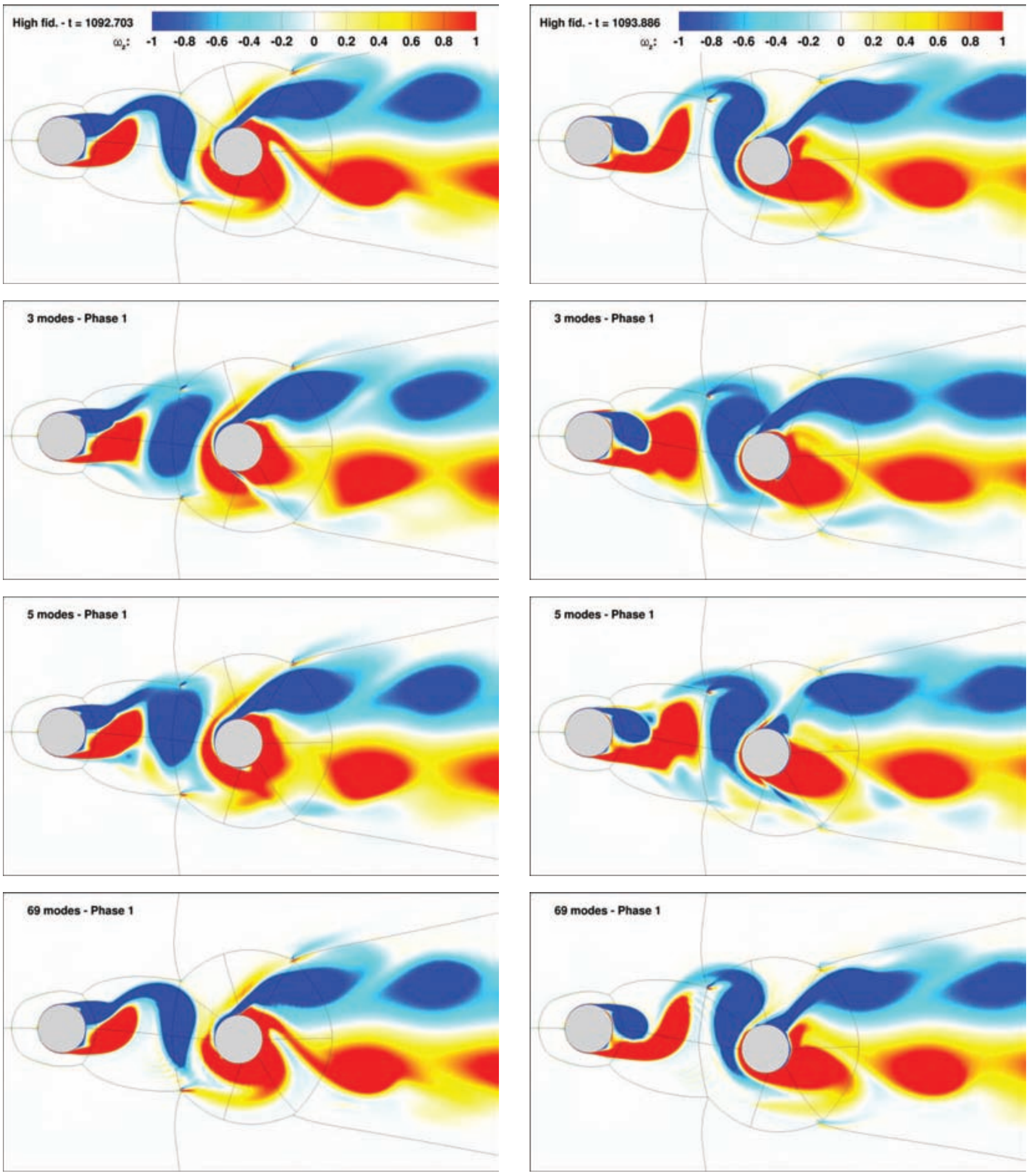

Figure 2.33: Vorticity field from URANS (top) and POD reconstruction from 3, 5 and 69 modes at $0 \times T_{VK}$ (left) and $T_{VK}/4$ (right) in dynamic case.

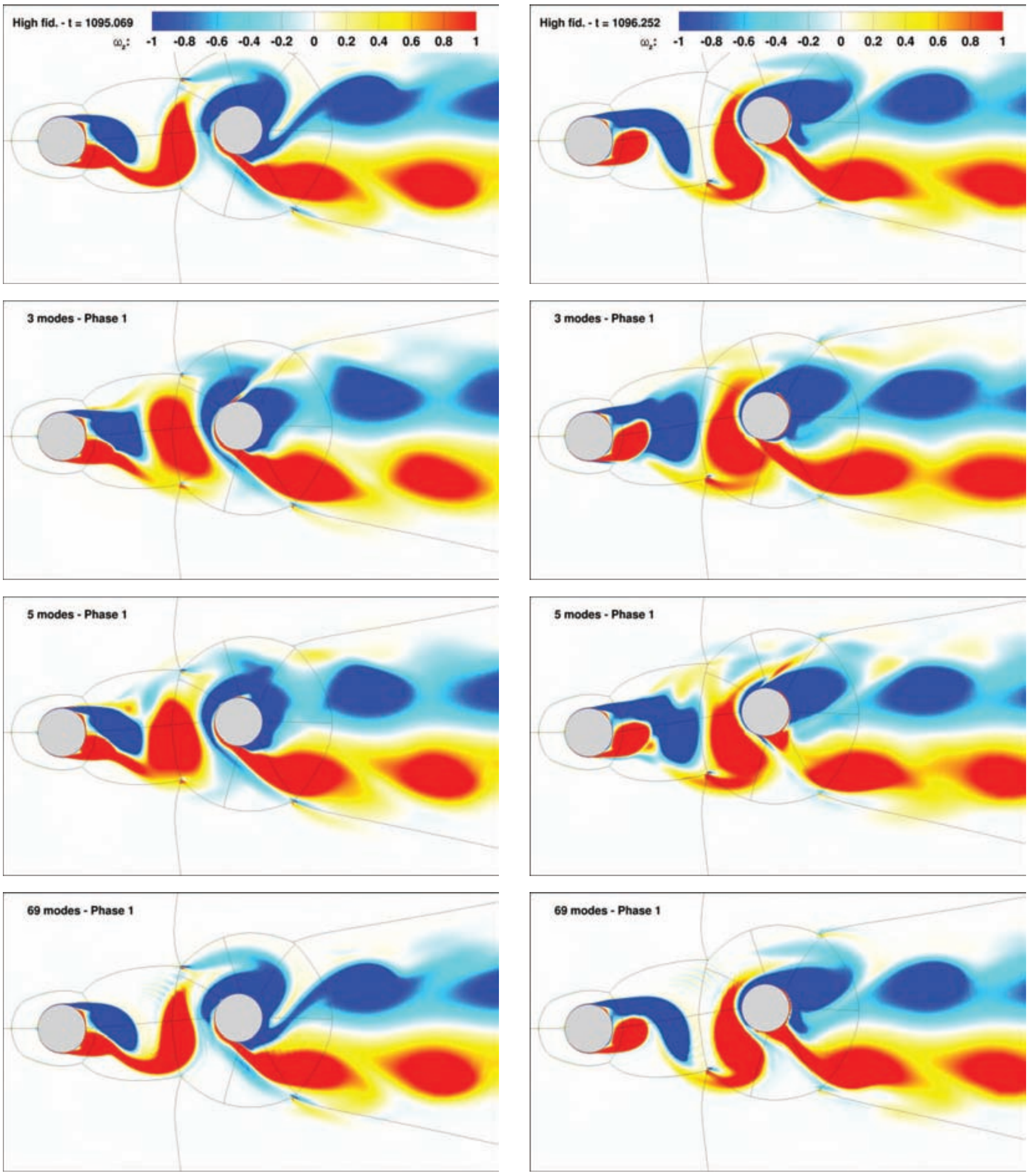

Figure 2.34: Vorticity field from URANS (top) and POD reconstruction from 3, 5 and 69 modes at $2T_{VK}/4$ (left) and $3T_{VK}/4$ (right) in dynamic case.

2.3 Conclusion

2D simulations of the tandem cylinders configuration have been performed to determine the optimal convergence criterion, as well as to study the capability of three turbulence models to predict the flow around this geometry, compared to experimental results. All these results have been used for DDES computations (Skopek et al., 2012), that highlighted the importance of the third dimension in the prediction , and confirmed that classical URANS modelling is not suitable to capture high-frequency phenomena, in particular in the noise range. However, hybrid modelling was able to predict with high accuracy these phenomena, as well as the mean flow properties.

The present study has shown the ability of spontaneous oscillatory motion generation on the downstream cylinder, which was allowed moving freely in the vertical direction along the lift coefficient. The computations have shown the passage from the VIV lock-in mechanism towards the MIV mechanism of vibrational instability characterized by negative damping. The corresponding progressive increase of the phase-lag from zero (in the VIV case) to higher values (in the MIV case) reaching also phase opposition by 180° has been quantified, as well as the appearance of negative damping in the transient phases of the motion. This behaviour is in qualitative agreement with the Connors experimental diagram as well as with other DDES simulations in the context of the ANR-Baresafe program (Shinde et al., 2014). These simulations predicted the von Kármán instability frequencies as well as the evolution as a function of the reduced velocity, of the von Kármán mode Strouhal number and of the RMS of lift coefficient. The fluid-structure interaction is currently being studied by means of hybrid DDES simulations aforementioned Fig.2.35)

Based on the present High-Fidelity approaches, the present thesis carried out a POD reconstruction of the static and dynamic structural oscillation flow cases, by using an adapted phasing of the POD snapshots in the dynamic case. The provided reconstructions are able to capture the principal dynamics of the flow field and the method is currently in use in the Baresafe context for the Reduced Order Modelling of the dynamic case.

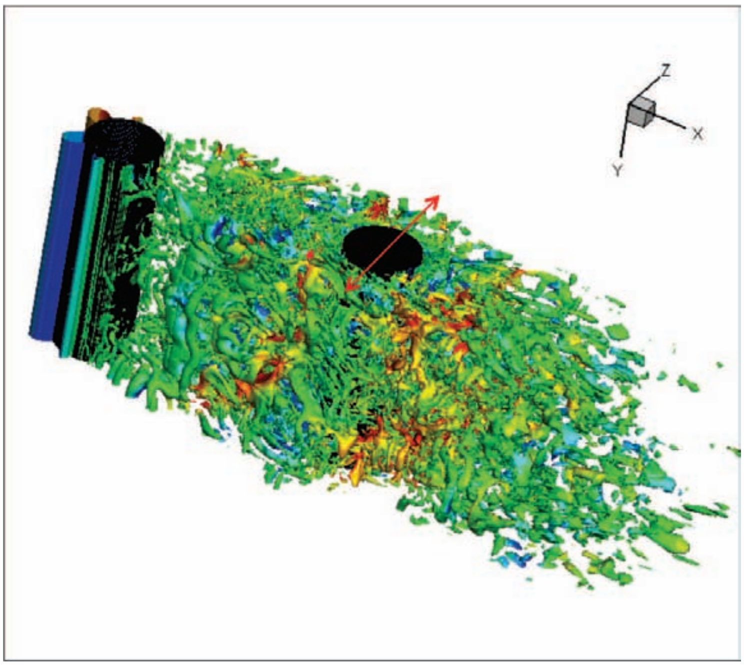

Figure 2.35: Q criterion field around the tandem cylinders in 3D and dynamic configuration by DDES-OES-k-ω-BSL.

Chapter 3

Physics and modelling around two supercritical airfoils

Contents

In this chapter, the flow around two supercritical airfoils, designed in the context of two different European projects, is analysed near and in transonic buffet conditions.

3.1 Shock-vortex shear-layer interaction in transonic buffet conditions

The OAT15A is a supercritical airfoil designed by ONERA (Jacquin et al., 2005) in the context of the ATAAC European project (same as the tandem of cylinders, chapt. 2). The numerical aspects of the simulations of this test case, as well as some physical properties, in transonic buffet conditions, have been investigated by Fernando Grossi in our research team in the context of a Master's and a Ph.D. theses (Grossi, 2010, 2014) and have been published in articles (Grossi et al., 2014) as well as proceedings from several oral communications (Grossi et al., 2011, 2012b,a). Enriched from all this work, new simulations have been performed and the physics of the interaction between the main phenomena developing around the airfoil has been analysed by mean of signal processing and proper orthogonal decomposition (POD). From the POD reconstruction, a localised stochastic forcing has been introduced in the transport equations of the initial turbulence model. This method, as well as the results on the physical analysis, have been the subject of an article accepted in the Journal of Fluids and Structures in March 2015 Szubert et al. (2015b). This article is fully reproduced in this manuscript in the following section to present the results, in addition to details about the geometry and the numerical method. A discussion about the upscale turbulence modelling, in the context of the ensemble-averaged approaches, is given in section 3.1.2.

3.1.1 Shock-vortex shear-layer interaction in the transonic flow around a supercritical airfoil at high Reynolds number in buffet conditions

Journal of Fluids and Structures 55 (2015) 276–302

Contents lists available at ScienceDirect

Journal of Fluids and Structures

journal homepage: www.elsevier.com/locate/jfs

Shock-vortex shear-layer interaction in the transonic flow around a supercritical airfoil at high Reynolds number in buffet conditions

Damien Szubert [a,*], Fernando Grossi [a], Antonio Jimenez Garcia [a], Yannick Hoarau [b], Julian C.R. Hunt [c], Marianna Braza [a]

[a] Institut de Mécanique des Fluides de Toulouse, UMR No 5502 CNRS-INPT-UPS, Allée du Prof. Camille Soula, F-31400 Toulouse, France
[b] Laboratoire ICUBE, UMR No 7357, Strasbourg, France
[c] Department of Earth Sciences, University College London, London WC1E 6BT, UK

ARTICLE INFO

Article history:
Received 4 April 2014
Accepted 7 March 2015
Available online 2 May 2015

Keywords:
Transonic flow
Buffet instabilities
Wavelets
POD
Turbulence modelling
Stochastic forcing

ABSTRACT

This paper provides a conceptual analysis and a computational model for how the unsteady 'buffeting' phenomenon develops in transonic, low incidence flow around a supercritical aerofoil, the OAT15A, at Reynolds number of 3.3 million. It is shown how a low-frequency buffet mode is amplified in the shock-wave region and then develops upstream and downstream interaction with the alternating von Kármán eddies in the wake past the trailing-edge as well as with the shear-layer, Kelvin–Helmholtz vortices. These interactions are tracked by wavelet analysis, autoregressive (AR) modelling and by Proper Orthogonal Decomposition. The frequency modulation of the trailing-edge instability modes is shown in the spectra and in the wall-pressure fluctuations. The amplitude modulation of the buffet and von Kármán modes has been also quantified by POD analysis. The thinning of the shear layers, both at the outer edge of the turbulent boundary layers and the wake, caused by an 'eddy-blocking' mechanism is modelled by stochastic forcing of the turbulent kinetic energy and dissipation, by small-scale straining of the higher-order POD modes. The benefits from thinning the shear-layers by taking into account the interfacial dynamics are clearly shown in the velocity profiles, and wall pressure distribution in comparison with the experimental data.

1. Introduction

Understanding the various mechanisms related to buffet instabilities in the transonic flow around a supercritical airfoil is the main objective of this paper. A detailed physical analysis is developed for the interactions between shock waves and the boundary layer over the aerofoil, as well as between wake vortices and the shock waves. A further complexity arises from the interactions between the wake vortices near the trailing edge and the fluctuating sheared interface that bounds the wake flow. Pioneering studies of Levy (1978) and Seegmiller et al. (1978), made evidence of a shock unsteadiness characterised by a low-frequency and high-amplitude, in the Mach number range 0.7–0.8 corresponding to aircraft's cruise-speed. Several experimental

---

[*] Corresponding author.

http://dx.doi.org/10.1016/j.jfluidstructs.2015.03.005

and numerical studies have been devoted to this flow phenomenon and its impact on the aerodynamic forces: McDevitt et al. (1976), Jacquin et al. (2005, 2009) and Brunet (2003).

Whereas the majority of the studies devoted to the transonic interaction deal with the high-Reynolds number range, the physical mechanisms of the buffet onset can be studied more easily in the lower Reynolds number range, allowing for Direct Numerical Simulation. For a NACA0012 airfoil, (Bouhadji and Braza, 2003a, 2003b) have analysed the successive states of the unsteadiness due to the compressibility effects in the Mach number range 0.3–1.0 by 2D and 3D Navier–Stokes simulations. The buffet instability was analysed in association with the von Kármán vortex shedding in the Mach number range 0.75–0.85, as well as the suppression of the buffet form Mach numbers beyond 0.85. The buffet mode has also been analysed by DNS of Bourdet et al. (2003), who used in addition the Stuart-Landau model (Landau, 1944) in order to quantify the linear and non-linear parts of the buffet instability.

These studies showed the sharp rise of the drag coefficient as the Mach number increases in the range 0.7–0.8, as well as the interaction of the shock wave with the von Kármán wake instability downstream of the trailing-edge. It was shown that this instability was formed in the wake and propagated towards the trailing-edge beyond a low-subsonic critical value of the Mach number, of order 0.2, for a NACA0012 airfoil at zero incidence and Reynolds number of 10 000 (Bouhadji, 1998). This instability (mode I) persists within the whole transonic speed interval, up to Mach number of order 0.85, independently on the appearance of the buffet. This second instability (mode II) was found to appear in the interval 0.75–0.8 and to strongly interact with mode I, where the buffet was sustained by mode I. Experimental evidence of mode I was made by the Schlieren visualisations of D.W. Holder (Fung, 2002), Fig. 7.

Numerical simulations in the high-Re range (Grossi et al., 2012b; Jimenez-Garcia, 2012), regarding a supercritical airfoil, the OAT15A, introduced a splitter-plate at the trailing edge, which suppressed the von Kármán mode. It was shown that in the cases where the von Kármán mode was remote (downstream of a critical length of the splitter plate), the buffet mode was considerably attenuated and disappeared. Therefore, it is worthwhile analysing the interaction of these two modes in the high-Reynolds number regimes for aerodynamics applications. In particular, there is little knowledge of this kind of interaction in the state of the art with regard to the high-Re range as well as more generally, of the trailing-edge dynamics feedback effect towards the shock-wave/boundary-layer interaction region (SWBLI) upstream of the trailing-edge. Lee (1990) reported a schematic explanation of the buffet interaction with Kutta waves coming from the trailing-edge, without a quantification of this interaction. Furthermore, it is worthwhile mentioning that the SWBLI is followed by separation of the boundary layer and by the formation of *thin* shear layers at the edges of the boundary layers and in the wake, where local Kelvin–Helmholtz (K–H) instabilities are observed.

In order to compute the interactions and feedback between the shear-layer and trailing-edge instabilities with the upwind shock-buffet mode, new methods are needed. These have to overcome the tendency of the shear layers to thicken downstream of the SWBLI, because of the turbulent shear stress modelling near the interface is usually approximated by employing eddy-viscosity concepts based on equilibrium turbulence hypotheses and direct cascade. In the flow physics however, upscale phenomena occur that increase the energy of the turbulence spectrum from intermediate range towards the lower wavenumbers (Braza et al., 2006). These mechanisms are not yet sufficiently taken into account in the modelling equations. However, theoretical analysis (Hunt et al., 2008) and experimental studies (e.g. Ishihara et al., 2015) show that these stresses are generated by the inhomogeneous small-scale motions in the turbulent region near the interface and thence increase the local "conditional" shear and "eddy blocking effect" within the interfacial layer (Fig. 1). This influence of small scales on the whole flow is effectively an "upscale" process. The local turbulence adjacent to the interface tends to reduce the Kelvin–Helmholtz instability modes of the interface (Dritschel et al., 1991).

A new approach for modelling the interface regions is needed, which can be based on recent numerical and experimental research into turbulent interfacial shear flows, on the outer edges of jets, wakes and the outer parts of boundary layers with thickness L. The thin randomly moving interfaces which separate regions of strong and weak turbulence have a thickness $\ell(\ll L)$. This general property of turbulent flows was in fact suggested and discussed by Prandtl in 1905, though he did not take it further once he became interested in the mixing length model of the mean properties of turbulent shear flows (see Bodenschatz and Eckert, 2011; Taveira and da Silva, 2014). Within these layers, the average shear (or in 2-dimensions the gradient of shear) is much stronger than that in the adjacent turbulent shear flows. At very high Reynolds numbers Re, determined by L and the *R.M.S.*, turbulent velocity u_o, the thickness ℓ of these interface layers is of the order of the Taylor microscale ℓ_v (i.e $L\,\mathrm{Re}^{-1/2}$), but within them very thin elongated vortices form with a thickness ℓ_v of the order of the Kolmogorov microscale (i.e. $\ell_v \sim L\,\mathrm{Re}^{-3/4}$, Eames and Flor, 2011). Numerical simulations show that these sharp interfaces occur even in complex turbulent flows, such as flows over aircraft wings (Braza, 2011).

These interfaces have their own mean local dynamics that keep the mean gradients at the interface at a maximum, through eddy blocking and enhanced vortex stretching (Hunt et al., 2008). Similar bounding interfaces also occur at the edges of patches of turbulence, such as puffs or vortex rings (Holzner et al., 2008). These intensely sheared layers interact with the motions outside the layers by blocking external eddies (through shear sheltering), which leads to a balance between sharpening of the velocity gradients in the layer and the tendency to diffuse outwards (Hunt et al., 2008). The typical spacing between the interfacial layers is of order of the "dissipation integral length scale" (Hunt et al., 2014).

Thus, the overall high-Re dynamics of the interface has to be modelled in order to correctly represent the turbulent transfers through the rotational–irrotational regions either side of these interfaces that have to be kept thin. This modelling has to include the complex interactions between the developing instability modes and the fine-scale turbulence. It is necessary to have a comprehensive turbulence model that should include the effects of the low-frequency organized motion and the transfers due to the random turbulence. Such models should take sufficient account of the large and small motion effects, especially the shear–stress gradients as studied at high-Re atmospheric flows by Hunt et al. (1984). The turbulence modelling in the present case should also accurately predict the pressure distribution and the unsteady loads in fluid–structure interaction.

In this context, approaches such as standard URANS, derived from assumptions of turbulence in statistical equilibrium and using downscale cascade, tend to produce higher rates of the turbulence kinetic energy and to underestimate the global coefficients (drag, lift) and their amplitudes (Haase et al., 2009).

The Large Eddy Simulation uses a number of degrees of freedom being orders of magnitude higher than the grid size needed for URANS and hybrid approaches. For moderate Reynolds number flows (Re O(10^4)), LES can capture the major instabilities past bodies, whereas for the high-Reynolds number range (Re $>10^6$), for industrial designs, it is not practical with typical computational capacity to apply LES for aerodynamic flows around lifting structures. Furthermore, even with LES methods, improvements can be expected by reconsidering the classical downscale energy transfer models for the small-scale eddies in the dissipative wave-number range by using upscale transfer processes in the turbulence modelling of the thin interfaces.

Recent efforts in turbulence modelling are devoted to accurately reproduce the flow physics in respect of instability amplification, strong flow detachment and accurate prediction of the associated frequencies, unsteady loads and in particular, of pressure fluctuations, representing a crucial need for aeroacoustics.

Hybrid RANS-LES methods are quite suitable for this category of *fluid–structure interaction* problems, because they associate the benefits of URANS in the near-region and those of LES in the regions of flow detachment, as reported the proceedings of the 4th HRLM, 'Hybrid RANS-LES Methods' symposium (Fu et al., 2012). Hybrid methods can be considerably improved by using adapted URANS modelling in the near-wall region and adapted LES modelling in the flow detachment areas, in order to allow for modification of the turbulent scales accounting for non-equilibrium turbulence.

In this context, improved URANS approaches can be used to reduce the turbulent viscosity levels and allow the amplification of instabilities, as for example the Scale Adaptive Simulation (SAS; Menter and Kuntz, 2003; Menter and Egorov, 2005), the Organised Eddy Simulation (OES; Braza et al., 2006; Bourguet et al., 2008, among others). SAS adapts the Kolmogorov turbulence scale according to flow regions governed by non-equilibrium turbulence effects. OES accounts for stress-strain directional misalignment in non-equilibrium turbulence regions thanks to a tensorial eddy-viscosity concept derived from Differential Reynolds Stress Modelling (DRSM) projection on the principal directions of the strain-rate tensor.

Although significant conceptual progress has been accomplished in the last decade, there still remain open questions with regard to the quantitative prediction of the above mechanisms with the accuracy required by the design. To our knowledge, the majority of the available modelling approaches produce less thin shear-layer interfaces, even by using considerably fine grids. This is generally due to a higher turbulence diffusion level than in the physical reality, produced by the modelling approaches, which mostly employ downstream turbulence cascade assumptions. In the present paper, the motivation is to enhance the eddy-blocking effect and vortex stretching in the sense of an upscale cascade.

On view of the above elements, the objectives of the present paper are as follows: to analyse in detail the interaction between two main instabilities, the buffet and the von Kármán modes in the transonic flow around a supercritical airfoil, whose configuration is involved in the next generation of civil aircraft design, by means of numerical simulation and adapted turbulence modelling concepts. A method of stochastic, *inhomogeneous* forcing of the turbulence transport equations is presented. This models the thin turbulent/non-turbulent, shear-layer interfaces and thence the large-scale flow structure on the purpose to provide the correct pressure fluctuations needed for fluid–structure interaction. The content of the following sections are as follows: Section 2 presents the flow configuration and the numerical approach. Section 3 presents the results regarding the buffet instability, its interaction with the shear-layer and near-wake instabilities based on conventional URANS/OES methods. This section includes in particular wavelet analysis and Proper Orthogonal Decomposition. In Section 4, the stochastic forcing approach for the higher modes is presented and compared with other methods and experimental results. Section 5 is the conclusion of the paper.

2. Flow configuration, numerical method and turbulence modelling

2.1. Test case description

The transonic buffet over the OAT15A airfoil was investigated in the experimental work by Jacquin et al. (2005, 2009), as well as by Brunet et al. (2003), by means of both experimental and numerical study at free-stream Mach numbers in the range of 0.70–0.75 and a chord-based Reynolds number of 3 million. The OAT15A is a supercritical wing section with a thickness-to-chord ratio of 12.3%. The wind tunnel model has a chord of $C=0.23$ m and a blunt trailing edge measuring $0.005C$. The airfoil was mounted wall-to-wall and the boundary layer was tripped on both sides at $x/C=0.07$ from the leading edge for fully-turbulent behavior. The results showed that a periodic self-sustained shock-wave motion (buffet) was obtained for angle of attack values higher or equal to 3.5°. A detailed experimental study, for this angle of attack, is reported in Jacquin et al. (2009). The main flow features concerning buffet were essentially two dimensional, and the buffet frequency was found 69–70 Hz. The shock-wave motion was coupled with an intermittent separation of the boundary layer. In the present study, this flow configuration is considered in two dimensions at an incidence of 3.5° and a free-stream Mach number of 0.73, in order to analyse the buffet onset and the interaction with the near-wake instability.

2.2. Numerical method

The simulations of the OAT15A configuration have been carried out with the Navier–Stokes Multi-Block (NSMB) solver. The NSMB solver is the fruit of a European consortium that included Airbus from the beginning of '90s, as well as main European aeronautics research Institutes, as KTH, EPFL, IMFT, ICUBE, CERFACS, Univ. of Karlsruhe, ETH-Ecole Polytechnique de Zurich, among other. This consortium is coordinated by CFS Engineering in Lausanne, Switzerland. NSMB is a structured code that includes a variety of efficient high-order numerical schemes and of turbulence modelling closures in the context of LES, URANS and of hybrid turbulence modelling. A first reference of the code description can be found in Vos et al. (1998) concerning the versions of this code in the decade of '90s. Since then, NSMB highly evolved up to now and includes an ensemble of the most efficient CFD methods, as well as adapted fluid–structure coupling for moving and deformable structures. These developments can be found in Hoarau (2002) regarding URANS modelling for strongly detached flows, Martinat et al. (2008), in the area of moving body configurations, Barbut et al. (2010) and Grossi et al. (2014) allowing for Detached Eddy Simulation with the NSMB code.

NSMB solves the compressible Navier–Stokes equations using a finite-volume formulation on multi-block structured grids.

In 3D cartesian coordinates (x, y, z), the unsteady compressible Navier–Stokes equations can be expressed in conservative form as

$$\frac{\partial}{\partial t}(\mathbf{W})+\frac{\partial}{\partial x}(\mathbf{f}-\mathbf{f}_v)+\frac{\partial}{\partial y}(\mathbf{g}-\mathbf{g}_v)+\frac{\partial}{\partial z}(\mathbf{h}-\mathbf{h}_v)=0, \tag{1}$$

where t denotes the time. The state vector W and the inviscid fluxes f, g and h are given in the following for the laminar model:

$$\mathbf{W}=\begin{pmatrix}\rho\\ \rho U\\ \rho V\\ \rho W\\ \rho E\end{pmatrix},\quad \mathbf{f}=\begin{pmatrix}\rho U\\ \rho U^2+p\\ \rho UV\\ \rho UW\\ U(\rho E+p)\end{pmatrix},\quad \mathbf{g}=\begin{pmatrix}\rho V\\ \rho VU\\ \rho V^2+p\\ \rho VW\\ V(\rho E+p)\end{pmatrix},\quad \mathbf{h}=\begin{pmatrix}\rho W\\ \rho WU\\ \rho WV\\ \rho W^2+p\\ W(\rho E+p)\end{pmatrix}. \tag{2}$$

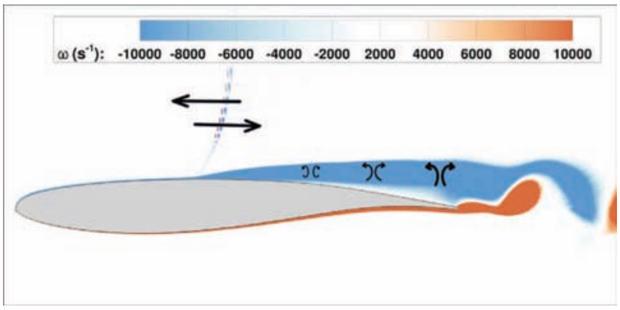

Fig. 1. Schematic diagram of shock, shear-layer and wake dynamics, including SWBLI, showing how the shear layer of the interface remains thin as a result of eddy-blocking mechanism.

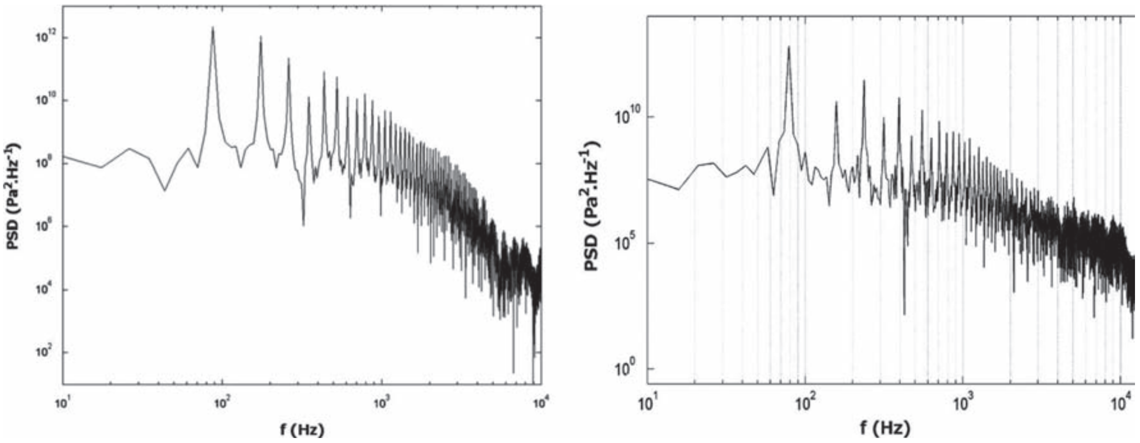

Fig. 2. Comparison of spectra of pressure signal for 2 different time steps; left: $\Delta t = 10^{-6}$ s; right: $\Delta t = 0.5 \times 10^{-6}$ s.

Here ρ is the density, U, V and W are the cartesian instantaneous velocity components, p is the pressure and E is the total energy. The viscous fluxes are defined as

$$\mathbf{f}_v = \begin{pmatrix} 0 \\ \tau_{xx} \\ \tau_{xy} \\ \tau_{xz} \\ (\tau\mathbf{U})_x - q_x \end{pmatrix}, \quad \mathbf{g}_v = \begin{pmatrix} 0 \\ \tau_{yx} \\ \tau_{yy} \\ \tau_{yz} \\ (\tau\mathbf{U})_y - q_y \end{pmatrix}, \quad \mathbf{h}_v = \begin{pmatrix} 0 \\ \tau_{zx} \\ \tau_{zy} \\ \tau_{zz} \\ (\tau\mathbf{U})_z - q_z \end{pmatrix}, \tag{3}$$

where τ_{ij} are the components of the stress tensor, q_i the heat flux (Fourier's law) and the work due to the viscous dissipation is expressed as $(\tau\mathbf{U})_i = \tau_{ix}U + \tau_{iy}V + \tau_{iz}W$.

The third-order of accuracy Roe upwind scheme (Roe, 1981) associated with the MUSCL van Leer flux limiter scheme (van Leer, 1979) is used to discretize the convective fluxes. Implicit time integration using the dual time stepping technique with 3 Gauss–Seidel iterations has been performed. A physical time step of 0.5 μs has been adopted ($\approx 5 \times 10^{-4} C/U_\infty$) after detailed tests carried out in Grossi (2010).

A study of the time step has been carried out with the grid used in this study. The Power Spectral Density (*PSD*) of the pressure signal on the airfoil at the location $x/C = 0.45$ for two time steps are shown in Fig. 2. The PSD spectrum on the left has been obtained from a calculation with a time step $\Delta t = 10^{-6}$ s, while the spectrum on the right comes from a calculation with a time step twice smaller and used in this study. A very similar distribution of the PSD can be observed in terms of frequency as well as of the energy level. A typical number of 30 inner iterations was necessary for the convergence in each time step. The convergence criterion at the inner step n is defined by the ratio between the L_2-norm of the density equation residual at the inner step n and the one at the initial inner step. The methodology adopted in the simulations is the same as in Grossi et al. (2014).

The grid has a C–H topology. Two different grids had been compared in previous studies (Grossi, 2014). The first is of size 110 000 cells approximately, used by Deck (2005) and provided within the partnership in the ATAAC (Advanced Turbulence Simulations for Aerodynamic Application Challengers) European program No. 233710 and a second, finer grid built in our research group, having 130,000 cells and a domain size of 80 chords. A comparison of these two grids is provided in Fig. 3. The mean value of the pressure coefficient (Fig. 3 left) and the RMS pressure distribution over the airfoil (Fig. 3 right) are very similar for the two grids. The buffet frequency is practically unchanged. The second grid has been used for the present

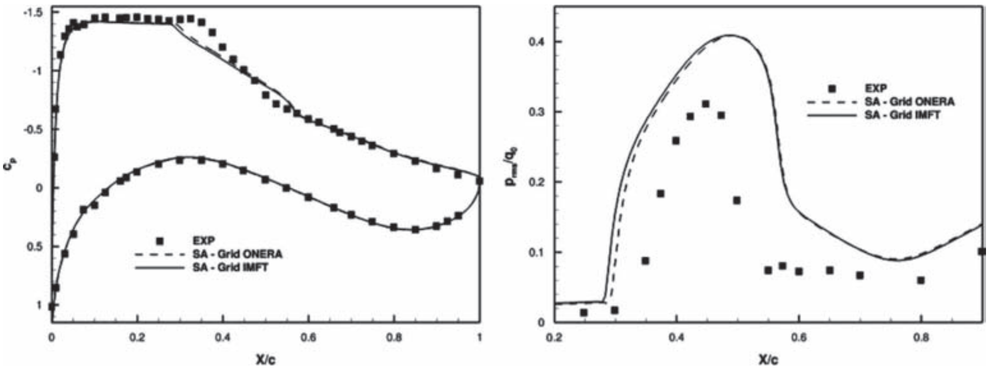

Fig. 3. Grid comparison concerning the mean wall-pressure coefficient (left) and the normalized *RMS* of the pressure fluctuations (right); experiment by Jacquin et al. (2009).

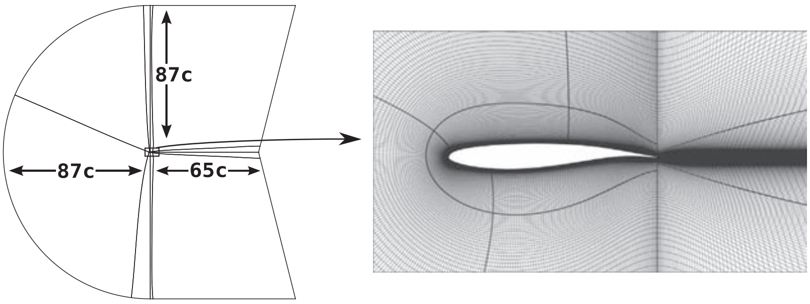

Fig. 4. Multiblock domain.

study. The y^+ coordinate regarding the turbulence modelling near the wall is smaller than 0.5 in the whole domain. Fig. 4 shows the grid and the computational domain.

2.2.1. Boundary conditions

On the solid wall, impermeability and no-slip conditions are employed. The far-field conditions are characteristic variables with extrapolation in time, defined by means of the experimental upstream values, the total pressure ($P_0 = 10^5$ Pa) and total temperature ($T_0 = 300$ K), as well as the upstream Reynolds number of 3 million. The upstream turbulence intensity is set equal to the experimental value of Tu=1%.

2.3. Turbulence modelling

Based on previous studies in our research group which examined the predictive ability of various turbulence models (Grossi et al., 2011, 2012a; Grossi, 2014), it was shown that the two-equation $k-\omega$-SST model (Menter, 1994) was not able to produce any unsteadiness at the present incidence value. The Spalart-Almaras model (SA; Spalart and Allmaras, 1994) in its standard version, and its Edwards and Chandra variant (SA-E; Edwards and Chandra, 1996) with compressibility correction of Secundov (SA-E+CC; Shur et al., 1995; Spalart, 2000), underpredicted the amplitudes of the shock motion, even by tripping the flow at $x/C = 0.07$ like in the experiment (*trip*), which does not have a significant effect on the flow. The strain adaptive formulation of the Spalart–Allmaras model (SALSA; Rung et al., 2003) gave good amplitudes but no secondary oscillations. The $k-\varepsilon$-OES model (Braza et al., 2006; Bourguet et al., 2008) involving in the present study an eddy-diffusion coefficient $C_\mu = 0.03$, was able to produce the shock unsteadiness with a frequency close to the experimental one. Moreover,

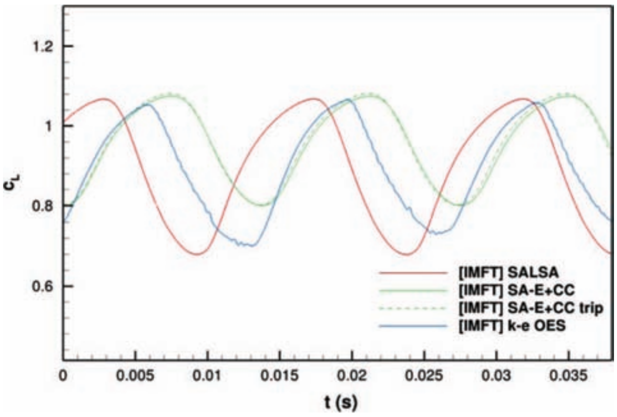

Fig. 5. Comparison of the time-dependent evolution of the lift coefficient between the strain adaptive formulation of the Spalart–Allmaras model (SALSA), the Edwards and Chandra variant of the Spalart–Allmaras model using compressibility corrections (SA-E+CC) without and with tripping at $x/C = 0.07$ (trip) and the $k-\varepsilon$-OES modelling.

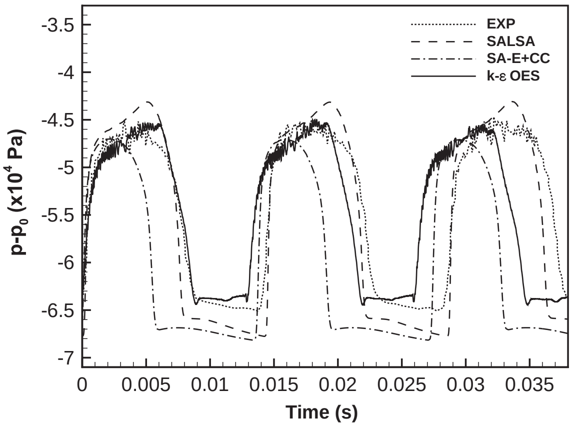

Fig. 6. Comparison of the time-dependent evolution of the surface pressure at $x/C = 0.45$ between three turbulence models as in Fig. 5; experiment by Jacquin et al. (2009).

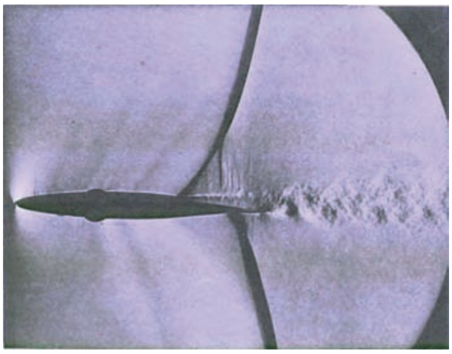

Fig. 7. Schlieren photograph of the eddying wake following a shock-induced flow separation (Courtesy of National Physical Laboratory, England; study by Duncan et al. (1932); photo by D.W. Holder.)

the formation of secondary oscillations within the buffet cycles, mainly due to intermittent von Kármán vortex shedding, has been captured. These results can be observed in Fig. 5 for the evolution of the lift coefficient and in Fig. 6 for the evolution of the pressure versus time at $x/C = 0.45$. The latter is compared with the experimental results from Jacquin et al. (2009) where the secondary oscillations are visible both in experiment and in the simulation with the $k-\varepsilon$-OES model.

3. Results

3.1. Buffet phenomenon and trailing-edge instabilities

According to the OES method, the resolved turbulence corresponds to an ensemble-averaged flow evolution, representing the organised, coherent part of the flow. A first overview of the buffet phenomenon and of the shear-layer and trailing-edge instabilities is represented in Fig. 8, by means of the velocity divergence field ($\nabla \cdot \mathbf{U} = \partial_x U + \partial_y V + \partial_z W$), which highlights compressibility effects around the airfoil and illustrates density gradients similar to the Schlieren visualizations. A qualitative similarity of the physical phenomena (shock waves, shock foot, wake) observed in the Schlieren visualization, for the experiment, by D.W. Holder (Fung, 2002; Fig. 7), and the field of divergence of velocity, for the CFD, is provided by the figures.

In the present study, the dimensionless time is $t^* = tU_\infty/C$. Furthermore, $t^* = 0$ was set to the maximum lift phase, with the shock wave at its most downstream position, as illustrated in Fig. 8(a). At that moment, in addition to the separation bubble at the foot of the shock, rear separation is also developed. These two regions grow simultaneously and fuse into a large separation area extending from the foot of the shock to the trailing edge. This scenario coincides with the well developed shock-wave motion towards the upstream direction, represented in Fig. 8(b). This figure shows the presence of a von Kármán instability, which quickly gives rise to alternate vortex shedding. In addition, Kutta-type waves are generated at the trailing edge of the airfoil and move upstream, at both sides of the airfoil. Upside, waves are refracted by the shock wave (Fig. 8(e)). As the shock moves towards the leading edge, the thickness of the separated region increases progressively, causing a dramatic decrease of the lift coefficient. As the shock wave comes towards its most upstream positions, the boundary layers becomes more and more detached. At the most upstream position (Fig. 8(f)), the reattachment process starts and reaches full reattachment while the shock is moving downstream (Fig. 8(g)), until $x/C = 0.60$ approximately (Fig. 8(h)). The alternate vortex shedding practically disappears, and the trailing-edge waves generation is temporarily attenuated, until the shear layer thickens again for a new cycle of buffeting.

The transonic flow around the symmetric NACA0012 airfoil (Bouhadji and Braza, 2003b), where a shock wave is observed on both upper and lower sides of the body, is cited in the introduction in order to comment the interaction between the buffet and the von Kármán modes. In the buffet regime ($M = 0.80$), the boundary layers downstream of the shock waves are alternately separated, inducing a thicker effective obstacle between the two separated shear layers that generates significant vorticity gradients in the trailing-edge region and hence creates the von Kármán mode. In the case of the supercritical OAT15A airfoil, at a slight angle of attack (3.5–3.9°), only one supersonic region exists at the upper side. In the buffet regime, the sequence of detachment and attachment still exists but only for the suction side. While the boundary layer is attached, the effective obstacle including the viscous region is thin enough to attenuate the vortex shedding which is only significant when the boundary layer is separated. It can be noted therefore that the shock wave, which thickens the boundary layer and the separated shear layers, creates favorable conditions for the von Kármán mode development, but this can happen even without buffet. In Bouhadji and Braza (2003a), where the successive stages of the von Kármán instability are analysed within a large Mach number interval including no-buffet and buffet regimes, the vortex shedding is developed according to the amplification of the von Kármán instability in the wake, as a result of the adverse pressure gradient due to the shape of the body, even without buffet appearance. Furthermore, at high Reynolds numbers ($1.4 \times 10^6 \leq \mathrm{Re} \leq 50 \times 10^6$), the von Kármán mode amplifies under similar conditions past a hydrofoil (incompressible flow; Bourgoyne et al., 2005). However,

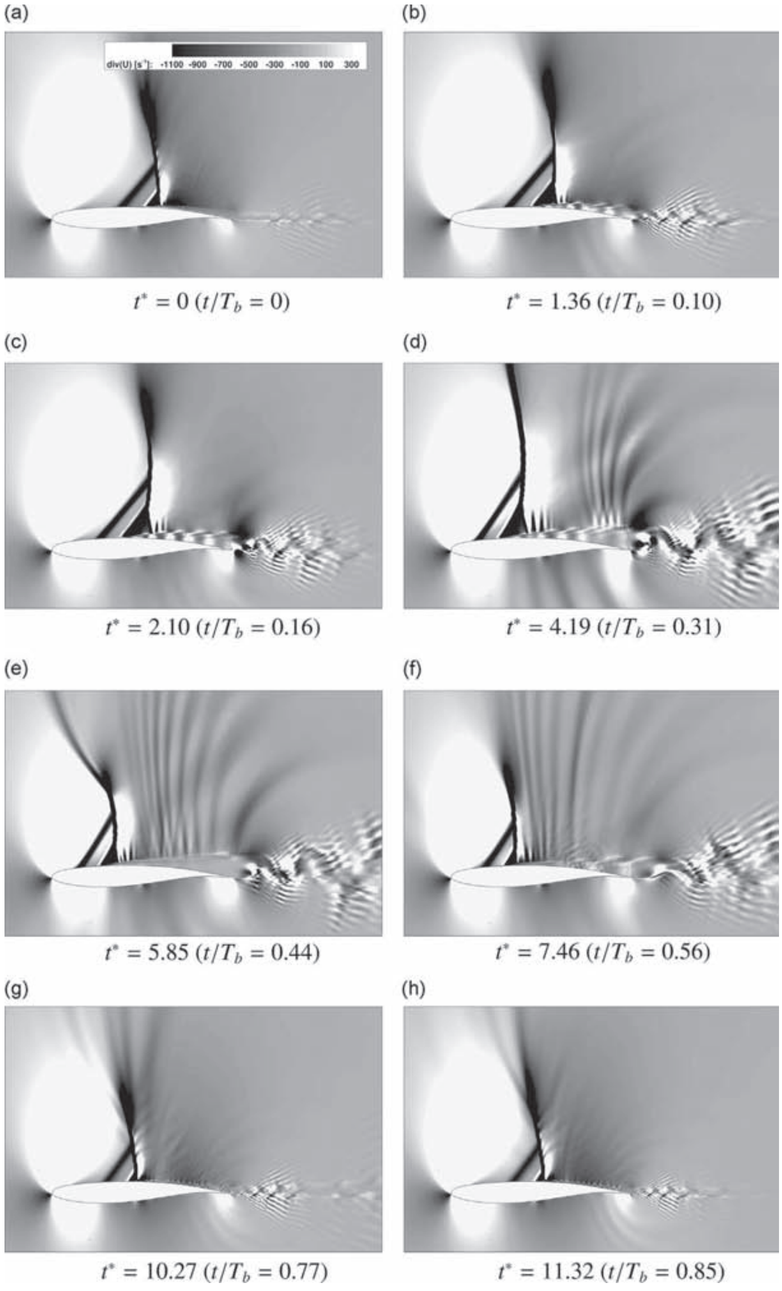

$t^* = 0$ ($t/T_b = 0$)

$t^* = 1.36$ ($t/T_b = 0.10$)

$t^* = 2.10$ ($t/T_b = 0.16$)

$t^* = 4.19$ ($t/T_b = 0.31$)

$t^* = 5.85$ ($t/T_b = 0.44$)

$t^* = 7.46$ ($t/T_b = 0.56$)

$t^* = 10.27$ ($t/T_b = 0.77$)

$t^* = 11.32$ ($t/T_b = 0.85$)

Fig. 8. Instantaneous fields of velocity divergence (T_b is the buffet period).

the buffet motion in the OAT15A test case thickens the boundary layer and hence favorizes the von Kármán mode appearance. The buffet also produces intermittently a thinning of the boundary layer when the shock moves downstream and leads to the intermittent disappearance of the von Kármán mode. Therefore, it can be mentioned that the buffet does not cause directly the von Kármán mode but it helps its appearance and disappearance.

3.2. Dynamic interaction between large-scale low-frequency shock motion and smaller-scale higher-frequency vortices

The buffeting process is analysed in more detail in terms of signal processing. Pressure signals containing 21 buffet periods and approximately 271 000 samples, have been recorded at the airfoil surface, as in the experiment of Jacquin et al.

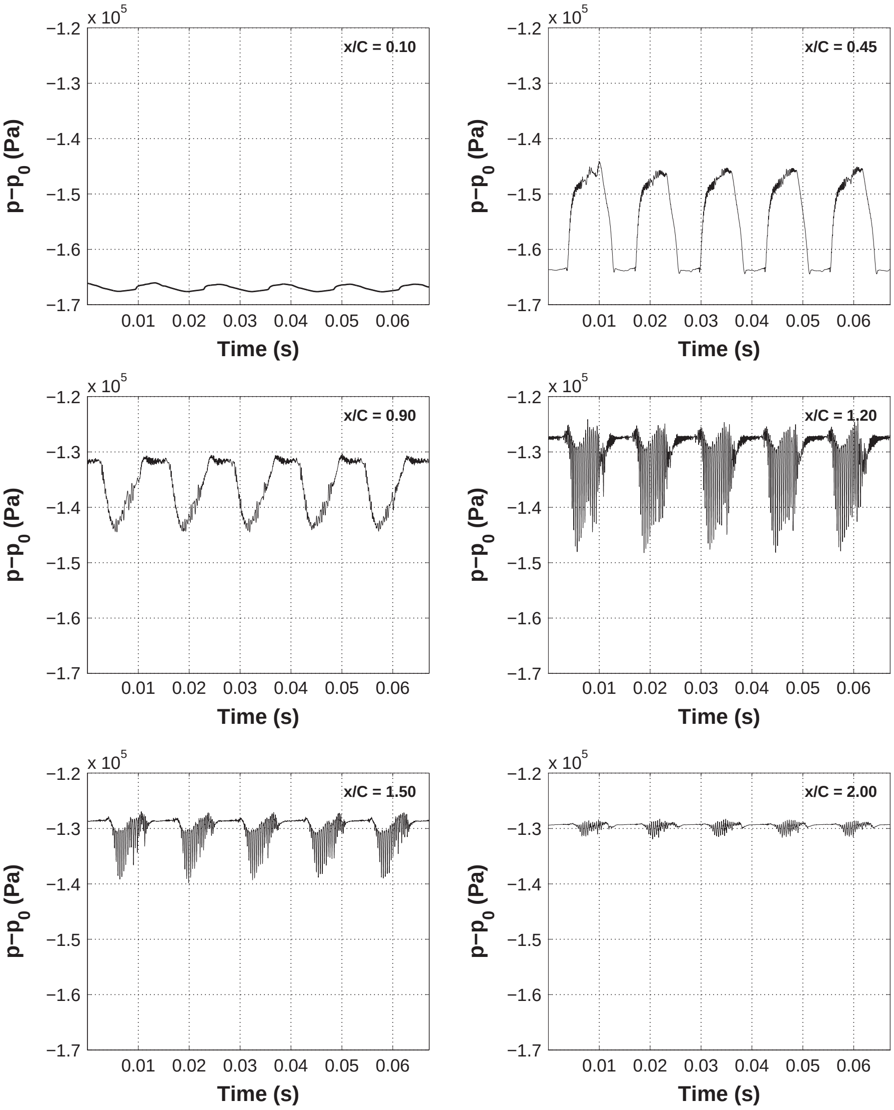

Fig. 9. Pressure fluctuations at the upper surface of the airfoil and in the wake.

(2009). In the present study, probe positions have been added in the wake, up to one chord downstream of the trailing edge. The sampling rate is 10^{-6} s. The signals are plotted in Fig. 9 for 5 buffet periods, at 6 positions from $x/C = 0.10$ to $x/C = 2.00$, and along $y/C = 0.03$ in the wake.

Upstream of the SWBLI, large-scale periodic oscillations corresponding to the buffet instability are obtained. At farther downstream positions, this mode is amplified, and secondary oscillations at a higher frequency appear. These oscillations, mainly generated near the trailing edge of the airfoil, reach a maximum amplitude in the near-wake at $x/C = 1.20$, and can be also observed in the div(**U**) field (Fig. 8). A significant part of these oscillations corresponds to a von Kármán mode, as will be discussed in the next section (Figs. 11 and 12). This mode presents a frequency modulation, due to the interaction with the trailing-edge and ambient turbulence, as highlighted by spectral analysis.

3.2.1. *Spectral analysis*

The mentioned instabilities and their interactions are studied by a spectral analysis and a time–frequency study using wavelets and auto-regressive (AR) modelling, allowing for frequency variation versus time. The spectra of the pressure fluctuations signals at four positions from $x/C = 0.10$ to $x/C = 1.20$ are presented in Fig. 10. The power spectral density is calculated by the Welch's overlapped segment averaging estimator in order to reduce the variance of the periodogram

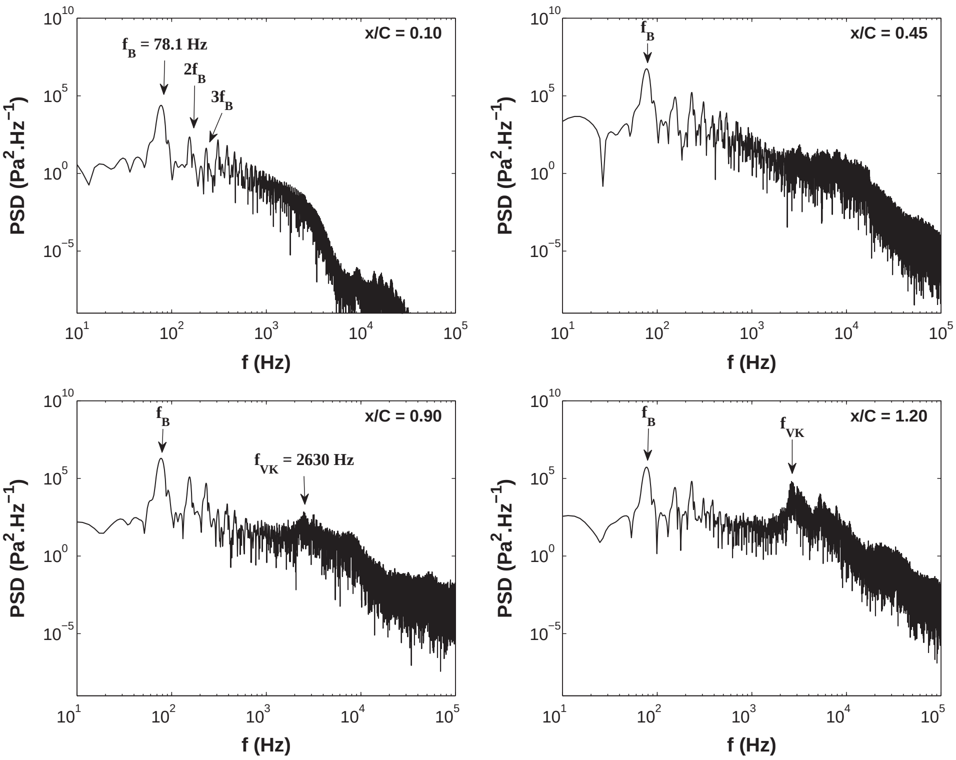

Fig. 10. PSD of the wall-pressure fluctuations at locations $x/C = 0.10$, 0.45 and 0.90 on the airfoil surface and at point $x/C = 1.20$, $y/C = 0.03$ in the wake.

(Welch, 1967). An overlapping of 80 % is applied on segments of size 60 % of the total length of the signal. Each segment is filtered by a Hanning window, and zero padding is used such that the number of samples on which the PSD is calculated equals to 2^{19}.

All the spectra show the appearance of the buffet frequency, at $f_B = 78.1$ Hz (St $= fC/U_\infty = 0.075$), and its harmonics. In the experiment, this frequency was equal to 69 Hz (St $=0.066$). At the most upstream position ($x/C = 0.10$), the spectrum does not display any predominant frequency beyond 4000 Hz. Farther downstream ($x/C = 0.45$), the spectrum displays a more significant spectral amplitude and more rich turbulence content in the area beyond 4000 Hz. This occurs because of the influence of the separated region downstream of the SWBLI. At this position, the spectrum can be compared with the experimental results (Jacquin et al., 2009, Fig. 10). In the range of frequencies available on the spectrum from the experiment, both spectra are similar in terms of the buffet frequency and its harmonics, although the shape of the peaks are different, which is due to the number of buffet periods (order of 20) in the numerical study which is less than in the experimental study. At this farther downstream position, the main mode is amplified and secondary oscillations at a higher frequency appear. This phenomenon becomes more pronounced for positions near the trailing edge ($x/C = 0.90$) and in the near-wake ($x/C = 1.20$; see Fig. 8). At $x/C = 0.90$, the power spectral density distribution can be compared with other URANS simulations (Brunet et al., 2003, Figs. 11 and 18). The comparison of the spectral peak amplitude and their frequency are close between the present study and the above reference. A frequency peak appears at around 2600 Hz (St $=2.5$). This peak becomes more pronounced at $x/C = 1.20$.

We can show that this frequency corresponds to the von Kármán vortex shedding. Fig. 11 presents snapshots of the vorticity field taken at four equidistant time intervals in respect of the period 1/2600 s. These fields clearly show the alternating von Kármán vortex shedding and the periodicity of the vortex pattern from $t = 0.00962$ s to $t = 0.01$ s. In order to quantify the frequency of this vortex shedding, a tracking of the vorticity values versus time has been carried out at the locations 1 and 2 (see Fig. 11) during one buffet period. The vorticity signals and their spectra are presented in Fig. 12, where a bump is identified at 2600 Hz. This fact insures the identification of a von Kármán mode at the present frequency.

The peak localized at 2600 Hz in the spectra of the pressure signals is characterised by a spreading of frequencies (spectral 'bump'). This is mainly due to a strong interaction of the von Kármán mode with the trailing-edge unsteadiness (appearance of grey fringes related to Kutta waves in the div(**U**) plots, Fig. 8) and to the turbulent motion. This spectral region is studied in more details in the next section, by means of time–frequency analysis.

Moreover, the Kelvin–Helmholtz vortices shown in Fig. 8(c) in the detached shear layer downstream of the shock foot can be identified by tracking them during the time-interval of 0.24 μs. Their convection velocity has been assessed of order

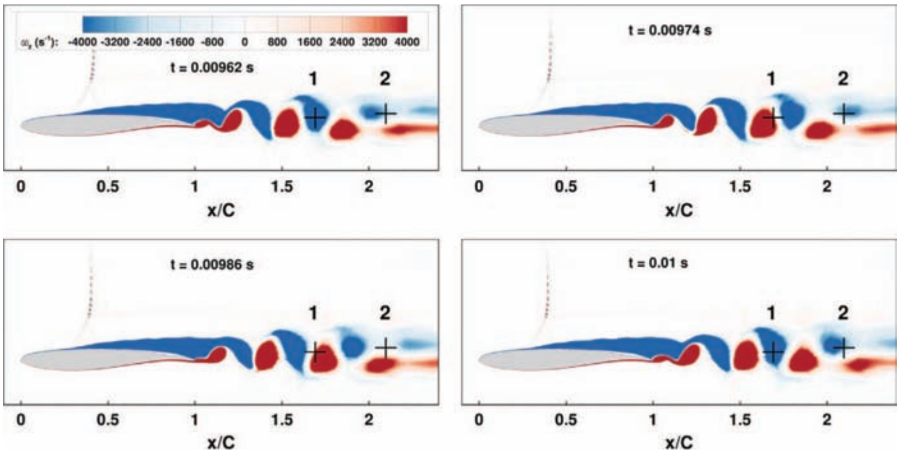

Fig. 11. Four instantaneous vorticity fields covering one period of trailing-edge vortex shedding and showing probing locations of the vorticity values used in next figure.

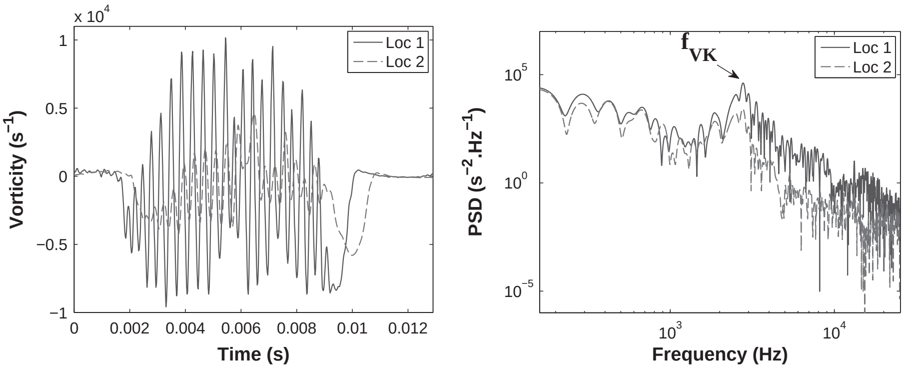

Fig. 12. Vorticity signals in the wake (left) and their power spectral density (right).

$202\ \mathrm{m\cdot s^{-1}}$, as well as their wavelength, λ, of order 1.9×10^{-2} m. From these parameters, their shedding frequency has been assessed of order 10^4 Hz (St $=9.5$) from the relation $U_{\mathrm{conv}}=\lambda\cdot f$. This is higher than the von Kármán frequency. By considering the energy spectrum at $x/C=1.20$ and $y/C=0.03$ with suitable window size and zero padding in order to better visualize the region of frequencies around 10^4 Hz (Fig. 13), a predominant frequency peak at 10^4 Hz can be identified, which corresponds to the Kelvin–Helmholtz shedding frequency.

As previously mentioned, the buffet frequency is found 78.1 Hz in the current study, while the vortex shedding frequency is about 2600 Hz when this phenomenon is well established. The ratio of these two frequencies is 33.29. The closest buffet harmonic regarding the von Kármán peak is $78.1\times33=2577$ Hz. This frequency slightly varies inside each buffet cycle, and from a cycle to another, which produces the bump observed in the spectra around 2600 Hz. This increases the uncertainty of this frequency value. As shown in the spectrum of Fig. 14, the higher buffet harmonics "merge" with the von Kármán bump onset and a synchronization may occur with von Kármán subharmonics. This interaction is difficult to analyse because the amplitudes of these higher harmonics and subharmonics are somehow "hidden" in the continuous part of the spectrum between the two events, the buffet and the von Kármán frequency peaks.

It is recalled that the present study aims at analysing the trailing-edge instabilities in association with the buffet mode. The fluctuations related to the von Kármán instability appear less explicitly in the spectra in Jacquin et al. (2009), Deck (2005), as well as in Thiery and Coustols (2005) and Brunet et al. (2003), because the main objective of these studies focused on the buffet phenomenon. Indeed, these studies measure the pressure fluctuations on the airfoil wall, with the most downstream position of the measurements located at $x/C=0.90$, where the level of the von Kármán fluctuations is still very small and the experimental spectrum cut-off is lower than the expected von Kármán frequency, captured by the present numerical study, which displays existence of a spectral bump region around a predominant frequency of order 2600 Hz (Fig. 10, see spectrum at $x/C=0.90$). As has been previously shown, this frequency corresponds to the alternating vortex shedding in respect of the von Kármán mode. In this figure, concerning a more downstream position in the wake, $x/C=1.20$, this spectral bump clearly appears.

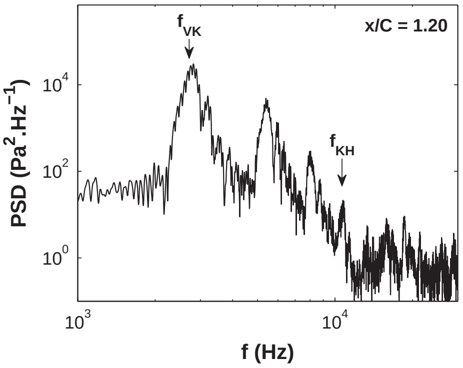

Fig. 13. PSD of pressure fluctuations at $x/C = 1.20$, $y/C = 0.03$. Detailed view of the range $10^3 - 3 \times 10^4$ Hz.

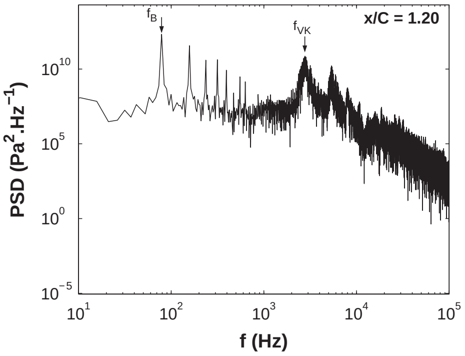

Fig. 14. PSD of pressure fluctuations at $x/C = 1.20$, $y/C = 0.03$.

In Fig. 20 of the experimental study by Jacquin et al. (2009), which displays four instants of the phase-averaged longitudinal velocity field, there is no proof of vortex shedding as identified in our study. This can be explained because a section of the wake is not visible due to the experimental setup, and also because the phase averaging, based on the buffet cycle, may have erased the marks of the vortex shedding, which has a frequency more than 30 times higher than the buffet one, and a phase which is not synchronized with the buffet. Figs. 15 and 16 of the present study show the instantaneous and the phase-averaged longitudinal velocity fields respectively, at four phases of the buffet cycle, similarly to the experimental results of Jacquin et al. (2009). These figures show the periodic motion of the accelerated region due to the buffet, as well as the boundary-layer detachment. In fact, the von Kármán vortices are visible in the instantaneous fields using a similar color scale as in the experimental results, but they are attenuated after phase-averaging over two buffet periods only (Fig. 16). Regarding Fig. 12 of Deck (2005) that displays the divergence of the velocity field, the color scale can be adapted in order to highlight the vortex shedding structures, as the divergence of velocity is much smaller within the vortices than in the area of the shock wave and Kutta waves. However, an alternating pattern can be distinguished in this figure too. If the above mentioned studies had been interested in the near-wake region and under the condition that the experimental and numerical grids be sufficiently fine in the wake, they would have been able to capture the von Kármán instability too. However, this was not an objective of the mentioned studies. An evidence of the existence of the von Kármán mode in these experiments can be seen in the appearance of secondary fluctuations observed in the experimental measurements of the time evolution of the pressure at $x/C = 0.45$ (Jacquin et al., 2009, Fig. 8). If the spectrum of Fig. 10 in Jacquin et al. (2009) would display a frequency range beyond 10^3 Hz, the von Kármán mode would also appear. This mode is characterised by a spectral bump, showing that it is subjected to the influence of other, more chaotic events in the time-space evolution. Moreover, small vortices in the trailing-edge region have been measured by Brunet et al. (2003), in URANS simulations of the OAT15A test case, but at a higher angle of attack ($\alpha = 5°$). Their signature seems to appear as a spectral bump in Fig. 11 of this reference. These vortices can also be observed in the Schlieren visualization in Fig. 7. Von Kármán vortices were also reported in several experiments on subsonic compressible flows around airfoils (Alshabu and Olivier, 2008; Fung, 2002) as well as in the direct simulation of transonic buffet at lower Reynolds numbers by Bouhadji and Braza (2003b) and Bourdet et al. (2003).

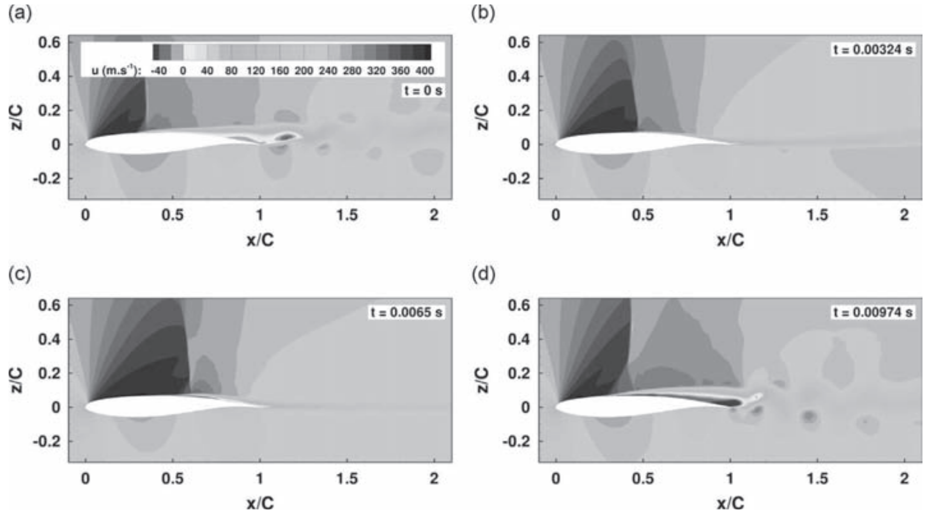

Fig. 15. Instantaneous longitudinal velocity at 4 phases of a buffet cycle: (a) shock upstream; (b) shock moving downstream; (c) most upstream position of the shock; (d) shock travelling upstream.

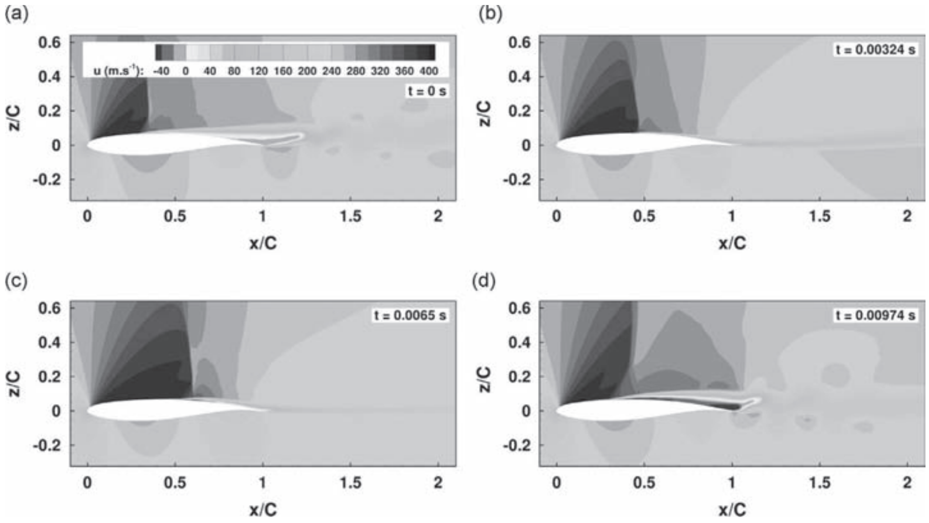

Fig. 16. Phase-averaged longitudinal velocity at 4 phases of a buffet cycle: (a) shock upstream; (b) shock moving downstream; (c) most upstream position of the shock; (d) shock travelling upstream.

3.2.2. Time–frequency analysis

The pressure signal in the wake at $x/C = 1.20$, a position where the amplitude of the secondary instabilities is maximum, corresponding to the bursts formed in the pressure evolution and to the spectral "bumps" (Figs. 9 and 10 respectively), are governed by the von Kármán mode and instabilities mainly coming from the trailing edge and the shear layers. This signal is filtered by a high-pass filter with a cutoff frequency of 1577 Hz, by means of Fast Fourier Transform (*FFT*). The filtered pressure signal, shown in Figs. 17 and 18, designated as P_f (f standing for filtered), is reconstructed by the inverse *FFT*. The physical phenomena whose frequency is higher than 1577 Hz are conserved. The remaining signal shows now more clearly the buffet effect on the higher-frequency phenomena within each buffet cycle (burst). Each burst contains an order of 15 counter-rotating vortex-shedding pairs, as well as time intervals where the vortex shedding is considerably attenuated. The instability evolution within the burst is studied by means of time–frequency analysis, carried out by a continuous wavelet transform, and segmentation of the filtered signal. The complex Morlet wavelet (Grossmann and Morlet, 1984) is used to

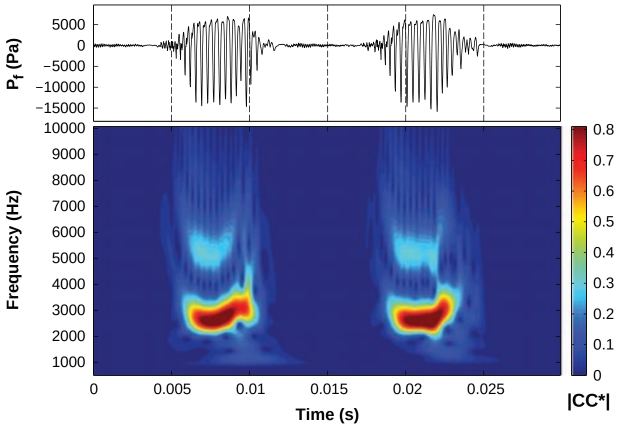

Fig. 17. Normalized absolute value of complex continuous wavelet transform coefficients.

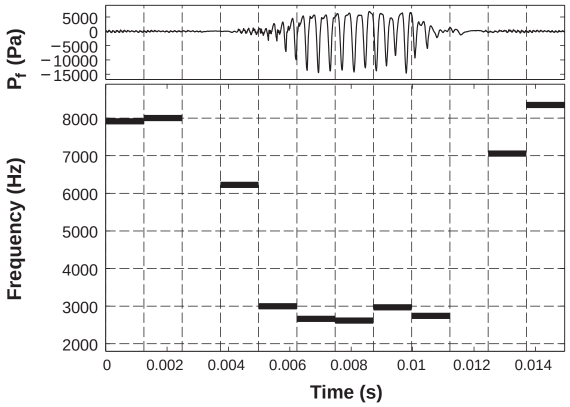

Fig. 18. Time–frequency analysis of the filtered pressure signal at $x/C=1.20$, $y/C=0.03$, using autoregressive modelling.

analyse two buffet periods:

$$\psi(t)=\frac{1}{\sqrt{4\pi}}e^{2i\pi f_0 t}e^{-t^2/2}, \tag{4}$$

where f_0 is the central frequency of the wavelet.

The wavelet transform coefficients are defined as

$$C(a,b)=\frac{1}{\sqrt{a}}\int_{-\infty}^{\infty}x(t)\,\psi^*\left(\frac{t-b}{a}\right)\,dt \tag{5}$$

where a and b are the scaling (in frequency) and the location (in time) parameters of the wavelet respectively, $x(t)$ the signal and ψ^* is the complex conjugate of the wavelet. The absolute value of these wavelet transform coefficients, $|C\ C^*|$, is plotted in Fig. 17. The scalogram allows analysing in more details the evolution of the vortex shedding frequency versus time inside each buffet cycle. When the shock starts moving upstream (Fig. 8(b)), the vortices are shed at a frequency of 4000 Hz with low amplitudes (see beginning of the burst Fig. 17). Afterwards, this frequency diminishes to reach 2600 Hz, which is the von Kármán frequency observed in the spectra. The vortex shedding is then well established within the burst and is maintained until the shock reaches its most upstream position (see evolution of the shock motion, Fig. 8(c)–(f)). Next, the generated vortices become smaller (Fig. 8(g)) and the shedding frequency increases to reach again the initial value of 4000 Hz, before this phenomenon be significantly attenuated and vanish while the shock moves downstream and the boundary layer becomes attached (Fig. 8(h)–(a)). This frequency modulation, associated with the location and size of the alternating vortices versus time, is linked to the spectral bump appearance around the von Kármán mode (Fig. 10). The repetitiveness of this modulation is clearly observed in the scalogram. The first harmonic is also present with the same modulation. Fig. 18 presents the frequency variation of the pressure coefficient versus time during one buffet period, by using the Yule–Walker autoregressive (AR) model. This kind of model conceptually ensures a high accuracy in the estimation of the frequency values versus time (Braza et al., 2001). The Yule–Walker equations, obtained by fitting the autoregressive

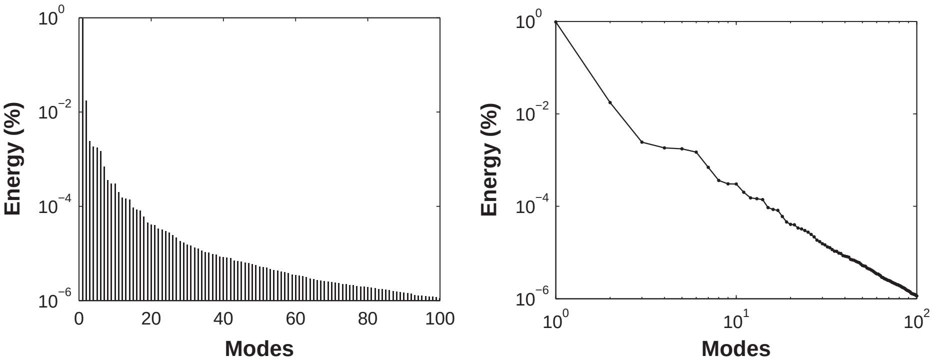

Fig. 19. Energy distribution of the POD modes (semi-log and log–log diagrams).

linear prediction filter model to the signal, by minimizing the forward prediction error in the least squares sense, are solved by the Levinson–Durbin recursion (Durbin, 1960). This method is applied with an AR order of 210 on a signal including a one burst cycle. 14 952 samples are used and the signal is segmented in windows of 1153 points. The fundamental frequency of each segment is obtained by calculating the PSD of the modelled signal, using zero-padding giving 2^{21} samples. The result of this method shows the same frequency modulation during the vortex shedding occurrence, as in case of the continuous wavelet transform.

In the next section, a POD analysis is presented which includes additional aspects of the interaction among the buffet, the von Kármán and the smaller-scale higher-frequency vortices, especially those of the shear layers.

3.2.3. Proper orthogonal decomposition

Based on the time-space solution from the previously mentioned simulations, a proper orthogonal decomposition (POD) has been carried out on the ensemble-averaged flow-fields, based on the separable POD method in respect of space and time (Sirovich, 1990; Aubry et al., 1991), as presented in the following relations. The POD modes are evaluated from a series of successive snapshots, which include in the present case 10 buffet periods. 646 snapshots, recorded by using a sampling rate of 10^{-5} s, are used per buffet period. As the first POD mode corresponds to the time-averaged solution contained in the data, the POD modes from order 2 correspond to the fluctuating part of the velocity fields:

$$\mathbf{U}(\mathbf{x},t)=\overline{\mathbf{U}}(\mathbf{x})+\mathbf{u}(\mathbf{x},t)=\overline{\mathbf{U}}(\mathbf{x})+\sum_{n=2}^{N_{\mathrm{POD}}} a_n(t)\boldsymbol{\phi}_n(\mathbf{x}), \tag{6}$$

where $\overline{\mathbf{U}}$ and $\mathbf{u}$ denote the mean and fluctuating parts of the velocity, respectively. The fluctuation mainly includes the effects of the buffet, von Kármán and shear-layer instabilities. This fluctuation includes the following contributions:

$$\mathbf{u}(\mathbf{x},t)=\tilde{\mathbf{u}}(\mathbf{x},t)+\check{\mathbf{u}}(\mathbf{x},t)+\hat{u}(\mathbf{x},t), \tag{7}$$

where $\tilde{\mathbf{u}}$ is the phase-averaging, $\check{\mathbf{u}}$ is the downscale contribution of the fluctuation, and $\hat{u}$ is the upscale one. Following a simple algebraic development for the decomposed phase-averaged Navier–Stokes equations, it can be shown that the new turbulent stresses contain a downscale part: $\langle\check{u}_i\check{u}_j\rangle$, and a cross term: $\hat{R_{ij}}=\langle\check{u}_j\hat{u}_i\rangle+\langle\hat{u}_j\check{u}_i\rangle+\langle\hat{u}_j\hat{u}_i\rangle$. As will be discussed in the next section, $\hat{R_{ij}}$ will be modelled by a stochastic forcing. At this stage, a major contribution is due to the downscale term.

The normalized shape-functions $\boldsymbol{\phi}_n$ are spatially orthogonal, while the temporal coefficients a_n are uncorrelated in time:

$$\left\langle\boldsymbol{\phi}_i\cdot\boldsymbol{\phi}_j\right\rangle=\delta_{ij}\quad\text{and}\quad\overline{a_i a_j}=\delta_{ij}\lambda_i. \tag{8}$$

The brackets and overbar indicate spatial integration and temporal averaging, respectively. λ_i is the eigenvalue of mode *i*. δ_{ij} is the Kronecker delta. The POD modes $\boldsymbol{\phi}_n$ are obtained as the eigen-modes of the two-point correlation matrix:

$$\overline{\overline{\mathbf{C}}}\boldsymbol{\phi}_n=\lambda_n\boldsymbol{\phi}_n\quad\text{with}\quad C_{ij}=\overline{\mathbf{u}(\mathbf{x}_i,t)\cdot\mathbf{u}(\mathbf{x}_j,t)}. \tag{9}$$

The eigenvalue λ_n represents the contribution of the corresponding POD mode to the total fluctuating energy:

$$\left\langle\overline{\mathbf{u}(\mathbf{x}_i,t)\cdot\mathbf{u}(\mathbf{x}_j,t)}\right\rangle=\sum_{n=1}^{N_{\mathrm{POD}}}\lambda_n. \tag{10}$$

Fig. 19 shows the energy of the POD modes as a function of the mode order. There is an energy decrease towards the higher modes. The decrease rate is slower than in DNS cases (El Akoury et al., 2008), because of the random turbulence effect, modelled by the solved transport equations. In the log–log energy diagram, a “plateau” followed by a slope change is observed. This feature represents the contribution of the organised motion and of the random turbulence effect, which

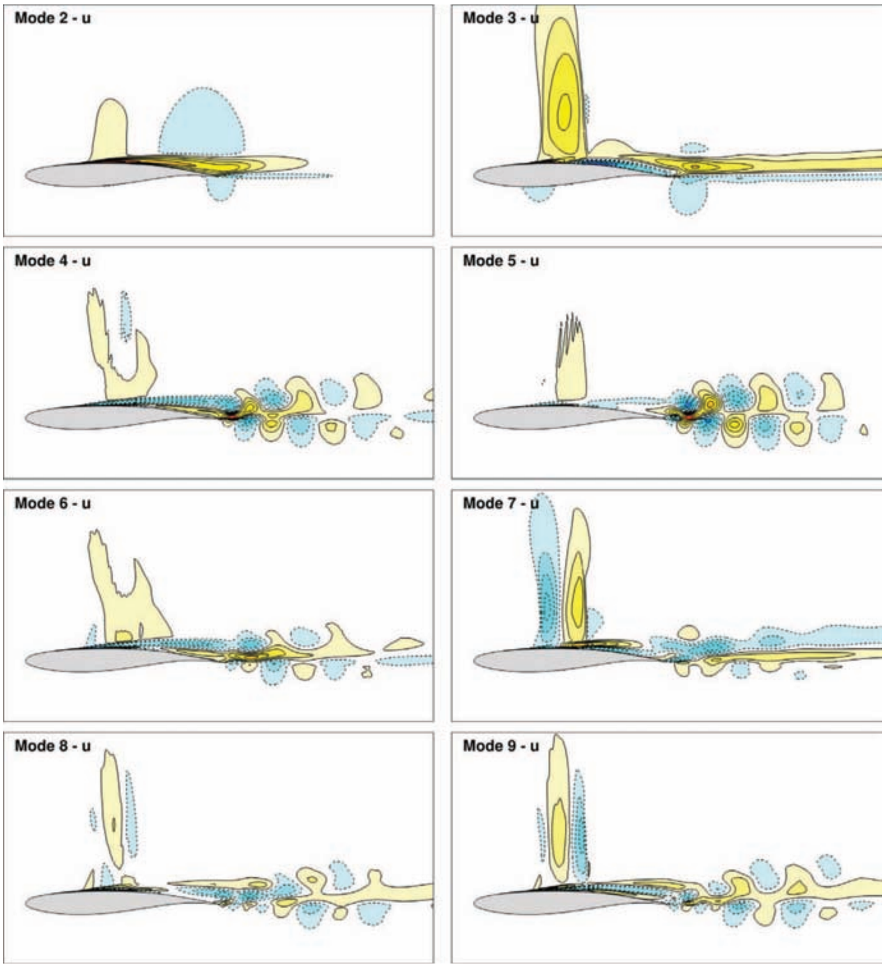

Fig. 20. First POD modes associated with the streamwise velocity.

becomes more pronounced, as the mode order increases. A similar behaviour was reported in experimental studies by Perrin et al. (2006).

The POD analysis allows extracting the most energetic modes (Fig. 20) which can reconstruct the main features of the interaction between the buffet and the downstream region as shown in the following. The modes 2 and 3 of the streamwise velocity U illustrate the buffet phenomenon and the boundary-layer intermittent detachment (Fig. 20).

Modes 4 and 5 clearly illustrate the von Kármán motion. A complex interaction among the buffet region (shock), the shear layer past the SWBLI and the von Kármán mode past the trailing edge is shown by means of the higher order modes. This interaction leads to creation of a more pronounced chaotic process (modes 6 and 7), because the frequencies of the mentioned instabilities are incommensurate. Furthermore, the von Kármán mode iso-contour levels affect also the shock-motion region (modes 4–9).

The temporal POD coefficients are shown in Fig. 21. They are in accordance with the spatial mode behaviour. As the order of the modes increases, a filling-up of the temporal coefficient signal by higher frequencies is noticed, showing the increasing complexity of the dynamic system, due to turbulence.

The energy spectra of the temporal POD coefficients for modes 2–9 are presented in Fig. 22. The first spectrum indicates the buffet frequency as a predominant one and confirms the fact that mode 2 is associated with this instability. The POD modes higher than 3 start progressively to be affected by the von Kármán instability, as shown also in the spatial distribution of these modes, Fig. 20. The amplitude of the von Kármán instability (Fig. 22) increases for modes 4 and 5, to reach a practically invariant level in the higher mode spectra. Simultaneously with this variation, the buffet instability amplitude decreases on the spectra and its harmonics slightly increase but the global level of the buffet instability amplitude remains lower than in case of the third POD mode. Therefore, in the mode ranges 4 and 5, the spectral amplitudes of the von Kármán and of the buffet become comparable.

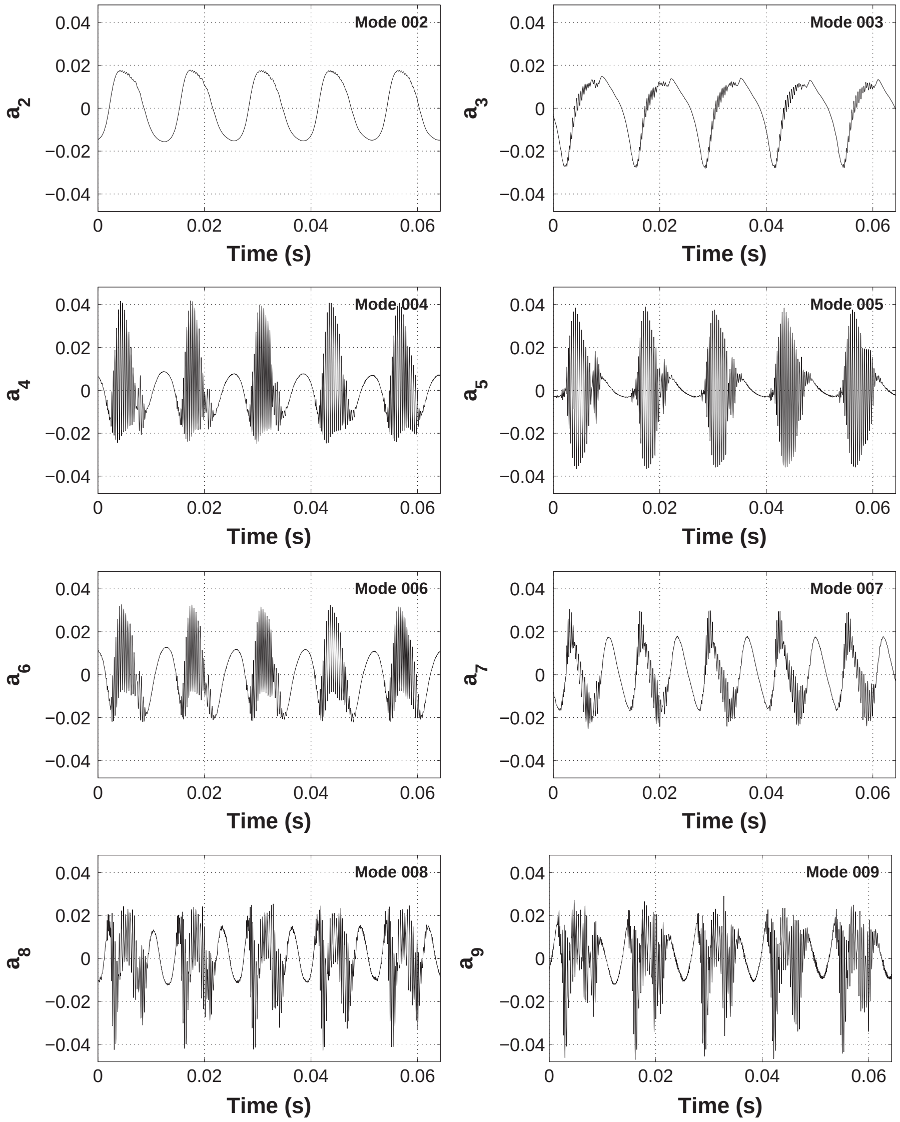

Fig. 21. Temporal coefficients a_n of the first POD modes.

From the dynamic system theory point of view, a non-linear interaction between two incommensurate instability modes that are rather close in terms of frequency produces linear combinations of these two modes in the energy spectrum (Newhouse et al., 1978; Guzmán and Amon, 1994). In the POD spectrum of mode 2 (Fig. 22), the interaction between the higher buffet harmonics and the von Kármán subharmonics is more visible, because these two sets are neighbours. We can detect for example a predominant frequency bump, f_{i1}, which can be expressed as $f_{VK}/2-5f_B$. Moreover, a second interaction can be extracted, $f_{i2}=f_{VK}/2-8f_B$. These interactions, as in the aforementioned papers, do not considerably change the frequency values of the instability modes (buffet and von Kármán). They rather change the amplitudes of these modes, which become comparable between the buffet mode and the von Kármán, as shown in Fig. 22 (spectra of POD modes 4 and 5, as well as spectra of POD modes 6 and 7). This illustrates a way the buffet mode is affected by the shedding mode and vice-versa.

The spectra of modes 12 and 13 are presented in Fig. 23. They show a broadening of the von Kármán area associated with the interaction between smaller-scale higher-frequency vortices (as for example the K–H around 10^4 Hz) and more chaotic turbulence effects. This fact persists for all the higher order modes. The corresponding spectra are plotted in Fig. 27 and they confirm this observation.

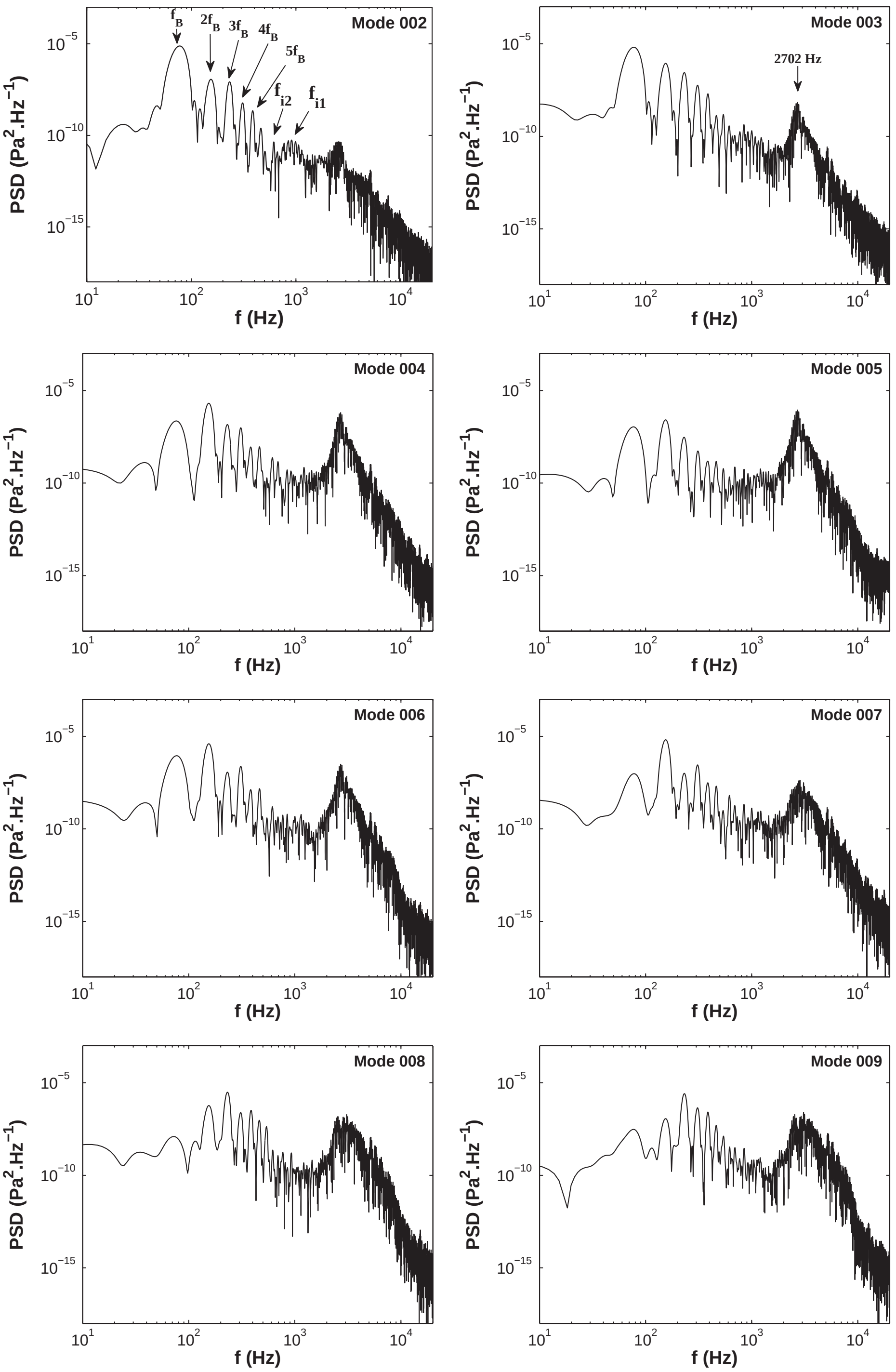

Fig. 22. PSD of POD mode temporal coefficients.

Based on the present discussion, the POD analysis illustrates in a complementary way the interaction between the buffet and the von Kármán modes as well as with the higher frequency structures, by means of the mode shape and the temporal coefficients amplitude modulations, as well as by the appearance of new frequency peaks in the spectra combining these instabilities.

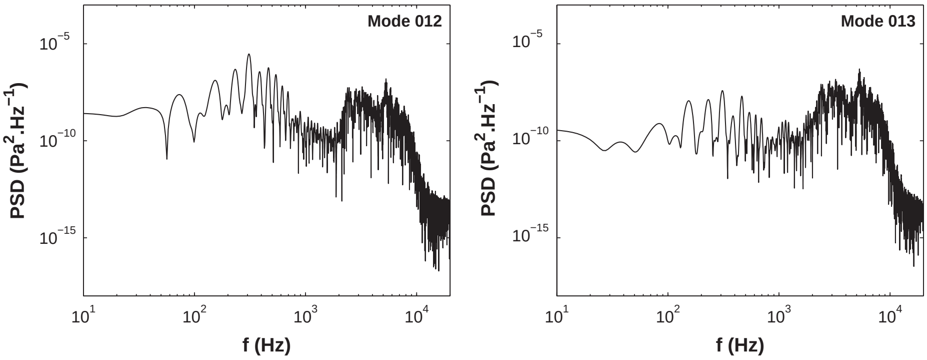

Fig. 23. PSD of temporal coefficient of POD modes 12 and 13.

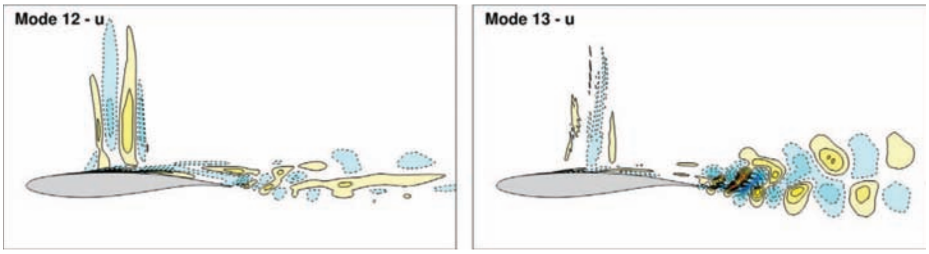

Fig. 24. POD modes 12 and 13 associated with the streamwise velocity.

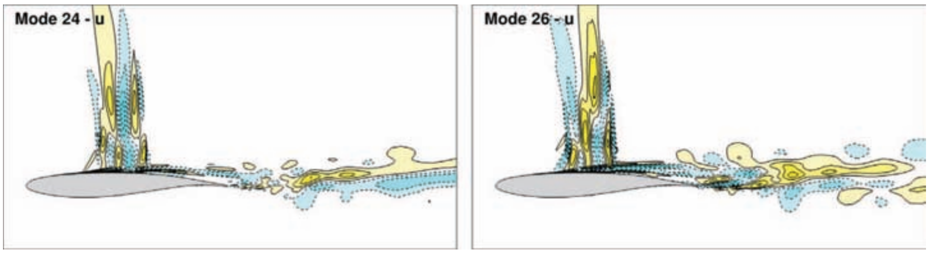

Fig. 25. Intermediate-range POD modes associated with the streamwise velocity.

Furthermore, the POD analysis illustrates the signature of the Kelvin–Helmholtz vortices (Figs. 24–26). In the 12th and 13th POD mode fields, the development of the lower shear-layer structure past the trailing edge can be observed. In the 24th and 26th mode fields, the impact of the upper shear-layer vortices can be seen. The higher POD modes (Fig. 26) influence all the high shearing rate regions, including also the shock area. Therefore, these figures show the filling of the shear layers by smaller-scale structures and illustrate their interactions with the shock-motion area. Indeed, the iso-contour levels of these smaller structures fill up the shock-motion region (Figs. 25 and 26).

4. Stochastic forcing by means of POD

The shear-layer interfaces between the turbulent and non-turbulent regions are now considered in association with those POD modes which particularly affect these areas as previously discussed. In order to maintain these interfaces thin and to limit the turbulent diffusion effect due to the direct cascade modelling assumptions, a small amount of kinetic energy is introduced as a “forcing” in the transport equations of the k and ε variables, acting as a “blocking effect” of the vorticity in the shear layer as in the schematic representation of Fig. 1, according to Westerweel et al. (2009). This small kinetic energy can be constructed from the “residual” high-order POD modes previously presented, by reconstructing fluctuating velocity components derived from the use of the last POD modes of very low energy. Therefore, an *inhomogeneous* stochastic forcing can be built and used as a source term in the transport equations regarding k (Eq. (11)) and ε (Eq. (12)). This term contains a small fluctuating velocity scale which acts within the shear layer and in the region below, without affecting the regions beyond the turbulent/non-turbulent interface. By dimensional analysis, this kind of source terms can take the form of Eq. (13), where the ambient value of the turbulent kinetic energy is $k_{amb} = k_{fs} U_\infty^2$, and $k_{fs} = 3/2\ \mathrm{Tu}^2$, with Tu the upstream

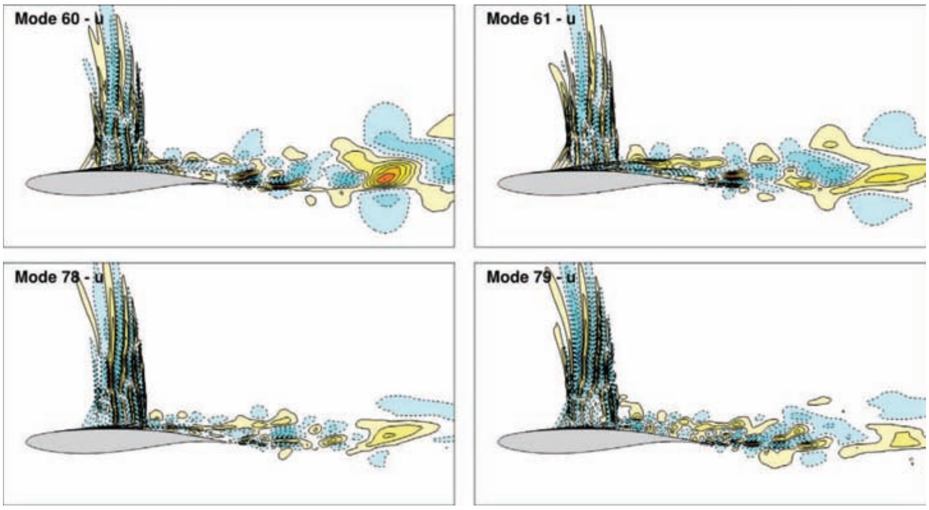

Fig. 26. Higher-range POD modes associated with the streamwise velocity.

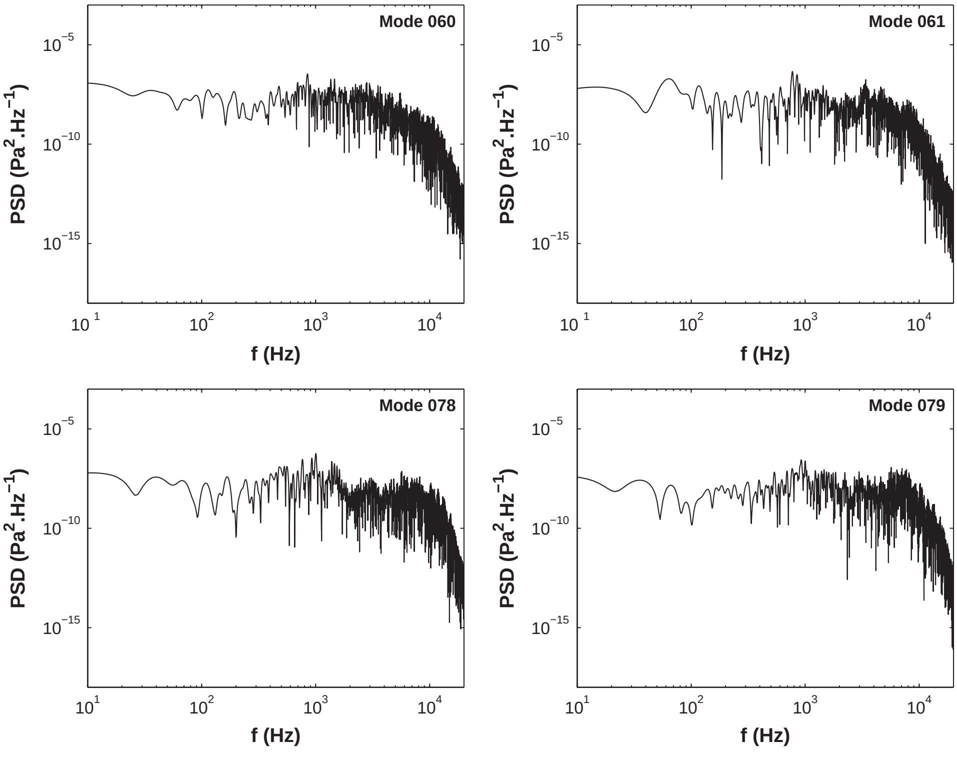

Fig. 27. PSD of temporal coefficient of higher POD modes.

turbulence intensity and $\tilde{r}$ is taken from a random number generator varying in the interval [0, 1]. This form is similar, from a dimensional point of view only, to the homogeneous ambient terms introduced by Spalart and Rumsey (2007) in order to sustains the turbulent kinetic energy level specified in the upstream conditions, which usually decays towards the body due to the dissipation rate:

$$\frac{Dk}{Dt} = P - \varepsilon + \frac{\partial}{\partial x_i}\left[\left(\nu + \frac{\nu_t}{\sigma_k}\right)\frac{\partial k}{\partial x_i}\right] + S_{\mathrm{POD}} \tag{11}$$

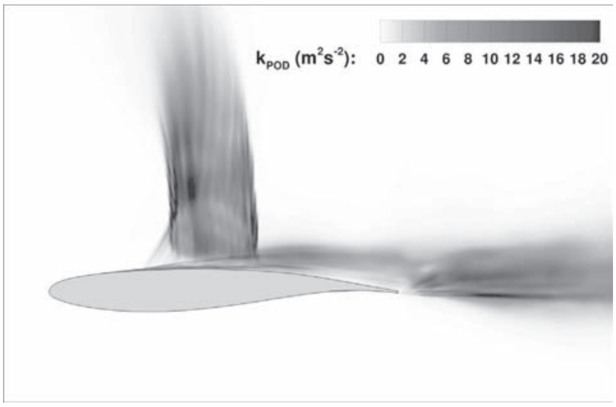

Fig. 28. Averaged turbulent kinetic enery field, k_{POD}, issued from fluctuating velocity reconstruction for higher-order modes 60–99.

$$\frac{\mathrm{D}\varepsilon}{\mathrm{D}t}=\frac{\varepsilon}{k}(C_{\varepsilon 1}P-C_{\varepsilon 2}\varepsilon)+\frac{\partial}{\partial x_i}\left[\left(\nu+\frac{\nu_t}{\sigma_\varepsilon}\right)\frac{\partial\varepsilon}{\partial x_i}\right]+\frac{C_{\varepsilon 2}S_{\mathrm{POD}}^2}{k_{\mathrm{amb}}} \tag{12}$$

with

$$S_{\mathrm{POD}}=\tilde{r}C_\mu(k_{\mathrm{amb}}^2+k_{\mathrm{POD}}^2)/\nu_{t\infty}, \tag{13}$$

and $\nu_t=C_\mu\ k^2/\varepsilon$ is the turbulent viscosity. $\nu_{t\infty}$ is the freestream turbulent viscosity.

In the present study, this source term is derived from the local-scale, higher-order POD modes. In Fig. 26, the higher-order POD shape modes, $\boldsymbol{\phi}_n(\mathbf{x})$, are maximum in the regions where the shearing rate is high (shear-layer and shock regions). In the present study, an order of the last 40 modes (from 60th to 99th) have this property, as shown in the previous section. This approach may be adapted for other cases. These POD modes are associated with the temporal coefficients by using the relation (6) in order to produce a reconstruction of the velocity components and to calculate a low-energy velocity scale, $\sqrt{u^2+v^2}$. This reconstruction used the whole snapshot sequence of 10 buffet periods as for the previous POD analysis. In this way, an averaged turbulent kinetic energy scale, k_{POD}, is calculated as: $k_{\mathrm{POD}}=0.5\times(\overline{u^2}+\overline{v^2})$. As a first approximation, a *time-averaged* kinetic energy is evaluated. These equations *are time-dependent* and yield to a solution with temporal variation of the shear-layer as in Fig. 8. These source terms lead to a forcing of the turbulent stresses by means of the turbulence behaviour law and the turbulent viscosity. The new stresses act as an energy transfer from the stochastic small-scale modes to the higher ones.

As mentioned above, this stochastic forcing is simultaneously *localised* in the shear layer, in the wake and in the shock wave areas, thanks to the properties of the higher-order POD modes presented in the previous section, without contaminating the neighboring regions, which remain irrotational, as shown in the spatial distribution of k_{POD}, Fig. 28. The time-dependent evolution of these regions is taken into account. As will be discussed, the solution is now improved in respect of the shear-layer thinning.

Fig. 29 shows the divergence of the velocity vector at eight representative instants within the buffet period, according to the simulation including the stochastic forcing detailed above. A qualitative comparison with Fig. 8 shows a reduced shock-motion amplitude, which is in good agreement with the experiment. Furthermore, the shear layer and separated regions, which remain time-dependent, are thinner than in the previous case without stochastic forcing. These facts are quantified in Figs. 30, 32 and 33.

Fig. 30 shows a comparison of the mean surface pressure distribution between $k-\varepsilon$-OES and its variants with the experimental results. "*amb*" stands for the homogeneous ambient terms described in Spalart and Rumsey (2007), and "*IOES*" (I standing for "improved") refers to the modelling by stochastic forcing involving the k_{POD} field as discussed at the beginning of this section. The $k-\varepsilon$-OES without ambient terms provides a larger shock amplitude than in the experiment. The $k-\varepsilon$-OES with the homogeneous ambient terms provides an improvement in the shock-amplitude motion compared to the basic $k-\varepsilon$-OES simulation. In the IOES case, the pressure coefficient shows an even improved shock-motion amplitude where the shock-motion amplitude is large, as well as a better estimation of the pressure distribution in the region from the most downstream position of the shock to the trailing edge. This can be explained by the fact that the ambient terms and the stochastic forcing "add" a slight level of eddy viscosity in the OES modelling which is designed to reduce the eddy viscosity and to allow the instability development. Therefore, the instability development becomes slightly moderate by compensating the OES eddy-viscosity reduction thanks to the stochastic forcing. Moreover, the stochastic forcing improves the C_p tendency to form a more horizontal "plateau", upstream of the shock-motion area, as measured in the experiments. These improvements ensure a better estimation of the lift coefficient.

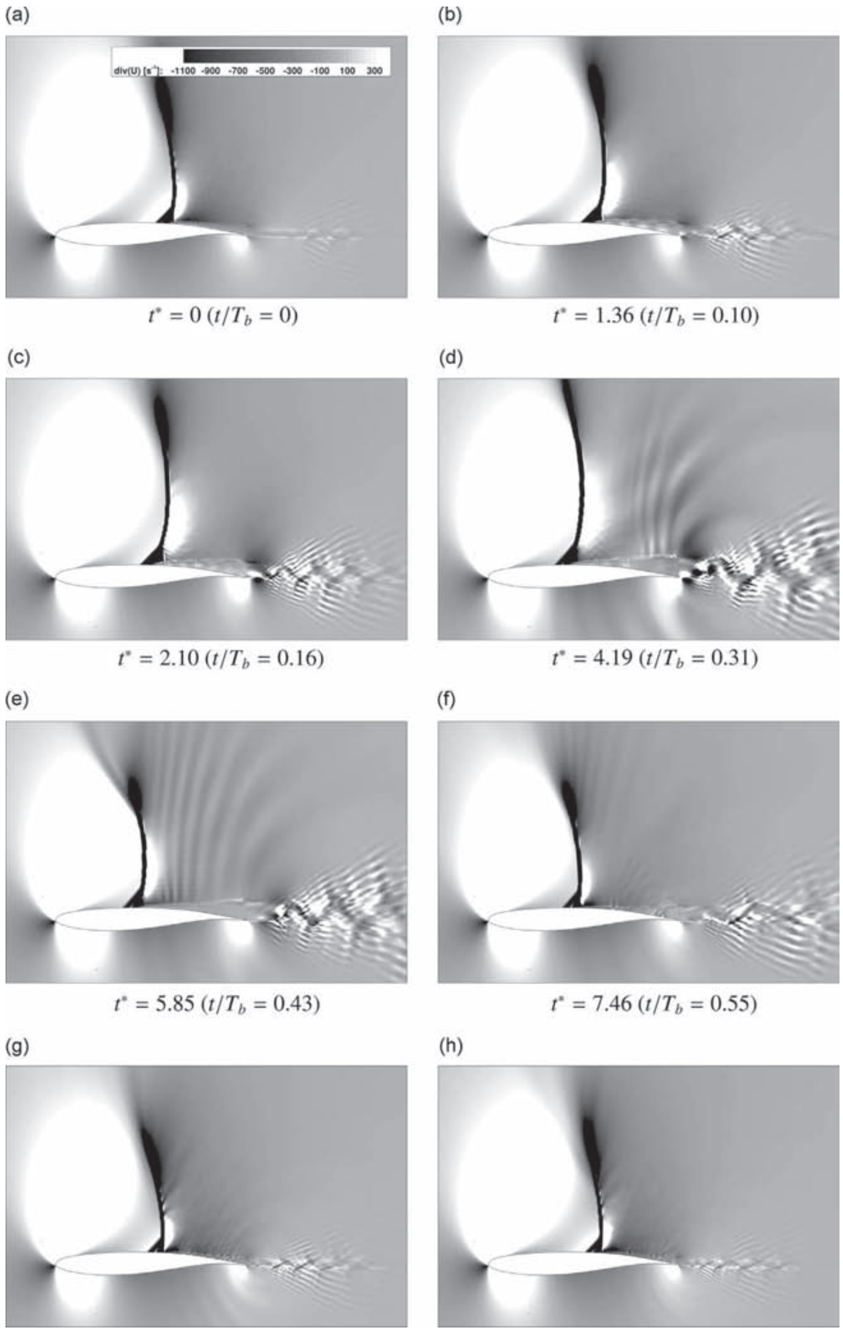

$t^* = 0$ $(t/T_b = 0)$

$t^* = 1.36$ $(t/T_b = 0.10)$

$t^* = 2.10$ $(t/T_b = 0.16)$

$t^* = 4.19$ $(t/T_b = 0.31)$

$t^* = 5.85$ $(t/T_b = 0.43)$

$t^* = 7.46$ $(t/T_b = 0.55)$

Fig. 29. Instantaneous fields of velocity divergence – application of the inhomogeneous stochastic forcing (T_b is the buffet period).

The TNT (Turbulent/Non-Turbulent) interface is localized where the vorticity gradient across the interface is maximum. The phase-averaged velocity and vorticity profiles derived from the $k-\varepsilon$-OES model, as well as from the IOES at the same phase, are compared in Figs. 32 and 33 at two positions: $x/C = 0.65$ and $x/C = 0.85$.

Fig. 31 shows the two locations where the phase-averaged velocity and vorticity profiles have been extracted at the same buffet phase to compare the stochastic forcing effects to the basic simulation.

Fig. 32 shows the comparison of these velocity profiles according to both approaches. It can be seen that the simulation with the forcing (IOES) leads to a significant thinning of the shear layer. This can also be observed in Fig. 33, where the two

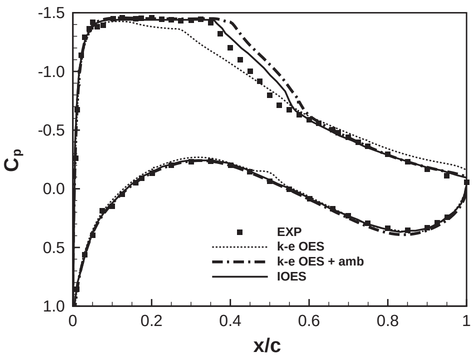

Fig. 30. Comparison of the mean surface pressure coefficient distribution between experiment, basic $k-\varepsilon$-OES modelling, $k-\varepsilon$-OES using the ambient terms of Spalart and Rumsey (2007): $k-\varepsilon$-OES + amb, stochastic forcing formulated in this study: IOES.

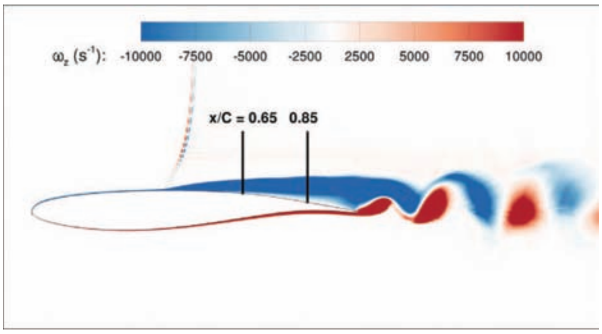

Fig. 31. Location of the phase-averaged velocity and vorticity profiles.

approaches are compared by means of the vorticity. The TNT interface, identified by a vorticity close to 0, is lowered by using the stochastic forcing. Its thickness is reduced by 30% at $x/C=0.65$, and by 19% at $x/C=0.85$, which has as a consequence the reduction of the drag, due to the reduction of the viscous region downstream of the shock. The present inhomogeneous forcing reproduces the blocking and thinning effect, similarly to the DNS results of Ishihara et al. (2015) regarding boundary-layer interface.

Fig. 34 left shows the velocity profile at the location $x/C=0.85$, as well as the vorticity gradient profile at the same position (Fig. 34 right). Two *inflexion points* of the velocity profile are identified, corresponding to the change in sign of the vorticity gradient ($d\omega/dy=0$). The existence of the inflexion points is associated indeed with the shear-layer instability development, illustrated in Fig. 29 as well as with the small series of Kelvin–Helmholtz vortices captured by the present simulation.

Following these results concerning the improved velocity profiles, a theoretical instability study can be carried out on the basis of the present velocity profiles in a future study, in order to accurately determine the critical shear rate beyond which the mentioned instabilities are amplified.

5. Conclusion

The present numerical study analyses in detail the flow physics of the transonic shock-wave, shear-layer and wake interaction around a supercritical airfoil at high Reynolds number (3 million), incidence of 3.5° and at a Mach number of 0.73. This set of physical parameters corresponds to the *onset* of the buffet instability, a challenge for the prediction of this instability appearance near the critical parameters by numerical simulation including turbulence modelling in the high-Reynolds number range. This study describes a new approach highlighting the dynamics of the transonic buffet in interaction with the near-wake von Kármán instability as well as with smaller-scale vortex structures in the separated shear layers, related to the Kelvin–Helmholtz instability.

This analysis is carried out by the Organized Eddy Simulation (OES) method, which resolves the organized coherent structures and models the random turbulence by adapted statistical modelling. This method has been improved in the present study to include stochastic forcing of smaller-scale vortex structures near the outer interfaces of the boundary layer, the shear layer and in the wake. Their effects are modelled as source terms in the turbulent kinetic energy and dissipation transport equations.

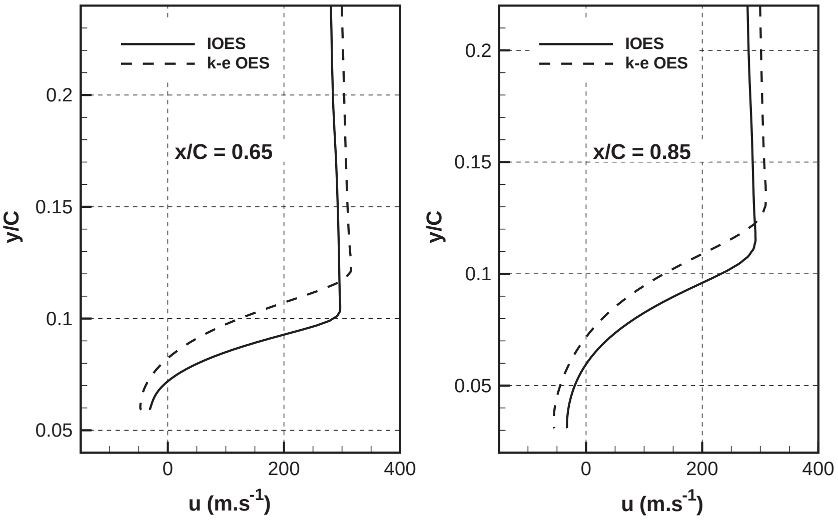

Fig. 32. Phase-averaged streamwise velocity profiles.

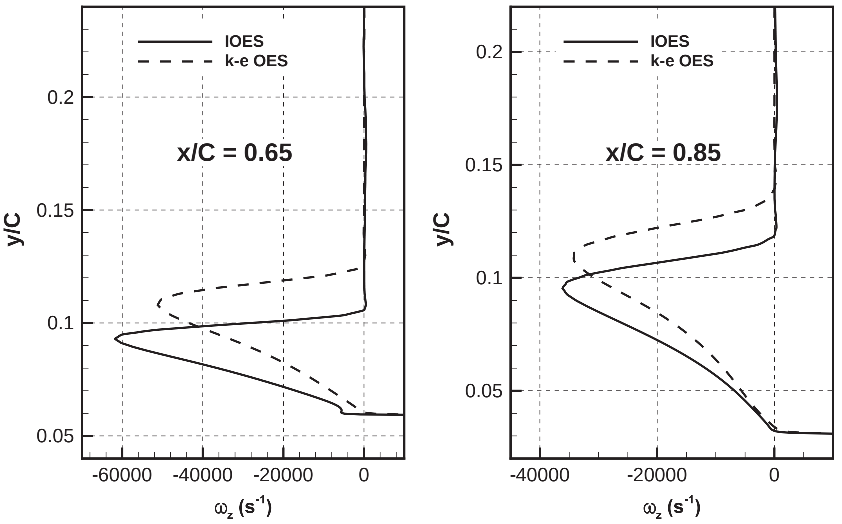

Fig. 33. Phase-averaged vorticity profiles.

By means of this modelling approach, the study contributes to complete experimental physical analysis of the transonic buffet, which was mainly interested in the shock motion and pressure-velocity distributions around the body and less in the interaction with the wake instabilities in the related literature. This study provides new results regarding the buffet interaction with the von Kármán mode and the smaller-scale vortex structures. The Proper Orthogonal Decomposition analysis has shown that this interaction creates an amplitude modulation of the buffet mode due to the von Kármán mode and vice-versa. The wavelet and autoregressive model analysis quantified a frequency modulation of the von Kármán instability due to the buffet. The predominant frequencies of these modes have been evaluated by spectral analysis and the interaction among them has been illustrated by the appearance of new frequencies in the energy spectrum, being combinations of the principal instability modes. Whereas the buffet mode is a well distinguished frequency peak in the spectrum, the von Kármán mode is characterized by a spectral 'bump' appearance around a frequency 33.3 times higher than the buffet frequency. The spectral analysis has shown the modification of the von Kármán mode 'bump' shape due to higher-order buffet harmonics and the amplification of the K–H instability peak of higher frequency.

Concerning these interactions, the POD analysis distinguished the shape modes involved in the formation of highly energetic coherent vortices and of the buffet dynamics from those of weaker energy involved in smaller-scale vortex structures appearing in the shear layers and influencing also the shock-motion area.

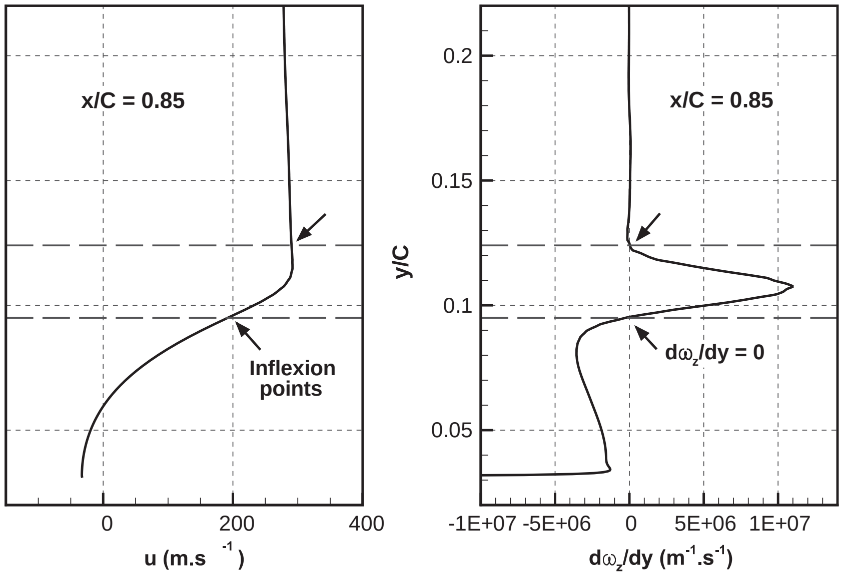

Fig. 34. IOES simulation: velocity (left) and vorticity gradient (right) profiles showing inflexion points outside and inside the upper thin shear layer interface.

Inspired from the POD reconstructions, an efficient inhomogeneous stochastic forcing has been built and applied as a source term in the turbulent kinetic energy and dissipation rate transport equations in the context of an improved OES (IOES) approach. By reconstructing the fluctuating velocity field corresponding to the higher-order POD modes, a kinetic energy fluctuation has been generated and employed in the stochastic forcing source terms. This forcing led to thinning of the turbulent/non-turbulent interfaces within the separated boundary layer and the shear layers.

An improved modelling of the shock amplitudes is obtained in comparison with experiments as well as a better physical representation of the instability regions and vortex structures around the body and in the wake. Furthermore, the present IOES method merits to be tested in 3D (although the buffet dynamics of a nominally 2D airfoil configuration are essentially two-dimensional) for a more accurate evaluation of the unsteady loads and pressure fluctuations generated by the fluid–structure interaction, a crucial issue in FIV (Flow-Induced Vibration) and aeroacoustics domains.

Acknowledgements

The authors acknowledge the financial and scientific support of the ATAAC (Advanced Turbulence Simulation for Aerodynamic Application Challenges) European Collaborative research program No. 233710, coordinated by DLR-Göttingen, by Dr. D. Schwamborn and including among the industrial partners Airbus, EADS, Dassault, Rolls Royce, Alenia and Eurocopter. The authors are grateful to the ONERA partner of this project for valuable scientific discussions and for the provision of a first numerical grid (S. Deck), as well as for the discussions on the impact of the two-dimensional character of the buffet around the wing, during the ATAAC project in the years 2009–2012. The computing time allocation was provided by the national computing centers CINES (Centre Informatique National de l'Enseignement Supérieur), CALMIP (Calcul en Midi-Pyrénées), IDRIS (Institut du Développement et des Ressources en Informatique Scientifique). This study partly used a computing allocation in the context of the PRACE-Tier1 and preparatory access supercomputing European initiative. The authors thank G. Harran and A. Sévrain for their scientific support concerning the dynamic systems analysis.

References

Alshabu, A., Olivier, H., 2008. Unsteady wave propagation phenomena on a supercritical airfoil. AIAA Journal 46 (8), 2066–2073.
Aubry, N., Guyonnet, R., Lima, R., 1991. Spatio-temporal analysis of complex signals: theory and applications. Journal of Statistical Physics 64 (3-4), 683–739.
Barbut, G., Braza, M., Hoarau, Y., Barakos, G., Sévrain, A., Vos, J.B., 2010. Prediction of transonic buffet around a wing with flap. In: Progress in Hybrid RANS-LES Modelling, Notes on Numerical Fluid Mechanics and Multidisciplinary Design, vol. 111. Springer, Gdansk, Poland. pp. 191–204.
Bodenschatz, E., Eckert, M., 2011. Prandtl and the Göttingen school. In: Davidson, P.A., et al. (Eds.), A Voyage Through Turbulence, Cambridge University Press, Cambridge.
Bouhadji, A., 1998. Analyse physique par simulation numérique de phénomènes de transition bi- et tridimensionnels dans l'écoulement compressible, visqueux autour d'une aile d'avion (Ph.D. thesis). INPT.

Bouhadji, A., Braza, M., 2003a. Organised modes and shock–vortex interaction in unsteady viscous transonic flows around an aerofoil. Part I. Mach number effect. Journal of Computers and Fluids 32 (9), 1233–1260.

Bouhadji, A., Braza, M., 2003b. Organised modes and shock–vortex interaction in unsteady viscous transonic flows around an aerofoil. Part II. Reynolds number effect. Journal of Computers and Fluids 32 (9), 1261–1281.

Bourdet, S., Bouhadji, A., Braza, M., Thiele, F., 2003. Direct numerical simulation of the three-dimensional transition to turbulence in the transonic flow around a wing. Flow, Turbulence and Combustion 71 (1–4), 203–220.

Bourgoyne, D.A., Ceccio, S.L., Dowling, D.R., 2005. Vortex shedding from a hydrofoil at high Reynolds number. Journal of Fluid Mechanics 531, 293–324.

Bourguet, R., Braza, M., Harran, G., El Akoury, R., 2008. Anisotropic organised eddy simulation for the prediction of non-equilibrium turbulent flows around bodies. Journal of Fluids and Structures 24 (8), 1240–1251.

Braza, M., 2011. NACA0012 with Aileron. In: Doerffer, P., Hirsch, C., Dussauge, J.-P., Babinsky, H., Barakos, G.N. (Eds.), Unsteady Effects of Shock Wave Induced Separation, Notes on Numerical Fluid Mechanics and Multidisciplinary Design, vol. 114. Springer, Berlin, Heidelberg, pp. 101–131.

Braza, M., Faghani, D., Persillon, H., 2001. Successive stages and the role of natural vortex dislocations in three-dimensional wake transition. Journal of Fluid Mechanics 439, 1–41.

Braza, M., Perrin, R., Hoarau, Y., 2006. Turbulence properties in the cylinder wake at high Reynolds number. Journal of Fluids and Structures 22 (6–7), 757–771.

Brunet, V., 2003. Computational study of buffet phenomenon with unsteady RANS equations. In: 21st AIAA Applied Aerodynamics Conference. Orlando, FL, USA, AIAA 2003-3679, 23–26 June.

Brunet, V., Deck, S., Molton, P., Thiery, M., 2005. A complete experimental and numerical study of the buffet phenomenon over the OAT15A airfoil. In: 40th Colloque d'Aérodynamique Appliquée, 21–23 March, Toulouse, France.

Deck, S., 2005. Numerical computation of transonic buffet over a supercritical airfoil. AIAA Journal 43 (7), 1556–1566.

Dritschel, D., Haynes, P., Juckes, M., Shepherd, T., 1991. The stability of a two-dimensional vorticity element under uniform strain. Journal of Fluid Mechanics 230, 647–665.

Duncan, W.J., Ellis, L., Scruton, C., 1932. First report on the general investigation of tail buffeting. Aeronaut. Research. Com. R. & M. 1457, part I.

Durbin, J., 1960. The fitting of time series models. Review of the International Statistical Institute 28, 233–243.

Eames, I., Flor, J., 2011. New developments in understanding interfacial processes in turbulent flows. Philosophical Transactions of the Royal Society A: Mathematical, Physical and Engineering Sciences 369 (1937), 702–705.

Edwards, J.R., Chandra, S., 1996. Comparison of eddy viscosity-transport turbulence models for three-dimensional, shock-separated flowfields. AIAA Journal 34 (9), 756–763.

El Akoury, R., Braza, M., Perrin, R., Harran, G., Hoarau, Y., 2008. The three-dimensional transition in the flow around a rotating cylinder. Journal of Fluid Mechanics 607, 1–11.

Fu, S., Haase, W., Peng, S.H., Schwamborn, D. (Eds.), 2012. Progress in Hybrid RANS-LES Modelling, Notes on Numerical Fluid Mechanics and Multidisciplinary Design, vol. 117, Springer, Beijing, China.

Fung, Y.C., 2002. An Introduction to the Theory of Aeroelasticity. Dover, Schlieren Picture Page 313 by D. W. Holder, National Physical Laboratory, England.

Grossi, F., 2010. Simulation numérique et analyse physique du tremblement transsonique d'un profil supercritique par approche de modélisation de la turbulence statistique avancée (Master's thesis). IMFT.

Grossi, F., 2014. Physics and Modeling of Unsteady Shock Wave/Boundary Layer Interactions Over Transonic Airfoils by Numerical Simulation (Ph.D. thesis). INP Toulouse.

Grossi, F., Braza, M., Hoarau, Y., 2011. Simulation numérique et analyse physique du tremblement transsonique d'un profil supercritique à Reynolds élevé. 20 th Congrès Français de Mécanique, 29 August–2 September.

Grossi, F., Braza, M., Hoarau, Y., 2012a. Delayed detached-eddy simulation of the transonic flow around a supercritical airfoil in the buffet regime. In: Progress in Hybrid RANS-LES Modelling. Notes on Numerical Fluid Mechanics and Multidisciplinary Design, vol. 117. Springer, Beijing, China, pp. 369–378.

Grossi, F., Braza, M., Hoarau, Y., 2014. Prediction of transonic buffet by delayed detached-eddy simulation. AIAA Journal 52, 2300–2312.

Grossi, F., Szubert, D., Braza, M., Sevrain, A., Hoarau, Y., 2012b. Numerical simulation and turbulence modelling of the transonic buffet over a supercritical airfoil at high Reynolds number. In: Proceedings of the ETMM9 9th International ERCOFTAC Symposium on Engineering Turbulence Modelling and Measurements. Thessaloniki, Greece, 6–8 June.

Grossmann, A., Morlet, J., 1984. Decomposition of Hardy functions into square integrable wavelets of constant shape. SIAM Journal on Mathematical Analysis 15 (4), 723–736.

Guzmán, A.M., Amon, C.H., 1994. Transition to chaos in converging-diverging channel flows: Ruelle-Takens-Newhouse scenario. Physics of Fluids 6.

Haase, W., Braza, M., Revell, A. (Eds.), 2009. DESider – A European Effort on Hybrid RANS-LES Modelling: Results of the European-Union Funded Project, 2004-2007, Notes on Numerical Fluid Mechanics and Multidisciplinary Design, vol. 103, Springer.

Hoarau, Y., 2002. Analyse physique par simulation numérique et modélisation des écoulements décollés instationnaires autour de surfaces portantes (Ph.D. thesis). INPT.

Holzner, M., Liberzon, A., Nikitin, N., Lüthi, B., Kinzelbach, W., Tsinober, A., 2008. A Lagrangian investigation of the small-scale features of turbulent entrainment through particle tracking and direct numerical simulation. Journal of Fluid Mechanics 598, 465–475.

Hunt, J., Richards, K., 1984. Stratified airflow over one or two hills. In: Kaplan, H., Dinar, N. (Eds.), Boundary Layer Structure, Springer, Zichron Yaacov, Israel, pp. 223–259.

Hunt, J. C.R., Eames, I., Westerweel, J., 2008. Vortical interactions with interfacial shear layers. In: Kaneda, Y. (Ed.), IUTAM Symposium on Computational Physics and New Perspectives in Turbulence, IUTAM Bookseries, vol. 4, Springer, Nagoya, Japan, pp. 331–338.

Hunt, J.C.R., Ishihara, T., Worth, N.A., Kaneda, Y., 2014. Thin shear layer structures in high Reynolds number turbulence. Flow, Turbulence and Combustion 92 (3), 607–649.

Ishihara, T., Ogasawara, H., Hunt, J.C.R., 2015. Analysis of conditional statistics obtained near the turbulent/non-turbulent interface of turbulent boundary layer. Journal of Fluids and Structures 53, 50–57. http://dx.doi.org/10.1016/j.jfluidstructs.2014.10.008.

Jacquin, L., Molton, P., Deck, S., Maury, B., Soulevant, D., 2005. An experimental study of shock oscillation over a transonic supercritical profile. In: 35th AIAA Fluid Dynamics Conference and Exhibit, Toronto, Ontario, Canada, AIAA 2005-4902, 6–9 June.

Jacquin, L., Molton, P., Deck, S., Maury, B., Soulevant, D., 2009. Experimental study of shock oscillation over a transonic supercritical profile. AIAA Journal 47 (9), 1985–1994.

Jimenez-Garcia, A., 2012. Etude de l'interaction tremblement transsonique – instabilité de von Kármán à l'aide d'une plaque de bord de fuite par approche de modélisation de la turbulence statistique avancée (Master's thesis). IMFT.

Landau, L.D., 1944. On the problem of turbulence. Comptes Rendus Academic Sciences URSS 44 (31), 1–314.

Lee, B.H.K., 1990. Oscillatory shock motion caused by transonic shock boundary-layer interaction. AIAA Journal 28 (5), 942–944.

Levy Jr., L.L., 1978. Experimental and computational steady and unsteady transonic flows about a thick airfoil. AIAA Journal 16 (6), 564–572.

Martinat, G., Braza, M., Hoarau, Y., Harran, G., 2008. Turbulence modelling of the flow past a pitching NACA0012 airfoil at 10^5 and 10^6 Reynolds numbers. Journal of Fluids and Structures 24 (8), 1294–1303.

McDevitt, J.B., Levy Jr., L.L., Deiwert, G.S., 1976. Transonic flow about a thick circular-arc airfoil. AIAA Journal 14 (5), 606–613.

Menter, F., Egorov, Y., 2005. A scale-adaptive simulation model using two-equation models. In: 43rd AIAA Aerospace Sciences Meeting and Exhibit, AIAA Paper 2005–1095, 10–13 January.

Menter, F., Kuntz, M., Bender, R., 2003. A scale-adaptive simulation model for turbulent flow prediction. In: 41st AIAA Aerospace Sciences Meeting and Exhibit, AIAA paper 2003–0767, 6–9 January .

Menter, F.R., 1994. Two-equation eddy-viscosity turbulence models for engineering applications. AIAA Journal 32 (8), 1598–1605.

Newhouse, S., Ruelle, D., Takens, F., 1978. Occurrence of strange axiom A attractors near quasi periodic flows on T_m, $m \le 3$. Communications in Mathematical Physics 64 (1), 35–40.

Perrin, R., Braza, M., Cid, E., Cazin, S., Moradei, F., Barthet, A., Sevrain, A., Hoarau, Y., 2006. Near-wake turbulence properties in the high Reynolds number incompressible flow around a circular cylinder measured by two- and three-component PIV. Flow, Turbulence and Combustion 77 (1–4), 185–204.

Roe, P.L., 1981. Approximate Riemann solvers, parameter vectors, and difference schemes. Journal of Computational Physics 43 (2), 357–372.

Rung, T., Bunge, U., Schatz, M., Thiele, F., 2003. Restatement of the Spalart–Allmaras eddy-viscosity model in strain-adaptive formulation. AIAA Journal 41 (7), 1396–1399.

Seegmiller, H.L., Marvin, J.G., Levy Jr., L.L., 1978. Steady and unsteady transonic flow. AIAA Journal 16 (12), 1262–1270.

Shur, M., Strelets, M., Zaikov, L., Gulyaev, A., Kozlov, V., Secundov, A., 1995. Comparative numerical testing of one- and two-equation turbulence models for flows with separation and reattachement. In: 33rd Aerospace Sciences Meeting and Exhibit, Reno, NV, USA, AIAA 95-0863, 9–12 January.

Sirovich, L., 1990. Turbulence and the dynamics of coherent structures, Parts I, II & III. Quarterly Journal of Applied Mathematics XLV (3), 561–582.

Spalart, P.R., 2000. Trends in turbulence treatments. In: Fluids 2000 Conference and Exhibit, Denver, CO, USA, AIAA Paper 2000–2306, 19–22 June.

Spalart, P.R., Allmaras, S.R., 1994. A one-equation turbulence model for aerodynamic flows. Recherche Aerospatiale 1, 5–21.

Spalart, P.R., Rumsey, C.L., 2007. Effective inflow conditions for turbulence models in aerodynamic calculations. AIAA Journal 45 (10), 2544–2553.

Taveira, R.R., da Silva, C.B., 2014. Characteristics of the viscous superlayer in shear free turbulence and in planar turbulent jets. Physics of Fluids 26 (2), 021702.

Thiery, M., Coustols, E., 2005. URANS computations of shock-induced oscillations over 2D rigid airfoils: Influence of test section geometry. Flow, Turbulence and Combustion 74 (4), 331–354.

van Leer, B., 1979. Towards the ultimate conservative difference scheme. V. A second-order sequel to Godunov's method. Journal of Computational Physics 32 (1), 101–136.

Vos, J.B., Rizzi, A.W., Corjon, A., Chaput, E., Soinne, E., 1998. Recent advances in aerodynamics inside the NSMB (Navier Stokes Multi Block) consortium. In: 36th AIAA Aerospace Sciences Meeting and Exhibit, Reno, NV, USA, AIAA Paper 98–0225, 12–15 January.

Welch, P.D., 1967. The use of fast fourier transform for the estimation of power spectra: a method based on time averaging over short, modified periodograms. IEEE Transactions on Audio and Electroacoustics 15 (2), 70–73.

Westerweel, J., Fukushima, C., Pedersen, J.M., Hunt, J.C.R., 2009. Momentum and scalar transport at the turbulent/non-turbulent interface of a jet. Journal of Fluid Mechanics 631, 199–230.

3.1.2 Upscale turbulence modelling

A stochastic forcing has been introduced in the previous section, inspired from the theoretical analysis (Hunt et al., 2008) and experimental studies (Ishihara et al., 2015) that introduced "eddy-blocking" mechanism near TNT interfaces. It is well known that the direct turbulence cascade modelling in the majority of the turbulence modelling methods, and based on turbulence hypothesis, generates excessive turbulence diffusion and as a consequence, the TNT interfaces cannot keep as thin as observed. A new decomposition of the resolved and modelled part in the context of the RANS modelling is proposed as a conjecture based on the separable POD and the introduced stochastic forcing.

The flow variables are still decomposed in an average and a fluctuating part. In this case, the ensemble average is considered:

$$U = \langle U \rangle + U' \tag{3.1}$$

and has the same properties as any Reynolds averaging, in particular:

$$\langle \langle U \rangle \rangle = \langle U \rangle, \tag{3.2}$$

$$\langle U' \rangle = 0 \tag{3.3}$$

Thus, the Reynolds-averaged Navier-Stokes equation (section 1.2.3 page 8) are still valid using the ensemble average, and the existence of the turbulent stress tensor remains:

$$\tau_{ij} = -\langle \rho \rangle \langle U_i' U_j' \rangle \tag{3.4}$$

From now, the fluctuations are decomposed in an upscale contribution $\hat{U}_j$ and a downscale one $\check{U}_j$, giving:

$$\begin{aligned} \langle U_i' U_j' \rangle &= \langle (\hat{U}_i + \check{U}_i) (\hat{U}_j + \check{U}_j) \rangle \\ &= \langle \hat{U}_i \hat{U}_j \rangle + \langle \hat{U}_i \check{U}_j \rangle + \langle \check{U}_i \hat{U}_j \rangle + \langle \check{U}_i \check{U}_j \rangle \end{aligned} \tag{3.5}$$

This decomposition gives a fully 'downscale' contribution $\langle \check{U}_i \check{U}_j \rangle$ which can be modelled in a usual way (e.g. Boussinesq assumption, section 1.2.4 page 9). The remaining part of the sum contains upscale contribution. This part is modelled by means of the stochastic forcing.

3.2 Laminar airfoil

The laminar airfoil studied here has been designed by Dassault Aviation in the context of the TFAST (Transition location effect on shock-wave/boundary-layer interaction) European project, where other geometries are handled such as turbine and compressor blades, as well as experimental supersonic shock-wave/boundary-layer interaction configuration (see chapter 4 page 117). Unfortunately, detailed experimental results are still not available, but all the partners of this project involved in the numerical study of the airfoil have produced a substantial set of data. Hence, our reserch team has carried out the study of the laminar-turbulent transition location effect on the transonic flow around the airfoil, in steady state (low angle of attack) as well as in the case of buffetting. This study have been subjected to a close collaboration between INRIA (Institut national de recherche en informatique et en automatique or French institute for research in computer science and automation) and our team in the context of an optimisation study, in the two cases. Finally, a 3D computation has been performed in terms of a hybrid RANS-LES simulation in the transonic buffet conditions. All the results of this study, as well as the details on the numerical and optimisation methods and the European project, have been gathered together in an article submitted on April 2015 to the European Journal of Mechanics - B/Fluids. This article has been included in this manuscript from the next page.

Numerical study of the turbulent transonic interaction and transition location effect involving optimisation around a supercritical airfoil

Damien Szubert[a,*], Ioannis Asproulias[a], Fernando Grossi[a], Régis Duvigneau[b],
Yannick Hoarau[c], Marianna Braza[a]

[a] *Institut de Mécanique des Fluides de Toulouse, UMR N°5502 CNRS-INPT-UPS, Allée du Prof. Camille Soula, F-31400 Toulouse, France*
[b] *INRIA Sophia Antipolis - Méditerranée, ACUMES Team*
[c] *Laboratoire ICUBE, UMR N°7357, Strasbourg*

Abstract

The present article analyses the turbulent flow around a supercritical airfoil at high Reynolds number and in the transonic regime, involving shock-wave/boundary-layer interaction (SWBLI) and buffet, by means of numerical simulation and turbulence modelling. Emphasis is put on the transition position influence on the SWBLI and optimisation of this position in order to provide a maximum lift/drag ratio. A non-classical optimisation approach based on Kriging method, coupled with the URANS modelling, has been applied on steady and unsteady flow regimes. Therefore, the present study contributes to the so-called 'laminar-wing design' with the aim of reducing the drag coefficient by providing an optimum laminar region upstream of the SWBLI.

---

1. Introduction

The present study has been carried out in the context of the European research program TFAST, "Transition location effect on shock-wave/boundary-layer interaction", project N°265455. One of the main objectives of this research is to provide optimal laminarity in the boundary layer upstream of the shock-wave/boundary-layer interaction (SWBLI), in order to reduce the skin friction comparing to the fully turbulent case and therefore reduce drag, in the context of greening

---

[*] Corresponding author

Preprint submitted to Eur. J. Mech. B/Fluid *December 7, 2015*

aircraft transport (a major objective of the *Horizon 2020* European programme). Due to increased aerodynamic loads and aero-engine components nowadays, supersonic flow velocities are more frequent, generating shock waves that interact with boundary layers. Laminar shock-wave/boundary-layer interaction can rapidly cause flow separation, which is highly detrimental to aircraft performance and poses a threat to safety. This situation can be improved by imposing the laminar-turbulent transition upstream of the interaction, but this should be carefully done in order to keep the aerodynamic efficiency high (lift/drag ratio).

In the context of the European research program TFAST, several ways of controlling the position of the transition is carried out. To this end, a supercritical laminar wing, the so-called V2C, has been designed by Dassault Aviation. This profile allows the boundary layer to remain laminar up to the shock foot, even in the environment of transonic wind tunnels of the laboratories involved in the project, and up to the angle of attack of 7.0°. Experimental results for the present configuration are not yet available in the present research project. Regarding the related literature, the transonic buffet has been studied experimentally in detail since the 70s on circular-arc airfoils [1, 2], and most recently on supercritical airfoils [3]. In this latest study, a fixed transition tripping was applied at 7% of the chord. The physics governing the transonic buffet is complex and several theories have been proposed, like the effect of the feedback mechanism of waves propagating from the trailing edge, or the onset of a global instability [3, 4, 5]. Comparison of numerical results by Deck [6], Grossi et al. [7] and Szubert et al. [5] with the experimental results by Jacquin et al. [8] concerning the transonic buffet around supercritical wings with fixed transition showed the predictive capability of recent CFD methods and a physical analysis of the interaction between buffet and trailing-edge instabilities. The SWBLI involving transonic buffet and laminar wing design currently highly interests the aeronautical industries (Cleansky European project, “Advanced, high aspect ratio transonic laminar wing” [9]). Laminar wing design in transonic regimes has been studied in respect of transition control by means of Discrete Roughness Elements (DRE’s) [10].

Navier-Stokes simulations of transonic buffet as well as of the shock-vortex interaction at moderate Reynolds numbers were reported by Bouhadji and Braza [11], as well as DNS by Bourdet et al. [12]. In the high Reynolds number range, typical of aerodynamic applications, the use of appropriate turbulence modelling is necessary. Concerning transonic buffet, the unsteady shock-wave/boundary-layer interaction represents a major challenge for turbulence models and the low frequencies associated with the shock-wave motion can make the simulations very expensive. Since the first simulations by Seegmiller et al. [2] and Levy Jr. [13] for a circular-arc airfoil, Unsteady Reynolds-Averaged Navier-Stokes (URANS) computations using eddy-viscosity turbulence models have been largely used to predict the phenomenon over two-dimensional airfoils. Pure LES simulations, even combined with specific wall-models, are yet quite costly for the high Reynolds number range of real flight configurations. For this reason, hybrid RANS-LES methods have been developed in the last decade and start to be largely used in the industrial context together with adapted, advanced URANS approaches. The hybrid methods combine the robustness and near-wall physics offered by URANS in the near region, as well as LES advantages in capturing the physics of unsteady vortices and instabilities development in the detached flow regions. Among the hybrid methods, the Detached-Eddy Simulation (DES) does not need to impose the interface between the statistical and LES regions. This is provided inherently by the choice of the turbulence length scale to use in the transport equations [14]. In order to avoid approaching the near-wall region by the LES zone, the Detached-Eddy Simulation has been improved in respect of the turbulence length scale, ensuring a quite significant statistical zone around the body, in the context of the Delayed Detached-Eddy Simulation (DDES) [15]. Moreover, improvement of the nearwall modelling has been achieved by means of a suitable Wall-Modelled LES (WMLES) in order to allow the flow physics modelling in the very near wall region covering the viscous sublayer by means of finer grids (but more economic than the LES) in the context of the Improved Delayed Detached-Eddy Simulation (IDDES) [16]. Regarding the transonic buffet simulations, Deck [6] has used a successful zonal DES approach, using mostly statistical modelling in the outer regions far from the body. He provided a detailed prediction of the transonic buffet around the supercritical airfoil OAT15A. Regarding the same configuration, Grossi et al. [7] performed a Delayed Detached-Eddy Simulation in the context of the ATAAC (Advanced Turbulence Simulations for Aerodynamic Application Challenges) European programme. This study succeeded in the prediction of the shock-wave self-sustained motion near the critical angle of incidence for the appearance of buffet, based on experimental results by Jacquin et al. [3, 8]. Moreover, Szubert et al. [5] provided a detailed analysis of the buffet dynamics by means of the Organised Eddy Simulation (OES) approach, resolving the organised coherent modes and modelling the random turbulence background and using upscale turbulence modelling through stochastic forcing in order to keep the turbulent–non-turbulent shear-layer interfaces thin. In the present paper, the transonic buffet is applied on the V2C airfoil within the TFAST program, at 7.0°, the maximum angle of attack allowed by the design, upstream Mach number 0.70 and Reynolds number 3.245×10^6. The fully turbulent case is studied by different URANS and DDES modelling in two and three dimensions respectively. The predictive capabilities of statistical and hybrid turbulence modelling approaches are discussed. A 2D study is first carried out to investigate the main flow characteristics in respect of the angle of attack as well as the influence of the transition location. The transition location effects are also studied in the buffeting regime, by imposing the laminarity at several positions. Based on these results, the main objective of the present article is to put ahead a coupling of the aforementioned CFD methods with a non-classical optimisation approach of the transition location in the steady and unsteady transonic regimes in respect of the drag reduction and lift to drag ratio maximisation.

2. Numerical method and turbulence modelling

2.1. Flow configuration

Concerning the design of the V2C wing, it was validated numerically by Dassault on a 0.25 m-chord length (c) profile by means of RANS computations for various angles of attack at freestream Mach numbers of 0.70 and 0.75, yielding chord-based Reynolds numbers of approximately 3.245×10^6 and 3.378×10^6 respectively. The study was performed using a compressible Navier-Stokes code adopting a two-layer $k-\varepsilon$ model, with the transition location being determined from the fully-turbulent flowfield using a three-dimensional compressible boundary-layer code by means of the N-factor amplification with a parabola method. The technique employed for laminarity and an initial design in respect of the transition prediction was based on the e^N method (Ref. [17] for instance). The airfoil surface was generated in such a way that the N-factor remains small for low-to-moderate turbulence intensity levels, similar to the wind tunnel turbulence levels used for the present test-case for the experimental study currently in progress in the TFAST project. At Mach number 0.70, the flow separated between $\alpha = 6°$ and $7°$. The amplification factor N was shown to be smaller than 3 up to the shock wave, thus guaranteeing laminar flow. At Mach 0.75, the value of N remained smaller than 2 up to $\alpha = 7°$. For this Mach number, there were not buffeting phenomenon, whatever the angle of attack. Moreover, for incidences higher than 1°, the shock induces a separation of the boundary layer up to the trailing edge.

2.2. Numerical method

The simulations of the V2C configuration at upstream Mach number $\mathrm{M} = 0.70$ and Reynolds number $\mathrm{Re} = 3.245 \times 10^6$ have been carried out with the Navier-

Stokes Multi-Block (NSMB) solver. The NSMB solver is the fruit of a european consortium that included Airbus from the beginning of 90s, as well as main European aeronautics research Institutes like KTH, EPFL, IMFT, ICUBE, CERFACS, Univ. of Karlsruhe, ETH-Ecole Polytechnique de Zurich, among other. This consortium is coordinated by CFS Engineering in Lausanne, Switzerland. NSMB solves the compressible Navier-Stokes equations using a finite volume formulation on multi-block structured grids. It includes a variety of efficient high-order numerical schemes and turbulence modelling closures in the context of URANS, LES and hybrid turbulence modelling. NSMB includes efficient fluid-structure coupling for moving and deformable structures. For the present study, the third-order of accuracy Roe upwind scheme [18] associated with the MUSCL flux limiter scheme of van Leer [19] is used for the spatial discretisation of the convective fluxes. A similar upwind scheme (AUSM) was used by Deck [6]. For the diffusion terms, second-order central differencing has been used. The temporal discretisation has been done by means of dual-time stepping and of second order accuracy. A physical time step of 5 μs has been adopted for 2D simulations. For the 3D simulations, the time step has been reduced to 0.1 μs after detailed numerical tests. A typical number of inner iterations of 30 was necessary for the convergence requirements in each time step.

The 2D grid has a $C-H$ topology, and is of size 163,584 cells. The downstream distance of the computational domain is located at a mean distance of 80 chords from the obstacle. A grid refinement study has been carried out, by means of steady-state computations and using local time stepping, for the flow at $M_\infty = 0.70$ and $\alpha = 4.0^\circ$ using the $k-\omega$ SST model [20] and assuming fully-turbulent boundary layer, with two other grids: one 50% coarser, and another 30% finer. Detailed results of this convergence study can be found in [7]. The grid retained for the present study gave a maximum value of non-dimensional wall distance y^+ of about 0.55 with respect to the turbulence modelling. Fig. 1 shows the grid and the computational domain. For the 3D computations, the planar grid has been extruded to 59 cells uniformly distributed in the spanwise direction over a distance of $0.33 \times c$. The 3D grid contains about 9.65 M cells.

Boundary and initial conditions

On the solid wall, impermeability and no-slip conditions are employed. The far-field conditions are the characteristic variables extrapolated in time: the total pressure ($P_0 = 10^5$ Pa) and total temperature ($T_0 = 290$ K), as well as the upstream Reynolds number of 3.245 million and Mach number of 0.70. The upstream turbulence intensity is $Tu = 0.08\%$.

The initial conditions are those of a steady-state generated field in each case.

Turbulence modelling

In the context of URANS and hybrid turbulence modelling, the following models have been used respectively: the two-equation $k-\omega$ SST model of Menter [20] as well as the OES-$k-\varepsilon$ [5, 21] and the DDES-$k-\omega$ SST models have been used with turbulence-sustaining ambiant terms to prevent the free decay of the transported turbulence variables [22].

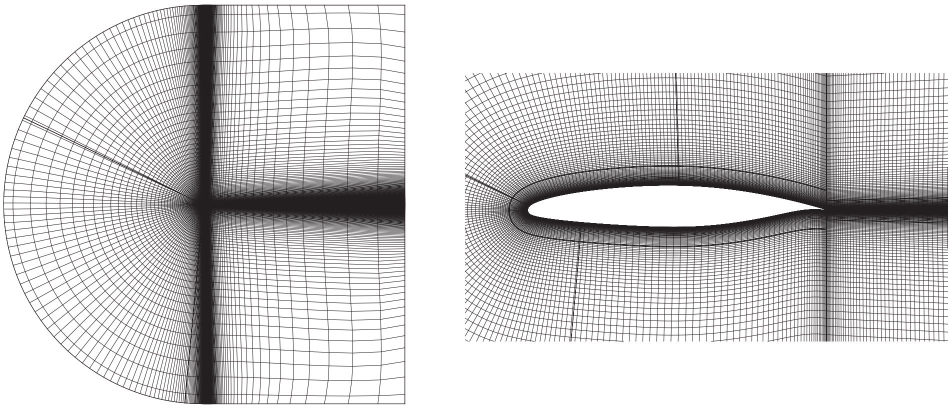

Figure 1: Multiblock domain

2.3. Optimisation method

In the context of the transition location study detailed in this paper, an optimisation of its location is proposed by employing a non-classical statistical learning approach. The principle consists in gathering a set of performance values, observed for different parameters, and construct a statistical model (Gaussian Process) on this basis, that reflects the knowledge and uncertainties related to the performance function. Then, this model is employed to determine the most interesting simulations to carry out, in a statistical sense. This approach is repeated until convergence [23].

More precisely, the statistical model for the performance function f is constructed on the basis of a set of observed values $\mathbf{F_N} = \{f_1, f_2, \ldots, f_N\}$ at some points $\mathbf{X_N} = \{x_1, x_2, \ldots, x_N\} \in \mathbb{R}^d$ (here $d = 1$). $\mathbf{F_N}$ is assumed to be one realization of a multivariate Gaussian Process which has a joint Gaussian distribution [24]:

$$p(\mathbf{F_N}|\mathbf{X_N}) = \frac{\exp\left(-\frac{1}{2}\mathbf{F_N}^\top C_N^{-1}\mathbf{F_N}\right)}{\sqrt{(2\pi)^N \det(C_N)}}, \tag{1}$$

for any collection of inputs $\mathbf{X_N}$. C_N is the $N \times N$ covariance matrix, whose elements C_{mn} give the correlation between the function values f_m and f_n obtained at points x_m and x_n. This is expressed in terms of a correlation function k, i.e., $C_{mn} = cov(f_m, f_n) = k(x_m, x_n; \Theta)$ with Θ a set of hyper-parameters, calibrated on the basis of known points (likelihood maximisation principle). The Matérn class of covariance stationary kernels, which gives a family of correlation functions of different smoothness [24], is used for k.

After calculations based on conditional probabilities, the probability density for the function value f_{N+1} at any new point x_{N+1} is:

$$p(f_{N+1}|\mathbf{X_N}, \mathbf{F_N}) \propto \exp\left[-\frac{(f_{N+1} - \hat{f}_{N+1})^2}{2\hat{\sigma}^2_{f_{N+1}}}\right], \tag{2}$$

where

$$\hat{f}_{N+1} = \mathbf{k_{N+1}}^\top C_N^{-1}\mathbf{F_N}, \tag{3}$$

$$\hat{\sigma}^2_{f_{N+1}} = \kappa - \mathbf{k_{N+1}}^\top C_N^{-1}\mathbf{k_{N+1}}, \tag{4}$$

with $\kappa = k(x_{N+1}, x_{N+1}; \Theta)$ and $\mathbf{k_{N+1}} = [k(x_1, x_{N+1}; \Theta), \ldots, k(x_N, x_{N+1}; \Theta)]^\top$. Thus, the probability density for the function value at the new point x_{N+1} is also Gaussian with mean $\hat{f}_{N+1}$ and standard deviation $\hat{\sigma}_{f_{N+1}}$. Therefore, the most likely value at the new point x_{N+1} is $\hat{f}_{N+1}$. This value will be considered as the prediction of the Gaussian Process model. The variance $\hat{\sigma}^2_{f_{N+1}}$ can be interpreted as a measure of uncertainty in the value prediction. If the evaluation is known to be noisy, the model can account for the observation noise by modifying the diagonal terms of the covariance matrix, on the basis of the noise variance estimated for each database point [25].

At each step of the optimisation procedure, this Gaussian Process model is exploited to determine new points to be simulated. The most popular strategy is the maximisation of the Expected Improvement (EI) criterion [23]. The maximisation of this criterion is numerically reached, by solving an internal optimisation problem using an evolution strategy.

3. Results

3.1. Two-dimensional study: angle of attack effects

This study has been carried out in URANS with the two-equation $k-\omega$ SST turbulence model [20] for an upstream Mach number $M_\infty = 0.70$. The angle of attack has been varied from 1.0° up to 7.0°, which is the maximum angle of attack for which the boundary layer is supposed to remain laminar from the leading edge to the shock wave. Initially, the computations adopt local time stepping. If convergence is not reached (i.e., a relative reduction of 10^{-6} in the residual), time-accurate simulations with a time step of $5 \times 10^{-6} s$ are then carried out. Near the critical angle regarding the buffet, the angle of attack has been varied by an increment of 0.5° in order to refine the critical buffet range.

Fig. 2 shows the averaged distributions of the pressure coefficient for the full range of incidences and skin-friction coefficient for the steady cases. For angles of attack up to 5.0°, the flow is steady and rear separation is always present. The shock wave can be distinguished at 2.0°. As the angle of attack is further increased, the shock initially moves downstream, then it goes upstream for $\alpha > 3°$. From $\alpha = 4.0°$, a separation bubble appears and develops. The size of the rear separation steadily increases with the angle of attack (Fig. 2(b)).

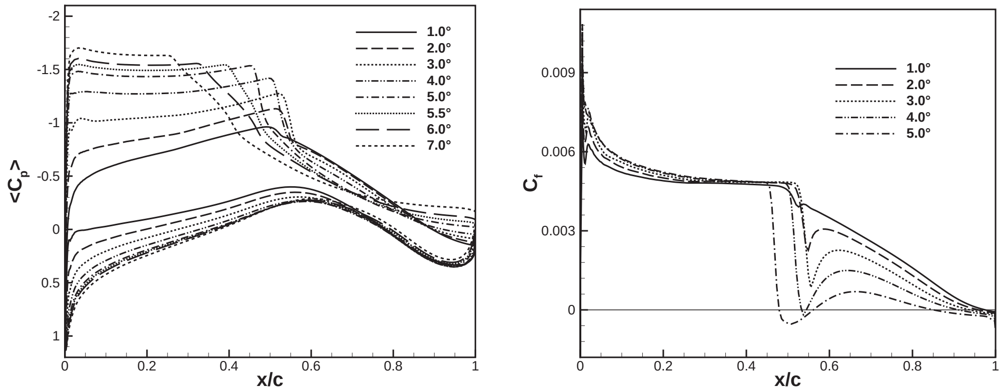

(a) Pressure coefficient

(b) Friction coefficient

Figure 2: Effect of the angle of attack on the steady and mean surface distributions and on the friction coefficient

The buffet onset, characterized by an oscillating shock wave, has been detected from 5.5°. The main frequency increases with incidence in the range of 80 − 82Hz.

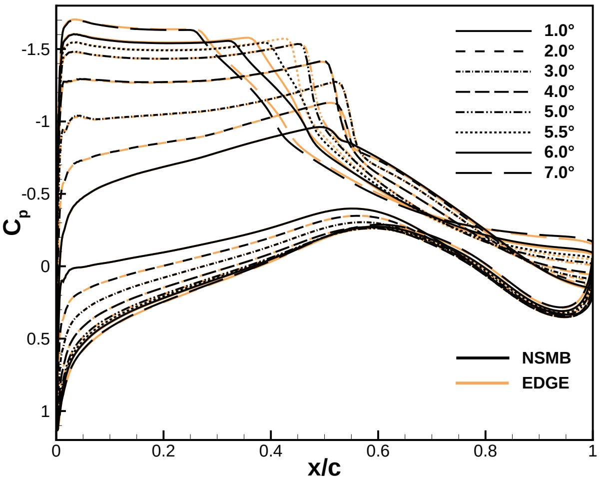

Figure 3: Comparison of the mean wall pressure coefficient between NSMB end Edge codes, for angles of attack between 1.0° and 7.0°

At 5.5°, the amplitude of the shock-wave motion is still small, resulting in a slight slope in the C_p curve.

A detailed comparison of the results obtained in the present study by the NSMB code has been carried out by using the Edge code, an unstructured compressible finite volume CFD code developed by the FOI since 1997 in collaboration with industrial and academic partners. The wall pressure distribution is plotted in Fig. 3 for angles of attack between 1.0° and 7.0°. This comparison showed small differences close to the critical angle, but the results were very similar at lower and higher angles of attack. This ensures about the validity of the present simulations, in absence of finalised experimental results within the TFAST programme.

3.2. Transition location effect

Two flow conditions have been selected for a numerical investigation of the transition location effect on the SWBLI, due to their interesting flow physics. First, the steady interaction arising at $\alpha = 4.0°$ is addressed, featuring a reasonably strong shock just below the critical angle of attack for buffet onset. The second flow condition is the fully-established buffet regime at $\alpha = 7.0°$, which presents a large shock-wave motion region.

The transition is forced at the position x_t by imposing the turbulent viscosity $\nu_t = 0$ for $x < x_t$. Its location x_t is varied from the leading edge up to as close as possible to the shock wave. The influence of the tripping point over the selected steady and unsteady transonic flow-fields is presented in the following two subsections.

3.2.1. Pre-buffet condition – Steady case

Results presented in the previous sections showed that, at $\alpha = 4.0^\circ$ and $M_\infty = 0.70$, the fully turbulent flow over the V2C airfoil is near critical with respect to transonic buffet. At that incidence, the shock wave is strong enough to induce a small separation bubble and the adverse pressure gradient over the rear part of the airfoil causes rear separation at about $x/c = 0.91$. The same flow condition has been recomputed considering different transition locations x_t from the leading edge up to the mid-chord, remaining steady in all cases. The pressure and friction coefficients distributions over the upper surface are plotted in figure 4 for some chosen values of x_t. The pressure coefficient indicates an increase of the suction effect as the transition position moves donwstream, while the shock position moves downstream. This facts yield an increase of lift. The trailing-edge pressure decreases, as well as the C_p on both sides of the rear airfoil part. The $x/C = 0.10$ case can be qualitatively compared with the case of the OAT15A airfoil with fixed transition at $x/C = 0.07$, numerically studied by Grossi et al. [7] (Fig. 9 in this reference) and compared with the experimental data of Jacquin et al. [8], where the same order of magnitude for the upstream and downstream pressure plateau is observed. A quite good comparison with the experiment is obtained. Therefore, despite the lack of experimental results up to now for the V2C airfoil, a fairly good agreement can be expected between the present CFD and experiments under way in the TFAST project. Moreover, the DDES results of Grossi et al. [7] provide a higher trailing-edge suction than URANS, associated with more intense separation. This feature is a similar tendency to the DDES behaviour of the present study, discussed in section 3.4, as well as with the zonal DES (ZDES) of Deck [6] (Fig. 6 in this reference). The effect of the transition location on the shock-wave position x_s, on the location x_b and length l_b of the separation bubble as well as on the rear separation position x_r are detailed in Table 1 for the complete set of simulations.

The tripping points can be easily identified on the friction coefficient by the sudden and high increase in the wall shear when the boundary layer becomes turbulent. They can also be distinguished on the pressure coefficient in the form of slight pressure disturbances in the supersonic region. As the transition location is shifted downstream, which induced a reduction in the boundary layer displacement thickness, the shock wave moves downstream, which can be noted in Fig. 4,

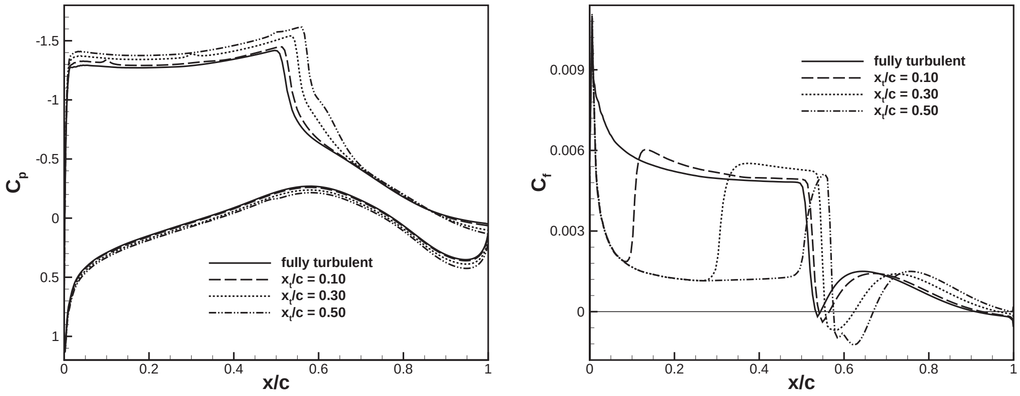

(a) Pressure coefficient

(b) Friction coefficient

Figure 4: Steady surface distributions for selected transition locations at angle of attack of 4°

resulting in a stronger shock wave. As the laminar region increases, the progressively stronger shock wave makes the separation bubble grow continuously as indicated in Table 1 and by means of the C_f distribution. On the contrary, the rear separation gets smaller, yielding a larger pressure recovery and eventually vanishing for $x_t/c \approx 0.5$.

Table 1 provides also the force coefficients as the tripping point is varied. As the length of the laminar region, and thus the shock wave position move downstream, the lift increases due to a higher pressure difference between the upper and lower surfaces. The lift-to-drag ratio L/D is also provided. An optimal value is found near $x_t/c = 0.3$. However, this position of transition does not give the minimum value of the global drag coefficient, which is obtained for a transition located near $x_t/c = 0.10$, with a short laminar boundary layer region. This drag coefficient then increases with a longer laminar region, while the friction drag always diminishes as the laminar region becomes longer.

3.2.2. Unsteady regime

This study has been carried out to assess the influence of the transition point on the properties of the well-developed buffeting flow at 7.0°. Besides the fully-turbulent case, three tripping locations have been considered: $x_t/c = 0.09$, 0.16 and 0.24. For the latter, the most upstream position of the shock wave during buffet has been of about $x_t/c = 0.25$. This limits the displacement of the tripping point, because imposing $\nu_t = 0$ inside the shock-motion region would not be an

x_t/c	fully turb.	0.10	0.20	0.30	0.40	0.50
x_s/c	0.523	0.532	0.541	0.552	0.564	0.574
x_b/c	0.533	0.541	0.547	0.556	0.566	0.575
l_b/c (%)	1.1	2.4	4.7	6.8	8.5	9.4
x_r/c	0.911	0.925	0.946	0.965	0.981	–
C_L	0.8873	0.9174	0.9556	0.9919	1.029	1.061
$C_{D_f} \times 10^2$	0.610	0.574	0.510	0.460	0.396	0.334
$C_D \times 10^2$	2.080	2.069	2.102	2.171	2.268	2.365
L/D	42.7	44.3	45.5	45.7	45.4	44.9

Table 1: Transition location effect on the shock position, on separation and on the global aerodynamic coefficients

acceptable approximation.

Fig. 5(a) presents the statistical pressure distributions obtained for each boundary layer tripping position. While the most upstream limit of the shock-motion range is not much sensitive to the transition location, its most downstream limit is strongly affected by the boundary layer state. As seen for the case $\alpha = 4.0°$, a larger extent of laminar boundary layer tends to move the shock wave further downstream by altering the displacement thickness distribution around the airfoil. In fact, this effect can also be observed in the unsteady case regarding the mean shock-wave position, which roughly corresponds to the point of maximum pressure unsteadiness in Fig. 5(b). As the tripping point is placed downstream, the amplitude of shock motion becomes wider, increasing the fluctuation levels in the shock-wave region as well as the trailing edge unsteadiness. This can be observed in the series presented in Fig. 6, in terms of statistical pressure fluctuation fields. Comparing the fully-turbulent simulation with the case of the most downstream transition location ($x_t/c = 0.24$), the pressure unsteadiness increases by approximately 20% in the shock region and gets nearly two times larger near the trailing edge. The development of the shock-motion area as a function of the transition location is clearly visible in Fig. 6. In the last section of the article, an optimisation of the transition location effect has been carried out in respect of increasing aerodynamic performance.

Table 2 gives the average lift, drag and pitching moment coefficients for the three transition cases as well as for the fully-turbulent computation. The standard deviation σ of the aerodynamic forces is also presented. As for the steady flow at 4.0°, the values of the mean lift and of the moment magnitude inscrease

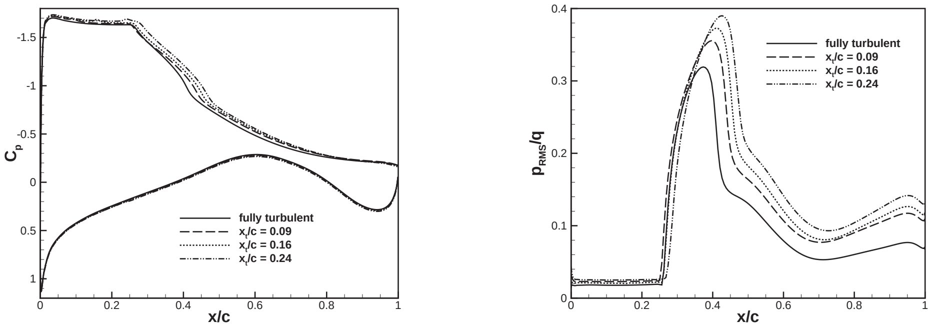

(a) Mean pressure coefficient (b) RMS value of pressure on the upper surface

Figure 5: Transition location effect on the statistical wall pressure at $\alpha = 7.0^{\circ}$

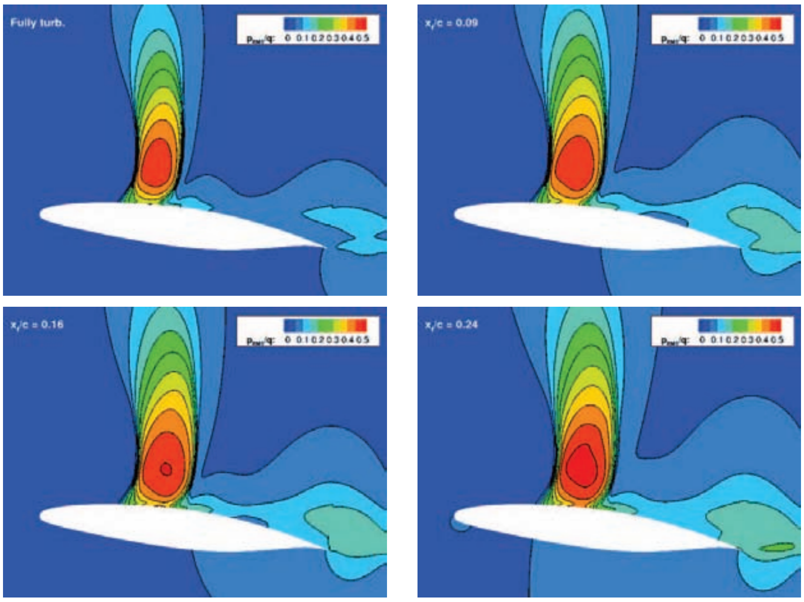

Figure 6: RMS pressure fields for different transition locations at $\alpha = 7.0^{\circ}$

x_t/c	Fully turb.	0.09	0.16	0.24
$\overline{C_D} \times 10^2$	6.163	6.501	6.604	6.715
$\sigma(C_D) \times 10^2$	0.9419	1.250	1.384	1.533
$\overline{C_L}$	0.9423	0.9718	0.9927	1.018
$\sigma(C_L)$	0.0854	0.1047	0.1132	0.1204
$\overline{C_m} \times 10^2$	-4.223	-4.932	-5.267	-5.676
$\overline{C_L}/\overline{C_D}$	15.3	14.9	15.0	15.2

Table 2: Transition location effect on the mean global coefficients, lift, drag and moment, for the unsteady

as the triggering location moves towards the trailing edge. A slight augmentation in the mean drag is also noticed. As a result of the increasing shock-motion amplitude and of the overall flow unsteadiness, the standard deviations of the lift and drag coefficients also become larger as the extent of laminar boundary layer gets longer. Therefore the mean lift over mean drag ratio doesn't show much improvement whereas the laminar region is inscreased. Indeed, as the transition is located closer to the shock wave/boundary layer interaction, the boundary layer downstream detaches more easily than the fully-turbulent case, which gave here the higher lift-to-drag ratio. Moreover, due to the high angle of attack, the most upstream shock location is near 25% of the chord, which limits the flexibility on the transition position.

3.3. Optimisation of the tripping location

3.3.1. Problem description

As observed in the results above, the location of the transition point may have a significant impact on the airfoil performance, in particular when unsteady boundary-layer/shock interactions occur. From designer point of view, it would be interesting to quantify this influence for the different cases (steady and unsteady) and determine the best tripping location, which maximises the airfoil performance. In this perspective, a study is presented for the optimisation problem formulated as:

$$\text{Maximise } f(x) = \overline{C_L/C_D} \text{ for } x \in I, \tag{5}$$

where x is the stripping location and I the allowed search interval. This is a PDE-constrained optimisation problem including a single parameter. The major difficulty arises from the computational cost related to the unsteady flow simulations and the possible noisy prediction of the performance due to the presence of nu-

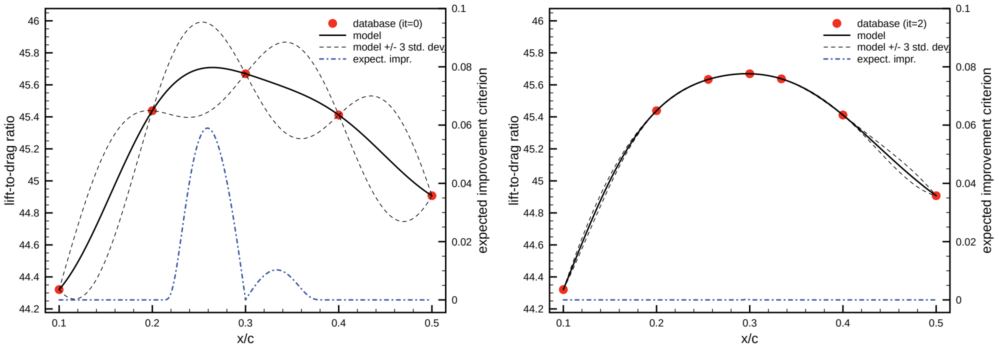

Figure 7: Statistical model for the lift-to-drag ratio with regards to the tripping location (steady case), for iteration 0 (left) and iteration 2 (right)

merical errors (discretization, time integration). The use of a classical descent optimisation method is tedious, due to the unsteady functional gradient estimation. Alternatively, stochastic approaches like genetic algorithms or evolution strategies require too many evaluations to be practically tractable.

3.3.2. Results for the steady case

A steady flow problem is first considered, corresponding to the 2D case described above for an incidence $\alpha = 4.0^\circ$. In this context, the performance is simply the lift-to-drag ratio computed at convergence. The tripping location can vary in the interval $I = [0.1c, 0.5c]$. Five configurations, corresponding to $x_1 = 0.1c$, $x_2 = 0.2c$, $x_3 = 0.3c$, $x_4 = 0.4c$ and $x_5 = 0.5c$, are achieved independently to construct a first database. A Gaussian Process model for the lift-to-drag ratio function is then constructed according to the previous section and illustrated by Fig. 7. On this figure, one can see the model itself, its associated standard deviation and the expected improvement (EI) criterion used to drive the search and select the next point to simulate. As can be seen, after two additional simulations, the standard deviation is strongly reduced and the expected improvement almost zero. Moreover, the next point to simulate, as proposed by the EI criterion, is very close to a know point and the mesh accuracy for the tripping point location is reached. As consequence, the optimisation process is stopped. Finally, two conclusions can be drawn from this optimisation exercise: a large area, from $x = 0.25c$ to $x = 0.35c$ corresponds to a very high lift-to-drag ratio, and the best performance is obtained for a tripping location close to $x = 0.3c$.

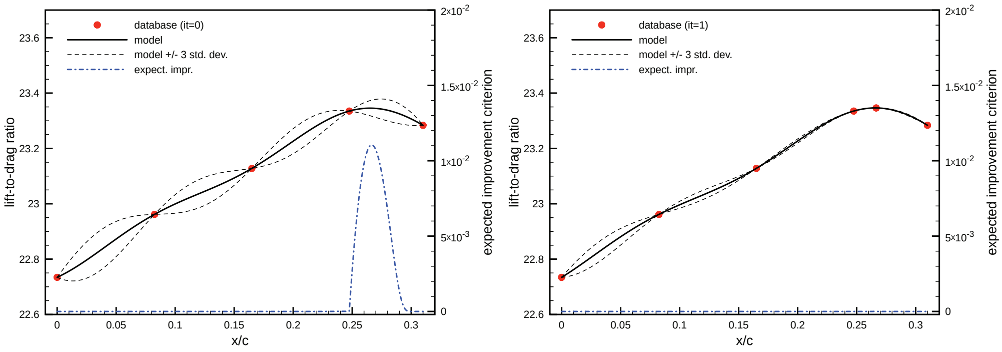

Figure 8: Statistical model for the lift-to-drag ratio regarding the tripping location (unsteady case), for iteration 0 (left) and iteration 1 (right)

3.3.3. Results for the unsteady case

We consider then the more challenging case corresponding to unsteady flows, for which shock-wave/boundary-layer interactions generate buffets. This study has been carried at an incidence of $\alpha = 5.8°$. In this case, the shock-motion amplitude is limited and allows for a wider range of transition locations than at higher incidence. Here, the performance function is the time-averaged lift-to-drag ratio, computed once a quasi-periodic flow is obtained. The admissible interval for the tripping point is moved upstream $I = [0, 0.31c]$, to avoid the shock to be located in the laminar area. Five configurations, corresponding to the fully turbulent case $x_1 = 0$, then $x_2 = 0.0825c$, $x_3 = 0.165c$, $x_4 = 0.2475c$ and $x_5 = 0.31c$, are achieved independently to construct a first database. Note that the configuration $x_5 = 0.31c$ exhibits instabilities after a long time integration. For this case, the time-averaging process has been shortened to avoid these phenomena.

Fig. 8 represents the Gaussian Process model for the time-averaged lift-to-drag ratio, at iterations 0 and 1. The initial model (iteration 0) yields an Expected Improvement criterion localized around a maximum at $x_6 = 0.2665c$. This configuration is simulated and added to the database, yielding an updated model (iteration 1). Since the lift-to-drag ratio computed by simulation is very close to the one predicted by the model, the variance of the model is strongly reduced, as well as the Expected Improvement criterion, as soon as the first iteration. Therefore, the optimum tripping value should be close to x_6.

To validate this result, three additional test points (TP) are simulated *a posteriori*, corresponding to $x_1^{TP} = 0.12c$, $x_2^{TP} = 0.2c$, $x_3^{TP} = 0.25c$ and the results

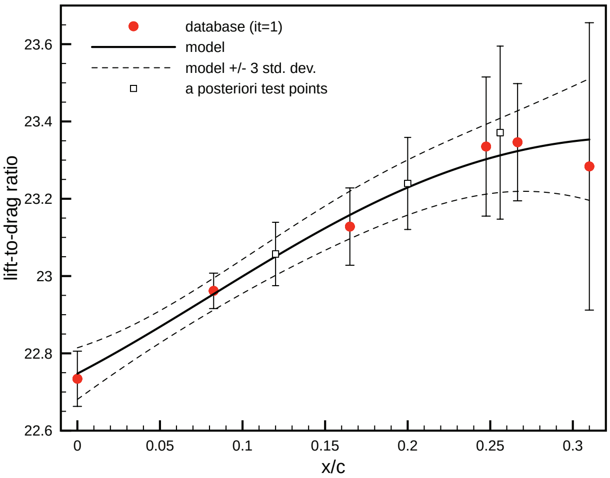

Figure 9: Statistical model for the lift-to-drag ratio as a function of the tripping location (unsteady case), accounting for the observation variance

are compared to the model prediction. It appears that the performance value for x_3^{TP} slightly differs from the model prediction, due to the fact that the unsteady flow exhibits some low frequency oscillations, which make the estimation of the time-averaged lift-to drag ratio more difficult. To account for this uncertainty in the performance estimation, a variance estimate of the time-averaged lift-to-drag ratio is computed for all configurations, by using a classical moving average procedure. This variance is introduced into the Gaussian Process model as an observation noise. Fig. 9 shows the resulting model, that does not interpolate database points anymore, against additional test points. As can be observed, the uncertainty in the performance estimation is not negligible in this context, especially when the tripping point is close to the shock wave location, which corresponds to the best performance area (x between $0.2c$ and $0.3c$). Nevertheless, the statistical model allows having a better analysis of the problem. In particular, one can underline that the confidence interval of the model is smaller than the standard deviation of the observations, in the zone where several points have been computed. In conclusion, for this unsteady case, the airfoil performance is better for a tripping point x between $0.2c$ and $0.3c$, but the corresponding flows exhibit additionnal unsteadiness because of interaction with the existing buffet instability, that could be dommageable in real conditions.

3.4. Three-dimensional simulation of the fully-turbulent case

The DDES-$k-\omega$ SST model has been applied, using the same numerical scheme as the 2D computations and time step $\Delta t = 10^{-7} s$), in order to examine the 3D dynamics of the fully developed transonic buffet occurring over the V2C airfoil at $M_\infty = 0.70$ and $\alpha = 7.0°$. The turbulence length scale provided by the RANS part is computed using local turbulence properties and is given by $\sqrt{k}/(\beta^*\omega)$. A comparison of the DDES results with the URANS $k-\omega$ SST [20] as well as the 2D and 3D OES-$k-\varepsilon$ [5, 21] is provided. Concerning the grid spacing, which has to be nearly isotropic in the LES region, in respect of the DDES choice of the turbulence length scale, 59 cells have been distributed over a $0.33c$ spanwise length with a constant spacing, resulting in a final grid of about 9.65 M cells. The computations have been carried out in the SGI Altix supercomputer at CINES (Centre informatique national de l'enseignement supérieur), by using 1024 parallel processors in MPI.

3.4.1. Flowfield dynamics

The time-dependent lift coefficient according to the aforementioned models is presented in Fig. 10 for the fully established regimes, beyond transient phases. While in URANS $k-\omega$ SST the lift coefficient oscillates quasi-harmonically at a frequency of 82 Hz, the DDES produces sharp-like and much stronger lift fluctuations. The high slope of the curve indicates that the shock-motion speed is relatively high, especially during the lift fall when the flow separates and the shock moves upstream. The predicted buffet frequency in the DDES case is approximately 108 Hz. The large amplitude of the fluctuations suggests existence of modelled-stress depletion (MSD) [15] and indicates that shock-wave motion is wider than in case of the $k-\omega$ SST model. The OES-$k-\varepsilon$ model provides an almost sinusoidal behaviour of the oscillations at 107 Hz and a slightly higher amplitudes than the $k-\omega$ SST. This behaviour is in-between the URANS and DDES evolutions. The spectral analysis of the lift coefficient is shown in Fig. 11, where $\mathrm{St} = f U_O/c$ is the non-dimensionalised frequency, with f the frequency in Hz, $U_O = 228\, m.s^{-1}$ the freestream velocity and $c = 0.25$ the chord of the airfoil. These spectra are similar to the experiments by Jacquin et al. [8, 3] concerning the buffet mode identification for the OAT15A supercritical airfoil configuration in the same Mach and Reynolds number range. Moreover, the OES modelling sensitised to reduce the turbulent diffusion and enhance coherent structure appearance, provides spectra of a similar shape to the study of Szubert et al [5] carried out for the OAT15A, showing the buffet frequency as well as a spectral bump related to the von Kármán mode associated with alternating vortices past the trailing edge,

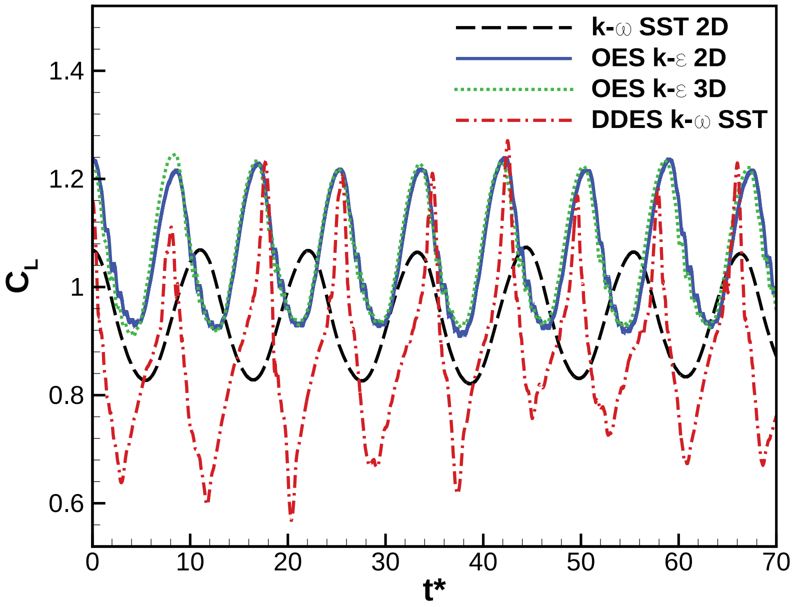

Figure 10: Comparison of the time-dependent evolution of the lift coefficients between URANS $k-\omega$ SST, 2D and 3D OES-$k-\varepsilon$ and DDES-$k-\omega$ SST

as shown in Fig. 17 for the V2C profile. This two-mode interaction sustains a feedback loop including also Kutta waves as shown in this figure, in qualitative comparison with experiments (Fig. 18). This aero-acoustic feedback mechanism was schematically presented in Lee [26].

Table 3 shows the values of the buffet frequency as well as the corresponding Strouhal numbers and mean and RMS values of lift coefficient per turbulence model.

In the spectra, the DDES-$k-\omega$ SST provides the highest continuous spectral level, indicating a lower turbulence diffusion rate predicted by this model (also shown in the turbulent viscosity field as discussed at the end of this section, Fig. 20). The $k-\omega$ SST and OES-$k-\varepsilon$ provide in addition to the main frequency bump corresponding to the buffet instability, bumps beyond 2000 Hz, which are related to the von Kármán instability and other vortex interactions past the trailing edge as discussed in [5]. In all the spectra, the presence of the buffet mode is illustrated by a frequency bump instead of a sharp peak, because of the non-linear interactions of the buffet mode with the von Kármán, shear-layer

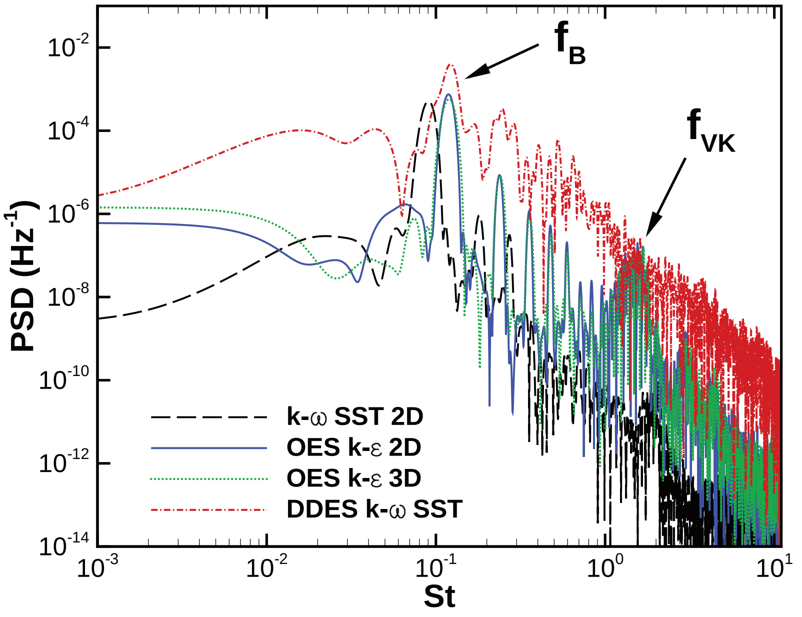

Figure 11: Comparison of the power spectra density of the lift coefficients time-dependent evolution between URANS $k-\omega$ SST, 2D and 3D OES-$k-\varepsilon$ and DDES-$k-\omega$ SST

Turb. model.	$k-\omega$ SST	OES-$k-\varepsilon$ 2D	OES-$k-\varepsilon$ 3D	DDES-$k-\omega$ SST
$\overline{C_D} \times 10^2$	6.163	8.119	8.188	9.106
$\overline{C_L}$	0.942	1.059	1.061	0.875
$\sigma(C_L)$	0.084	0.106	0.106	0.145
RMS(C_L)	0.946	1.067	1.067	0.886
f_B (Hz)	82	107	108	108
St $= f_B\, c/U_0$	0.09	0.118	0.12	0.12

Table 3: Comparison of the aerodynamic coefficients and buffet frequency between turbulence modelling methods for 9 periods of buffeting

and other more random motions downstream. Therefore, the present simulations capture the dynamics of the buffet and near trailing-edge instability modes and of their interaction producing a multitude of frequencies between these modes, which sustain a feedback loop among the shock oscillation region, the separated shear layer and the near wake. These interactions and feedback loop, schematically reported in [26], have been analysed in detail by [5], using time-frequency analysis by means of wavelets and Proper Orthogonal Decomposition in addition to a spectral analysis. Fig. 12 shows the mean surface pressure coefficient. All models are in agreement in the suction side, with a slight increase of lift near the trailing edge in case of OES-$k-\varepsilon$, which corresponds to a higher averaged lift coefficient (Table 3). The $k-\omega$ SST model produces the shortest inclination of the C_p within the shock region and therefore the less developed shock oscillation amplitudes. The largest amplitudes correspond to the DDES-$k-\omega$ SST, as can be implied by the high amplitude lift coefficient oscillations. This feature, accompanied by a higher trailing-edge pressure plateau, is similar to a thicker airfoil's C_p, as for example in the experimental study of McDevitt et al. [1] for a circular-arc airfoil in transonic regime, as well as in the ZDES of Deck [6] (Fig. 6 in this reference) and in the DDES-Spalart-Allmaras study of Grossi et al. [7] (Fig. 9 of this reference). This common tendency occurs among these approaches using different numerical schemes (the AUSM in Deck's study, the 3$^{\text{rd}}$ order Roe upwind scheme in Grossi's study as well as in the current study). Therefore, it seems that the hybrid RANS-LES models provide a higher level of suction and flow detachment in the present family of supercritical airfoils. This behaviour can be explained by means of turbulent viscosity levels of the three modelling approaches used in the present study and by considering the frontier between the URANS and LES regions, commented in a dedicated discussion at the end of this section. The OES-$k-\varepsilon$ produces an in-between behaviour, similar to the flow simulations around the supercritical OAT15A airfoil with fixed transition at 7% (Szubert et al. [5]) which compare quite well to experimental results by Jacquin et al. [8, 3]. Therefore, it can be reasonably supposed that in the V2C case, a fairly good comparison of the present URANS studies (better than the DDES behaviour) is expected from the ongoing experimental campaign in the TFAST project.

Fig. 13 shows the mean pressure fields superimposed with streamlines according to the previous models. The DDES illustrates the largest separation area and the OES indicates a higher circulation intensity, corresponding to the lift increase. The $k-\omega$ SST and OES-$k-\varepsilon$ provide qualitatively comparable recirculation regions. The same feature stands for the mean velocity profiles shown in Fig. 14, in the near-wall region concerning the locations $x/c = 0.2$, 0.4, 0.6 and 0.8. In the

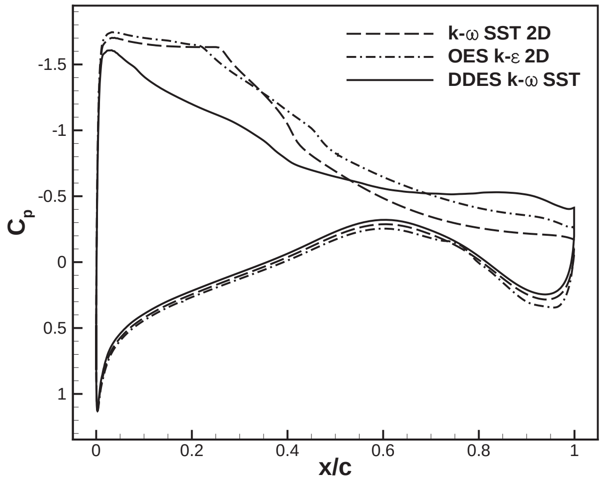

Figure 12: Comparison of the wall pressure coefficient between URANS $k-\omega$ SST, OES-$k-\varepsilon$ and DDES-$k-\omega$ SST

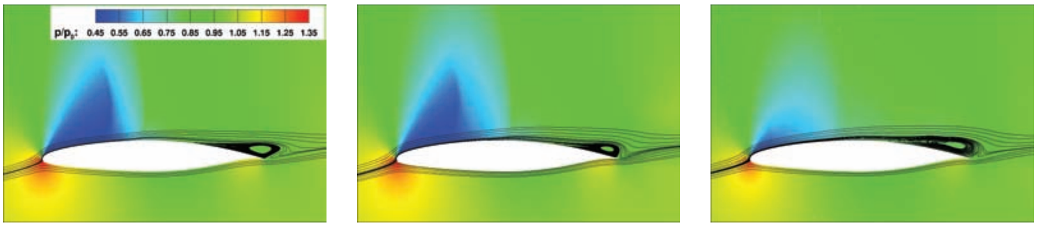

(a) URANS $k-\omega$ SST (b) OES-$k-\varepsilon$ (c) DDES-$k-\omega$ SST

Figure 13: Mean pressure fields and streamlines around the profile

intermediate region at $x/c = 0.4$, the $k-\omega$ SST shows a narrower boundary-layer thickness. The DDES illustrates the wider shock motion, yielding to a less expanded velocity profile at $x/c = 0.2$ and a much more separated one at $x/c = 0.8$ than the other two models.

A series of flow snapshots is presented in Fig. 15 for one period of buffet in the case of the DDES-$k-\omega$ SST. It helps understanding the dynamics of the flow predicted. The figures illustrate instantaneous isosurfaces of non-dimensional Q-criterion for $Q(c/U)^2 = 75$ as a function of the non-dimensional time $t^* = tU/c$, where $t^* = 0$ is an instant of maximum lift. Surfaces are colored with the Mach number. During the upstream travel of the shock (Fig. 15(a)), alternate vortex

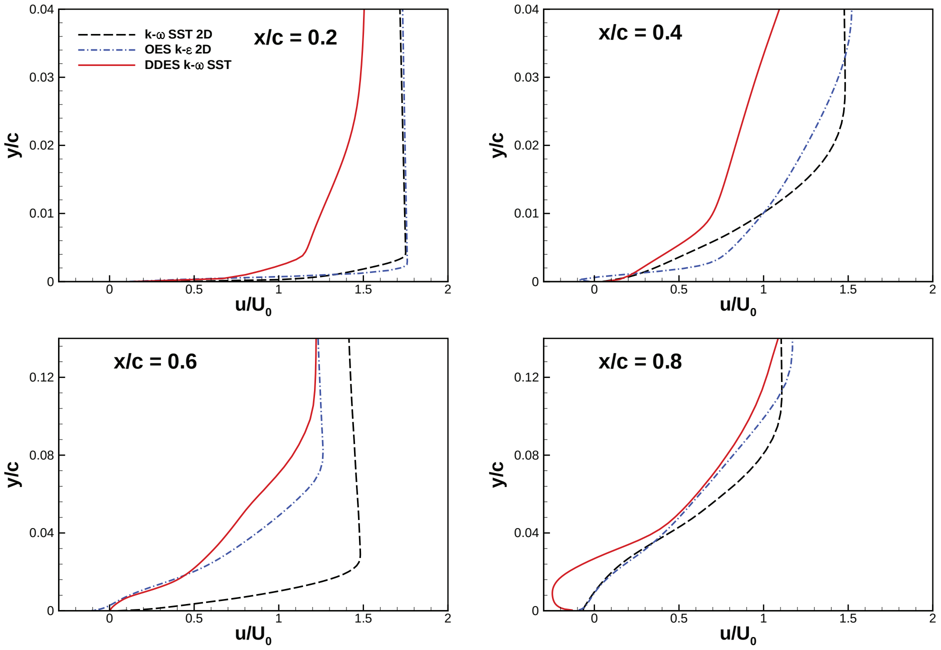

Figure 14: Mean velocity profiles at locations $x_t/c = 0.2$, 0.4, 0.6 and 0.8 for URANS $k-\omega$ SST, OES-$k-\varepsilon$ and DDES-$k-\omega$ SST

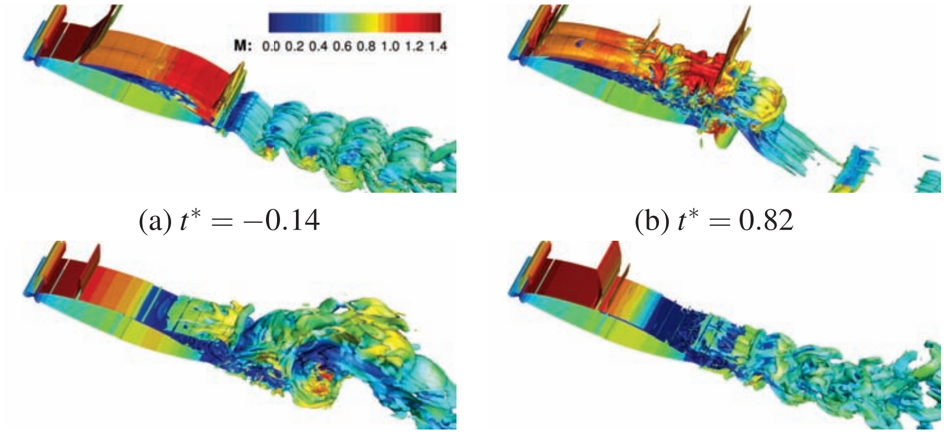

(a) $t^* = -0.14$ (b) $t^* = 0.82$

(c) $t^* = 3.28$ (d) $t^* = 4.92$

Figure 15: Instantaneous Q-criterion isosurfaces for $Q(c/U)^2 = 75$

shedding can be observed at the trailing edge. The primary structures are always three-dimensional. As the shock approaches the leading edge, the flow over the upper surface gets fully separated and the shear layer becomes unstable (Fig. 15(b)). Such intense separation generates a large wake combining the eddies produced in the shear layer and the trailing edge structures. As the shock and the separation point move downstream, the height and streamwise extension of the separation region decrease and the amount of resolved flow structures reduces as seen in the sequence in Fig. 15(c). Unlike in URANS, a considerable amount of separation always exists on the rear part of the airfoil. While the shear layer becomes stable as the shock wave approaches its most downstream position, the alternate vortex shedding at the trailing edge is always present during buffet (Fig. 15(d)).

A series of mid-span plane snapshots is presented in Fig. 16 and in Fig. 17 for one period of buffet regarding the DDES-$k-\omega$ SST and the OES-$k-\varepsilon$ respectively. These instantaneous fields are similar to Schlieren visualisations and illustrate the shock motion, the Kutta waves travelling from the trailing edge to upstream positions, the von Kármán vortices past the trailing edge and the smaller-scale Kelvin-Helmholtz vortices in the separated shear layers, among other more chaotic vortex structures. The DDES-$k-\omega$ SST simulations provide a quite rich turbulence content and a large shock motion and separation regions, extended near the leading edge. The OES-$k-\varepsilon$ provides a shorter shock-motion amplitude

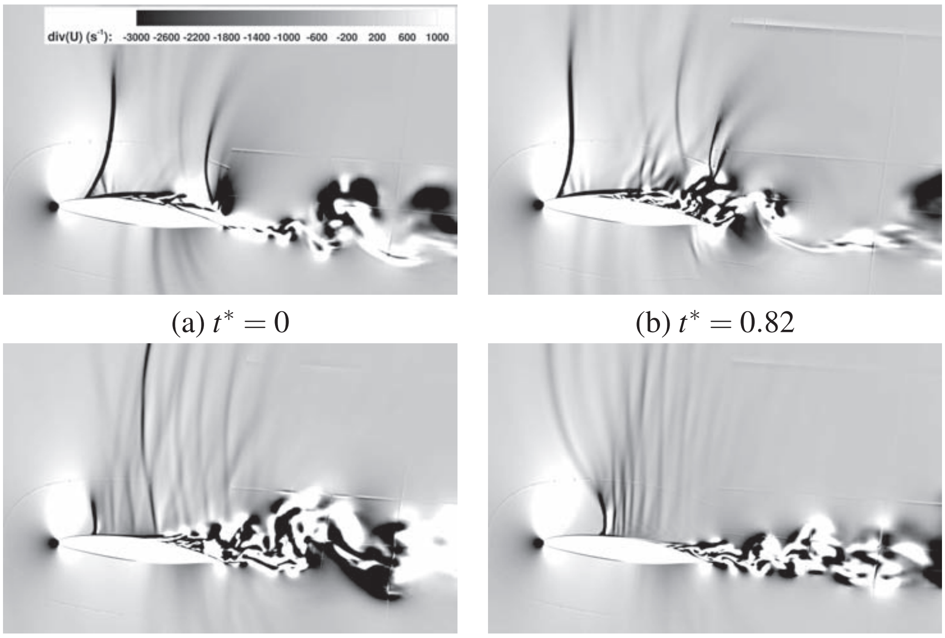

(a) $t^* = 0$ (b) $t^* = 0.82$

(c) $t^* = 3.28$ (d) $t^* = 4.92$

Figure 16: Divergence of velocity field - DDES-$k-\omega$ SST

and a visualization of the compressibility effects in qualitative agreement with D. W. Holder [27], Fig. 18.

In order to understand the DDES behaviour which provided such a large separation, the distribution of the RANS and LES regions has been monitored allowing assessment of the present DDES ability to switch between the two modes (URANS and LES) during buffet and of the size of the two regions. The instantaneous distributions of the delaying function $1-f_d$ of the DDES at four phases of buffet are given in Fig. 19. The irregular black areas over the upper surface indicate large regions of separation, even when the shock is at its most downstream position (Fig. 19(d)), where a large amount of rear separation exists on the upper surface. This analysis shows the existence of a RANS-mode layer covering the near-wall region around the V2C airfoil. The overall height of this layer seems to be relatively small. This might cause some degree of MSD [15] due to the erroneous penetration of the LES mode into attached boundary layers, which facilitates separation. This behaviour was also observed in the DDES studies by

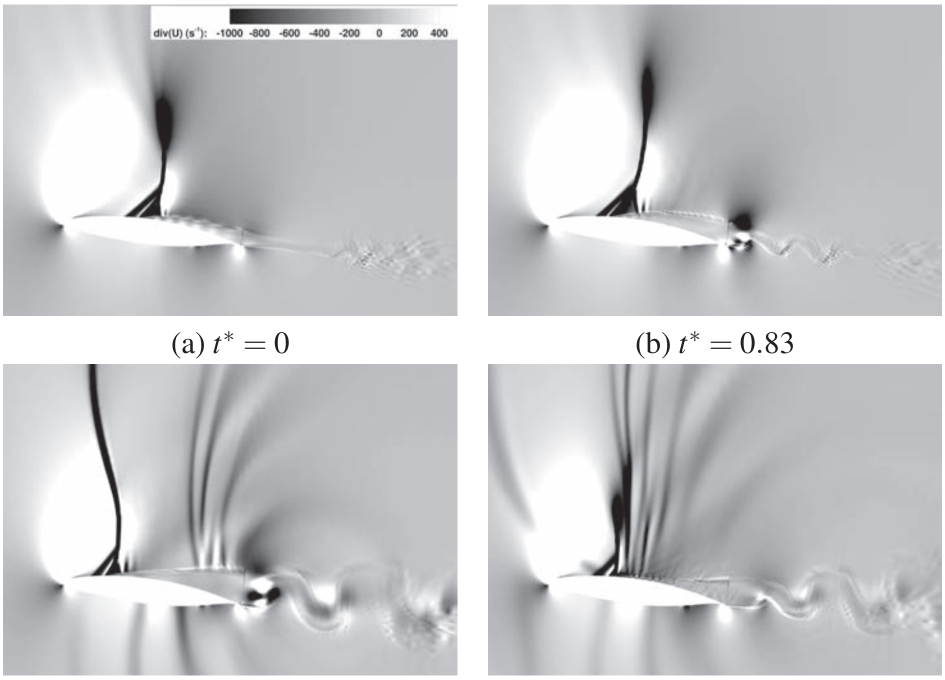

(a) $t^* = 0$ (b) $t^* = 0.83$

(c) $t^* = 3.28$ (d) $t^* = 4.92$

Figure 17: Divergence of velocity field - OES-$k-\varepsilon$

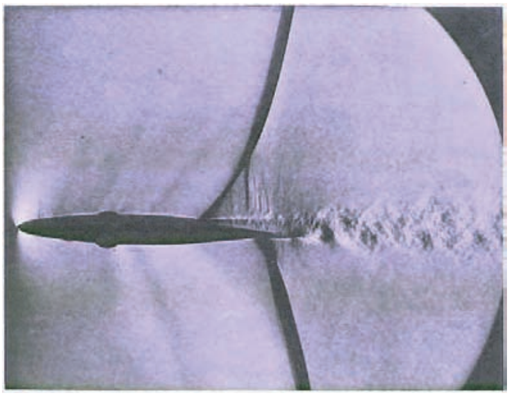

Figure 18: Schlieren photograph of the eddying wake following a shock-induced flow separation (Courtesy of National Physical Laboratory, England; study by Duncan et al. [28]; photo by D. W. Holder)

Deck [29] improved by a zonal DES approach. In this article, Fig. 19, the development of the shear layer instabilities appear at a considerable distance past the separation point, whereas in our case they appear earlier (Fig. 15). The article also by Uzun et al. [30] has been referenced thanks to a clear representation of the f_d function delimiting the RANS region in the boundary layer around the body (Fig. 7 in their study), which is similar to the behaviour of this function in the present study and the fact that the shear layers past the cylinder are treated by LES in that study. In addition, these shear layers (Fig. 8 in that paper) display the instability development at a considerable distance downstream of the separation point in respect of the appearance of Kelvin-Helmholtz vortices. The same behaviour was reported by Mockett et al. [31] concerning the acceleration of the transition between RANS and LES in a free shear layer by various DES approaches. The present DDES behaviour illustrated by the previous flow visualisations, the mean C_p and lift coefficients can be explained as follows: the pressure near the trailing edge (Fig. 12) is underestimated in the case of DDES, displaying a significant suction comparing with the URANS cases. The DDES provides a higher shock's excursion from the leading edge up to more than half of the chord yielding a pressure increase in this area. Therefore, the resulting lift is lower than in URANS and consequently, the corresponding circulation is lower.

In this case, the pressure aspiration effect on the suction side and the overall separated region seems to be more intense than in other cases. The related instabilities are more pronounced and start more upstream in the shear layers than in cases where the excursion of the shock has a shorter amplitude. These results are not linked to a strong delay in the formation of instabilities in the shear layer and in the overall suction region but on a too early onset of instabilities. This is viewed in the 3D plots of Fig. 15 where a strong and rich statistical content of vortices are developed in the suction area from practically the leading edge. Indeed, the difference between the "peaky" shape and the more "sinusoidal" one indicates that at the same instant, the lift is lower in the DDES case, upstream and downstream of the sharp peak. This behaviour is in accordance with the "peaky" shape of the lift coefficient displayed by the DDES-SST, comparing to the OES simulations (Fig. 10). This is in accordance with the aforementioned elements concerning the pressure distribution and the mean lift. The reasons for this can be as follows. In Fig. 19, the frontier between RANS and LES regions are shown. It can be seen that a significant part of the shear layer is handled by RANS computation (see dark zone past the separation point), but this does not inhibit the development of instabilities which are quite displayed in the upstream region. Moreover, the dark region surrounding the airfoil near the wall is associated with RANS computation within the boundary layer. Therefore, the LES approaches drastically the wall region. This would need a finer grid in this area. Moreover, the reason for the DDES behaviour, also depicted by another partner (URMLS) within the TFAST European program (M. Bernardini, S. Pirozzoli, private communication), by using DDES-SA and a different numerical code, may be due to the turbulent viscosity produced by the model in association with the grid. In order to illustrate the effect of the turbulent viscosity produced by the turbulence model, the ratio ν_t/ν is plotted in Fig. 20. It can be seen that the DDES produces a much lower turbulence viscosity (order of 200 in the separated regions) than the URANS-OES (order of 1800), leading to a lower dissipation level which excessively amplifies smaller-scale structures in the separated area and a more intense separation. In the OES case, the higher ν_t level improves this feature. The use of the Spalart-Allmaras model instead of the $k-\omega$ SST in the DDES provided even higher shock amplitude oscillations because the maximum ratio ν_t/ν was of order 250 [32], Fig. 6.15 in this reference. This behaviour was shown for the lift oscillation in [33], Fig. 13. As can be shown in the lift oscillations, the 'peaky' behaviour disappears on the benefit of a more sinusoidal shape with a higher pressure plateau up to 30% of the chord, a shorter excursion of the shock as well as an improved effect on the pressure 'plateau' near the trailing edge with less suction (see Fig. 12).

In a study in progress, the OES-$k-\varepsilon$ model results will be analysed in detail, in order to take benefit from the more regular buffet oscillations and simultaneously from the formation of the additional frequency bumps shown in Fig. 11, as in the study by Szubert et al. [5].

(a) Maximum lift ($t^* = 0$) (b) Shock upstream ($t^* = 1.46$)

(c) Minimum lift ($t^* = 2.96$) (d) Shock downstream ($t^* = 6.02$)

Figure 19: RANS and LES regions around the V2C airfoil according to the DDES-$k-\omega$ SST

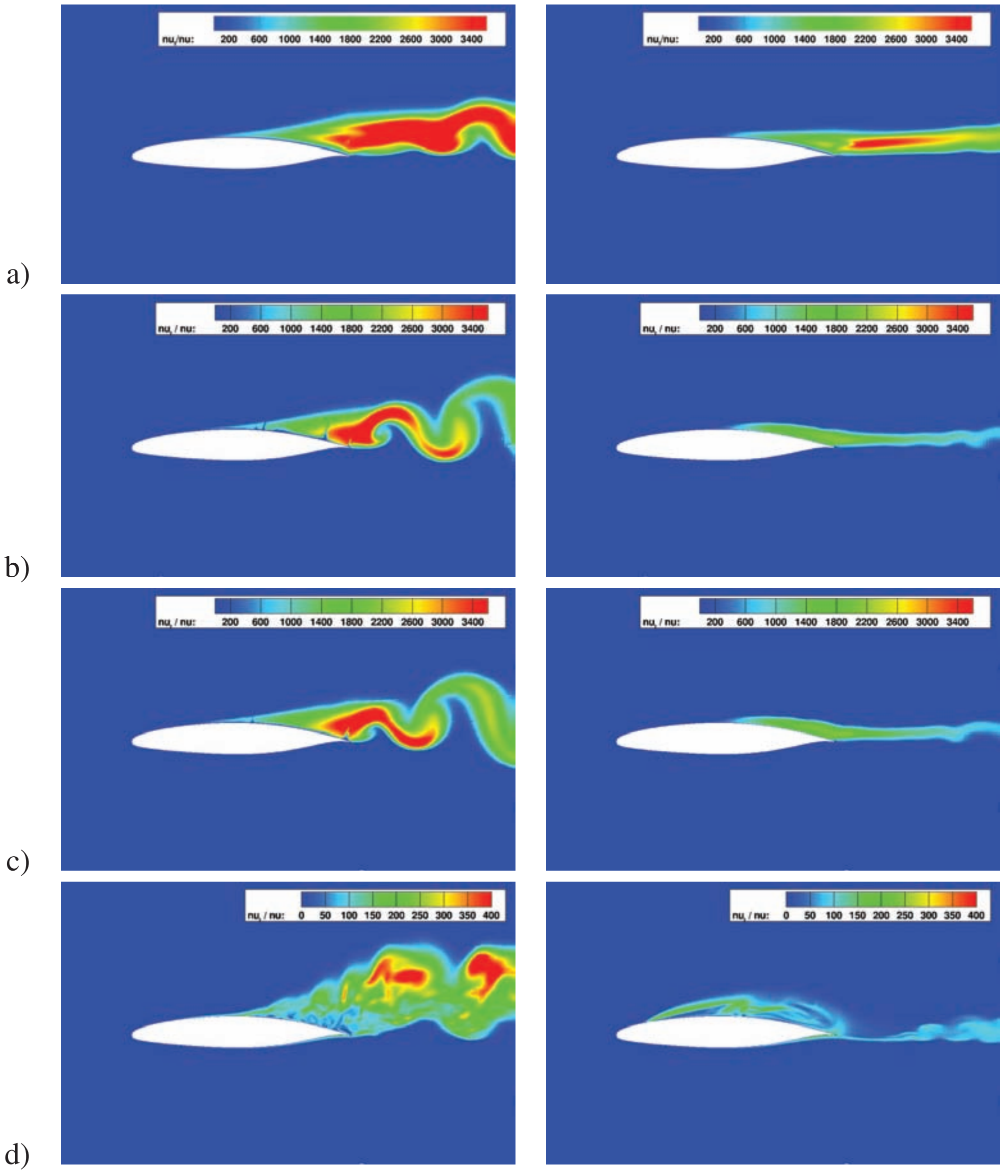

Figure 20: Comparison of the turbulence viscosity field between URANS $k-\omega$ SST (a), 2D (b) and 3D (c) OES-$k-\varepsilon$ and DDES-$k-\omega$ SST (d) at minimum (left) and maximum (right) lift

4. Conclusion

The present study analysed the SWBLI in the case of the transonic flow around the V2C-Dassault Aviation profile in two and three dimensions by means of statistical and hybrid RAND-LES turbulence modelling in the high Reynolds number regime of 3.245 million. The critical range of angle of attack for the buffet appearance has been investigated by means of 2D URANS computations and found near 5.5°. The different flow phenomena occurring around the airfoil for various angles of attack at Mach number 0.70 have been analysed. The pressure and skin friction distributions have shown the angle of attack effect on the shock wave position, as well as on the state of the boundary layer interaction with the shock foot. The influence of a fixed transition location on the flow physics has been studied in the steady and unsteady cases and particularly on the buffet dynamics. Based on these results, a major outcome is a non-classical optimisation procedure coupling the CFD results with a Kriging method, applied to the transition location regarding the averaged aerodynamic coefficients. In the steady case, an optimal position of the fixed transition has been found near $x_t/c = 0.30$ regarding the averaged lift/drag ratio. Particularly, the transition location effect on the unsteady case with buffeting conditions (angle of attack of 5.8°) has been analysed with the same method and yields an optimum position at $x_t/c = 0.2665$. These elements contribute to the improvement of laminar wing design for future generation of aircraft's wings, in respect of the greening requirements of the *Horizon 2020* objectives. Furthermore, the flow dynamics of a fully developed buffet case at angle of incidence of 7.0° have been investigated in respect of the predictive abilities of statistical and hybrid turbulence modelling. The DDES simulations displayed a rich content of resolved flow structures and provided a strongly detached flow and a large shock amplitude, extended from the leading to the trailing edge. This behaviour has been analysed and discussed in respect the MSD and eddy-viscosity levels induced by this modelling associated to the present grid and numerical parameters. The URANS simulations based on the $k-\omega$ SST model have indicated a high turbulence diffusion level and a decrease in the appearance of instabilities pas the trailing edge, as well as a short shock amplitude. The OES approach provided an intermediate behaviour between the two mentioned with a reasonably extended shock amplitude and capturing of the von Kármán and shear-layer vortices donwstream of the SWBLI and of the trailing edge. In a study in progress, the association of DDES with OES will be examined in order to take relative benefits from both approaches.

Acknowledgements

The present work was supported by the TFAST European project N°265455 – Transition location effect on shock-wave/boundary-layer interaction. The research team thankfully acknowledges the French computing centers CINES (Centre informatique national de l'enseignement supérieur) and CALMIP (Calcul en Midi-Pyrénées) for the allocated resources as well as for their availability. They thank Matteo Bernardini and Sergio Pirozzoli for their valuable discussions about the turbulence modelling behaviour in the context of the TFAST collaboration.

References

[1] J. B. McDevitt, L. L. Levy Jr., G. S. Deiwert, Transonic flow about a thick circular-arc airfoil, AIAA Journal 14 (5) (1976) 606–613.

[2] H. L. Seegmiller, J. G. Marvin, L. L. Levy Jr., Steady and unsteady transonic flow, AIAA Journal 16 (12) (1978) 1262–1270.

[3] L. Jacquin, P. Molton, S. Deck, B. Maury, D. Soulevant, Experimental study of shock oscillation over a transonic supercritical profile, AIAA Journal 47 (9) (2009) 1985–1994.

[4] B. H. K. Lee, Oscillatory shock motion caused by transonic shock boundary-layer interaction, AIAA Journal 28 (5) (1990) 942–944.

[5] D. Szubert, F. Grossi, A. Jimenez Garcia, Y. Hoarau, J. C. R. Hunt, M. Braza, Shock-vortex shear-layer interaction in the transonic flow around a supercritical airfoil at high reynolds number in buffet conditions, Journal of Fluids and Structures 55 (2015) 276–302.

[6] S. Deck, Numerical computation of transonic buffet over a supercritical airfoil, AIAA Journal 43 (7) (2005) 1556–1566.

[7] F. Grossi, M. Braza, Y. Hoarau, Prediction of transonic buffet by delayed detached-eddy simulation, AIAA Journal 52 (2014) 2300–2312.

[8] L. Jacquin, P. Molton, S. Deck, B. Maury, D. Soulevant, An experimental study of shock oscillation over a transonic supercritical profile, in: 35^{th} AIAA Fluid Dynamics Conference and Exhibit, Toronto, Ontario, Canada, 2005, AIAA 2005-4902.

[9] Cleansky European project, Call 11 - GRA-02-019, “Advanced, high aspect ratio transonic laminar wing for regional aircraft with load controll & alleviation devices” (2013-2016).

[10] M. Belisle, M. Roberts, T. Williams, M. Tufts, A. Tucker, W. Saric, H. Reed, A transonic laminar-flow wing glove flight experiment: Overview and design optimization, in: 30th AIAA Applied Aerodynamics Conferenceth AIAA Applied Aerodynamics Conference, New Orleans, LA, 2012.

[11] A. Bouhadji, M. Braza, Organised modes and shock–vortex interaction in unsteady viscous transonic flows around an aerofoil: Part I: Mach number effect, Computers & Fluids 32 (9) (2003) 1233–1260.

[12] S. Bourdet, A. Bouhadji, M. Braza, F. Thiele, Direct numerical simulation of the three-dimensional transition to turbulence in the transonic flow around a wing, Flow, Turbulence and Combustion 71 (1-4) (2003) 203–220.

[13] L. L. Levy Jr., Experimental and computational steady and unsteady transonic flows about a thick airfoil, AIAA Journal 16 (6) (1978) 564–572.

[14] P. R. Spalart, W.-H. Jou, M. Strelets, S. R. Allmaras, Comments on the feasibility of LES for wings, and on a hybrid RANS/LES approach, in: C. Liu, Z. Liu (Eds.), Advances in LES/DNS, Greyden Press, Louisiana Tech University, 1997, pp. 137–147.

[15] P. R. Spalart, S. Deck, M. L. Shur, K. D. Squires, M. K. Strelets, A. Travin, A new version of detached-eddy simulation, resistant to ambiguous grid densities, Theoretical and Computational Fluid Dynamics 20 (6) (2006) 181–195.

[16] M. L. Shur, P. R. Spalart, M. K. Strelets, A. K. Travin, A hybrid RANS-LES approach with delayed-DES and wall-modelled LES capabilities, International Journal of Heat and Fluid Flow 29 (6) (2008) 1638–1649.

[17] J. D. Crouch, L. L. Ng, Variable N-factor method for transition prediction in three-dimensional boundary layers, AIAA Journal 38 (2) (2000) 211–216.

[18] P. L. Roe, Approximate Riemann solvers, parameter vectors, and difference schemes, Journal of Computational Physics 43 (2) (1981) 357–372.

[19] B. van Leer, Towards the ultimate conservative difference scheme. V. A second-order sequel to Godunov’s method, Journal of Computational Physics 32 (1) (1979) 101–136.

[20] F. R. Menter, Two-equation eddy-viscosity turbulence models for engineering applications, AIAA Journal 32 (8) (1994) 1598–1605.

[21] R. Bourguet, M. Braza, G. Harran, R. El Akoury, Anisotropic organised eddy simulation for the prediction of non-equilibrium turbulent flows around bodies, Journal of Fluids and Structures 24 (8) (2008) 1240–1251.

[22] P. R. Spalart, C. L. Rumsey, Effective inflow conditions for turbulence models in aerodynamic calculations, AIAA Journal 45 (10) (2007) 2544–2553.

[23] D. R. Jones, M. Schonlau, W. J. Welch, Efficient global optimization of expensive black-box functions, Journal of Global Optimization 13 (4) (1998) 455–492.

[24] J. Sacks, W. J. Welch, T. J. Mitchell, H. P. Wynn, Design and analysis of computer experiments, Statistical Science 4 (4) (1989) 409–423.

[25] V. Picheny, D. Ginsbourger, Y. Richet, Noisy expected improvement and on-line computation time allocation for the optimization of simulators with tunable fidelity, in: 2nd Int. Conf. on Engineering Optimization, 2010.

[26] B. H. K. Lee, Self-sustained shock oscillations on airfoils at transonic speeds, Progress in Aerospace Sciences 37 (2) (2001) 147–196.

[27] Y. C. Fung, An Introduction to the Theory of Aeroelasticity, Dover, 2002, Schlieren picture page 313 by D. W. Holder, National Physical Laboratory, England.

[28] W. J. Duncan, L. Ellis, C. Scruton, First report on the general investigation of tail buffeting, British Aeronautical Research Committee R&M-1457 1457 (1932) part I.

[29] S. Deck, Recent improvements in the zonal detached eddy simulation (zdes) formulation, Theoretical and Computational Fluid Dynamics 26 (6) (2012) 523–550.

[30] A. Uzun, M. Y. Hussaini, An application of delayed detached eddy simulation to tandem cylinder flow field prediction, Computers & Fluids 60 (2012) 71–85.

[31] C. Mockett, M. Fuchs, A. Garbaruk, M. Shur, P. Spalart, M. Strelets, F. Thiele, A. Travin, Two non-zonal approaches to accelerate rans to les transition of free shear layers in des, in: Progress in Hybrid RANS-LES Modelling, Vol. 130 of Notes on Numerical Fluid Mechanics and Multidisciplinary Design, Springer, 2015, pp. 187–201.

[32] F. Grossi, Physics and modeling of unsteady shock wave/boundary layer interactions over transonic airfoils by numerical simulation, Ph.D. thesis, INP Toulouse (2014).

[33] D. Szubert, F. Grossi, Y. Hoarau, M. Braza, Hybrid RANS-LES and URANS simulations of a laminar transonic airfoil, in: Progress in Hybrid RANS-LES Modelling, College Station, TX, 2014, pp. 329–343.

Chapter 4

Numerical study of an oblique-shock/boundary-layer interaction

This study is also carried out in the context of the TFAST European project. The oblique-shock/boundary-layer interaction in one of the test cases handles by the programme, among with normal-shock/boundary-layer interaction, turbine and compressor blades and a laminar airfoil in transonic speed presented and studied in the previous chapter (section 3.2 page 3.2). The Center for Turbulence Research summer program 2014 was a great opportunity for a collaboration between the researchers and students working there and our team, exchanging our knowledge, skills and opinion on the methods and strategies handled by each team, as well as other invited researchers. This programme leads to an substantial number of proceedings available online[1]. The paper presenting the results from wall-modelled LES on the CTR side, and from delayed-detached eddy simulation on our side (Szubert et al., 2014b), has been included in this manuscript, from the following page.

---

[1] ctr.stanford.edu/publications.html

Center for Turbulence Research
Proceedings of the Summer Program 2014

Numerical simulations of oblique shock/boundary-layer interaction at a high Reynolds number

By D. Szubert†, I. Jang, G. I. Park AND M. Braza†

This study investigates numerical analysis of the oblique shock/boundary-layer interaction (OSBLI) in a Mach 1.7 flow with a unit Reynolds number of 35 million. Two methods of simulations are performed and compared with an experiment. While two different delayed detached-eddy simulations (DDES) are performed to simulate the full-span geometry, a wall-modeled large-eddy simulation (WM-LES) is carried out to study the physics near the mid-span area. In the experiment, the boundary layer is tripped at the leading edge of the flat plate to ensure fully turbulent boundary layer at the interaction zone. The tripping device in the WM-LES computations was simulated by artificial blowing and suction, while in the DDES simulation turbulence is generated by a Reynolds-Averaged Navier-Stokes (RANS) model and its intensity is adjusted to match the experimental one. Challenges to simulate this test case as well as comparison between the two numerical studies with the experimental results a re highlighted in this paper.

1. Introduction

Research for more effective transport systems and the reduction of emissions, which places severe demands on aircraft velocity and drag reduction, is intense. In order to diminish the shock-induced separation, the boundary layer at the point of interaction should be turbulent. However, the greening of air transport systems means a reduction of drag and losses, which can be obtained by keeping laminar boundary layers on external and internal airplane parts. Therefore, it is very important to develop predictive capabilites of shock-wave/boundary-layer interaction (SBLI) corresponding to new generation of flight conditions and of turbomachinery applications. For example, oblique shock/boundary-layer interaction (OSBLI) has been intensively studied in the European program TFAST (Giepman *et al.* 2014; Szubert *et al.* 2014).

Although computational fluid dynamics (CFD) tools have been frequently used to understand the physical dynamics of OSBLI, the existing computational techniques are in need of further improvement. In their review on the topic, Knight & Degrez (1998) conclude that traditional eddy-viscosity-based Reynolds averaged Navier-Stokes (RANS) approaches may provide unsatisfactory predictions of important features of OSBLI. While interest in higher-fidelity simulations such as DNS or wall-resolved LES is growing, the computational costs quickly become extremely expensive for such complex flows at large Reynolds numbers. Therefore, an optimal compromise between predictive accuracy and computational cost is required to support the design process of supersonic applications. A possible candidate could be a hybrid RANS-LES modeling (for example, delayed-detached eddy simulation (DDES) by Spalart *et al.* 2006). Another candidate is LES

---

† Institut de Mécanique des Fluides de Toulouse, UMR 5502 (CNRS, INPT, UPS), France

coupled with wall modeling that directly models wall shear stress τ_w and wall heat flux q_w(Kawai & Larsson 2012). Unlike DDES, this wall-modeled LES (WM-LES) resolves the flow all the way down to the wall, but instaneous τ_w and q_w are provided by the wall model as a wall boundary condition.

The objective of this study is to evaluate the performance of DDES and WM-LES in the context of a fully turbulent boundary layer interacting with an oblique shock wave in a supersonic flow. More specifically, the test case treated by the computational techniques is an experimental Mach 1.7 oblique shock wave configuration studied by Giepman *et al.* (2014).

2. Methodology

2.1. *Geometry and conditions*

The geometry of interest for this study is taken from the experiment performed in a transonic/supersonic wind tunnel at the Technical University of Delft (Giepman *et al.* 2014). The cross-sectional area of the test section is 270 mm (height) × 280 mm (width), and the tunnel was operated at a Mach number of 1.7 with a unit Reynolds number of 35 million. The total pressure and the total temperature were 2.3 bar and 278 K, respectively. The free-stream turbulence level was about 0.5%.

The setup consists of two models, a full-span flat plate with a sharp leading edge ($R \sim 0.15$ mm) and a symmetric partial-span shock generator whose deflection angle is 3°, as shown in Figure 1 (left). The length of the flat plate (L) is 120 mm, and the leading-edge shock of the flat plate itself was very weak ($\theta \sim 0.1°$). The span-wise width of the flat plate (W) is 272 mm, whereas the shock generator has a partial span of 180 mm ($0.66W$). The oblique shock from the shock generator impinges at $x_{LE} = 71$ mm on the flat plate, where x_{LE} is the distance from the leading edge of the flat plate.

In the experiment, the flow is tripped at $x_{LE} = 5$ mm by a zig-zag strip to ensure the presence of a fully turbulent boundary layer entering the shock/boundary-layer interaction. The zig-zag strip is 0.2 mm thick and located in the zone between $x_{LE} = 5$ mm and $x_{LE} = 16$ mm. The span-wise period of the zig-zag shape is 6 mm, and the traversal length of the strip, from the leading edge to the trailing edge of the strip, is 5.8 mm. Without this tripping device, the natural transition is located approximately at $x_{LE} =$ 71 mm.

2.2. *Hybrid RANS-LES modeling (DDES)*

The DDES simulations of the oblique-shock configuration have been performed with the Navier-Stokes Multi-Block (*NSMB*) solver. The NSMB solver is the fruit of a European consortium coordinated by CFS Engineering in Lausanne, Switzerland. NSMB is a structured, finite-volume based, compressible code that includes a variety of efficient high-order numerical schemes and of turbulence modeling closures in the context of LES, URANS and of hybrid turbulence modeling. In this study, a third-order Roe upwind scheme associated with the MUSCL van Leer flux limiter scheme has been used for spatial discretization of the convective fluxes.

The DDES formulation used in this study (Spalart *et al.* 2006) is based, for the unsteady RANS part, on the Edwards-Chandra (Edwards & Chandra 1996) modified Spalart-Allmaras model (Spalart & Allmaras 1994). The Edwards-Chandra modifications result in smooth and faster convergence. A recent application of the DDES method with the NSMB solver can be found in Grossi *et al.* (2014). Implicit time integration us-

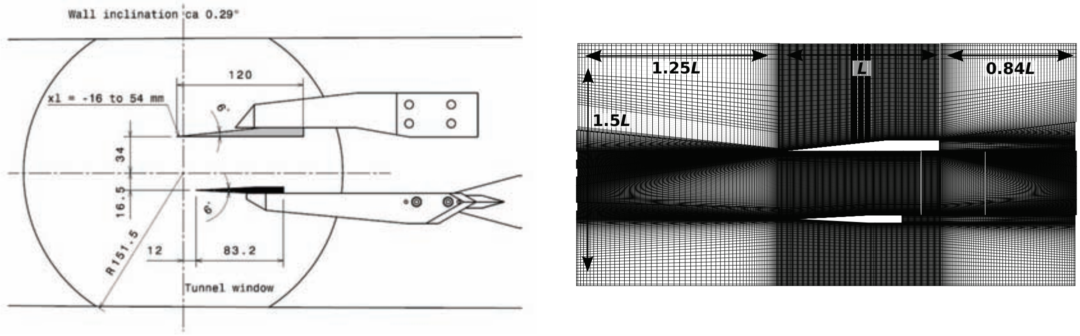

Figure 1. Left: Side view of the experimental geometry; right: computational grid for the DDES (mid-span plane) and main dimensions

	N_{total}	Δ_x^+	$\Delta_{y,\min}^+$	Δ_z^+	Δ_x/δ_o	$\Delta_{y,\min}/\delta_o$	Δ_z/δ_o	h_{wm}^+	h_{wm}/δ_o
DDES	31×10^6	296.0	0.04	1006.4	0.42	5.7×10^{-5}	1.42		
WM-LES	4.7×10^6	63.0	8.2	46.3	0.089	0.011	0.065	31.0	0.046

Table 1. Grid properties: the grid sizes are normalized by $\delta_{\nu,o}^+$ or δ_o, where the wall viscous unit $\delta_{\nu,o}^+ = \mu_w/(\rho_w u_{\tau,o}) = 1.35 \times 10^{-3}$ mm calculated from the flow values.

ing the dual-time stepping technique has been performed. Typically, 70 inner iterations were necessary for convergence in each time step.

The DDES computations are performed on a full-span domain (272 mm, $W_{DDES}/W = 1$) using symmetry conditions. Two hundred cells are distributed along the span-wise direction. Far-field conditions using the Riemann invariant are imposed at the inlet and outlet, as well as at the top and bottom boundaries. The boundary conditions of the two geometrical elements are adiabatic solid walls. Figure 1 (right) shows a vertical sliced plane of the grid used for the DDES computation. Details of the resolution of this grid are indicated in Table 1. Two DDES calculations are performed. Since previous 2D RANS calculations (Szubert *et al.* 2014) showed an early transition, the first DDES calculation uses no treatments to simulate the effect of the zig-zag tripping in the experiment. A second DDES computation has been carried out by conditionning the flow in a region of short length from the leading edge of the flat plate. This conditioning consists in imposing the turbulent viscosity ν_t to be equal to zero in a defined area of the flow, forcing laminarity in this area, while everywhere else ν_t is evolved from the inlet boundary, based on the experimental value, through the RANS modeling. The rectangle conditioning zone has a height of 1.5 mm from the flat-plate surface and a length of $x_{LE} = 23$ mm ($0.20L$) from the leading edge, which corresponds to the onset location of the transition in this new simulation. In this case, the development of the turbulent boundary layer is spatially delayed and shows a better agreement with the experiment. This simulation is refered in this study as *transitional DDES*. All the other simulation parameters remained the same as those in the initial DDES computation.

2.3. *Wall-modeled LES*

We use the unstructured compressible LES solver CharLES^x, developed at the Center for Turbulence Research (Bodart & Larsson 2012). CharLES^x utilizes energy-conserving

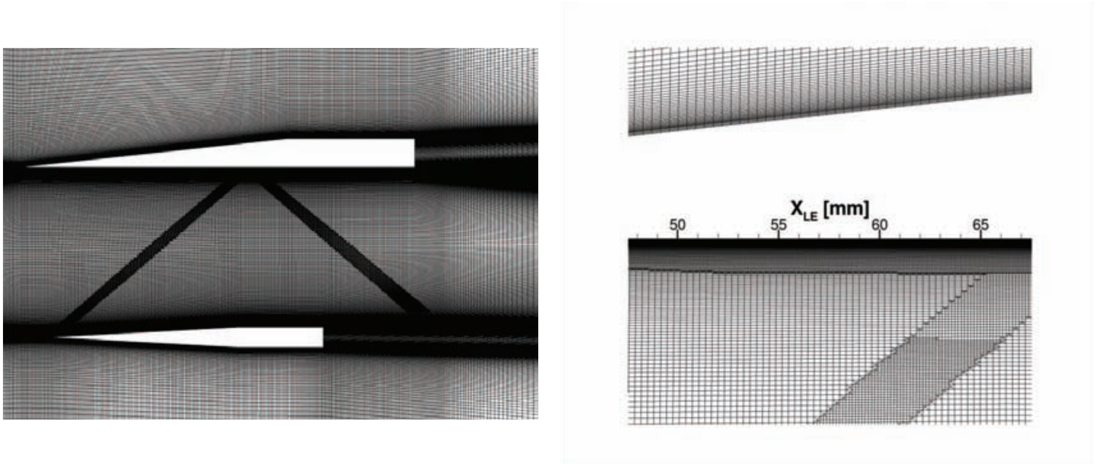

Figure 2. WM-LES mesh: (left) computational grids near flat-plate and shock-generator models; (right) enlarged image in the middle of the flat plate

numerics and shows nearly second-order spatial errors for unstructured grids. It also has the ability to detect shocks and switch its central scheme to a 2nd-order ENO method near the detected shocks. For time integration, we use a 3-stage Runge-Kutta method. The Vreman model (Vreman 2004) is applied to model the sub-grid scale motions.

The wall model implemented in CharLES^x was initially proposed by Kawai & Larsson (2012) and generalized by Bodart & Larsson (2012). Since the LES grids do not resolve the inner layer of boundary layers, the wall model calculates the wall shear-stress vector τ_w and the wall heat-flux q_w and provides them to the LES solver as wall boundary conditions. The model equations are derived from the momentum and energy equations in boundary layers. Based on the assumption of equilibrium boundary layers, all the other terms in the boundary layer equations except the diffusion terms are neglected, which reults in a coupled set of ordinary differential equations. A matching location h_{wm} is specified, at which the solution from the LES grid, (ρ, u, T), is imposed as the upper boundary condition to the wall-model equations. As discussed in Kawai & Larsson (2012), there are at least four LES grid points below h_{wm}.

The WM-LES were performed on a domain whose total stream-wise length is $2.16L$, where again $L = 120$ mm is the stream-wise length of the flat plate. The leading edge of the flat plate is located $0.32L$ from the supersonic inlet, and the domain ends $0.84L$ from the trailing edge of the flat plate. The domain height is the same as the wind-tunnel height of the experiment (0.255 mm). The span-wise domain length ($W_{\text{WM-LES}}$) is 3 mm ($W_{\text{WM-LES}}/W = 0.011$, $W_{\text{WM-LES}}/L = 0.025$), and periodic boundary conditions are used. The LES grids are locally refined in the flat-plate boundary layer (0 mm $\leq x_{LE} \leq$ 98.25 mm) and near the shocks. Figure 2 shows a close view of the refined mesh. The resolutions of the LES mesh and the matching location height are indicated in Table 1.

The inflow turbulence is generated by the digitally filtered synthetic turbulence by Touber & Sandham (2008) that is implemented in CharLES^x by Bermejo-Moreno *et al.* (2011). The turbulent intensity of the synthesized turbulence is the same as the experiment. A supersonic characteristic boundary condition is imposed at the outlet boundary. The top and bottom boundaries are slip walls, and thus the flow cannot penetrate through those boundaries. The walls of the flat plate and the shock generator are adiabatic. As previously explained, periodic boundary conditions are enforced in the span-wise direction. The flow field is initialized with a steady-state two-dimensional RANS simulation result, and the simulation runs for a total run time of $634.3T$ (statistics are taken after $422.9T$), where the time sacle T is defined as $T = \delta_o/u_\infty$.

In the experiment, the flow is tripped at the leading edge by a 0.2 mm thick zig-zag strip to generate a fully turbulent boundary layer. In the WM-LES simulation, turbulence is triggered by blowing-and-suction at the wall. Following Huai *et al.* (1997), the blowing and suction boundary condition has the form of the following oblique-wave function,

$$v(x,z,t) = A_1 f(x)\sin(\omega t) + A_2 f(x) g(z) \sin\left(\frac{\omega}{2}t\right). \tag{2.1}$$

The stream-wise mode $f(x)$ is taken from Fasel & Konzelmann (1990), which is given as

$$\begin{aligned} |f(x)| =& 15.1875\zeta^5 - 35.4375\zeta^4 + 20.25\zeta^3, \\ \text{where } \zeta =& \begin{cases} \frac{x-x_s}{2(x_e-x_s)} & \text{for } x_s \le x \le x_m \\ \frac{x_e-x}{2(x_e-x_s)} & \text{for } x_m \le x \le x_e \end{cases}, \end{aligned} \tag{2.2}$$

and the stream-wise coordiates are $x_s = 7.75$ mm, $x_m = 10.5$ mm, and $x_e = 13.25$ mm from the leading edge of the flat plate. The span-wise mode $g(z)$ is defined as $g(z) = \cos(2\pi z/\lambda_z)$. The wave amplitudes are $A_1 = 0.05U_\infty$ and $A_2 = 0.005U_\infty$. In order to obtain a strong response from the blowing-and-suction boundary condition similar to that in the experimental tripping device, the amplitudes A_1 and A_2 are taken to be much greater than those in the H-type transition studies such as Fasel & Konzelmann (1990), Huai *et al.* (1997), and Sayadi *et al.* (2013). The non-dimensional frequency is $F = 5.42 \times 10^{-4}$, where $F = 2\pi\omega\,(\mu_\infty/\rho_\infty U_\infty^2)$, and the span-wise wavelengh λ_z is 3 mm. Since the other frequencies and magnitudes except the given values are not investigated in this study, the effects of different blowing-and-suction parameters are not clear.

3. Results and discussion

Since turbulence is generated by mechanisms different from those in the experiment, it is important to verify that the upstream laminar boundary layer becomes the equilibrium turbulent boundary layer by the time when it reaches the shock impingement point ($x_{LE} = 71$ mm). In order to compare compressible results against incompressible skin-friction correlations, we transformed the skin-friction coefficient by using the van Driest II transformation (van Driest 1951), which is given as

$$C_{f_{VD}} = \frac{\overline{T_w}/T_\infty - 1}{\arcsin^2\psi} C_f, \quad \psi = \frac{\overline{T_w}/T_\infty - 1}{\sqrt{\overline{T_w}/T_\infty\left(\overline{T_w}/T_\infty - 1\right)}}, \quad \mathrm{Re}_{\theta VD} = \frac{\mu_\infty}{\mu_w}\mathrm{Re}_\theta. \tag{3.1}$$

The transformed skin-friction coefficient $C_{f_{VD}}$ is then compared with the Blasius laminar profile and the turbulent theory by von Kármán & Shoenherr (Hopkins & Inouye 1971) given as

$$C_{f_B} = 0.26\mathrm{Re}_\theta^{-0.25} \tag{3.2}$$

and

$$C_{f_{KS}} = \left\{17.08\left(\log_{10}\mathrm{Re}_\theta\right)^2 + 25.11\log_{10}\mathrm{Re}_\theta + 6.012\right\}^{-1}. \tag{3.3}$$

Figure 3 shows the skin-friction coefficients in the simulations compared with the two theoretical profiles. The WM-LES data are taken in the region of $x_{LE} = 18$ - 65 mm. The turbulent boundary layer in WM-LES matches very well with the theoretical curve after it becomes turbulent ($\mathrm{Re}_\theta > 1000$) by using blowing and suction. The DDES result first

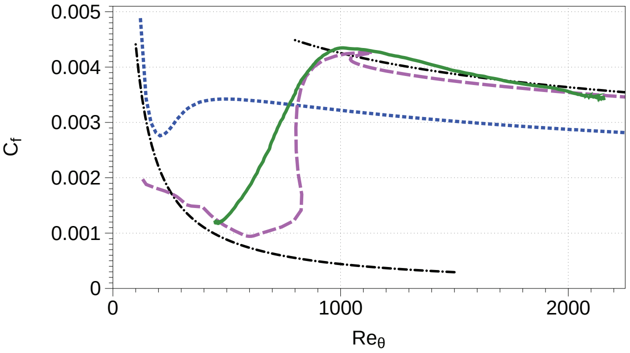

FIGURE 3. Upstream skin-friction coefficient distribution: -·-·-·- Blasius, -··-··- von Kárman & Shoenherr, ········ DDES, - - - - DDES (transitional), —— WM-LES

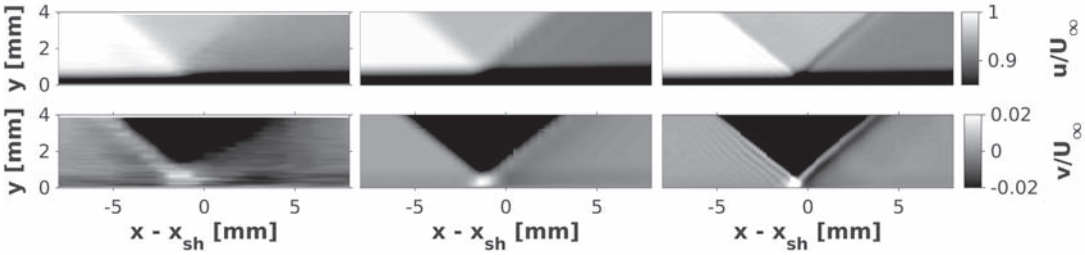

FIGURE 4. Comparison of normalized cross and streamwise velocity fields in the SBLI region. Left: experiment; middle: DDES; right: WM-LES.

follows the laminar Blasius profile but undergoes transition to turbulence much earlier than WM-LES. After transition, a significant discrepancy between the DDES and the theoretical skin friction for equilibrium boundary layers is observed. With regard to the transitional DDES, the boundary layer is not free to develop in terms of turbulence, which explains the unusual aspect of the curve up to $Re_\theta < 1150$. Downstream of this location, outside the conditioning area, the skin-friction coefficient confirms that the boundary layer is fully turbulent, matching well with the theoretical and the WM-LES values, which endorses the use of the boundary-layer conditioning. A qualitative comparison of the stream-wise and wall-normal velocity fields are provided in Figure 4. In the figures, the horizontal axis is the distance from the shock impingement point x_{sh}, where x_{sh} is 71 mm from the leading edge of the flat plate. The vertical axis of the figures is the distance from the flat plate. The averaged fields from DDES and WM-LES are compared with the steady experimental PIV measurements. Despite extra waves generated by the WM-LES and visible in the v/U_∞ field from the SBLI, the two numerical methods compare well with the experiment.

In Figure 5, the mean stream-wise velocity profiles of the boundary-layer, around x_{sh}, are provided at eight different stream-wise locations and allow a more detailed comparison. The velocity profiles are normalized by the corresponding local free-stream velocities in the experiment at each location. In the DDES case, the mean stream-wise velocity is underestimated compared to the experiment, which can be understood as an overestimation of the development of the turbulence in the boundary layer. The Spalart-Allmaras model induces a quasi-instantaneous laminar-turbulent transition from the leading edge in the RANS layer (Figure 3), while in the experiment, the transition is triggered in

Numerical simulations of OSBLI at high Re 495

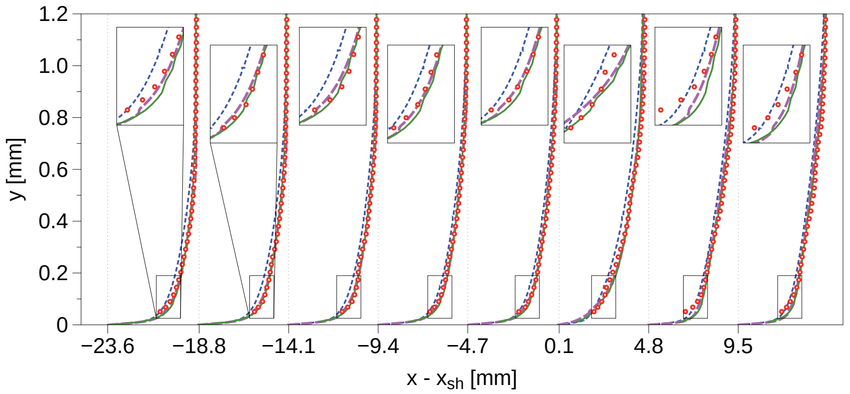

FIGURE 5. Velocity profiles at 8 stream-wise locations: normalized by experimental u_∞ at each location: ········ DDES, - - - - DDES (transitional), —— WM-LES, ○ experiment

the zone of x_{LE} = 5 - 16 mm by the zig-zag tripping. The result of the transitional DDES matches better with the experiment by using the conditioning of the boundary layer, which delays its development to the turbulent state, until the flow approaches the interaction zone where the decrease in velocity observed in the experiment is underpredicted. WM-LES profiles matches well with the experiment, especially in the upstream and downstream directions of the OSBLI zone. In the interaction zone ($x - x_{sh} = 0.1$ and 4.8 mm), however, there are noticeable discrepancies from the experiment, similar to the transitional DDES. Since an equilibrium WM-LES formulation is used in this study, non-equilibrium effects such as strong pressure gradient and flow recirculation cannot be achieved in the wall model. Dawson *et al.* (2013) also observed poor predictions through interaction in their study of a supersonic compression ramp using a WM-LES. By investigating the magnitude of each term in a wall-resolved LES in the same configurations, they concluded that the convective and pressure gradient terms are dominant in near interaction zone. However, previous attempts to include dominant terms measured at the matching location (h_{wm}) in the equilibirum formulation such as that by Hickel *et al.* (2012) not only had difficulties in showing a satisfactory result but also suffered from numerical stability problems. As the flow goes downstream of the interaction and recovers equilibrium behavior, the WM-LES profiles is getting close to the experiment. Therefore, it may be necessary to solve the full non-equilibrium equations in the wall model. However, the accuracy of the PIV measurements in the SBLI region is reduced compared to that of the other regions of the boundary layer.

Figure 6 shows the distributions of boundary-layer thickness (δ_{99}), displacement thickness (δ^*), momentum thickness (θ), and shape factor ($H = \delta^*/\theta$) as a function of x_{LE}. For δ_{99}, DDES and WM-LES match relatively well with the upstream of the SBLI, given the fact that in general δ_{99} cannot be accurately defined for such complex flows. For δ^* and θ, however, the DDES slightly overestimates the integral values, which confirms the remarks of the previous paragraph: without any conditioning, the DDES generates an early development of the turbulent boundary layer compared to the experiment. This can be corrected by imposing the transition at x_{LE} = 23 mm, as explained above. In this case, the development of the boundary layer is delayed, as shown in all the graphs, and the integral values downstream of the transition location get closer to the WM-LES and the experiment. In the interaction zone, none of the numerical methods can predict

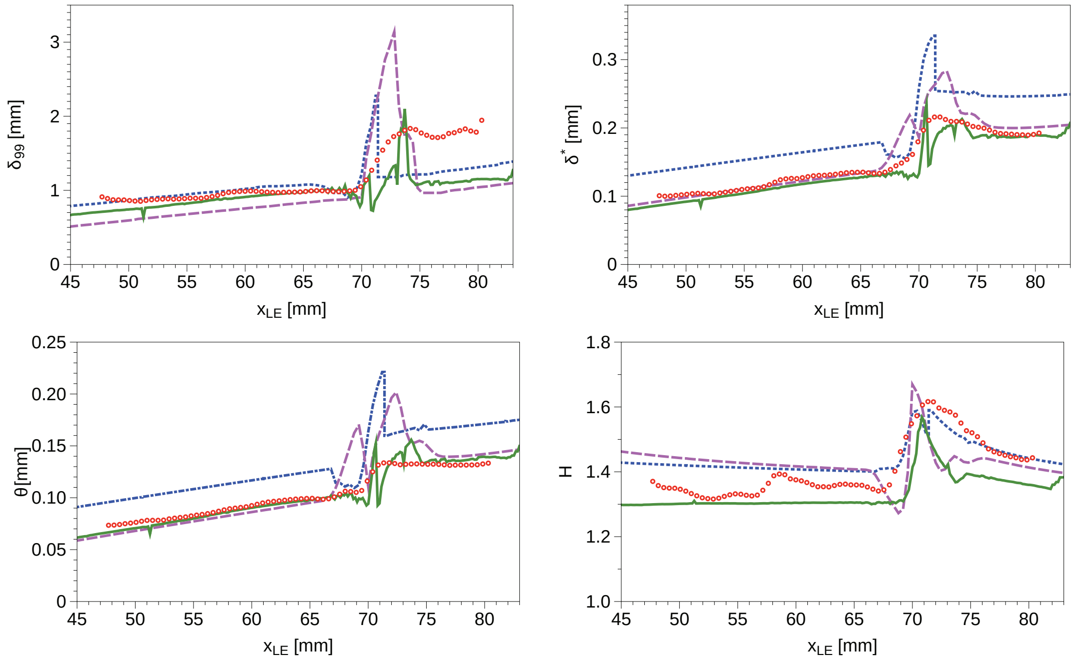

FIGURE 6. Boundary layer thicknesses: (top left) 99% boundary-layer thickness (δ_{99}) (top right) displacement thickness (δ^*) (bottom left) momentum thickness (θ) (bottom right) shape factor (H); ········ DDES, - - - - DDES (transitional), ——— WM-LES, ○ experiment

accurately the quantities. In the downstream of the interaction, the WM-LES approaches the experimental values as well as the transitional DDES, as observed in Figure 5. For the shape factor (H), both the transitional DDES and the WM-LES are reasonably close to the experimental value in $x_{LE} < x_{sh}$. In the interaction zone, the transitional DDES and the WM-LES follows the general trend of the experiment but shows noticeable discrepancies from the experiment. In the downstream of the interaction zone, the transitional DDES shows a better agreement with the experiment. Interestingly, the DDES results are closer to the experiment for $x_{LE} \geq x_{sh}$ than for the other two calculations despite its poor predictions of the upstream flow for the other quantities without conditioning. We briefly recall that the PIV measurements are less accurate in the SBLI region than in the other regions of the boundary layer.

4. Concluding remarks and future work

Two different simulation tools (a hybrid RANS-LES (DDES) and an equilibrium WM-LES) are used to predict an OSBLI problem in a Mach 1.7 flow. The flow is tripped very close to the leading edge in the experiment to insure a turbulent interaction, and both numerical approaches use different techniques to simulate the tripped fully turbulent boundary layer. All calculations compare reasonably well with the overall features in the experiment. While the results of the DDES modeling show an overestimation of the integral values of the boundary layer, the transitional DDES and the WM-LES match well with the boundary-layer characteristics found in the experiment for the supersonic equilibrium flows. The results of DDES show an overestimation of the development of the boundary layer compared to the reference results. Therefore, DDES requires a preconditioning of the upstream boundary layer in an analogy with the WM-LES that used blowing and suction for the tripping in the experiment.

Despite the good agreement with the experiment in the upstream equilibrium boundary layer, all the numerical methods show discrepancies in the zone of the OSBLI. Strong pressure gradient and complex flow features near the wall at the interaction cannot be represented in the numerical methods. Similar to the findings of Dawson *et al.* (2013), the WM-LES needs to incorporate non-equilibirum dynamics for strong non-equilibrium regions. A possible future approach is the non-equilibirum WM-LES formulation suggested by Park & Moin (2014), which uses a full non-equilibrium formulation to calculate the transient wall shear stress τ_w and heat flux q_w. However, even the full non-equilibrium WM-LES formulation cannot guarantees a more exact prediction in some strongly separated flows (see Balakumar *et al.* (2014), this volume).

Moreover, in the context of the original TFAST project, a study of the laminar-turbulent transition location can be carried out to analyze the effects of this location on the SBLI and the downstream shear layer properties such as characteristic sizes, coefficients, unsteadinesses.

Acknowledgments

The authors acknowledge use of computational resources from the Certainty cluster awarded by the National Science Foundation to CTR. The authors acknowledge underwrote the French Supercomputing Centers CINES and CALMIP for the CPU allocation that permitted the DDES study, Y. Hoarau (ICUBE - Université de Strasbourg, France) and Technical University of Delft (R. Giepman, F. Schrijer, B. van Oudheusden) for providing the experimental results. This study has been carried out in the context of the TFAST European programme (Transition Location Effect on Shock Wave Boundary Layer Interaction).

REFERENCES

Balakumar, P., Park, G.I. & Pierce, B. 2014 DNS, LES, and wall-modeled LES of separating flow over periodic hills. *Proceedings of the Summer Program,* Center for Turbulence Research, Stanford University, pp. 407–415.

Bermejo-Moreno, I., Larsson, J., Campo, L., Bodart, J., Vicquelin, R., Helmer, D. & Eaton, J. 2011 Wall-modeled large eddy simulation of shock/turbulent boundary-layer interaction in a duct. *Annual Research Briefs*, Center for Turbulence Research, Stanford University, pp. 49–62.

Bodart, J. & Larsson, J. 2012 Wall-modeled large eddy simulation of the Mcdonnell-Douglas 30p/30n high-lift airfoil in near-stall conditions. In *30th AIAA Applied Aerodynamics Conference*.

Dawson, D. M., Bodart, J. & Lele, S. K. 2013 Assessment of wall-modeled large eddy simulation for supersonic compression ramp flows. In *49th AIAA/ASME/SAE/ASEE Joint Propulsion Conference*.

van Driest, E. R. 1951 Turbulent boundary layer in compressible fluids. *J. Aeronaut. Sci.* **18**, 145–160.

Edwards, J. R. & Chandra, S. 1996 Comparison of eddy viscosity-transport turbulence models for three-dimensional, shock-separated flowfields. *AIAA J.* **34**, 756–763.

Fasel, H. & Konzelmann, U. 1990 Non-parallel stability of a flat-plate boundary layer using the complete Navier–Stokes equations. *J. Fluid Mech.* **221**, 311–347.

Giepman, R., Schrijer, F. & van Oudheusden, B. 2014 High-resolution piv measurements of a transitional shock wave-boundary layer interaction. In *44th AIAA Fluid Dynamics Conference*.

Grossi, F., Braza, M. & Hoarau, Y. 2014 Prediction of transonic buffet by delayed detached-eddy simulation. *AIAA J.* **52**, 2300–2312.

Hickel, S., Touber, E., Bodart, J. & Larsson, J. 2012 A parametrized non-equilibrium wall-model for large-eddy simulations. *Proceedings of the Summer Program,* Center for Turbulence Research, Stanford University, pp. 127–136.

Hopkins, E. J. & Inouye, M. 1971 An evaluation of theories for predicting turbulent skin friction and heat transfer on at plates at supersonic and hypersonic mach numbers. *AIAA J.* **9**, 993–1003.

Huai, X., Joslin, R. & Piomelli, U. 1997 Large-eddy simulation of transition to turbulence in boundary layers. *Theor. Comput. Fluid Dyn.* **9**, 149–163.

Kawai, S. & Larsson, J. 2012 Wall-modeling in large eddy simulation: Length scales, grid resolution, and accuracy. *Physics of Fluids* **24**, 015105.

Knight, D. D. & Degrez, G. 1998 *Shock wave boundary layer interactions in high mach number flows: a critical survey of current numerical prediction capabilities.* AGARD Advisory Report no. 287.

Park, G. I. & Moin, P. 2014 An improved dynamic non-equilibrium wall-model for large eddy simulation. *Phys. Fluids* **26**, 015108.

Sayadi, T., Hamman, C. W. & Moin, P. 2013 Direct numerical simulation of complete h-type and k-type transitions with implications for the dynamics of turbulent boundary layers. *J. Fluid Mech.* **724**, 480–509.

Spalart, P. R. & Allmaras, S. R. 1994 A one-equation turbulence model for aerodynamic flows. *La Recherche Aérospatiale* **1**, 5–21.

Spalart, P. R., Deck, S., Shur, M. L., Squires, K. D., Strelets, M. K. & Travin, A. 2006 A new version of detached-eddy simulation, resistant to ambiguous grid densities. *Theor. Comput. Fluid Dyn.*, 181–195.

Szubert, D., Ashton, N., van Veen, W., Grossi, F., Hoarau, Y., Braza, M., Giepman4, R., Schrijer, F. & van Oudheusden, B. 2014 Physics and modelling of the transonic and supersonic shock wave boundary layer interaction of oblique and normal shock at high Reynolds number. In *10th International ERCOFTAC Symposium on Engineering Turbulence Modelling and Measurements*.

Touber, E. & Sandham, N. D. 2008 Oblique shock impinging on a turbulent boundary layer: Low-frequency mechanisms. In *38th AIAA Fluid Dynamics Conference and Exhibit*.

Vreman, A. 2004 An eddy-viscosity subgrid-scale model for turbulent shear flow: Algebraic theory and applications. *Phys. Fluids* **16**, 3670–3681.

Chapter 5

Conclusion

The present thesis investigated by numerical simulation and turbulence modelling the following unsteady turbulent flows in the high-Reynolds number regime, interesting the domain of industrial applications in the hydrodynamics and aerodynamics domains, covering low subsonic, transonic and supersonic regimes:

1. Unsteady separation and fluid-structure interaction in the incompressible flow around a tandem of cylinders: application in marine hydrodynamics and oil and gaz platforms, as well as aerodynamic configuration of the landing gear cylindrical supports.

2. Unsteady separated flows around airfoils in the high-transonic regime involving buffet instability and shock/boundary-layer interaction: application in aircraft flows at cruise speeds with the aim of producing optimal laminar wing design with reduced drag and maximum aerodynamic efficiency. Two configurations characterised by normal shock interaction have been investigated: the flow around the OAT15A (ONERA) and V2C (Dassault-Aviation) airfoils, ATAAC and TFAST European projects test-cases respectively.

3. Supersonic shock reflection and shock/boundary-layer interaction over a profiled plate: application to the future aircraft in supersonic speeds and in flows arising in turbomachinery aero-engines. This test case is also handles by the TFAST European project.

The simulations have been carried out with the NSMB (Navier Stokes Multi-block) code in which we have implemented in the present thesis the $\gamma - \mathrm{Re}_\theta$ transition model (Langtry and Menter, 2009). It is recalled that the present Hi-Fi simulations already demanded a high grid refinement near the walls, leading to grid sizes going up to an order of 30 million points and that the unsteadiness capturing demanded considerable computing times in the national supercomputing centres CINES[1] and IDRIS[2] and consequently, long 'human' times for the results restitution.

---

[1] Centre informatique national de l'enseignement supérieur or National Computer Center for Higher Education, www.cines.fr

[2] Institut du développement et des ressources en informatique scientifique or Institute for Development and Resources in Intensive Scientific Computing, www.idris.fr

The main contributions of the thesis are as follows:

1. In the first case, the unsteady loads and complex turbulence structures around and between the tandem cylinders has been predicted by means of statistical and hybrid approaches among which: URANS k-ω-SST, OES (Organized Eddy Simulation) and DDES (Delayed Detached Eddy Simulation) involving SST or OES in the statistical part (DDES-SST and DDES-OES). The prediction by the DDES-OES method was able to provide the frequency peak of the Kelvin-Helmholtz instability, responsible for acoustic noise past the downstream cylinder in agreement with the physical experiments carried out in the NASA Langley research Center. Moreover, a good agreement has been obtained in respect of the time-averaged flow structure in comparison with these experiments at Reynolds number 166,000. In the case of vertical motion of the downstream cylinder, the fluid-structure interaction (FSI) was investigated by means of the ALE (Arbitrary Lagrangian Eulerian) method in the NSMB code. It is the first study to our knowledge in which the FSI is predicted in the high-Reynolds number range. The synchronisation ("lock-in") phenomenon between the lift force and the cylinder's displacement has been predicted in the low range of the reduced velocity $[1, 3]$ and for a Scruton (mass-damping) number of 1. The progressive increase of the phase-lag between force and displacement has been also predicted in the higher reduced velocity range $[4, 10]$, illustrating the passage from VIV (Vortex Induced Vibration regime) to MIV (Movement Induced Vibration), which has been also an original aspect in the state of the art. These aspects are included in an article under final redaction for the Journal of Fluids and Structures.

2. In the second case, the contribution of this thesis is as follows: URANS one and two-equation turbulence models as well as OES two-equation modelling have been previously investigated concerning their predictive ability of the normal shock and of the buffet phenomenon in the transonic flow around supercritical aerofoils at Reynolds number of 3.3 million. In this case, it has been shown that the OES method was able to predict the evolution of the buffet instability and of the interaction with the von Kármán mode and other trailing-edge instabilities in the wake. This leaded to a detailed analysis of the flow fields by means of wavelets, autoregressive modelling and POD. The interaction of the wake instabilities as for example the von Kármán one on the buffet mode and vice-versa have been clearly pointed out as an original contribution in the state of the art Szubert et al. (2015b). Indeed, most of the studies around buffet were focused on the near-wall dynamics and less on this kind of interactions, able to be suitably used in order to control the buffet instability. These aspects are currently contributing in on-going studies in the present research group, by manipulating the shear-layer and trailing-edge vortex structures and turbulence by means of electroactive morphing for smart wing design[3], in collaboration with Airbus "Emerging Technologies and Concepts-Toulouse". Moreover, a contribution of the present thesis in improved prediction of these instability modes, of pressure and forces is based on an upscale turbulence modelling, investigated in the context of the OES method (the so-called IOES - Improved OES), based on stochastic forcing of the separated shear layer by means of the high-range POD modes. This method is able

---

[3] www.smartwing.org

to constrict the turbulent/non-turbulent (TNT) interfaces and to keep them thin against the well known excessive turbulence diffusion tendency produced by direct turbulence cascade modelling in the majority of the turbulence modelling methods, from URANS including DRSM (differential Reynolds stress model) up to LES and hybrid ones. This principle has been inspired from the "eddy-blocking" effect in TNT interfaces, studied by Eames et al. (2011) as well as Ishihara et al. (2015). Therefore, the present approach can be beneficial in a more wide context too. In the present thesis, as a further conjecture similar to the one advanced in the JFM paper by Cantwell and Coles (1983) concerning decomposition of the flow field in phase-averaging and fluctuation, we can suggest a decomposition to an ensemble average and fluctuation. The ensemble average can be described by POD reconstruction by considering a first set of most energetic POD modes, covering the coherent organized motion and the high-energy flow properties. The fluctuation regroups the low-energy POD modes. This fluctuation can be splitted in two parts, the downscale and upscale ones; the downscale turbulent stresses can be modelled by an advanced URANS or OES approach or similar, ensuring a low eddy-viscosity level. The upscale ones can be modeled by the present stochastic forcing, represented as a source term in the transport equations of the kinetic energy and dissipation rate (Szubert et al., 2015b). Concerning the studies towards a 'laminar' wing shape in the transonic regime, the Dassault-V2C aerofoil, the present thesis illustrated the effect of the transition to turbulence position on the ratio lift/drag and depicted the optimal region of the transition position. Thanks to collaboration with INRIA-Sophia Antipolis (research group ACUMES, J. A. Desideri and R. Duvigneau), the transition location was further optimised, based on the present Hi-Fi simulations by using a Kriging approach (cf. Szubert et al., 2015a, under review). The 3D Hi-Fi simulations around the V2C wing (Reynolds number of 3 million) by means of DDES using the Spalart-Allmaras and k-ω-SST models in the statistical part of this hybrid approach, indicated a higher amplitude of the buffet instability than in case of URANS and OES modelling and a strong separation starting practically at the leading edge. The same behaviour with similar hybrid approaches has been reported by the partner of University Roma - "La Sapienza" by M. Bernardini and S. Pirozzoli, in the context of the TFAST European project. The experiments in this project did not yet provide finalised results ready for comparison in the Mach number and incidence range carried out by the present simulations corresponding to the buffet development. Therefore, these simulations have been accomplished as a 'blind' test case. The URANS Spalart-Allmaras and k-ω-SST models reached steady state, where the OES-k-epsilon model provided, as in the case of the OAT15A, moderate amplitudes of buffet comparing to the DDES results, as well as separation starting downstream than the leading edge. This investigation, including also the DDES-OES-k-ε modelling, are under continuation within the TFAST project in comparison with the experiments, where IMFT will exploit the experimental pressure signals with the same tools (wavelets, autoregressive modelling, spectral analysis), as in the simulations of Szubert et al. (2015b) in a similar effort as in the previous UFAST European programme concerning the IoA (Institute of Aviation of Warsaw) airfoil. From the 3D physics point of view, the DDES simulations provided a clear representation of the buffet dynamics in interaction with the complex vortex structure in the separation region, in the shear layers (Kelvin-Helmholtz vortices) and in the wake (3D undulation of the von Kármán vortices), illustrating the development of the well known secondary instability since DNS studies in the same research group (Haase et al., 2002; Braza et al., 2001, among others). Furthermore, a 3D-POD analysis is being in progress based on the present thesis DDES simulations, in order to spatially 'filter' this complex vortex dynamics and provide a description of the principal organised modes governing the shock/boundary-layer interaction. An efficient 3D-POD reconstruction is an important step towards building Reduced Order Modelling for the present complex transonic interaction, as previously in our research group in much lower Reynolds number based on DNS in the context of the Ph.D. thesis of R. Bourguet (Bourguet et al., 2009) and in collaboration with INRIA (Bourguet, Braza, and Dervieux, 2011).

3. The contribution of the present thesis in the test-case in the supersonic oblique shock reflection has been carried out in collaboration with the experimental studies carried out in TFAST and coordinated by IUSTI (J. P. Dussauge, P. Dupont). More specifically, the comparisons concern the experiments carried out by the University of Delft partner (TUD) because of several early-stage results provided by this University, as well as comparisons with the LES studies carried out by the group of P. Moin in Stanford University, CA, where this test-case participated in collaboration of IMFT with this Stanford team (P. Moin, I. Jang, G. I. Park et al.) in the bi-annual CTR meeting in July-August 2014 (Szubert et al., 2014b). The principal contribution of this thesis has been the effect of the transition location on the SWBLI. An optimum transition location has been indicated, offering a good comparison with the experiments particularly concerning the velocity profiles of the DDES-Spalart-Allmaras approach with the experiments and the LES results of Stanford, which used a blowing/suction technique in order to trigger the boundary-layer laminar/turbulent transition as in the experiment. Spectral analysis of the pressure signals have depicted predominant frequencies in the range $[10^4, 10^5]$ also reported in previous oblique shock reflection studies by IUSTI (Doerffer et al., 2011; Dussauge et al., 2006). Furthermore, an improved version of the DDES approach suggested by (Shur et al., 2008), the so-called IDDES method, has been used and provided a higher turbulence level in the boundary layer within the SWBLI with a detailed view of the honey-comb and 'horse-shoe' vortex structures, similar to experimental visualisations by Cambridge Univ., reported in the book "An Album of Fluid Motion" of M. van Dyke. The IDDES allowed providing details of this complex structure, because the level of resolved turbulence conceptually ensured by this method is higher and closer to the viscous sublayer than in case of DDES, but it appears that the integral parameter levels within the SWBLI are higher than the experimental results and those of the URANS and DDES simulations in this thesis. Therefore, an even finer grid in the boundary layer and along the span is being employed in order to compare the results with the IDDES, as well as with DDES-OES-k-ε methods.

On view of the present concluding discussion, a general comment can be made on the use of more 'standard' turbulence models, whose behaviour varied upon the test case used, from the practically incompressible to the supersonic regimes. It has been seen that no general preference on using DDES over URANS can be stated, because it depends on the test case and Mach number range. The DDES approaches captured and enhanced separation and strong vortex dynamics and turbulence levels within the separated regions around the bodies. The OES and IOES have proved quite successful amplitudes of the global instability, where all methods provided approximately the same order of low frequency instability modes whenever the URANS methods were able keep up with no considerable damping these instabilities. Concerning the spontaneously moving solid structures under the effect of vibrational instability, as well as for analysis of the complex vortex structures in case of normal shock interaction, the POD modal analysis indicates a potential interest and a successful capturing of the dynamic regimes in FSI, offering a realistic flow filed reconstruction, useful for further ROM studies in the design.

Appendix A

Turbulence models

Contents

A.1 One-equation eddy-viscosity models

A.1.1 Spalart-Allmaras model

The Spalart-Allmaras (SA) model (Spalart and Allmaras, 1994) is based on a single transport equation of a modified eddy viscosity variable $\tilde{\nu}$. It was developed for aerodynamic flows based upon empiricism and dimensional analysis. In its most common formulation assuming fully turbulent flow, the non-conservative form of the transport equation of $\tilde{\nu}$ reads:

$$\underbrace{\frac{D\tilde{\nu}}{Dt}}_{convection} = \underbrace{c_{b1}\tilde{S}\tilde{\nu}}_{production} + \underbrace{\frac{1}{\sigma}\left[\nabla\cdot((\nu+\tilde{\nu})\nabla\tilde{\nu}) + c_{b2}(\nabla\tilde{\nu})^2\right]}_{diffusion} \underbrace{- c_{w1}f_w(r)\left(\frac{\tilde{\nu}}{d_w}\right)^2}_{destruction} \qquad (A.1)$$

where d_w is the distance to the wall.

The eddy viscosity is computed as:

$$\nu_t = \tilde{\nu} f_{v1}. \tag{A.2}$$

The damping function f_{v1} is a correction for the buffer and viscous layers and is calculated from the local variable $\chi = \tilde{\nu}/\nu$ as follows:

$$f_{v1} = \frac{\chi^3}{\chi^3 + {c_{v1}}^3}. \tag{A.3}$$

This function allows the transported variable $\tilde{\nu}$ to reach the value of ν_t in the logarithmic layer.
In the production term, $\tilde{S}$ is defined as:

$$\tilde{S} = S + \frac{\tilde{\nu}}{(\kappa d_w)^2} f_{v2} \tag{A.4}$$

where S is a scalar measure of the deformation tensor $\partial U_i/\partial x_j$, which was originally chosen as the magnitude of the rotation tensor (Spalart and Allmaras, 1994):

$$S = \Omega = \sqrt{2\Omega_{ij}\Omega_{ij}} \qquad \text{where} \qquad \Omega_{ij} = \frac{1}{2}\left(\frac{\partial U_i}{\partial x_j} + \frac{\partial U_j}{\partial x_i}\right). \tag{A.5}$$

The magnitude of the strain-rate tensor $S_{ij} = (\partial U_i/\partial x_j + \partial U_j/\partial x_i)/2$ can be used instead as a measure of the deformation tensor.

The quantity $\tilde{S}$ involves a second damping function defined as:

$$f_{v2} = 1 - \frac{\chi}{1 + \chi f_{v1}}. \tag{A.6}$$

The destruction term depends on the wall distance and on f_w which is a non dimensional function that adjusts the skin friction:

$$f_w(r) = g\left(\frac{1 + {c_{w3}}^6}{g^6 + {c_{w3}}^6}\right)^{1/6} \tag{A.7}$$

where

$$g = r + c_{w2}\left(r^6 - r\right) \qquad et \qquad r = \frac{\tilde{\nu}}{\tilde{S}\left(\kappa d_w\right)^2} \tag{A.8}$$

g acts as a limiter that prevent large values of f_w and r is a near-wall parameter that involves the square of the mixing length $\sqrt{\tilde{\nu}/\tilde{S}}$. In this way, the destruction is annihilated outside of the boundary-layer region.
The closure constants of the model are:

$$c_{b1} = 0.1355, \quad c_{b2} = 0.622, \quad \sigma = 2/3, \quad \kappa = 0.41, \quad c_{v1} = 7.1,$$
$$c_{w1} = \frac{c_{b1}}{\kappa^2} + \frac{1 + c_{b2}}{\sigma}, \quad c_{w2} = 0.3, \quad c_{w3} = 2. \tag{A.9}$$

The SA model is robust and low-sensitive to the freestream condition of $\tilde{\nu}$. It uses trivial Dirichlet boundary conditions and allows $\tilde{\nu} = 0$ in the freestream. Spalart and Rumsey (2007) suggest using $\tilde{\nu}_\infty/\nu$ between 3 and 5 in fully-turbulent computations.

Treatment of laminar region

To allow the simulation of laminar zone as well as to ensure smooth transition to turbulence, the function f_{t2} is introduced and is defined as:

$$f_{t2} = c_{t3} e^{-c_{t4}\chi^2}. \tag{A.10}$$

This function is included in the turbulence model by multiplying the production term of equation A.1 by $(1 - f_{t2})$, resulting in a better stability of the solution when $\tilde{\nu} = 0$. The destruction term is also modified to include f_{t2} in order to balance the budget near the wall, becoming:

$$\left(c_{w1} f_w(r) - \frac{c_{b1}}{\kappa^2} \right) \left(\frac{\tilde{\nu}}{d_w} \right)^2. \tag{A.11}$$

The coefficients of the additional function are $c_{t3} = 1.2$ and $c_{t4} = 0.5$.

A.1.2 Modified Spalart-Allmaras models

A.1.2.1 Edwards-Chandra model

Edwards and Chandra (1996) propose a modified version of the Spalart-Allmaras model to fix stability problems related to the original formulation of $\tilde{S}$ (Eq. A.4). This quantity is modified as follows:

$$\tilde{S} = S\left(\frac{1}{\chi} + f_{\nu 1}\right) \quad \text{where} \quad S = \left[\left(\frac{\partial U_i}{\partial x_j} + \frac{\partial U_j}{\partial x_i} \right) \frac{\partial U_i}{\partial x_j} - \frac{2}{3} \left(\frac{\partial U_k}{\partial x_k} \right)^2 \right]^{1/2}. \tag{A.12}$$

Furthermore, the near-wall parameter becomes:

$$r = \frac{\tanh\left[\tilde{\nu} / \left(\tilde{S} \kappa^2 d_w^2 \right) \right]}{\tanh(1.0)} \tag{A.13}$$

According to Edwards and Chandra (1996), such modifications result in a better robustness of the solution in the sublayer, as well as a smooth and rapid convergence while preserving the near-wall accuracy of the original SA model.

A.1.2.2 Secundov's compressibility correction

As suggested by Spalart and Allmaras (1994), the behavior of the SA model in compressible mixing layers can be improved by using the Secundov's compressible correction used in the ν_t-92 model (Shur et al., 1995). Effects of the work of compression can be taken in accound by ading to the right hand of Eq. A.1 the term:

$$-c_5 \left(\frac{\tilde{\nu}}{a} \right)^2 \frac{\partial U_i}{\partial x_j} \frac{\partial U_i}{\partial x_j}, \tag{A.14}$$

where a is the local speed of sound and $c_5 = 3.5$ an empirical constant. This correction acts as a destruction term, lowering the eddy-viscosity levels in turbulent region of high deformation to accound for the reduced spreading rates of compressible shear layers and can be significant in supersonic flows.

A.2 Two-equation eddy-viscosity models

A.2.1 Chien's k-ε model

The k-ε was one of the most popular two-equation turbulence model until the nineties (Spalart, 2000). The k-ε of Chien (1982) is one variation frequently used in aerodynamics. It has been developed in order to improve the near-wall flows, in particular the friction coefficient, the heat transfers and the kinetic energy of the fluctuations. In conservation form, the transport equation read:

$$\frac{D\rho k}{Dt} = \tau_{ij}\frac{\partial U_i}{\partial x_j} + \frac{\partial}{\partial x_j}\left[\left(\mu+\frac{\mu_t}{\sigma_k}\right)\frac{\partial k}{\partial x_j}\right] - \rho\varepsilon - \frac{2\mu k}{d_w^2} \tag{A.15}$$

$$\underbrace{\frac{D\rho\varepsilon}{Dt}}_{convection} = \underbrace{C_{\varepsilon 1} f_1 \frac{\varepsilon}{k}\tau_{ij}\frac{\partial U_i}{\partial x_j}}_{production} + \underbrace{\frac{\partial}{\partial x_j}\left[\left(\mu+\frac{\mu_t}{\sigma_\varepsilon}\right)\frac{\partial \varepsilon}{\partial x_j}\right]}_{diffusion} \underbrace{- C_{\varepsilon 2} f_2 \frac{\rho\varepsilon^2}{k} - \frac{2\mu\varepsilon e^{-0.5\rho U_\tau d_w/\mu}}{d_w^2}}_{destruction} \tag{A.16}$$

The eddy viscosity is then computed as:

$$\nu_t = C_\mu f_\mu \frac{k^2}{\varepsilon} \tag{A.17}$$

This model is based on the equations of Jones and Launder (1972), accounting for the effects of the molecular diffusion of k and ε on the turbulence structure, and who introduced the three functions f_1, f_2 and f_μ. f_1 is generally equals to the unity. The production/destruction ratio near the wall is ajusted by the f_2 function, which is defined as: $1-(0.4/1.8)e^{-(k^2/6\nu\varepsilon)^2}$. In Eq. A.17, $C_\mu = 0.09$ is the turbulent diffusivity coefficient and f_μ accounts for the wall damping effect:

$$f_\mu = 1 - e^{0.0115 d_w^+} \tag{A.18}$$

where $d_w^+ = d_w u_\tau/\nu$ is the normal wall distance, which is not a local variable.
The last term of Eq. A.15 represents the true finite rate of energy dissipation at the wall and is used to balance the molecular diffusion term. The last term of Eq. A.16 acts similarly.
The closure constants of the model are:

$$C_{\varepsilon 1} = 1.35, \qquad C_{\varepsilon 2} = 1.80, \tag{A.19}$$

$$\sigma_k = 1.0, \qquad \sigma_\varepsilon = 1.3. \tag{A.20}$$

As boundary conditions, $k=0$ and $\varepsilon=0$ at solid wall, $\partial k/\partial x_i = 0$ and $\partial\varepsilon/\partial x_i = 0$ in the farfield.
The variables computed by the models can be used to calculate the turbulence length scale l:

$$l = C_\mu \frac{k^{\frac{2}{2}}}{\varepsilon} \tag{A.21}$$

A.2.2 Wilcox' k-ω model

This model is not directly used in this study. However, the k-ε presented in previous section and the k-ω SST model (subsection A.2.3.2) have been used instead, among others. As the latest involves the k-ε and the Wilcox' k-ω models, it is useful to present its equations.

In their first formulation, the two transport equations of the k-ω model of Wilcox (1988) are defined as follows:

$$\frac{D\rho k}{Dt} = \tau_{ij}\frac{\partial U_j}{\partial x_i} + \frac{\partial}{\partial x_j}\left[(\mu+\sigma_k\mu_t)\frac{\partial k}{\partial x_j}\right] - \beta^*\rho k\omega \tag{A.22}$$

$$\underbrace{\frac{D\rho\omega}{Dt}}_{convection} = \underbrace{\gamma\frac{\omega}{k}\tau_{ij}\frac{\partial U_j}{\partial x_i}}_{production} + \underbrace{\frac{\partial}{\partial x_j}\left[(\mu+\sigma_\varepsilon\mu_t)\frac{\partial\omega}{\partial x_j}\right]}_{diffusion} - \underbrace{\beta\rho\omega^2}_{destruction} \tag{A.23}$$

The turbulent eddy viscosity is computed from:

$$\nu_t = \frac{k}{\omega} \tag{A.24}$$

The values of the constants are:

$$\beta^* = 0.09, \quad \beta = 3/40, \quad \gamma = 5/9, \quad \sigma_k = 0.5, \quad \sigma_\omega = 0.5. \tag{A.25}$$

The relation between ε, ω and k is:

$$\varepsilon = \beta^*\omega k \tag{A.26}$$

A.2.3 Menter's k-ω models

In the early nineties, Menter (1994) introduced two new eddy-viscosity models constructed upon an empirical approach and combined the best properties of the Wilcox' model (see previous section A.2.2 and Wilcox, 1988) with those of a standard k-ε model.

A.2.3.1 Baseline model

The k-w-transformed equations from the k-ε model are as follows:

$$\frac{D\rho k}{Dt} = \tau_{ij}\frac{\partial U_j}{\partial x_i} - \beta^*\rho k\omega + \frac{\partial}{\partial x_j}\left[(\mu+\sigma_k\mu_t)\frac{\partial k}{\partial x_j}\right] \tag{A.27}$$

$$\frac{D\rho\omega}{Dt} = \frac{\gamma}{\nu_t}\tau_{ij}\frac{\partial U_j}{\partial x_i} - \beta\rho\omega^2 + \frac{\partial}{\partial x_j}\left[(\mu+\sigma_\omega\mu_t)\frac{\partial\omega}{\partial x_j}\right] + 2\rho\sigma_\omega\frac{1}{\omega}\frac{\partial k}{\partial x_j}\frac{\partial\omega}{\partial x_j} \tag{A.28}$$

After the transformation, the main differences with the original k-ω are the value of the constants and the appearance of an additional cross-diffusion term in the ω equation. The blending function F_1 is introduced to smoothly switch between the two formulations and the corresponding variables value. The two sets of equations are added and the formulation of the k-w-BSL model becomes:

$$\frac{D\rho k}{Dt} = \tau_{ij}\frac{\partial U_j}{\partial x_i} - \beta^* \rho k\omega + \frac{\partial}{\partial x_j}\left[(\mu + \sigma_k \mu_t)\frac{\partial k}{\partial x_j}\right] \tag{A.29}$$

$$\frac{D\rho\omega}{Dt} = \frac{\gamma}{\nu_t}\tau_{ij}\frac{\partial U_j}{\partial x_i} - \beta\rho\omega^2 + \frac{\partial}{\partial x_j}\left[(\mu + \sigma_\omega \mu_t)\frac{\partial \omega}{\partial x_j}\right] + 2(1-F_1)\rho\sigma_\omega \frac{1}{\omega}\frac{\partial k}{\partial x_j}\frac{\partial \omega}{\partial x_j} \tag{A.30}$$

The blending function is defined as:

$$F_1 = \tanh\left(\arg_1^4\right), \tag{A.31}$$

where

$$\arg_1 = \min\left[\max\left(\frac{\sqrt{k}}{\beta^*\omega d_w}, \frac{500\nu}{d_w^2\omega}\right), \frac{4\rho\sigma_{\omega_2}k}{CD_{k\omega}d_w^2}\right] \tag{A.32}$$

and $CD_{k\omega}$ is the positive value of the cross-diffusion in Eq. A.30:

$$CD_{k\omega} = \max\left(2\rho\sigma_{\omega_2}\frac{1}{\omega}\frac{\partial k}{\partial x_j}\frac{\partial \omega}{\partial x_j}, 10^{-20}\right) \tag{A.33}$$

In $\arg_1$, the first argument is the ratio between the turbulence length scale and the distance to the nearest wall. The second argument forces F_1 to be 1 in the viscous sublayer whereas the third one ensures that the solution remains insensitive to the freestream. All arguments vanish far from the wall. In this way, F_1 is equal to one in the viscous and logarithmic layers: the original k-ω is activated in theses regions. As the wall distance increases, the transformed k-ε is progressively actived as F_1 goes to 0.

The constants of the two models are used and the switch between the “inner” (Wilcox’ k-ω) and “outer” (transformed k-ε) values is performed the same way as for the transport equation by using the F_1 blending function :

$$\phi = F_1\phi_1 + (1-F_1)\phi_2 \tag{A.34}$$

ϕ_1 corresponds to the “inner” values (Wilcox, 1988) while ϕ_2 corresponds to the “outer” ones (Launder and Sharma, 1974).

ϕ	σ_k	σ_ω	β	β^*	κ	γ
ϕ_1	0.5	0.5	0.0750	0.09	0.41	$\beta/\beta^* - \sigma_k\kappa^2/\sqrt{\beta^*}$
ϕ_2	1.0	0.856	0.0828			

Table A.1: Constant values used in the k-ω Baseline model

In that case, $\sigma_{\omega 2} = 0.856$.

The recommended freestream conditions are:

$$1 < \frac{\omega L}{U_\infty} < 10 \quad \text{and} \quad 10^{-5} < \frac{k\mathrm{Re}_L}{U_\infty^2} < 10^{-1} \tag{A.35}$$

where L is the length of the computational domain. The combination of the two farfield values yields: $10^{-5} < \nu_{t\infty}/\nu_{\infty} < 10^{-2}$. At solid walls:

$$\omega = 10 \frac{6\nu}{\beta_1 \left(\Delta d_1\right)^2} \qquad \text{and} k = 0 \tag{A.36}$$

with Δd_1 the first-cell height, which should verify $d^+ \leqslant 3$ for k-ω models for a correct representation of the boundary layer.

A.2.3.2 Shear Stress Transport model

This version of k-ω model is the same as the Baseline formulation except that $\sigma_{k1} = 0.85$ instead of 0.5 and the definition of the turbulent viscosity based on the transported variables is different (Menter, 1994):

$$\nu_t = \frac{a_1 k}{\max(a_1\omega\, , \Omega F_2)} \tag{A.37}$$

where Ω is the absolute value of the vorticity (strain can also be used) and $a_1 = 0.31$. The function F_2 is defined as:

$$F_2 = \tanh\left(\arg_2^2\right) \qquad \text{with} \qquad \arg_2 = \max\left(2\frac{\sqrt{k}}{\beta^*\omega d_w}\, , \frac{500\nu}{d_w^2\omega}\right). \tag{A.38}$$

The F_2 function is equal to 1 in the boundary layer and 0 in the free-shear region. In adverse wall pressure gradient, Ω is usually larger than $a_1\omega$ and the proportionality between the turbulent shear stress and k is preserved, which is often the case in the boundary-layer region. Other two-equation models, for which the standard definition $\nu_t = k/\omega$ is used, usually overpredict the eddy viscosity in non-equilibrium adverse pressure gradient flows where the production k becomes much larger than dissipation. For the rest of the flow, Eq. A.37 reduces to $\nu_t = k/\omega$.

Appendix B

$\gamma - \mathrm{R}_\theta$ laminar/turbulent transition model

Direct Numerical Simulation (DNS) would be the best method in terms of CFD to get the finest estimation of flows. However, due to the limits in the computation speed, it is not yet possible to benefit this method in a satisfactory time, particularly around complex geometries involving wall flows in the industrial context. On the contrary, RANS/URANS methods, involving laminar/turbulent transition modelling, are suitable in most cases.

Many studies have been carried out to develop and include laminar/turbulent transition modelling in RANS codes. A part of them are built from experimental correlations (Granville, 1953; Abu-Ghannam and Shaw, 1980; Mayle, 1991). In that case, the momentum-thickness Reynolds number is correlated to the local flow conditions (pressure gradient or freestream turbulence level) that are easy to calibrate et precise enough to get the main transition phenomena. These criteria have been widely checked. Another part of the transition criteria are the e^N methods and are based on the theory of linear stability (Arnal, 1993). It is used to calculate the increase of the perturbations amplitude between the critical point in the laminar boundary layer and the transition point. When this increase of amplitude N is higher than a threshold, transition goes off. The main issue of these methods is that N is not the amplitudes themselves but the amplification factor of these amplitudes that are *a priori* unknown (Warren and Hassan, 1998). Moreover, this N factor is not universal and needs to be determined in real conditions (flight, wind tunnel).

In all cases, the laminar boundary layer has to be evaluated up to the transition point. In this way, a dedicated boundary-layer code can be used and coupled to a Navier-Stokes solver to determine the whole flow. This approach allows to compensate the possible low precision of the integral parameters due to the grid resolution near the wall. However, it shows its limits when transition is triggered by a bubble detachment or in 3D, where hypotheses need to by applied to the outer flow. Another strategy consists in implementing these criteria directly in the Navier-Stokes solver without using a separate boundary-layer code, avoiding the possible difficulties of coupling two codes. However, integral values related to the boundary layer still need to be estimated and their calculations are not suitable for massively parallelised code. Finally, several "low-Reynolds" models have been introduced, able to generate transition. However, the position of this transition is often estimated mush more upstream than the physical results. Moreover, when these models are numerically robust, they are not well sensitive to the pressure gradient and are not able to predict the transition in detached boundary layers.

To overcome the limits of the aforementioned approaches and to benefit the main Navier-Stokes codes structure that are fully parallelised and use local cell values, Menter et al. (2002) first introduced a transport equation of the intermittency based on criteria and flow values already used or calculated by the existing transport equation models and necessary to evaluated the transition location. The intermittency factor γ is injected in the transport equation of the turbulent kinetic energy k of the $k-\omega$ SST model of Menter (1994). It is equal to 0 in the laminar region of the boundary layer (production of k is annihilated) et 1 everywhere else (k is free to be calculated by the turbulence model). The transport equation of γ is based on the vorticity Reynolds number Re_ν (van Driest and Blumer, 1963; Eq. B.1) and can be used to provide a relation between the transition onset Reynolds number $\mathrm{Re}_{\theta t}$ from an empirical correlation and the local boundary-layer quantities. Indeed, contrary to Re_θ, Re_ν depends only on variables local to each cell.

$$\mathrm{Re}_\nu = \frac{\rho y^2 \Omega}{\mu} \tag{B.1}$$

where y is here the distance to the wall. The vorticity Reynolds number is scaled to match the value of the momentum-thickness Reynolds number in the boundary layer, and needs to be compared with the transition onset momentum-thickness Reynolds number. In this case, $\mathrm{Re}_{\theta t}$ is evaluated from experimental correlations (e.g. criterium of Abu-Ghannam and Shaw, 1980: $\mathrm{Re}_{\theta t}(\lambda_\theta, \mathrm{Tu})$ where λ_θ is a pressure gradient parameter, and Tu the freestream turbulence level). As this Reynolds number is estimated at the boundary layer interface (by definition), its value needs to be communicated inside the boundary layer to be compared with Re_ν. This is achieved by introducing a second transport equation initially described in Menter et al. (2004) and Langtry et al. (2004) and summarized in (Langtry and Menter, 2005). The second transported variable $\overline{\mathrm{Re}_{\theta t}}$ is equals to $\mathrm{Re}_{\theta t}$ in the freestream as a function of the local conditions. Its value is then transported inside the boundary layer (where conditions are different).

Several empirical correlations involved in this model, including $\mathrm{Re}_{\theta t}(\lambda_\theta, Tu)$ and $\mathrm{Re}_{\theta c}(\overline{\mathrm{Re}_{\theta t}})$, were not initially published as they were proprietary ($\mathrm{Re}_{\theta c}$ is the critical momentum-thickness Reynolds number and used to compare with Re_ν to calculate the location(s) where the instabilities start to grow in the boundary layer upstream the transitional and fully turbulent state). The enthusiasm regarding this transition model was great due to its numerous advantages and several research teams tried to discover or to established themselves these correlations (e.g. Toyoda et al., 2007; Content and Houdeville, 2010) applying in specific situations (bypass transition, low speed wings, high speed flow around compressor and turbine blades, 2D/3D, etc). These correlations have finally been published in 2009 (Langtry and Menter, 2009).

In the context of the TFAST project, among others, it has been decided to implement this correlation-based transition model in the code NSMB. For this work, I summarized all this equations of the model in a single page and has been included in this thesis on the next page. This model have finally been implemented with the precious help from Yannick HOARAU (Laboratoire ICube, IMFS, Strasbourg) and Jan VOS (CFS Engineering, EPFL, Lausanne). Unfortunately, while there are no more bugs in execution of the model, no final results nor validation are available as this manuscripted is written. However, I find this page of equations useful to anybody who would like to implement the model in a code or to have an overview of it. Nevertheless, for more details about the relation between the equations, their effects and the definition of the symbols, it is highly advised to read the aforementioned references, as well as Langtry (2006) and Content (2011).

$\gamma - \mathrm{R}_\theta$ LAMINAR-TURBULENT TRANSITION MODEL IN NAVIER-STOKES COMPUTATIONS

ROBIN B. LANGTRY & FLORIAN R. MENTER

EQUATIONS

INTERMITTENCE γ

$$\frac{\partial(\rho\gamma)}{\partial t}+\frac{\partial(\rho U_j\gamma)}{\partial x_j}=P_\gamma-E_\gamma+\frac{\partial}{\partial x_j}\left[\left(\mu+\frac{\mu_t}{\sigma_f}\frac{\partial\gamma}{\partial x_j}\right)\right] \tag{1}$$

$$P_{\gamma 1}=F_{length}\,c_{a1}\rho S(\gamma\,F_{onset})^{0.5}\underbrace{(1-c_{e1}\gamma)}_{\Rightarrow P_{\gamma 1}\leq 1} \tag{2}$$

$$F_{onset1}=\frac{\mathrm{Re}_v}{2.193\cdot\,\mathrm{Re}_{\theta c}\,(\overline{\mathbf{Re}_{\theta t}})} \tag{3}$$

$$F_{onset2}=\min\left(\max\left(F_{onset1},F_{onset1}^4\right),2.0\right) \tag{4}$$

$$F_{onset3}=\max\left(1-\left(\frac{\mathrm{R}_T}{2.5}\right)^3,0\right) \tag{5}$$

$$F_{onset}=\max\left(F_{onset2}-F_{onset3},0\right) \tag{6}$$

$$\mathrm{Re}_{\theta c_{\mathrm{CH}}}=\min(1.0,1.623\cdot 10^{-6}\overline{\mathrm{Re}_{\theta t}}^2-1.228\cdot 10^{-3}\overline{\mathrm{Re}_{\theta t}}+0.849)\cdot\overline{\mathrm{Re}_{\theta t}} \tag{7}$$

$$\mathrm{Re}_{\theta c_{\mathrm{LM}}}=\begin{cases}\overline{\mathrm{Re}_{\theta t}}-(396.035\cdot 10^{-2}-120.656\cdot 10^{-4}\overline{\mathrm{Re}_{\theta t}} \\ +868.203\cdot 10^{-6}\overline{\mathrm{Re}_{\theta t}}^2\quad-696.506\cdot 10^{-9}\overline{\mathrm{Re}_{\theta t}}^3 \\ +174.105\cdot 10^{-12}\overline{\mathrm{Re}_{\theta t}}^4) & \overline{\mathrm{Re}_{\theta t}}\leq 1870 \\ \overline{\mathrm{Re}_{\theta t}}-(593.11+(\overline{\mathrm{Re}_{\theta t}}-1870.0)\times 0.482) & \overline{\mathrm{Re}_{\theta t}}>1870\end{cases} \tag{8}$$

$$F_{length_{\mathrm{CH}}}=\exp(-1.325\cdot 10^{-8}\overline{\mathrm{Re}_{\theta t}}^3+7.42\cdot 10^{-6}\overline{\mathrm{Re}_{\theta t}}^2+8.16\cdot 10^{-3}\overline{\mathrm{Re}_{\theta t}}+2.5652) \tag{9}$$

$$F_{length_{\mathrm{LM}}}=\begin{cases}398.189\cdot 10^{-1}-119.270\cdot 10^{-4}\overline{\mathrm{Re}_{\theta t}} \\ \quad -132.567\cdot 10^{-6}\overline{\mathrm{Re}_{\theta t}}^2 & \overline{\mathrm{Re}_{\theta t}}<400 \\ 263.404-123.939\cdot 10^{-2}\overline{\mathrm{Re}_{\theta t}} \\ \quad +194.548\cdot 10^{-5}\overline{\mathrm{Re}_{\theta t}}^2-101.695\cdot 10^{-8}\overline{\mathrm{Re}_{\theta t}}^3 & 400\leq\overline{\mathrm{Re}_{\theta t}}<596 \\ 0.5-(\overline{\mathrm{Re}_{\theta t}}-596.0)\times 3.0\cdot 10^{-4} & 596\leq\overline{\mathrm{Re}_{\theta t}}<1200 \\ 0.3188 & 1200\leq\overline{\mathrm{Re}_{\theta t}}\end{cases} \tag{10}$$

$$F_{sublayer}=e^{\left(-\frac{\mathrm{R}_\omega}{0.4}\right)^2} \tag{11}$$

$$\mathrm{R}_\omega=\frac{\rho y^2\omega}{500\mu} \tag{12}$$

$$F_{length}=F_{length}(1-F_{sublayer})+40.0\times F_{sublayer} \tag{13}$$

$$E_\gamma=c_{a2}\rho\Omega\gamma F_{turb}(c_{e2}\gamma-1) \tag{14}$$

$$F_{turb}=e^{-\left(\frac{\mathrm{R}_T}{4}\right)^4}\qquad \mathrm{R}_T=(\rho k)/(\mu\omega) \tag{15}$$

INTERMITTENCE WITH SEPARATION γ_{eff}

$$\gamma_{sep}=\min\left(s_1\max\left[0,\left(\frac{\mathrm{Re}_v}{3.235\mathrm{Re}_{\theta c}}\right)-1\right]F_{reattach},2\right)F_{\theta t} \tag{16}$$

$$F_{reattach}=e^{-\left(\frac{\mathrm{R}_T}{20}\right)^4} \tag{17}$$

$$s_1=2 \tag{18}$$

$$\gamma_{eff}=\max(\gamma,\gamma_{sep}) \tag{19}$$

TRANSITION MOMENTUM-THICKNESS REYNOLDS NUMBER $\overline{\mathrm{RE}_{\theta t}}$

$$\frac{\partial\left(\rho\overline{\mathrm{Re}_{\theta t}}\right)}{\partial t}+\frac{\partial\left(\rho U_j\overline{\mathrm{Re}_{\theta t}}\right)}{\partial x_j}=P_{\theta t}+\frac{\partial}{\partial x_j}\left[\sigma_{\theta t}(\mu+\mu_t)\frac{\partial\overline{\mathrm{Re}_{\theta t}}}{\partial x_j}\right] \tag{20}$$

$$P_{\theta t}=c_{\theta t}\frac{\rho}{t}\left(\mathrm{Re}_{\theta t}-\overline{\mathrm{Re}_{\theta t}}\right)(1.0-F_{\theta t}) \tag{21}$$

$$t=\frac{500\mu}{\rho U^2}$$

$$F_{\theta t}=\min\left(\max\left[F_{wake}\cdot e^{-\left(\frac{y}{\delta}\right)^4},1.0-\left(\frac{\gamma-1/c_{e2}}{1.0-1/c_{e2}}\right)^2\right],1.0\right) \tag{22}$$

$$F_{wake}=e^{-\left(\frac{\mathrm{Re}_\omega}{1\cdot 10^{-5}}\right)^2}\qquad \mathrm{Re}_\omega=\frac{\rho\omega y^2}{\mu} \tag{23}$$

$$\delta=\frac{50\Omega y}{U}\cdot\delta_{BL}\qquad \delta_{BL}=\frac{15}{2}\cdot\theta_{BL}\qquad \theta_{BL}=\frac{\overline{\mathrm{Re}_{\theta t}}\mu}{\rho U} \tag{24}$$

$$Tu=100\frac{\sqrt{2k/3}}{U} \tag{25}$$

$$\lambda_\theta=\frac{\rho\theta^2}{\mu}\frac{dU}{ds} \tag{26}$$

$$\mathrm{Re}_{\theta t}=\left[1173.51-589.428Tu+\frac{0.2196}{Tu^2}\right]\cdot F(\lambda_\theta)\qquad Tu\leq 1.3 \tag{27}$$

$$\mathrm{Re}_{\theta t}=331.50\left[Tu-0.5658\right]^{-0.671}\cdot F(\lambda_\theta)\qquad Tu>1.3 \tag{28}$$

$$F(\lambda_\theta)=1-\left[-12.986\lambda_\theta-123.66\lambda_\theta^2-405.689\lambda_\theta^3\right]e^{-\left(\frac{Tu}{1.5}\right)^{1.5}},\lambda_\theta\leq 0 \tag{29}$$

$$F(\lambda_\theta)=1+0.275\times\left[1-e^{-35.0\lambda_\theta}\right]e^{\frac{-Tu}{0.5}}\qquad \lambda_\theta>0 \tag{30}$$

BOUNDARY CONDITIONS

For γ equation:
Walls: zero normal flow
Inlet: $\gamma = 1$
$\mathrm{y}^+ \approx 1$ ($\lesssim 1$?)

For $\overline{\mathrm{Re}_{\theta t}}$ equation:
Walls: zero normal flow
Inlet: based on inlet *Tu*
(cf. eq. (27) et (28))

CONSTANTS

$\sigma_f = 1.0$
$c_{e1} = 1.0$
$c_{a1} = 2.0$
$c_{e2} = 50.0$
$c_{a2} = 0.06$

$\sigma_{\theta t} = 2$ (= 10 in CH2010)
$c_{\theta t} = 0.03$

REFERENCES

Robin B. Langtry, *A Correlation-Based Transition Model using Local Variables for Unstructured PArallelized CFD codes*, PhD thesis, 2006
Robin B. Langtry and Florian R. Menter, *Correlation-Based Transition Modelling for Unstructured Parallelised Computational Fluid Dynamics Code*, **AIAA Journal**, Vol.47, No.12, december 2009
C. Content and R. Houdeville, *Application of the $\gamma - R_\theta$ laminar-turbulent model in Navier-Stokes computations*, **40th Fluid Dynamics Conference and Exhibit**, Chicago, Illinois, 2010

Appendix C

Tecplot 360

Contents

Tecplot 360 is one of the Tecplot family software tools developed by Tecplot, Inc. It is a powerful post-processing software that is widely used in CFD and numerical simulation in general. ParaView is an equivalent software, which is available under BSD license, imposing minimal restrictions on the redistribution of the software, and allowing to include and reuse part or all of it in a free or proprietary software, contrary to Tecplot. Paraview is able to load Tecplot data file.

The aim of this appendix is to give some hints to use Tecplot, based on my experience, in order for new users to start to use it quickly to plot 2D and 3D fields as well as XY lines and have basis to explore the menus, understand the philosophy of the software and develop their own scripts. Many more possibilities, options, parameters, compositions are available in Tecplot and the user is highly invited to read the documentation to produce high quality graphs and field images, static or animated. Only Tecplot format files are considered here.

C.1 Quick start

C.1.1 Load data

Data are loaded via the menu `File > Load data file(s)`. Then, the format of the data file has to be selected in the list (Tecplot 2013). It is the Tecplot one by default. The file(s) is (are) selected in the next window. In Tecplot 2013, to load multiple files, click on the corresponding button in the `Tecplot data loader` window. Select the files in the corresponding list, then click on the `Add` button, and finally on `OK`. The next step is for choosing the initial plot type. This depends on the data to be displayed. Specific menus and tools will be available depending on this plot type, which can be changed later.

Data can also be directly loaded while opening Tecplot in a terminal:

```
tecplot data_file.dat
```

After having loaded the data, the white rectangle that appears and that contains the axis and all the elements of the visualization is the *frame*. Its properties will be modified later.

C.1.2 2D data

While 2D fields can be displayed in the `3D cartesian` mode, this `2D` mode is the most suitable to deal with this type of data.

- After having loaded the data, Tecplot might not identify correctly the **axis variables** from the data file, or the user might want to choose other than the default ones (XZ instead of XY for example). This can be modified in the menu `Plot > Assign XY`.
- **Zoom** can easily be modified by clicking on the middle/3$^{\text{rd}}$ button of the mouse and holding it down while moving the cursor up or down. Similarly, the data can be **translated** by using the right button of the mouse.
- The **frame** defines the aspect ratio of the image that is exported. This aspect ratio might not be adapted to the content of the plot. It can be modified in the menu `Frame > Edit active frame`. In the `Edit active frame` window, the width and height of the frame can be changed. In the same window, the border of the frame (and thus, the border of the exported image) can be removed, as often envisaged.
- On the left sidebar, several *layers* can be displayed (mesh, blocks edges...). The field of the physical variables can be displayed by toggling-on **Contour**. The properties of the contour plot are modified by clicking on the button just near the `Contour` box. The contour variable is selected at the top of the `Contour & Multi-coloring Details` window. The other properties are defined in specific tabs:
    - **Coloring**: when `Banded` color distribution is selected, color levels are discrete and defined by the levels selected in the corresponding tab (see

next point). However, when `Continuous` is selected, the whole colormap is continuously distributed between minimum and maximum values, independently of the contour levels. These two values can be defined manually, or set to the Min/Max values of the current contour variable, or set to the Min/Max values of the defined contour levels. The latest choice is often the best. The colormap distribution can be reversed by ticking the box at the bottom of the window.

  - **Levels**: the entries of the legend are defined in this tab. When `Banded` color distribution is selected in the `Coloring` tab (see previous point), it defines also the color levels. However, it has no effect at all on the color distribution when `Continuous` is selected in the `Coloring` tab. By clicking on the `New levels` button, a new levels distribution is defined between minimum and maximum values, and by the number of levels between these two values or by a step value (`Delta`).

    Procedure to define the levels (suggestion):

    1. Select `Banded` color distribution in the `Coloring` tab.
    2. Defined the levels in the `Levels` tab.
    3. When you are satisfied with the levels distribution go back to the `Coloring` tab, toggle-on `Continuous` and reset the color limits to Min/Max contour levels to have a continuous color distribution (if needed).

    Another way consists in defining first the Min/Max values of the continuous color distribution, and then to define the levels distribution between these Min/Max values.

  - **Legend**: the orientation of the legend can be changed from vertical to horizontal (`Alignment` parameter). Its position can also be precisely defined (`X` and `Y` parameters, as a percentage of the frame size, depending of the anchor alignment). The space between the levels defined in the legend is modified with the `Line spacing` parameter. The header and number font properties are also defined in this window. Finally, it is common to have the legend in a white *filled* box whithout edge (set `Legend box` to filled, and `Box color` to white). The parameter to change the internal margin between the box edges and its content is `Margin`.

- **Probing** data in the contour field can be helpful to have precise values of the field at specific locations, but also to define the contour levels and the color distribution limits. Probe tool is activated by clicking on the corresponding button in the tool bar, just below the menu bar. Then, the user can click anywhere in the field: the `Probe` window opens and displays all the field values at the specific points, including the coordinates. By selecting `Zone/Cell info` at the top of this window, it gives information of the block where the data has been probed, as well as the I, J (and K) coordinates in the context of structured grids. This can be helpful to determine the orientation of the grid, block by block. Finally, by clicking twice on the same tool button (or menu `Data > Probe at`), data can be probed at specific axis coordinates (`Position` tab in the small `Probe at` window; this is useful to find block number and I, J and K coordinates of a point to monitor the time-dependent evolution of the physical field at this point) or at grid coordinates (`Index` tab).

- **Axis properties** are modified via the menu `Plot > Axis`. Properties of each axis can be modified separately, by selecting the corresponding axis at the top of the `Axis Details` window. Axis can also be deactivated by unselecting the corresponding tick box, as often in 2D and 3D plots. However, a white space is remaining around the plot zone, between this zone and the border of the frame. This margin can be removed or modified in the `Area` tab. By entering 0% for left and bottom, and 100% for right and top, the margin is totally removed and the plot zone occupies the whole frame. As observed, the size of this area can be adapted side by side to fit the labels and title position and size, that should be modified (increased font size; see corresponding tabs) in purpose to export the plot as an image for publication. By default, Tecplot chooses automatically the more suitable step in labels. However, if the user wants to specify another step, this can be done in the `Labels` tab, by unselecting `Auto Spacing` and entering a specific value just after. A fixed line (to identify one specific value) can be drawn by selecting `Marker gridline` in the `Grid` tab and choosing `Constant` as the `Position marker`. This function was not found in version 2014. Other properties are quite straightforward and will not be developed here.

C.1.3 3D data

Most of the commands presented for 2D data are also available in 3D mode. However:

- Tecplot sometimes adapts the **aspect ratio** of the whole domain when loading data when it is far from 1. The aspect ratio can be redefined to the original one in the menu `Plot > Axis...`. In the `Dependency` section of `Range` tab, `XYZ Dependent` has to be selected and `X to Y` and `X to Z` ratios have to be set to 1. The original shape of the geometry is recovered.

- In 3D, *contours* are plotted on **slices**. Slices are activated in the left sidebar and their properties can be modified by clicking on the corresponding `"..."` (details) button. The orientation and the location of the slice(s) are defined in the first tab. The contours properties are defined as in 2D mode, by opening the `Contour & Multi-Coloring Details` window (`"..."` (details) button on the left sidebar, near `Contour` activation box, or in the `Contour` tab).

- **Isosurfaces** are a suitable way of displaying data in 3D. They are activated in the left sidebar, similarly to slices, and their properties are modified by clicking on the details button nearby. This opens the `Iso-surfaces details` window. The variable used to define the isosurfaces as well as the isosurface level(s) (1, 2 or 3 specific values or the levels in the contour properties can be used; see the `Draw iso-surfaces at` parameter) are chosen in the first tab. Many style options are available in the second tab. Isosurfaces are colored by contours (*flood*). In this case, another variable can be used to color the isosurfaces (see parameter `Flood by`). Another *contour group* needs to be defined (C1, C2...).

Remark: In 3D mode, Tecplot 2014 might displays orange dashed lines that define boxes containing the blocks of the domain. They are supposed to not be displayed in exported images. These lines are also deactivated when blocks edges are displayed (but these edges are printed in exported images).

C.1.4 XY lines

In *XY Line* mode, most of the lines properties are defined in the `Mapping style` window. This window is opened by clicking on the corresponding button on the left sidebar. In this window, one row in the array corresponds to one line (one *map*) in the graph. To modify the properties of specific line(s), the corresponding row(s) need(s) to be selected. Then, the user have to click on the header of the column (Tecplot 2013) or right-click directly on the cell (Tecplot 2014) to modify the corresponding property.

- In the first tab, the **X** and **Y** variables as well as the ***zone*** of the data can be chosen. Each zone corresponds to a data set. When several data sets are imported, new zones are created and have to be properly selected in this array. The **map name** defines the entry in the legend. By default, it is set to the Y variable. However, this is often not the best choice. An alternative is to set it to zone name and, if necessary, change the name of the zone(s) (menu `Data > Data set info`).
- Lines properties are modified in the `Lines` tab. Same for `Symbols`, in their dedicated tab. To be displayed, `Lines` and `Symbols` needs to be activated in the left sidebar.
- The **legend** is activated via the menu `Plot > Line legend`.
- Extra **axis** can be added in the `Definitions` tab, column `Which Y-Axis` (or `Which X-Axis` if needed). Properties of each axis can be modified via the menu `Plot > Axis` (see more detailed explanation for 2D fields, subsection C.1.2). To plot the **grid border** (usually on top and on the right of the axis zone), the user needs to activate them in the `Lines` tab (`Show grid border` parameter).

Remark: the rendering of exported image (lines pattern in particular) is sometimes no satisfying and does not correspond to what is displayed on the screen. The reason may come from a huge density of data (too many data points in a small X interval). In this case, the density of displayed points can be reduced in the `Indices` tab in `Mapping style` (column `I-Index Range`; change `Skip` parameter from 1 to 100, 1000... for instance).

C.1.5 Export and save

- The frame can be **exported** to a vectoriel or a bitmap **image**, via the menu `File > Export`. The format can be selected from the list at the top of the `Export` window. For each format, specific options are proposed. By default, the EPS images are exported in black and white. They can be exported in colors simply by ticking the corresponding option. This vector graphics format is typically used to export XY lines (graphs). It should not by used to export 2D and 3D fields. Raster gaphics formats like PNG are recommanded instead. For this format, the width of the image in pixels should be given (the default resolution is quite low). The height is given by the aspect ratio of frame size. Antialiasing should be used (the default factor, 3, is often sufficient).

- The plot can be **saved** in a **layout** file (menu `File > Save layout`). It is an ASCII file linked to the data file(s) (its (their) name(s) is (are) given at the beginning of the layout). Tecplot finds in the layout file all the necessary properties to be able to plot the data as it has been saved, including colormap definition as well as equations and functions used to alter data or calculate new variables (see section C.2). When opening a layout file, Tecplot loads the corresponding data and applies all the properties saved in the layout. Layouts can be used to load other data files, as long as these data have the same structure as the original one (number and position of variables, grid size, etc...).

  Frame style files have a similar role, except that they don't contain the data file(s) name(s), nor any alterating equations of the data, nor information concerning the colormap. However, they are very useful in scripting (see section C.3). The frame style is saved in the menu `Frame > Save frame style`.

C.2 In more details

- Information about the loaded data (number of zones/blocks, variables, number of elements...) can be found in the menu `Data > Data set info`. From this menu, the name of the variables and of the zones can be changed. This can have an influence on the axis title, the legend header, etc...

- **Superscript characters** can be inserted by using `<sup>...</sup>`. Similarly, the markups `<sub>...</sub>` are used to insert **subscript** characters. For **greek** characters, the markups `<greek>...</greek>` are used (for example, `<greek>w</greek>` gives ω).

- The user can **alter data** by entering **equations**, in the menu `Data > Alter data`. Existing variables can be refered by their exact name, into braces (e.g. `{u}`). The second way is to use the position of the variables in their list (e.g. `V1`, `V2`). The first method allow to not take in accound the order of the variables, but their name have to be exactly the same from a dataset to another one if they need to be reused. However, variables name can become very complex (e.g. `{<greek>w</greek><sub>z</sub> (s<sup>-1</sup>)}`[1]) and the second method is prefered in this situation. Several equations can be entered (one line per equation), and they can be saved in a file (ASCII) and loaded later. For more complex usage of equations (derivatives, internal variables...), the user is invited to read the documentation.

  Remark: equations are saved in layouts, but not in frame style files. If the user wants to use frame style files to plot calculated variables, these variables

---

[1] This expression gives ω_z (s^{-1})

need to be calculated before. However, they are automatically calculated when opening layouts.

- **New variables** related to the field or the grid can also be directly calculated by Tecplot in a very simple way. To process these new variables, Tecplot may need to know some field variables. They are defined in the menu `Analyse > Field variables`. Don't forget to select `Velocity` instead of `Momentum` in the new window, if this applies. Once data are indentified, a series a new variables are calculated via the menu `Analyse > Calculate variables`. `Calculate on demand` should be deactivated when there is enough memory (RAM). New variables are added at the end of the list of the existing ones.

- A set of many predefined **colormaps** is available in Tecplot. In version 2014 of Tecplot 360, the colormap is selected directly in the list at the top of the `Coloring` tab in the `Contours` details/properties (see subsection C.1.2). In version 2013, the user needs to click on the `"..."` button. This opens the Color map window and allows to change the current colormap, but also to change its distribution and the colors defined at specific control points (click on the ▲ and ▼ buttons to select the control point, then change the red, green and/or blue levels).

- When **time dependent** data are loaded (by loading multiple files for example; see subsection C.1.1), specific information need to be given to Tecplot, via the menu `Data > Edit time strands`. In the case of 2D or 3D fields, `Multiple zones per time steps` needs to be selection, and the number of zones per time step have to be given (usually the number of block in the domain). Specific information on time is given in the `Solution time` zone. Select `Constant delta` and change the `Initial` and the `Delta` (physical time step) values as desired, and click on the `Apply` button. The animation controls appear in the left sidebar.

  Remark: Time dependent data can be exported in a video format by clicking on the `"..."` (details) button near the animation controls. In the `Time animation details` window, select `To file` in `Destination`, then click on `Animate to file`. In the `Export` window that just opens, the format of the file can be selected, as well as the size of the images and the animation speed. Flast (SWF) format is suitable of the web. AVI and MPEG-4 formats can give codec problems. This is the reason why it is preferable to process and export data time step by time step in image format (e.g. PNG), using scripts with internal loop (see section C.3), and then using an external program to build a video file from the series of images.

- Tecplot can be executed in a terminal in **batch mode** (i.e. without launching the graphical user interface), by using the option `-b`. This mode is very useful to process big amount of data on a remote computer having enough memory (RAM). Scripts are executed in batch mode using the option `-p`. The complete command is:

  ```
  tecplot -b -p script_file.mcr
  ```

  Remark: antialiasing is not available in batch mode.

C.3 Scripting

C.3.1 Overview

Tecplot allows for using scripts to simplify the repetition of data post-processing and accelerate it. A specific language is used and documentation on Tecplot scripting is available. Two examples are given here. However, if the user needs more functions or commands, scripts can be recorded while manipulating the Tecplot interface. The recording is launched in menu `Scripting > Record macro` and by specifying a script file name. All the user operations will be saved step by step in the script file, and the corresponding commands can be reused and adapted.

C.3.2 Examples

The two examples given here are a good basis to start to use scripts, in particular when processing a series of data set by using loops.

In the first example (listing C.1), data are loaded and altered explicitly, the colormap is modified to apply a frame style. Then, a text is insert (containing here the current time step in the case of time dependent data with edited time information; see section C.2). Finally, the current frame is exported in PNG and deleted to load a new data set at the next loop step.

The second example (listing C.2) shows the interest of using frame styles when several variables needs to be diplayed and exported to images, by loading data once (with the layout) and then applying one are several frame styles.

All examples are well commented to understand each step.

Listing C.1: Tecplot script example

```
#!MC 1400
# Define new variables.
$!VARSET |FILENBR| = 20
$!VARSET |FIRSTINDEX| = 10
$!VARSET |IDXSTEP| = 2

# The loop goes from 1 to |FILENBR| (here, 20).
$!LOOP |FILENBR|

# Inide the loop, the variable |LOOP| is the current step (1, 2, 3...).
# To do arithmetics, parenthesis are required.
   $!VARSET |INDEX| = (|FIRSTINDEX|+(|LOOP|-1)*|IDXSTEP|)

### Read data.
   $!READDATASET '"AIRFOIL_|INDEX%05d|.plt" '
      READDATAOPTION = NEW
      RESETSTYLE = YES
      INCLUDETEXT = NO
      INCLUDEGEOM = NO
      INCLUDECUSTOMLABELS = NO
      VARLOADMODE = BYNAME
      ASSIGNSTRANDIDS = YES
      INITIALPLOTTYPE = CARTESIAN2D
      VARNAMELIST = '"X" "Y" "Z" "VELOx" "VELOy" "VELOz" "MACH" "PRES"'
```

```
### Modify data by means of new variables and equations. Variables can be
    identified by their name (inside braces) and their number in the variables
    list (V1, V2...).
   $!VARSET |umax| = (MAX(|MAXVAR[4]|,ABS(|MINVAR[4]|)))
   $!ALTERDATA
    EQUATION = '{u}={u}/|umax|'
   $!ALTERDATA
     EQUATION = 'V1=V1-0.034'

### Define or change the colormap.
   $!GLOBALCOLORMAP 1 CONTOURCOLORMAP = SMRAINBOW

### Read and apply a frame style.
   $!READSTYLESHEET "AIRFOIL_Mach.sty"
     INCLUDEPLOTSTYLE = YES
     INCLUDETEXT = YES
     INCLUDEGEOM = YES
     INCLUDEAUXDATA = YES
     INCLUDESTREAMPOSITIONS = YES
     INCLUDECONTOURLEVELS = YES
     MERGE = NO
     INCLUDEFRAMESIZEANDPOSITION = YES

### Insert text at X=2% of the data area, from the left, and Y=97% from the
    top.
   $!ATTACHTEXT
     ANCHORPOS
     {
     X = 2
     Y = 97
     }
     TEXTSHAPE
     {
     ISBOLD = YES
     HEIGHT = 14
     }
     ANCHOR = HEADLEFT
     TEXT = 't = &(SOLUTIONTIME%.5f) s'

### Export to a png image of width 1024 pixels, applying default antialiasing.
   $!EXPORTSETUP EXPORTFORMAT = PNG
   $!EXPORTSETUP IMAGEWIDTH = 1024
   $!EXPORTSETUP USESUPERSAMPLEANTIALIASING = YES
   $!EXPORTSETUP EXPORTFNAME = 'AIRFOIL_Mach_|INDEX%05d|.png'
   $!EXPORT
     EXPORTREGION = CURRENTFRAME

### Delete the active frame and data to load a new set of data in a new frame.
   $!FRAMECONTROL DELETEACTIVE

$!ENDLOOP

$!REMOVEVAR |FILENBR|
$!REMOVEVAR |FIRSTINDEX|
$!REMOVEVAR |IDXSTEP|
$!REMOVEVAR |INDEX|
$!REMOVEVAR |umax|
```

Listing C.2: Tecplot script example: frame style interest

```
#!MC 1400
$!VARSET |FILENBR| = 20

# The loop goes from 1 to |FILENBR| (here, 20).
$!LOOP |FILENBR|

### Open layout (Load data once, calculate normalised coordinates, plot the
    Mach field with a specific colormap).
   $!OPENLAYOUT "layout_AIRFOIL_Mach_|LOOP%05d|.lay"

### Export Mach field to a png image.
#   Here, |LOOP%05d| gives 00001, 00002...
   $!EXPORTSETUP EXPORTFORMAT = PNG
   $!EXPORTSETUP IMAGEWIDTH = 1024
   $!EXPORTSETUP USESUPERSAMPLEANTIALIASING = YES
   $!EXPORTSETUP EXPORTFNAME = ’AIRFOIL_Mach_|LOOP%05d|.png’
   $!EXPORT
      EXPORTREGION = CURRENTFRAME

### Read and apply a frame style to plot pressure field.
#   Data have already been loaded and data altered by opening the layout. It is
    not necessary to do these operations again, saving time, particularly when
    loading 3D data.
   $!READSTYLESHEET "AIRFOIL_pressure.sty"
      INCLUDEPLOTSTYLE = YES
      INCLUDETEXT = YES
      INCLUDEGEOM = YES
      INCLUDEAUXDATA = YES
      INCLUDESTREAMPOSITIONS = YES
      INCLUDECONTOURLEVELS = YES
      MERGE = NO
      INCLUDEFRAMESIZEANDPOSITION = YES

### Export pressure field to a png image.
   $!EXPORTSETUP EXPORTFORMAT = PNG
   $!EXPORTSETUP IMAGEWIDTH = 1024
   $!EXPORTSETUP USESUPERSAMPLEANTIALIASING = YES
   $!EXPORTSETUP EXPORTFNAME = ’AIRFOIL_pressure_|LOOP%05d|.png’
   $!EXPORT
      EXPORTREGION = CURRENTFRAME

### Delete the active frame and data to load a new set of data in a new frame.
   $!FRAMECONTROL DELETEACTIVE

$!ENDLOOP

$!REMOVEVAR |FILENBR|
```

Appendix D

Monitoring files extractor GUI

I created a Matlab graphical user interface (Fig. D.1) that allows for processing the ASCII monitoring files generated by NSMB in a fast and easy way. The user needs to give the path of these data files and select the appropriate parameters from the computation. The programme identifies the files (one file per monitoring point), displays a progression bar while reading the data, and concatenate them in Matlab or ASCII format (one file per variable), for a faster post-processing. The programme can also save the time evolution of the variables as graphs in png or pdf format.

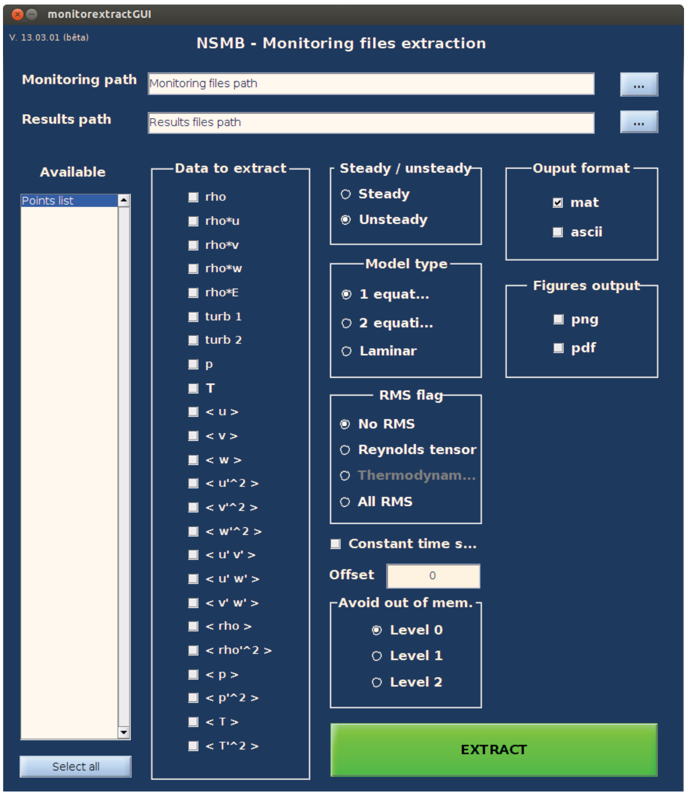

Monitoring path: Monitoring files path

Results path: Results files path

Data to extract
- ☐ rho
- ☐ rho*u
- ☐ rho*v
- ☐ rho*w
- ☐ rho*E
- ☐ turb 1
- ☐ turb 2
- ☐ p
- ☐ T
- ☐ < u >
- ☐ < v >
- ☐ < w >
- ☐ < u'^2 >
- ☐ < v'^2 >
- ☐ < w'^2 >
- ☐ < u' v' >
- ☐ < u' w' >
- ☐ < v' w' >
- ☐ < rho >
- ☐ < rho'^2 >
- ☐ < p >
- ☐ < p'^2 >
- ☐ < T >
- ☐ < T'^2 >

Steady / unsteady
- ○ Steady
- ● Unsteady

Model type
- ● 1 equat...
- ○ 2 equati...
- ○ Laminar

RMS flag
- ● No RMS
- ○ Reynolds tensor
- ○ Thermodynam...
- ○ All RMS

☐ Constant time s...

Offset: 0

Avoid out of mem.
- ● Level 0
- ○ Level 1
- ○ Level 2

Ouput format
- ☑ mat
- ☐ ascii

Figures output
- ☐ png
- ☐ pdf

Figure D.1: Matlab graphical user interface of the programme to extract data from NSMB monitoring files.

,

Bibliography

Abu-Ghannam, B. J. and Shaw, R. Natural transition of boundary layers – the effects of turbulence, pressure gradient, and flow history. *Journal of Mechanical Engineering Science*, **22**(5):213–228, 1980. [143 and 144]

Alshabu, A. and Olivier, H. Unsteady propagation phenomena on a supercritical airfoil. *AIAA Journal*, **46**(8):2066–2073, 2008.
URL `https://dx.doi.org/10.2514/1.35516`.

Arnal, D. Boundary layer transition: predictions based on linear theory. In *AGARD FDP/VKI Special Course on Progress in Transition Modelling*, Vol. **AGARD Report n°793**, 1993. [143]

Aubry, N., Guyonnet, R., and Lima, R. Spatio-temporal analysis of complex signals: theory and applications. *Journal of Statistical Physics*, **64**(3-4):683–739, 1991.
URL `https://dx.doi.org/10.1007/BF01048312`. [27]

Balakumar, P., Park, G. I., and Pierce, B. DNS, LES, and wall-modeled LES of separating flow over periodic hills. In *Proceedings of the Summer Program 2014*, pages 407–415, Center for Turbulence Research, Stanford, CA, July - August 2014.

Barbut, G., Braza, M., Hoarau, Y., Barakos, G., Sévrain, A., and Vos, J. B. Prediction of transonic buffet around a wing with flap. In *Progress in Hybrid RANS-LES Modelling*, Vol. **111** of *Notes on Numerical Fluid Mechanics and Multidisciplinary Design*, pages 191–204. Springer, Gdańsk,Poland, 2010.
URL `https://dx.doi.org/10.1007/978-3-642-14168-3_16`.

Bermejo-Moreno, I., Larsson, J., Campo, L., Bodart, J., Vicquelin, R., Helmer, D., and Eaton, J. Wall-modeled large eddy simulation of shock/turbulent boundary-layer interaction in a duct. *CTR Annual Research Briefs*, pages 49–62, 2011.

Blazek, J. *Computational Fluid Dynamics: Principles and Applications.* Elsevier, 2nd edition, 2005. [8]

Bodart, J. and Larsson, J. Wall-modeled large eddy simulation of the McDonnell-Douglas 30P/30N high-lift airfoil in near-stall conditions. In *30th AIAA Applied Aerodynamics Conference*, New Orleans, LA, 25-28 June 2012.
URL `https://dx.doi.org/10.2514/6.2012-3022`.

Bodenschatz, E. and Eckert, M. Prandtl and the Göttingen school. In P.A. Davidson et al., editor, *A Voyage Through Turbulence*. Cambridge Univ. Press, Cambridge, 2011.

Bouhadji, A. *Analyse physique par simulation numérique de phénomènes de transition bi- et tridimensionnels dans l'écoulement compressible, visqueux autour d'une aile d'avion*. PhD thesis, INPT, 1998.

Bouhadji, A. and Braza, M. Organised modes and shock–vortex interaction in unsteady viscous transonic flows around an aerofoil: Part I: Mach number effect. *Computers & Fluids*, **32**(9):1233–1260, 2003a.
URL `https://dx.doi.org/10.1016/S0045-7930(02)00100-7`.

Bouhadji, A. and Braza, M. Organised modes and shock–vortex interaction in unsteady viscous transonic flows around an aerofoil: Part II: Reynolds number effect. *Computers & Fluids*, **32**(9):1261–1281, 2003b.
URL `https://dx.doi.org/10.1016/S0045-7930(02)00101-9`.

Bourdet, S., Bouhadji, A., Braza, M., and Thiele, F. Direct numerical simulation of the three-dimensional transition to turbulence in the transonic flow around a wing. *Flow, Turbulence and Combustion*, **71**(1-4):203–220, 2003.
URL `https://dx.doi.org/10.1023/B%3AAPPL.0000014932.28421.9e`.

Bourdet, S., Braza, M., Hoarau, Y., El Akoury, R., Ashraf, A., Harran, G., Chassaing, P., and Djeridi, H. Prediction and physical analysis of unsteady flows around a pitching airfoil with the dynamic mesh approah. *European Journal of Computational Mechanics - B/Fluids*, **16**(3-4):451–476, 2007.
URL `https://dx.doi.org/10.3166/remn.16.451-476`. [10]

Bourgoyne, D. A., Ceccio, S. L., and Dowling, D. R. Vortex shedding from a hydrofoil at high Reynolds number. *Journal of Fluid Mechanics*, **531**:293–324, 2005.
URL `https://dx.doi.org/10.1017/S0022112005004076`.

Bourguet, R. *Analyse physique et modélisation d'écoulements turbulents instationnaires compressibles autour de surfaces portantes par approches statistiques haute-fidélité et de dimension réduite dans le contexte de l'interaction fluide-structure*. PhD thesis, INP Toulouse, 2008.
URL `http://ethesis.inp-toulouse.fr/archive/00000705`. [36]

Bourguet, R., Braza, M., Harran, G., and El Akoury, R. Anisotropic organised eddy simulation for the prediction of non-equilibrium turbulent flows around bodies. *Journal of Fluids and Structures*, **24**(8):1240–1251, 2008.
URL `https://dx.doi.org/10.1016/j.jfluidstructs.2008.07.004`. [9]

Bourguet, R., Braza, M., Sévrain, A., and Bouhadji, A. Capturing transition features around a wing by reduced-order modeling based on compressible Navier-Stokes equations. *Physics of Fluids*, **21**(9):094104, 2009.
URL `https://dx.doi.org/10.1063/1.3234398`. [132]

Bourguet, R., Braza, M., and Dervieux, A. Reduced-order modeling of transonic flows around an airfoil submitted to small deformations. *Journal of Computational Physics*, **230**(1):159–184, 2011.
URL `https://dx.doi.org/10.1016/j.jcp.2010.09.019`. [36 and 132]

Boussinesq, J. Essai sur la théorie des eaux courantes. *Mémoires présentés par divers savants á l'Académie des Sciences*, **23**(1):1–680, 1877. [9]

Braza, M. NACA0012 with Aileron. In Doerffer, P., Hirsch, C., Dussauge, J.-P., Babinsky, H., and Barakos, G. N., editors, *Unsteady Effects of Shock Wave Induced Separation*, Vol. **114** of *Notes on Numerical Fluid Mechanics and Multidisciplinary Design*, pages 101–131. Springer, 2011.
URL `https://dx.doi.org/10.1007/978-3-642-03004-8_4`.

Braza, M., Chassaing, P., and Minh, H. Numerical study and physical analysis of the pressure and velocity fields in the near wake of a circular cylinder. *Journal of fluid mechanics*, **165**:79–130, 1986.
URL `https://dx.doi.org/10.1017/S0022112086003014`. [14]

Braza, M., Faghani, D., and Persillon, H. Successive stages and the role of natural vortex dislocations in three-dimensional wake transition. *Journal of Fluid Mechanics*, **439**:1–41, 2001.
URL `https://dx.doi.org/10.1017/S002211200100458X`. [14 and 132]

Braza, M., Perrin, R., and Hoarau, Y. Turbulence properties in the cylinder wake at high Reynolds number. *Journal of Fluids and Structures*, **22**(6–7):757–771, 2006.
URL `https://dx.doi.org/10.1016/j.jfluidstructs.2006.04.021`. [10]

Brunet, V. Computational study of buffet phenomenon with unsteady RANS equations. In *21*st *AIAA Applied Aerodynamics Conference*, Orlando, FL, USA, 23-26 June 2003.
URL `https://dx.doi.org/10.2514/6.2003-3679`. AIAA 2003-3679.

Brunet, V., Deck, S., Molton, P., and Thiery, M. A complete experimental and numerical study of the buffet phenomenon over the OAT15A airfoil. In *40*^{ème} *Colloque d'Aérodynamique Appliquée*, Toulouse, France, 21-23 March 2005.

Cantwell, B. and Coles, D. An experimental study of entrainment and transport in the turbulent near wake of a circular cylinder. *Journal of Fluid mechanics*, **136**:321–374, 1983.
URL `https://dx.doi.org/10.1017/S0022112083002189`. [131]

Chien, K.-Y. Predictions of channel and boundary-layer flows with a low-reynolds-number turbulence model. *AIAA Journal*, **20**(1):33–38, 1982.
URL `https://dx.doi.org/10.2514/3.51043`. [138]

Content, C. *Méthode innovante pour le calcul de la transition laminaire-turbulent dans les codes Naviers-Stokes*. PhD thesis, ISAE, 2011. [145]

Content, C. and Houdeville, R. Application of the $\gamma - r_\theta$ laminar-turbulent transition model in Navier-Stokes computations. In *40th Fluid Dynamics Conference and Exhibit*, Chicago, IL, 28 June - 1 July 2010.
URL https://dx.doi.org/10.2514/6.2010-4445. [144]

Crouch, J. D. and Ng, L. L. Variable N-factor method for transition prediction in three-dimensional boundary layers. *AIAA Journal*, **38**(2):211–216, 2000.
URL https://dx.doi.org/10.2514/2.973.

Dawson, D. M., Bodart, J., and Lele, S. K. Assessment of Wall-Modeled Large Eddy Simulation for supersonic compression ramp flows. In *49th AIAA/ASME/SAE/ASEE Joint Propulsion Conference*, San Jose, CA, 15-17 July 2013.
URL https://dx.doi.org/10.2514/6.2013-3638.

Deck, S. Numerical computation of transonic buffet over a supercritical airfoil. *AIAA Journal*, **43**(7):1556–1566, 2005.
URL https://dx.doi.org/10.2514/1.9885.

Doerffer, P., Hirsch, C., Dussauge, J.-P., Babinsky, H., and Barakos, G. N. *Unsteady Effects of Shock Wave Induced Separation*, Vol. **114** of *Notes on Numerical Fluid Mechanics and Multidisciplinary Design*. Springer, 2011.
URL https://dx.doi.org/10.1007/978-3-642-03004-8. [132]

Dritschel, D. G., Haynes, P. H., Juckes, M. N., and Shepherd, T. G. The stability of a two-dimensional vorticity element under uniform strain. *Journal of Fluid Mechanics*, **230**:647–665, 1991.
URL https://dx.doi.org/10.1017/S0022112091000915.

Duncan, W. J., Ellis, L., and Scruton, C. First report on the general investigation of tail buffeting. *British Aeronautical Research Committee R&M-1457*, **1457**:part I, 1932.

Durbin, J. The fitting of time-series models. *Revue de l'Institut International de Statistique*, **28**:233–243, 1960.

Dussauge, J., Dupont, P., and Debiève, J. Unsteadiness in shock wave boundary layer interactions with separation. *Aerospace Science and Technology*, **10**, 2006. [132]

Eames, I. and Flor, J. B. New developments in understanding interfacial processes in turbulent flows. *Philosophical Transactions of the Royal Society A: Mathematical, Physical and Engineering Sciences*, **369**(1937):702–705, 2011.

Eames, I., Hunt, J. C. R., Braza, M., and da Silva, C. B. Interfaces in turbulence and implications for advanced modelling methods. *ERCOFTAC Bulletin*, **87**, 2011. [131]

Edwards, J. R. and Chandra, S. Comparison of eddy viscosity-transport turbulence models for three-dimensional, shock-separated flowfields. *AIAA Journal*, **34**(9):756–763, 1996.
URL https://dx.doi.org/10.2514/3.13137. [21 and 137]

El Akoury, R. *Analyse physique des effets de rotation de paroi en écoulements transitionnels et modélisation d'écoulements turbulents autour de structures portantes*. PhD thesis, INP Toulouse, 2007.
URL `http://ethesis.inp-toulouse.fr/archive/00000567`. [10]

El Akoury, R., Braza, M., Perrin, R., Harran, G., and Hoarau, Y. The three-dimensional transition in the flow around a rotating cylinder. *Journal of Fluid Mechanics*, **607**:1–11, 2008.
URL `https://dx.doi.org/10.1017/S0022112008001390`.

Fasel, H. and Konzelmann, U. Non-parallel stability of a flat-plate boundary layer using the complete navier–stokes equations. *Journal of Fluid Mechanics*, **221**:311–347, 1990.
URL `https://dx.doi.org/10.1017/S0022112090003585`.

Fu, S., Haase, W., Peng, S. H., and Schwamborn, D., editors. *Progress in Hybrid RANS-LES Modelling*, Vol. **117** of *Notes on Numerical Fluid Mechanics and Multidisciplinary Design*, Beijing, China, 2012. Springer.
URL `https://dx.doi.org/10.1007/978-3-642-31818-4`. [2]

Fung, Y. C. *An Introduction to the Theory of Aeroelasticity*. Dover, 2002. Schlieren picture page 313 by D. W. Holder, National Physical Laboratory, England.

Giepman, R., Schrijer, F., and van Oudheusden, B. High-resolution piv measurements of a transitional shock wave-boundary layer interaction. In *44th AIAA Fluid Dynamics Conference*, Atlanta, GA, 16-20 June 2014.
URL `https://dx.doi.org/10.2514/6.2014-3333`.

Girimaji, S., Haase, W., Peng, S., and Schwamborn, D., editors. *Progress in Hybrid RANS-LES Modelling, Papers Contributed to the 5th Symposium on Hybrid RANS-LES Methods*, Vol. **130** of *Notes on Numerical Fluid Mechanics and Multidisciplinary Design*, College Station, A&M University, TX, 19-21 March 2014.
URL `https://dx.doi.org/10.1007/978-3-319-15141-0`. [2]

Granville, P. S. The calculation of the viscous drag of bodies of revolution. Technical report, David Taylor Model Basin Report 849, 1953. [143]

Grossi, F. Simulation numérique et analyse physique du tremblement transsonique d'un profil supercritique par approche de modélisation de la turbulence statistique avancée. Master's thesis, IMFT, 2010. [51]

Grossi, F. *Physics and modeling of unsteady shock wave/boundary layer interactions over transonic airfoils by numerical simulation*. PhD thesis, INP Toulouse, 2014.
URL `http://ethesis.inp-toulouse.fr/archive/00002643`. [2 and 51]

Grossi, F., Braza, M., and Hoarau, Y. Delayed Detached-Eddy Simulation of the transonic flow around a supercritical airfoil in the buffet regime. In *Progress in Hybrid RANS-LES Modelling*, Vol. **117** of *Notes on Numerical Fluid Mechanics*

and Multidisciplinary Design, pages 369–378. Springer, 2012a.
URL `https://dx.doi.org/10.1007/978-3-642-31818-4_32`. [51]

Grossi, F., Szubert, D., Braza, M., Sevrain, A., and Hoarau, Y. Numerical simulation and turbulence modelling of the transonic buffet over a supercritical airfoil at high reynolds number. In *Procs. ETMM9: 9th International ERCOFTAC Symposium on Engineering Turbulence Modelling and Measurements*, Thessaloniki, Greece, 6 - 8 June 2012b. [51]

Grossi, F., Braza, M., and Hoarau, Y. Prediction of transonic buffet by delayed detached-eddy simulation. *AIAA Journal*, **52**:2300–2312, 2014.
URL `https://dx.doi.org/10.2514/1.J052873`. [51]

Grossi, F., Braza, M., and Hoarau, Y. Simulation numérique et analyse physique du tremblement transsonique d'un profil supercritique à reynolds élevé. *20ème Congrès Français de Mécanique*, 29 August - 2 September 2011. [51]

Grossmann, A. and Morlet, J. Decomposition of Hardy functions into square integrable wavelets of constant shape. *SIAM journal on mathematical analysis*, **15**(4):723–736, 1984.
URL `https://dx.doi.org/10.1137/0515056`.

Guzmán, A. M. and Amon, C. H. Transition to chaos in converging–diverging channel flows: Ruelle–Takens–Newhouse scenario. *Physics of Fluids*, **6**(6):1994–2002, 1994.
URL `https://dx.doi.org/10.1063/1.868206`.

Haase, W., Selmin, V., and Winzell, B. *Progress in Computational Flow-structure Interaction: Results of the Project UNSI, Supported by the European Union 1998-2000*, Vol. **81** of *Notes on Numerical Fluid Mechanics and Multidisciplinary Design*. Springer, 2002.
URL `https://dx.doi.org/10.1007/978-3-540-45489-2_1`. [132]

Haase, W., Braza, M., and Revell, A., editors. *DESider – A European Effort on Hybrid RANS-LES Modelling: Results of the European-Union Funded Project, 2004–2007*, Vol. **103** of *Notes on Numerical Fluid Mechanics and Multidisciplinary Design*. Springer, 2009.
URL `https://dx.doi.org/10.1007/978-3-540-92773-0`.

Hickel, S., Touber, E., Bodart, J., and Larsson, J. A parametrized non-equilibrium wall-model for large-eddy simulations. In *Proceedings of the Summer Program 2014*, pages 127–136, Center for Turbulence Research, Stanford, CA, 2012.

Hoarau, Y. *Analyse physique par simulation numérique et modélisation des écoulements décollés instationnaires autour de surfaces portantes.* PhD thesis, INPT, 2002.

Hoarau, Y., Perrin, R., Braza, M., Ruiz, D., and Tzabiras, G. Advances in turbulence modelling for unsteady flows - imft. In Haase, W., Aupoix, B.,

BUNGE, U., and SCHWAMBORN, D., editors, *FLOMANIA – A European Initiative on Flow Physics Modelling*, Vol. **94** of *Notes on Numerical Fluid Mechanics and Multidisciplinary Design*, pages 85–88, 2006.
URL `https://dx.doi.org/10.1007/978-3-540-39507-2_13`. [10]

HOLMES, P., LUMLEY, J. L., and BERKOOZ, G. *Turbulence, coherent structures, dynamical systems and symmetry.* Cambridge Univ. Press, 1996. [27 and 31]

HOLZNER, M., LIBERZON, A., NIKITIN, N., LÜTHI, B., KINZELBACH, W., and TSINOBER, A. A Lagrangian investigation of the small-scale features of turbulent entrainment through particle tracking and direct numerical simulation. *Journal of Fluid Mechanics*, **598**:465–475, 2008.
URL `https://dx.doi.org/10.1017/S0022112008000141`.

HOPKINS, E. J. and INOUYE, M. An evaluation of theories for predicting turbulent skin friction and heat transfer on at plates at supersonic and hypersonic mach numbers. *AIAA Journal*, **9**(6):993–1003, 1971.
URL `https://dx.doi.org/10.2514/3.6323`.

HUAI, X., JOSLIN, R., and PIOMELLI, U. Large-eddy simulation of transition to turbulence in boundary layers. *Theoretical and Computational Fluid Dynamics*, **9**(2):149–163, 1997.
URL `https://dx.doi.org/10.1007/s001620050037`.

HUNT, J. C. R. and RICHARDS, K. J. Stratified airflow over one or two hills. In KAPLAN, H. and DINAR, N., editors, *Boundary Layer Structure: Modeling and Application to Air Pollution and Wind Energy*, pages 223–259, Zichron Yaacov, Israel, 1984.
URL `https://dx.doi.org/10.1007/978-94-009-6514-0_10`.

HUNT, J. C. R., EAMES, I., and WESTERWEEL, J. Vortical interactions with interfacial shear layers. In KANEDA, Y., editor, *IUTAM Symposium on Computational Physics and New Perspectives in Turbulence*, Vol. **4** of *IUTAM Bookseries*, pages 331–338, Nagoya, Japan, 11-14 September 2008.
URL `https://dx.doi.org/10.1007/978-1-4020-6472-2_50`. [80]

HUNT, J. C. R., ISHIHARA, T., WORTH, N. A., and KANEDA, Y. Thin shear layer structures in high reynolds number turbulence. *Flow, Turbulence and Combustion*, **92**(3):607–649, 2014.
URL `https://dx.doi.org/10.1007/s10494-013-9518-0`.

ISHIHARA, T., OGASAWARA, H., and HUNT, J. C. R. Analysis of conditional statistics obtained near the turbulent/non-turbulent interface of turbulent boundary layer. *Journal of Fluids and Structures*, **53**:50–57, 2015.
URL `https://dx.doi.org/10.1016/j.jfluidstructs.2014.10.008`. [80 and 131]

JACQUIN, L., MOLTON, P., DECK, S., MAURY, B., and SOULEVANT, D. An experimental study of shock oscillation over a transonic supercritical profile. In *35th AIAA Fluid Dynamics Conference and Exhibit*, Toronto, Ontario, Canada,

6-9 June 2005.
URL `https://dx.doi.org/10.2514/6.2005-4902`. AIAA 2005-4902. [51]

Jacquin, L., Molton, P., Deck, S., Maury, B., and Soulevant, D. Experimental study of shock oscillation over a transonic supercritical profile. *AIAA Journal*, **47**(9):1985–1994, 2009.
URL `https://dx.doi.org/10.2514/1.30190`.

Jenkins, L. N., Khorrami, M. R., Choudhari, M. M., and McGinley, C. B. Characterization of unsteady flow structures around tandem cylinders for component interaction studies in airframe noise. In *11th AIAA/CEAS Aeroacoustics Conference*, Monterey, CA, 23-25 May 2005.
URL `https://dx.doi.org/10.2514/6.2005-2812`. [15, 22, 23, 24, and 42]

Jenkins, L. N., Neuhart, D. H., McGinley, C. B., Khorrami, M. M., and Choudhari, M. R. Measurements of unsteady wake interference between tandem cylinders. In *36th AIAA Fluid Dynamics Conference and Exhibit*, San Francisco, CA, 5-8 June 2006.
URL `https://dx.doi.org/10.2514/6.2006-3202`. [16]

Jimenez Garcia, A. Etude de l'interaction tremblement transsonique - instabilité de von Kármán à l'aide d'une plaque de bord de fuite par approche de modélisation de la turbulence statistique avancée. Master's thesis, IMFT, 2012.

Jin, G. and Braza, M. Two-equation turbulence model for unsteady separated flows around airfoils. *AIAA Journal*, **32**(11):2316–2320, 1994.
URL `https://dx.doi.org/10.2514/3.12292`. [9 and 10]

Jones, D. R., Schonlau, M., and Welch, W. J. Efficient global optimization of expensive black-box functions. *Journal of Global Optimization*, **13**(4):455–492, 1998.
URL `https://dx.doi.org/10.1023/A:1008306431147`.

Jones, W. P. and Launder, B. E. The prediction of laminarization with a two-equation model of turbulence. *International Journal of Heat and Mass Transfer*, **15**(2):301–314, 1972.
URL `https://dx.doi.org/10.1016/0017-9310(72)90076-2`. [138]

Kawai, S. and Larsson, J. Wall-modeling in large eddy simulation: Length scales, grid resolution, and accuracy. *Physics of Fluids*, **24**(1):015105, 2012.
URL `https://dx.doi.org/10.1063/1.3678331`.

Khorrami, M. R., Choudhari, M. M., Lockard, D. P., Jenkins, L. N., and McGinley, C. B. Unsteady flowfield around tandem cylinders as prototype component interaction in airframe noise. *AIAA Journal*, **45**(8):1930–1941, 2007.
URL `https://dx.doi.org/10.2514/1.23690`. [15]

Knight, D. D. and Degrez, G. Shock wave boundary layer interactions in high Mach number flows: a critical survey of current numerical prediction capabilities. In *Hypersonic Experimental and Computational Capability, Improveent and Validation*, Vol. **AGARD Advisory Report n°319**, 1998.

Landau, L. D. On the problem of turbulence. *CR Acad. Sci. URSS*, **44**(31):1–314, 1944.

Langtry, R. B. and Menter, F. R. Correlation-based transition modeling for unstructured parallelized computational fluid dynamics codes. *AIAA Journal*, **47** (12):2894–2906, 2009.
URL `https://dx.doi.org/10.2514/1.42362`. [129 and 144]

Langtry, R. B., Menter, F. R., Likki, S. R., Suzen, Y. B., Huang, P. G., and Völker, S. A correlation-based transition model using local variables – Part II: Test cases and industrial applications. *Journal of Turbomachinery*, **128** (3):423–434, 2004.
URL `https://dx.doi.org/10.1115/1.2184353`. [144]

Langtry, R. and Menter, F. Transition modeling for general cfd applications in aeronautics. In *43rd AIAA Aerospace Sciences Meeting and Exhibit*, Reno, NV, 10-13 January 2005.
URL `https://dx.doi.org/10.2514/6.2005-522`. [144]

Langtry, R. B. *A correlation-based transition model using local variables for unstructured parallelized CFD codes*. PhD thesis, Universität Stuttgart, 2006.
URL `http://elib.uni-stuttgart.de/opus/volltexte/2006/2801`. [145]

Launder, B. E. and Sharma, B. I. Application of the energy-dissipation model of turbulence to the calculation of flow near a spinning disc. *Letters in Heat and Mass Transfer*, **1**(2):131–137, 1974.
URL `https://dx.doi.org/10.1016/0094-4548(74)90150-7`. [140]

Lee, B. H. K. Oscillatory shock motion caused by transonic shock boundary-layer interaction. *AIAA Journal*, **28**(5):942–944, 1990.
URL `https://dx.doi.org/10.2514/3.25144`.

Levy Jr., L. L. Experimental and computational steady and unsteady transonic flows about a thick airfoil. *AIAA Journal*, **16**(6):564–572, 1978.
URL `https://dx.doi.org/10.2514/3.60935`.

Lockard, D. P., Khorrami, M. R., Choudhari, M. M., Hutcheson, F. V., F., B. T., and Stead, D. J. Tandem cylinder noise predictions. In *13th AIAA/CEAS Aeroacoustics Conference (28th AIAA Aeroacoustics Conference)*, Rome, Italy, 21-23 May 2007.
URL `https://dx.doi.org/10.2514/6.2007-3450`. [16]

Lumley, J. L. The structure of inhomogeneous turbulent flows. *Atmospheric Turbulence and Radio Wave Propagation*, pages 166–178, 1967. [27]

Marcel, T. *Simulation numérique et modélisation de la turbulence statistique et hybride dans un écoulement de faisceau de tubes à nombre de Reynolds élevé dans le contexte de l'interaction fluide-structure*. PhD thesis, INP Toulouse, 2011.
URL `http://ethesis.inp-toulouse.fr/archive/00001745`. [17]

MARTINAT, G., BRAZA, M., HOARAU, Y., and HARRAN, G. Turbulence modelling of the flow past a pitching NACA0012 airfoil at 10^5 and 10^6 Reynolds numbers. *Journal of Fluids and Structures*, **24**(8):1294–1303, 2008.
URL `https://dx.doi.org/10.1016/j.jfluidstructs.2008.08.002`.

MAYLE, R. E. The role of laminar-turbulent transition in gas turbine engines. *ASME Journal of Turbomachinery*, **113**(4):509–536, 1991.
URL `https://dx.doi.org/10.1115/1.2929111`. [143]

MCDEVITT, J. B., LEVY JR., L. L., and DEIWERT, G. S. Transonic flow about a thick circular-arc airfoil. *AIAA Journal*, **14**(5):606–613, 1976.
URL `https://dx.doi.org/10.2514/3.61402`.

MENTER, F. and EGOROV, Y. A scale-adaptive simulation model using two-equation models. In *43rd AIAA Aerospace Sciences Meeting and Exhibit*, 10-13 January 2005.
URL `https://dx.doi.org/10.2514/6.2005-1095`. AIAA paper 2005-1095.

MENTER, F. R. Two-equation eddy-viscosity turbulence models for engineering applications. *AIAA Journal*, **32**(8):1598–1605, 1994.
URL `https://dx.doi.org/10.2514/3.12149`. [20, 21, 139, 141, and 144]

MENTER, F. R., ESCH, T., and KUBACKI, S. Transition modelling based on local variables. In *5th International Symposium on Turbulence Modeling and Measurements*, Mallorca, Spain, September 2002. [144]

MENTER, F. R., KUNTZ, M., and BENDER, R. A scale-adaptive simulation model for turbulent flow prediction. In *41st AIAA Aerospace Sciences Meeting and Exhibit*, 6-9 January 2003.
URL `https://dx.doi.org/10.2514/6.2003-767`. AIAA paper 2003-0767.

MENTER, F. R., LANGTRY, R. B., LIKKI, S. R., SUZEN, Y. B., HUANG, P. G., and VÖLKER, S. A correlation-based transition model using local variables – Part I: Model formulation. *Journal of Turbomachinery*, **128**(3):413–422, 2004.
URL `https://dx.doi.org/10.1115/1.2184352`. [144]

NEWHOUSE, S., RUELLE, D., and TAKENS, F. Occurrence of strange axiom A attractors near quasi periodic flows on T_m, $m \leq 3$. *Communications in Mathematical Physics*, **64**(1):35–40, 1978.
URL `https://dx.doi.org/10.1007/BF01940759`.

PARK, G. I. and MOIN, P. An improved dynamic non-equilibrium wall-model for large eddy simulation. *Physics of Fluids*, **26**(1):015108, 2014.
URL `https://dx.doi.org/10.1063/1.4861069`.

PERRIN, R., BRAZA, M., CID, E., CAZIN, S., MORADEI, F., BARTHET, A., SEVRAIN, A., and HOARAU, Y. Near-wake turbulence properties in the high Reynolds number incompressible flow around a circular cylinder measured by two- and three-component PIV. *Flow, Turbulence and Combustion*, **77**(1-4):185–204, 2006. ISSN 1386-6184.
URL `http://dx.doi.org/10.1007/s10494-006-9043-5`.

Perrin, R., Braza, M., Cid, E., Cazin, S., Barthet, A., Sevrain, A., Mockett, C., and Thiele, F. Obtaining phase averaged turbulence properties in the near wake of a circular cylinder at high Reynolds number using POD. *Experiments in Fluids*, **43**(2-3):341–355, 2007.
URL `https://dx.doi.org/10.1007/s00348-007-0347-6`. [14]

Persillon, H. and Braza, M. Physical analysis of the transition to turbulence in the wake of a circular cylinder by three-dimensional Navier-Stokes simulation. *Journal of Fluid Mechanics*, **365**:23–88, 1998.
URL `https://dx.doi.org/10.1017/S0022112098001116`. [14]

Picheny, V., Ginsbourger, D., and Richet, Y. Noisy expected improvement and on-line computation time allocation for the optimization of simulators with tunable fidelity. In *2nd Int. Conf. on Engineering Optimization*, 2010.

Roe, P. L. Approximate Riemann solvers, parameter vectors, and difference schemes. *Journal of Computational Physics*, **43**(2):357–372, 1981.
URL `https://dx.doi.org/10.1016/0021-9991(81)90128-5`.

Roshko, A. On the drag and shedding frequency of two-dimensional bluff bodies. Technical Report 3169, NACA technical note, 1954. [14]

Rung, T., Bunge, U., Schatz, M., and Thiele, F. Restatement of the Spalart-Allmaras eddy-viscosity model in strain-adaptive formulation. *AIAA Journal*, **41** (7):1396–1399, 2003.
URL `https://dx.doi.org/10.2514/2.2089`.

Sacks, J., Welch, W. J., Mitchell, T. J., and Wynn, H. P. Design and analysis of computer experiments. *Statistical Science*, **4**(4):409–423, 1989.
URL `http://www.jstor.org/stable/2245858`.

Sayadi, T., Hamman, C. W., and Moin, P. Direct numerical simulation of complete H-type and K-type transitions with implications for the dynamics of turbulent boundary layers. *Journal of Fluid Mechanics*, **724**:480–509, 2013.
URL `https://dx.doi.org/10.1017/jfm.2013.142`.

Seegmiller, H. L., Marvin, J. G., and Levy Jr., L. L. Steady and unsteady transonic flow. *AIAA Journal*, **16**(12):1262–1270, 1978.
URL `https://dx.doi.org/10.2514/3.61042`.

Shinde, V., Marcel, T., Hoarau, Y., Deloze, T., Harran, G., Baj, F., Cardolaccia, J., Magnaud, J.-P., Longatte, E., and Braza, M. Numerical simulation of the fluid–structure interaction in a tube array under cross flow at moderate and high Reynolds number. *Journal of Fluids and Structures*, **47**: 99–113, 2014.
URL `https://dx.doi.org/10.1016/j.jfluidstructs.2014.02.013`. [43 and 49]

Shur, M., Strelets, M., Zaikov, L., Gulyaev, A., KozIov, V., and Secundov, A. Comparative numerical testing of one- and two-equation turbulence models for flows with separation and reattachement. In *33rd Aerospace Sciences*

Meeting and Exhibit, Reno, NV, USA, 9-12 January 1995.
URL `https://dx.doi.org/10.2514/6.1995-863`. AIAA 95-0863. [137]

Shur, M. L., Spalart, P. R., Strelets, M. K., and Travin, A. K. A hybrid RANS-LES approach with delayed-DES and wall-modelled LES capabilities. *International Journal of Heat and Fluid Flow*, **29**(6):1638–1649, 2008.
URL `https://dx.doi.org/10.1016/j.ijheatfluidflow.2008.07.001`. [132]

Sirovich, L. Turbulence and the dynamics of coherent structures, Parts I, II & III. *Quarterly of Applied Mathematics*, **XLV**(3):561–582, 1987. [27]

Skopek, M. G., Braza, M., Hoarau, Y., and Thiele, F. Hybrid RANS-LES modeling of a strongly detached turbulent flow around a tandem cylinders configuration. In *Progress in Hybrid RANS-LES Modelling*, Vol. **117** of *Notes on Numerical Fluid Mechanics and Multidisciplinary Design*, pages 219–229. Springer, 2012. [41, 42, 45, and 49]

Spalart, P. R. Trends in turbulence treatments. In *Fluids 2000 Conference and Exhibit*, Denver, CO, USA, 19-22 June 2000. AIAA Paper 2000-2306. [138]

Spalart, P. R. and Allmaras, S. R. A one-equation turbulence model for aerodynamic flows. *Recherche Aérospatiale*, **1**:5–21, 1994. [21, 135, 136, and 137]

Spalart, P. R. and Rumsey, C. L. Effective inflow conditions for turbulence models in aerodynamic calculations. *AIAA Journal*, **45**(10):2544–2553, 2007.
URL `https://dx.doi.org/10.2514/1.29373`. [136]

Spalart, P. R., Jou, W.-H., Strelets, M., and Allmaras, S. R. Comments on the feasibility of LES for wings, and on a hybrid RANS/LES approach. In Liu, C. and Liu, Z., editors, *Advances in LES/DNS*, pages 137–147, Louisiana Tech University, 1997. Greyden Press.

Spalart, P. R., Deck, S., Shur, M. L., Squires, K. D., Strelets, M. K., and Travin, A. A new version of detached-eddy simulation, resistant to ambiguous grid densities. *Theoretical and Computational Fluid Dynamics*, **20**(6): 181–195, 2006.
URL `https://dx.doi.org/10.1007/s00162-006-0015-0`.

Sutherland, W. The viscosity of gases and molecular force. *Philosophical Magazine, Series 5*, **36**(223):507–531, 1893. [7]

Szubert, D., Ashton, N., van Veen, W., Grossi, F., Hoarau, Y., Braza, M., Giepman, R., Schrijer, F., and van Oudheusden, B. Physics and modelling of the transonic and supersonic shock wave boundary layer interaction of oblique and normal shock at high Reynolds number. In *10th International ERCOFTAC Symposium on Engineering Turbulence Modelling and Measurements*, ERCOFTAC, Marbella, Spain, 17-19 September 2014a.

Szubert, D., Jang, I., Park, G. I., and Braza, M. Numerical simulations of oblique shock/boundary-layer interaction at a high Reynolds number. In *Proceedings of the Summer Program 2014*, pages 489–498, Center for Turbulence

Research, Stanford, CA, July - August 2014b.
URL `https://ctr.stanford.edu/Summer/SP14/09_Large-eddy_simulation/13_szubert.pdf`. [117 and 132]

Szubert, D., Asproulias, I., Grossi, F., Duvigneau, R., Hoarau, Y., and Braza, M. Numerical study of the turbulent transonic interaction and transition location effect involving optimisation around a supercritical airfoil. *European Journal of Mechanics – B/Fluids*, 2015a.
URL `https://dx.doi.org/10.1016/j.euromechflu.2015.09.007`. [131]

Szubert, D., Grossi, F., Jimenez Garcia, A., Hoarau, Y., Hunt, J. C. R., and Braza, M. Shock-vortex shear-layer interaction in the transonic flow around a supercritical airfoil at high reynolds number in buffet conditions. *Journal of Fluids and Structures*, **55**:276–302, 2015b.
URL `https://dx.doi.org/10.1016/j.jfluidstructs.2015.03.005`. [11, 16, 45, 52, 130, and 131]

Taveira, R. R. and da Silva, C. B. Characteristics of the viscous superlayer in shear free turbulence and in planar turbulent jets. *Physics of Fluids*, **26**(2): 021702, 2014.
URL `https://dx.doi.org/10.1063/1.4866456`.

Thiery, M. and Coustols, E. URANS computations of shock-induced oscillations over 2D rigid airfoils: Influence of test section geometry. *Flow, Turbulence and Combustion*, **74**(4):331–354, 2005. ISSN 1386-6184.
URL `https://dx.doi.org/10.1007/s10494-005-0557-z`.

Touber, E. and Sandham, N. D. Oblique shock impinging on a turbulent boundary layer: Low-frequency mechanisms. In *38th Fluid Dynamics Conference and Exhibit*, AIAA, Seattle, WA, 23-26 June 2008.
URL `https://dx.doi.org/10.2514/6.2008-4170`.

Toyoda, A., Misaka, T., and Obayashi, S. An application of local correlation-based transition model to JAXA high-lift configuration model. In *25th AIAA Applied Aerodynamics Conference*, Miami, FL, 25-28 June 2007.
URL `https://dx.doi.org/10.2514/6.2007-4286`. [144]

van Driest, E. R. Turbulent boundary layer in compressible fluids. *Journal of the Aeronautical Sciences*, **18**(3):145–160, 1951.
URL `https://dx.doi.org/10.2514/8.1895`.

van Driest, E. R. and Blumer, C. B. Boundary layer transition: Freestream turbulence and pressure gradient effects. *AIAA Journal*, **1**(6):1303–1306, 1963.
URL `https://dx.doi.org/10.2514/3.1784`. [144]

van Leer, B. Towards the ultimate conservative difference scheme. V. A second-order sequel to Godunov's method. *Journal of Computational Physics*, **32**(1): 101–136, 1979.
URL `https://dx.doi.org/10.1016/0021-9991(79)90145-1`.

Vreman, A. An eddy-viscosity subgrid-scale model for turbulent shear flow: Algebraic theory and applications. *Physics of Fluids*, **16**(10):3670–3681, 2004.
URL https://dx.doi.org/10.1063/1.1785131.

Warren, E. and Hassan, H. Alternative to the e^N method for determining onset of transition. *AIAA journal*, **36**(1):111–113, 1998.
URL https://dx.doi.org/10.2514/2.361. [143]

Weiss, J. M. and Smith, W. A. Preconditioning applied to variable and constant density flows. *AIAA Journal*, **33**(11):2050–2057, 1995.
URL https://dx.doi.org/10.2514/3.12946. [17]

Welch, P. D. The use of fast fourier transform for the estimation of power spectra: a method based on time averaging over short, modified periodograms. *IEEE Transactions on audio and electroacoustics*, **15**(2):70–73, 1967. [23]

Westerweel, J., Fukushima, C., Pedersen, J. M., and Hunt, J. C. R. Momentum and scalar transport at the turbulent/non-turbulent interface of a jet. *Journal of Fluid Mechanics*, **631**:199–230, 2009.
URL https://dx.doi.org/10.1017/S0022112009006600.

Wilcox, D. C. Reassessment of the scale-determining equation for advanced turbulence models. *AIAA journal*, **26**(11):1299–1310, 1988.
URL https://dx.doi.org/10.2514/3.10041. [139 and 140]

Williamson, C. H. K. The natural and forced formation of spot-like ‘vortex dislocations’ in the transition of a wake. *Journal of Fluid Mechanics*, **243**:393–441, 1992.
URL https://dx.doi.org/10.1017/S0022112092002763. [14]

Physics and modelling of unsteady turbulent flows around aerodynamic and hydrodynamic structures at high Reynold number by numerical simulation

This thesis aims at analysing the predictive capabilities of statistical URANS and hybrid RANS-LES methods to model complex flows at high Reynolds numbers and carrying out a physical analysis of the near-region turbulence and coherent structures. This study handles configurations included in the European research programmes ATAAC (Advanced Turbulent Simulation for Aerodynamics Application Challenges) and TFAST (Transition Location Effect on Shock Wave Boundary Layer Interaction). First, the detached flow in a configuration of a tandem of cylinders, positionned behind one another, is investigated at Reynolds number 166000. A static case, corresponding to the layout of the support of a landing gear, is initially considered. The fluid-structure interaction is then studied in a dynamic case where the downstream cylinder, situated in the wake of the upstream one, is given one degree of freedom in translation in the crosswise direction. A parametric study of the structural parameters is carried out to identify the various regimes of interaction. Secondly, the physics of the transonic buffet is studied by means of time-frequency analysis and proper orthogonal decomposition (POD), in the Mach number range 0.70–0.75. The interactions between the main shock wave, the alternately detached boundary layer and the vortices developing in the wake are analysed. A stochastic forcing, based on reinjection of synthetic turbulence in the transport equations of kinetic energy and dissipation rate by using POD reconstruction, has been introduced in the so-called organised-eddy simulation (OES) approach. This method introduces an upscale turbulence modelling, acting as an eddy-blocking mechanism able to capture thin shear-layer and turbulent/non-turbulent interfaces around the body. This method highly improves the aerodynamic forces prediction and opens new ensemble-averaged approaches able to model the coherent and random processes at high Reynolds number. Finally, the shock-wave/boundary-layer interaction (SWBLI) is investigated in the case of an oblique shock wave at Mach number 1.7 in order to contribute to the so-called “laminar wing design” studies at European level. The performance of statistical URANS and hybrid RANS-LES models is analysed with comparison, with experimental results, of integral boundary-layer values (displacement and momentum thicknesses) and wall quantities (friction coefficient). The influence of a transitional boundary layer on the SWBLI is featured.

Keywords: URANS, hybrid RANS-LES methods, fluid-structure interactions, transonic buffet, shock-wave/boundary-layer interaction, laminar-turbulent transition, proper orthogonal decomposition, time-frequency analysis, wavelets, stochastic forcing.

Analyse physique et modélisation d’écoulements turbulents instationnaires autour d’obstacles aérodynamiques et hydrodynamiques à haut nombre de Reynolds par simulation numérique

Les objectifs de cette thèse sont d’étudier les capacité prédictive des méthodes statistiques URANS et hybrides RANS-LES à modéliser des écoulements complexes à haut nombre de Reynolds et de réaliser l’analyse physique de la turbulence et des structures cohérentes en proche paroi. Ces travaux traitent de configurations étudiées dans le cadre des projets européens ATAAC (Advanced Turbulent Simulation for Aerodynamics Application Challenges) et TFAST (Transition Location Effect on Shock Wave Boundary Layer Interaction). Premièrement, l’écoulement décollé autour d’une configuration de cylindre en tandem, positionnés l’un derrière l’autre, est étudiée à un nombre de Reynolds de 166000. Un cas statique, correspondant schématique aux support de train d’atterrissage, est d’abord considéré. L’interaction fluide-structure est ensuite étudiée dans le cas dynamique, dans lequel le cylindre aval possède un degré de liberté en translation dans la direction perpendiculaire à l’écoulement. Une étude paramétrique est menée afin d’identifier les différents régimes d’interaction en fonction des paramètres structuraux. Dans un deuxième temps, la physique du tremblement transsonique est étudiée au moyen d’une analyse temps-fréquence et d’une décomposition orthogonale en modes propres (POD), dans l’intervalle de nombre de Mach 0.70–0.75. Les interactions entre le choc principal, la couche limite décollée par intermittence et les tourbillons se développant dans le sillage, sont analysées. Un forçage stochastique, basée sur une réinjection de turbulence synthétique dans les équations de transport de l’énergie cinétique et du taux de dissipation générée à partir de la reconstruction POD, a été introduit dans l’approche OES (organised-eddy simulation). Cette méthode introduit une modélisation de la turbulence “upscale” agissant comme un mécanisme de blocage par tourbillons capable de prendre en compte les interfaces turbulent/non-turbulent et de couches de cisaillement autour des géométries. Cette méthode améliore grandement la prédiction des forces aérodynamiques et ouvre de nouvelles perspectives quant aux approaches de type moyennes d’ensemble pour modéliser les processus cohérents et aléatoires à haut nombre de Reynolds. Enfin, l’interaction onde de choc/couche limite (SWBLI) est traitée, dans le cas d’un choc oblique à nombre de Mach 1.7, contribuant aux études de “design d’ailes laminaires” au niveau européen. Les performances des modèles URANS et hybrides RANS-LES ont été analysées en comparant, avec les résultats expérimentaux, les valeurs intégrales de la couche limite (épaisseurs de déplacement et de quantité de mouvement) et les valeurs à la paroi (coefficient de frottement). Les effets de la transition dans la couche limite sur l’interaction choc/couche limite sont caractérisés.

Mots-clés : URANS, méthodes hybrides RANS-LES, interactions fluide-structure, tremblement transsonique, interaction onde de choc/couche limite, transition laminaire-turbulent, décomposition orthogonale en modes propres, analyse temps-fréquence, ondelettes, forçage stochastique.